

# Structural properties of organometallic halide perovskite and their application in photodetectors

Présentée le 26 juin 2020

à la Faculté des sciences de base  
Laboratoire de physique de la matière complexe  
Programme doctoral en physique

pour l'obtention du grade de Docteur ès Sciences

par

**Anastasiia GLUSHKOVA**

Acceptée sur proposition du jury

Prof. F. Courbin, président du jury  
Prof. L. Forró, directeur de thèse  
Dr R. Pugin, rapporteur  
Prof. F. Simon, rapporteur  
Prof. G. Chapuis, rapporteur





The man who believes he knows everything  
learns nothing  
— Manson

To those who inspired it  
and will not read it. . .

And Joachim,  
he said he would..  
and made it.



# Acknowledgements

During the last 3.5 years I've learned a lot due to the people around me. With their help I could fully appreciate the journey towards the achievement of the PhD degree and become the person I am today. So they can't escape my acknowledgments now.

First of all, I would like to thank my thesis director, Laszlo Forro, for giving me the chance to work on all possible interesting projects in his lab. His door was always open for me to receive further guidance or even advice on spelling or how to shake a hand.

Secondly, the thesis jury for accepting to be a part of my exam and for their constructive comments, which helped to improve this manuscript.

I want to thank all people in the lab for the time we had. Without Alla I would not get into crystallography, her passion to it is contagious. She was kind to me and helped me a lot through these years on so many levels. Gaetan for being that guy who will help me out any time on the slope. Kostya M. for all the help with the Hall setup which is, surprisingly, working and many fruitful work together. Kostya S. for always being ready to discuss physics in the corridors, I felt welcome to intrude your office at any moment. Especially I would like to say thank you to Pavao and Endre, with whom I worked a lot on the biggest project for this thesis. They taught me a lot. Including improvement in my writing: "the cation can't fit into inorganic framework" - leave it for Sat beer explanation (c) Endre.

I am grateful to Michael Zervas for building up my attitude towards the work in the cleanroom and teaching. His "just think" helped a lot in understanding and discussing why something does not work.

I would like to say "thank you" to Martina, Michael and Gedis for pushing my limits to another level. King Hendrik will always rock.

I am grateful to my old great dorm-mate and dear friend Anya, who made this ten years of academic life easier to go through. Through time and distance I feel her support. It's amazing to have her as a friend.

I am grateful to Evgenii for the last decade of my life. For all the support and great moments together. For helping me on the way to get where I am today.

There is a special gratitude to Vladislav Adadurov, Winnie, the math teacher, who is not here. He made me believe I can do it.

I would like to thank my family for their support, patience and faith. For being there for me. I would like to acknowledge my granddad, Andrey, who is not here, for making me play chess before I could read properly. Somewhere on the way he made me want to become a electrical-engineer as he was. To my brother, Vova, who pushed me to aim for the best technical university in Russia. To Olga, who made my days in Switzerland brighter. And to my parents, Natalia and Vladimir, who were amazed with the results that they did not expect to happen.

Finally, I would like to thank Joachim, a true model of will and hard work. But mostly I am grateful for his tremendous care and understanding at difficult times in my life.

## Acknowledgements

---

*Lausanne, May 28, 2020*

A. G.

# Abstract

Hybrid organometallic halide perovskites have been intensively investigated in the past years as highly efficient light harvesters for various optoelectronic applications for both sensing and emitting light. However, many open questions remain regarding the crystallization process, environmental impact and implementation of the material into electrical circuits.

The central theme of this PhD dissertation is the structural characterization of hybrid organic-inorganic perovskites and device fabrication based on these materials. The focus is on methylammonium lead iodide,  $\text{CH}_3\text{NH}_3\text{PbI}_3$  as one of the most efficient photovoltaic materials.

External factors such as temperature, pressure, humidity, etc. affect the materials properties. Thus, it is crucial to study their influence for further applications. In this thesis, it will be shown, that under high pressure (20 GPa) inert gases as Ar and Ne form high-pressure-induced compounds with  $\text{CH}_3\text{NH}_3\text{PbI}_3$ . For Ne pressure transmitting media such high-pressure transformation is reversible and the Ne-incorporated compound is even stable at ambient conditions after decompression.

We show that when the material undergoes repeated phase transitions during thermal cycling around both 330 and 160 K,  $\text{CH}_3\text{NH}_3\text{PbI}_3$  does not return to the initial state. Instead, at 330 K, the crystal stabilizes an incommensurately modulated tetragonal phase with successive transitions. On the other hand, performing thermal cycling around 160 K generates an increase in the concentration of domains of different phases.

In addition, we studied the influence of thermal treatment on the crystal structure in the absence of any phase transition. For that reason, the lower dimensional compound of  $\text{NH}_3\text{CH}_2\text{CH}_2\text{NH}_3\text{PbI}_4$  was synthesized and characterized before and after annealing process. We observe and discuss a correlation between photoconductivity and increased disorder.

In this work a novel approach of aerosol jet printing deposition of  $\text{CH}_3\text{NH}_3\text{PbI}_3$  has been developed. Making use of intermediate phases of the crystallization process, this deposition method enables the creation of 3D structures of organic-inorganic perovskites on various surfaces. This technique was successfully used in the fabrication of heterostructures based on  $\text{CH}_3\text{NH}_3\text{PbI}_3$  and graphene. Due to large trap-assisted photogain, these heterostructures are very promising for photoconductors. Taking into account the strong X-ray stopping power of the high atomic number Pb and I, devices based on  $\text{CH}_3\text{NH}_3\text{PbI}_3$ /graphene heterostructures are excellent for X-ray detection. Such X-ray detectors demonstrate a record high sensitivity value of  $2.2 \times 10^8 \mu\text{C Gy}^{-1}\text{cm}^{-2}$ .

**Keywords:** Hybrid organometallic halide perovskite, methylammonium lead iodide, XRD, X-ray detector, photodetectors, nanowire, solution growth, thermal cycling, aerosol jet printing, 3D printing.



# Résumé

Les pérovskites aux halogénures organométalliques hybrides ont fait l'objet d'une recherche intense au cours des dernières années en tant que collecteurs de lumière hautement efficaces pour diverses applications optoélectroniques, à la fois pour la détection et l'émission de lumière. Cependant, de nombreuses questions restent ouvertes concernant le processus de cristallisation, l'impact environnemental et la mise en œuvre du matériau dans les circuits électroniques. Le thème central de cette thèse est la caractérisation structurale des pérovskites hybrides organiques-inorganiques et la fabrication des dispositifs basés sur ces matériaux. Le sujet principal est l'iodure de plomb méthylammonium,  $\text{CH}_3\text{NH}_3\text{PbI}_3$  qui est un des matériaux photovoltaïques les plus efficaces.

Des facteurs externes tels que la température, la pression, l'humidité, etc. affectent les propriétés de ces matériaux. Ainsi, il est important d'étudier l'influence de ces paramètres sur la structure cristalline. Dans cette thèse, il sera montré que sous haute pression (20 GPa) des gaz inertes comme Ar et Ne forment des composants induits par haute pression avec  $\text{CH}_3\text{NH}_3\text{PbI}_3$ . En utilisant le Ne comme moyen de transfert de pression, cette transformation à haute pression est réversible et les atomes de Ne incorporés dans la structure rendent le composant stable aux conditions ambiantes après décomposition.

Nous montrons que lors de l'application de plusieurs transitions de phases répétées pendant des cycles thermiques autour de 330 et autour de 160 K,  $\text{CH}_3\text{NH}_3\text{PbI}_3$  ne revient pas à l'état initial. Plutôt, à 330 K, le cristal stabilise dans une phase tétragonale modulée de façon incommensurable après plusieurs transitions successives. Dans le cas où on effectue un cycle thermique autour de 160 K on génère une augmentation de la concentration des domaines de phases différentes.

De plus, nous avons étudié l'influence du traitement thermique sur la structure cristalline dans l'absence de transition de phase. Pour cette raison, le composant 2D  $\text{NH}_3\text{CH}_2\text{CH}_2\text{NH}_3\text{PbI}_4$  a été synthétisé et caractérisé avant et après le processus de recuit. Nous observons et discutons une corrélation entre la photoconductivité et l'augmentation du désordre.

Dans ce travail, une nouvelle technique de dépôt : l'impression par jet d'aérosol du  $\text{CH}_3\text{NH}_3\text{PbI}_3$  a été développée. Utilisant des phases intermédiaires du processus de cristallisation, cette méthode de dépôt permet la création des structures 3D des pérovskites organiques-inorganiques sur différents substrats. Nous avons utilisée cette technique utilisée avec succès dans la fabrication d'hétérostructures à base de  $\text{CH}_3\text{NH}_3\text{PbI}_3$  et de graphène. Grâce à la grande photogain assistée par les défauts, ces hétérostructures sont très prometteuses pour les photoconducteurs. En plus, le fort pouvoir d'arrêt des rayons X, lié au nombre atomique élevé du Pb et du I, les hétérostructures  $\text{CH}_3\text{NH}_3\text{PbI}_3$ /graphène sont excellentes pour la détection des rayons X. Ces détecteurs à rayons X ont une sensibilité record de  $2.2 \times 10^8 \mu\text{C Gy}^{-1} \text{cm}^{-2}$ .

**Mots clés :** Perovskite halogénure organométallique hybride, iodure de plomb méthylammo-

## Résumé

---

nium, DRX, détecteur de rayons X, photodétecteurs, nanofil, cristallisation depuis une solution, cyclage thermique, impression par jet d'aérosol, impression 3D.



# Contents

<b>Acknowledgements</b>	<b>i</b>
<b>Abstract (English/Français)</b>	<b>iii</b>
<b>Introduction</b>	<b>1</b>
<b>I Hybrid organic-inorganic perovskites and relative compounds</b>	<b>7</b>
<b>1 Methylammonium lead halide compounds</b>	<b>9</b>
1.1 Crystal structure . . . . .	9
1.1.1 General perovskite structure . . . . .	9
1.1.2 Structural transition . . . . .	10
1.2 Electronic structure . . . . .	10
1.2.1 Electronic bandgap . . . . .	11
1.2.2 Charge carriers . . . . .	11
1.2.3 Carrier mobility and lifetime . . . . .	13
1.2.4 Ionic transport . . . . .	14
1.2.5 Tuning the electronic properties by chemical engineering . . . . .	14
1.2.6 Stability . . . . .	16
1.3 Crystallization process . . . . .	17
1.3.1 Intermediate phases . . . . .	18
1.3.2 Structure refinement . . . . .	19
<b>2 Effect of thermal cycling on structural evolution</b>	<b>25</b>
2.1 Structural transformations of MAPbX <sub>3</sub> in temperature . . . . .	25
2.2 The low-temperature tetragonal to orthorhombic phase transition . . . . .	26
2.2.1 X-ray data . . . . .	27
2.2.2 Resistivity measurements . . . . .	30
2.2.3 Heat capacity measurements . . . . .	31
2.3 The high-temperature tetragonal to cubic phase transition . . . . .	32
2.3.1 X-ray data . . . . .	32
2.3.2 Resistivity measurements . . . . .	38
2.3.3 Heat capacity measurements . . . . .	39
2.4 Conclusions . . . . .	40
<b>3 Pressure-induced transformation of CH<sub>3</sub>NH<sub>3</sub>PbI<sub>3</sub></b>	<b>43</b>
3.1 Single-crystal XRD experiments . . . . .	45
3.1.1 The high-pressure NeMAPbI <sub>3</sub> compounds . . . . .	47
3.1.2 The high-pressure ArMAPbI <sub>3</sub> compounds . . . . .	51

## Contents

---

3.2	Impact of Ne and Ar pressure transmitting medium . . . . .	52
3.2.1	Influence of Ne and Ar on the MA cation mobility . . . . .	53
3.3	Conclusions . . . . .	54
<b>4</b>	<b>Influence of the cation disorder on the crystal properties</b>	<b>55</b>
4.1	Crystallization of ethylenediammonium lead iodide . . . . .	56
4.1.1	Chemical composition . . . . .	57
4.1.2	Thermogravimetry . . . . .	57
4.2	Single crystal XRD . . . . .	58
4.2.1	Structure solution and refinement . . . . .	58
4.3	Photocurrent measurements . . . . .	62
4.4	Influence of the organic cation disorder on photoconductivity . . . . .	62
4.4.1	Disorder of the organic cation in the thermally treated crystal . . . . .	63
4.4.2	Correlation between the organic cation disorder and photoconductivity .	65
4.4.3	Stability of crystals against moisture . . . . .	65
4.5	Conclusions . . . . .	66
<b>II</b>	<b>Photodetector fabrication</b>	<b>67</b>
<b>5</b>	<b>3D Aerosol jet printing of hybrid halide perovskites</b>	<b>69</b>
5.1	Aerosol jet printing deposition . . . . .	69
5.2	Solution preparation and 3D printing . . . . .	71
5.2.1	Fluorescence . . . . .	73
<b>6</b>	<b>Characterization of aerosol-jet-printed MAPbI<sub>3</sub> photodetectors</b>	<b>75</b>
6.1	X-ray imaging . . . . .	75
6.2	Photocurrent measurements under VIS . . . . .	76
6.3	Heterostructures based on aerosol-jet-printed MAPbX <sub>3</sub> . . . . .	77
6.3.1	Graphene . . . . .	77
6.3.2	MAPbX <sub>3</sub> -graphene interface . . . . .	78
6.3.3	Photodetector architecture . . . . .	79
6.4	X-ray photodetector . . . . .	81
6.4.1	Sensitivity . . . . .	86
6.5	Conclusions . . . . .	87
	<b>Conclusions</b>	<b>89</b>
	<b>Outlook</b>	<b>91</b>
<b>A</b>	<b>Appendix: X-ray diffraction</b>	<b>93</b>
A.1	XRD experiments background . . . . .	93
A.1.1	X-ray data . . . . .	95
A.1.2	Reliability index . . . . .	97
A.1.3	Peak width . . . . .	98

A.1.4	Commensurated and incommensurated modulations . . . . .	98
A.2	XRD measurements details . . . . .	100
A.3	Refinements details . . . . .	102
A.4	Crystallographic tables . . . . .	106
<b>B</b>	<b>Appendix: Experimental details</b>	<b>113</b>
B.1	Synthesis . . . . .	113
B.2	Dose-rate calibration . . . . .	113
B.3	Temperature dependent resistivity measurements . . . . .	114
B.4	Two-point resistivity measurements under VIS and X-ray illumination . . . . .	115
B.5	Thermogravimetric analysis . . . . .	117
B.6	Heat capacity measurements . . . . .	118
<b>C</b>	<b>Appendix: Fabrication</b>	<b>119</b>
C.1	Electron beam lithography . . . . .	119
C.2	Ion beam etching . . . . .	120
C.3	Lift-off . . . . .	121
<b>D</b>	<b>Appendix: Humidity sensor based on methylammonium bismuth bromide</b>	<b>123</b>
D.1	Methylammonium bismuth bromide . . . . .	123
D.1.1	Synthesis . . . . .	123
D.1.2	Crystal structure . . . . .	124
D.2	Sensor characterisation . . . . .	125
D.2.1	Detection range . . . . .	126
D.2.2	Stability . . . . .	127
D.2.3	Humidity response time . . . . .	127
D.3	Conclusion . . . . .	130
	<b>Bibliography</b>	<b>131</b>
	<b>Curriculum Vitae</b>	<b>147</b>



# List of Acronyms

0...3D	0...3 dimensional	IR	Infrared
ADP	Atomic displacement parameters	MA	Methylammonium
AJP	Aerosol jet printing	MAPbBr <sub>3</sub>	Methylammonium lead bromide
CB	Conduction band	MAPbCl <sub>3</sub>	Methylammonium lead chloride
CIF	Crystallographic information file	MAPbI <sub>3</sub>	Methylammonium lead iodide
CSD	Cambridge structural database	MRI	Magnetic resonance imaging
CT	Computed tomography	Ort-1	Orthorhombic phase
CW	Continuous wave	Ort-2	Boundary (orthorhombic) phase
DAC	Diamond anvil cell	PDMS	Polydimethylsiloxane
DC	Direct current	P(MMA)	Poly(methyl methacrylate)
DMA	Dimethylacetamide	ppm	Parts per million
DMF	Dimethylformamide	PTM	Pressure transmitting media
DMSO	Dimethyl sulfoxide	PV	Photovoltaics
ED	Ethylenediammonium	(P)XRD	(Powder) X-ray diffraction
EDPbI <sub>4</sub>	Ethylenediammonium lead iodide	RH	Relative humidity
EDX	Energy dispersive X-ray	SEM	Scanning electron microscopy
e-beam	Electron beam	Tetr	Tetragonal phase
FWHM	Full width at half maximum	TGA	Thermogravimetric analysis
GBL	$\gamma$ -butyrolactone	UV	Ultraviolet
GOF	Goodness of fit	VB	Valence band
IBE	Ion beam etching	V <sub>OC</sub>	Open-circuit voltage
		VIS	Visible light



# List of Symbols

<b>a, b, c</b>	Basis vectors of the direct lattice	$I_{dark}$	Current in the dark
$a, b, c, \alpha, \beta, \gamma$	Unit cell parameters	$I_{light}$	Total current under illumination
<b>a*, b*, c*</b>	Basis of a reciprocal lattice	$I_{ph}$	Photocurrent
$\alpha_a$	Absorption coefficient	$k_1, k_2, k_3$	Contribution of the Tetr, Ort, and Ort-1 phases
<b><math>\alpha, \gamma</math></b>	Coefficients in modulation vector	$k_B$	Boltzmann constant
$C_p$	Heat capacity	$\lambda$	Wavelength
$d$	Interplanar distance of neighbouring net planes	$\mu$	Carrier mobility
	$(h, k, l)$	$\sigma$	Charge plane density
E	Energy	$m_0$	Free electron mass
$E_B$	Binding energy	$m_{e(h)}^*$	Electron (hole) effective mass
$E_g$	Bandgap energy	$c$	Vacuum speed of light
$e$	Elementary charge	$P$	Pressure
e-h	Electron-hole pair	$p$	Momentum
$\eta$	Efficiency	$\mathbf{q}_i$	Modulation vector
$f(\mathbf{H})$	Atomic scattering factor	$Rl, Rint, wR$	Reliability factors
$F(\mathbf{H})$ or $F(h, k, l)$	Structure factor	$R_A, R_M, R_X$	ionic radii of A, M and X sites
Gy	Unit of ionizing radiation dose	$\rho$	Charge density
$h, k, l$	Laue indices : indices of the Bragg reflection from the set of parallel equidistant net planes $(h, k, l)$	$S$	Entropy
		$S_x$	Sensitivity
		$t$	Goldschmidt's tolerance factor
$(h, k, l)$	Miller indices : indices of a single net plane in a crystal	$T$	Temperature
<b>H</b>	Vector from Fourier module for a modulated phase	$\tau$	Scattering time
		$\tau_r$	Carrier lifetime
$I-V$	Current vs. voltage	$v$	Velocity
$J-V$	Current density vs. voltage	$V(avr)$	Average unit cell volume
$I(\mathbf{H})$	Scattering intensity	$Z$	Atomic number





# Introduction

After two centuries of vast energy consumption and greenhouse gas emissions, our society faces several serious challenges to maintain our quality of life in a sustainable way. In order to fulfill the ever-growing energy demands for electricity, transport, heating, cooling, etc., we need to continue developing new technologies.

Another challenge of perpetual importance is health. Science should help the population to have a better healthcare with new concepts for better devices, for example, X-ray machines using less harmful X-rays for medical imaging.

This thesis work contributes to a technical solution for both of these challenges.

Today, more than half of the world's energy comes from fossil fuels extracted from the ground. The amount of released carbon dioxide due to burning of coal, oil and gas is the leading contributor to climate change [1]. Therefore, we have to develop electrical energy production forms which drastically reduce CO<sub>2</sub> emission, with renewable energy sources like solar, wind, geothermal etc. Of these, sunlight has an enormous weight, since Earth receives more energy from the Sun in one hour than the world uses in one year [2]. We have to convert just a fraction of it into electricity!

Solar cells provide exactly this conversion. They use the photovoltaic (PV) effect, which converts light into electric energy. In a semiconductor, which is used as the active material in a solar cell, electrons do not move easily, they are bound to the atoms. In order to make them propagate in the material, electrons need some external energy input to leave the nuclei. In a solar cell, this is provided by the sunlight, which can be described as light particles, called photons, that carry different, but well-defined energy. The minimum energy to knock electrons free varies from one material to another, and is called the bandgap. Upon illumination, photons, with energies higher than the bandgap, free electrons, which will allow a current to flow in the material, towards the contacts and to the electric circuit. How easily the electrons flow in the semiconducting material, what current density could they produce, in other words what is the efficiency of the photon to produce a flowing electron, depends on many things: on the structure of the material, defects, impurities, etc. For example, in the most popular Si-based solar cells, the improvement of the material was progressing from the mid-seventies to nowadays steadily, and the efficiency ( $\eta$ ), how well the photon energy could be transformed into electrical current, reached the record value of 26% [3] (see Figure 1). This is the case for Si single crystal, a "perfect" material, but when in the amorphous form, so the Si atoms are not ordered (which is the case for the cheaper commercial solar panels),  $\eta$  is only in the 16-17% range.

There is a strong drive among scientists to find novel materials which have high efficiency, while being easy and cheap to produce. In 2012, perovskites brought a lot of excitement, since  $\eta$  of methylammonium lead iodide ( $\text{CH}_3\text{NH}_3^+\text{PbI}_3$ , abbreviated as MAPbI<sub>3</sub>) was above 10%, a

## Introduction

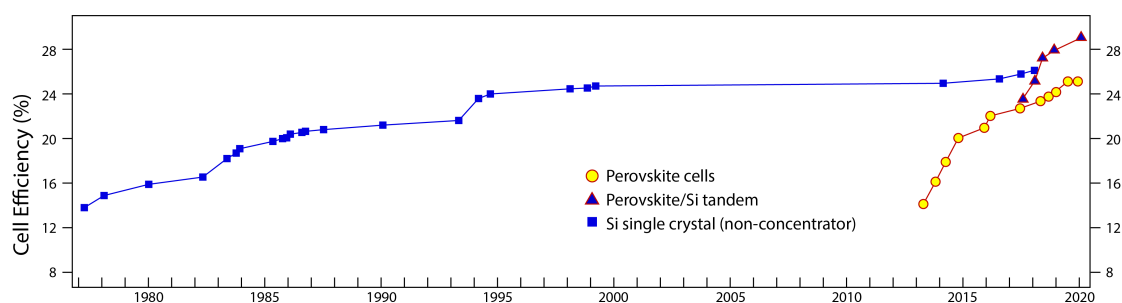
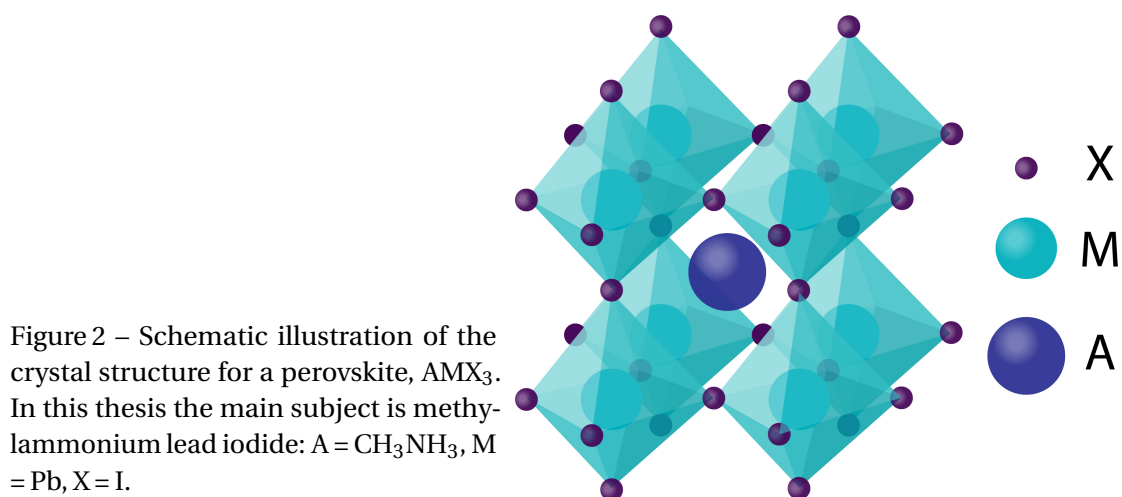


Figure 1 – The development . The improvement of the Si and  $\text{CH}_3\text{NH}_3\text{PbI}_3$ -based solar cells efficiency with years. Its increase is due to the improvement of the material quality and of the architecture of the device. The combination of the two in one device, called tandem cell, reached 29.1 % (selected part of the National Renewable Energy Laboratory (NREL) Efficiency chart).



very good starting point for further improvement [4]. The chemical formula of hybrid organic-inorganic perovskites is  $\text{AMX}_3$ , the sketch of its structure is in Figure 2. It can be represented as an organic cation in an inorganic framework. Since then, perovskite-based solar cells have made a rapid progress in terms of efficiency, up to 25.2% [5] (see Figure 1). In tandem with Si solar cells,  $\eta$  up to 30% can be obtained. As such cells are fabricated by simple solution-based methods, there is no need in a high-tech approaches (as my supervisor says, it is the technology of Robinson Crusoe), and despite this simplicity, it shows such an amazing efficiency. There are many open questions regarding this material: i) where does this high performance come from; ii) how can one extract electrons so well from this material; iii) what is the effect of disorder; iv) how exactly does  $\text{MAPbI}_3$  crystallize and how can one control this process; v) can one make a similarly highly efficient material without lead, because Pb is poisonous for the human body; and last but not least vi) can one fabricate other devices than solar cells from this material, like an X-ray detector, which uses much less X-ray flux for imaging?

I tried to contribute to all these questions, with my skills: structural studies and microfabrication which are described in this dissertation. The study of the crystallization was investigated

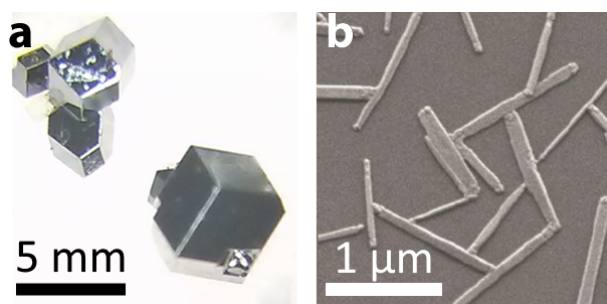


Figure 3 – (a) Optical photograph of a bulk crystal of MAPbI<sub>3</sub>. (b) Scanning Electron Microscopy (SEM) image of nanowires of the same material. Both forms were studied in this PhD work.

at the European Synchrotron Radiation Facility in Grenoble, while the microfabrication was performed at CMI center of EPFL. For my work it was also very important, that I had the chance to work with a chemist with a lot of expertise in my laboratory, who provided the necessary crystals for my investigations. These crystals were ranging from bulk, big crystals, to nanometer sized ones (Figure 3).

Chapter 1 is devoted to the general presentation of the perovskite material and the intermediate phases, which lead to the formation of wire-shaped MAPbI<sub>3</sub>. In Chapter 2, I analyze the crystal structure upon multiple thermal cycling. Since a real device, like a solar panel, is warmed up and cooled down on a daily basis, it is important to investigate the changes in the material properties and device performance under different conditions. When performing thermal cycling around a phase transition temperature, phase stabilization is observed.

Not only temperature, but also high pressure affects the structure. Our study gave spectacular results. When using inert pressure transmitting media, such as Neon and Argon, usually no chemical reaction occurs. However, we observed that these noble gases are incorporated in MAPbI<sub>3</sub> under high pressure. This high-pressure study is described in Chapter 3.

Chapter 4 investigates the influence of crystal structure on efficiency. This was addressed through the study of a related compound, the ethylenediammonium lead iodide. I show that depending on the disorder of the ethylenediammonium cation, which varies by the thermal treatment, the photon-to-electron conversion changes.

What is fascinating about this material is that applications are not limited to solar cells. For instance, they show a great potential for light-emitting diodes [6], lasers [7], gas sensors [8], and photodetectors [9]. In the case of photodetectors, the direct conversion of illumination into an electrical signal in halide perovskites enables higher spatial and intensity resolution compared to scintillator-based detectors [10] and reduced device cost. Along these lines, I was involved in the elaboration of an X-ray detector module with record-high sensitivity, by using an original deposition technique, given in Chapter 5.

MAPbI<sub>3</sub> is especially appealing for X-ray detection, as the atomic numbers of lead and iodide are high, giving the material sufficient stopping power [11, 12]. MAPbI<sub>3</sub> also exhibits long-term stability to high radiation doses [13, 10], which makes it a promising material in operationally stable X-ray detectors. Our laboratory has developed a novel aerosol jet printing (AJP) technology in collaboration with the Swiss Center for Electronics and Microtechnology (CSEM

## Introduction

Figure 4 – Optical and SEM images of MAPbI<sub>3</sub> deposited by an Aerosol Jet Printing technique elaborated by my group in collaboration with CSEM. This method allows fabrication of versatile structures in optoelectronic applications, enabling the design of an X-ray imaging module with outstanding sensitivity.

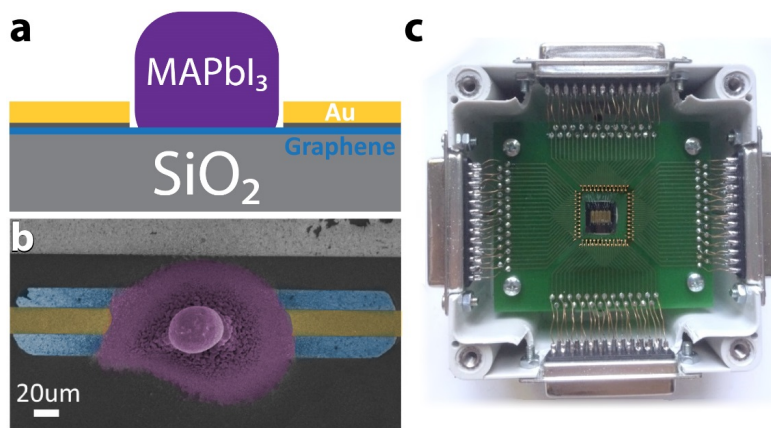
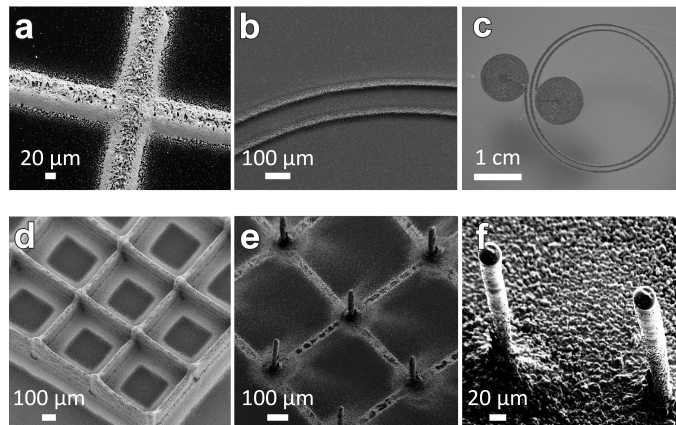


Figure 5 – (a) Sketch of the heterostructure for a basic element of the X-ray detector, MAPbI<sub>3</sub> deposited by APJ on graphene which amplifies the signal. (b) SEM with a top view on the structure. (c) X-ray detector modules wire-bonded for testing.

SA) in Neuchatel, enabling the creation of three dimensional (3D) structures of MAPbX<sub>3</sub> on a variety of substrates. This technique gives a large freedom in creating various architectures, even 3D ones (see Figure 4). This is feasible, because during the deposition, the solution of the material, undergoes a sequence of structural transformations upon solvent evaporation, which are described in Chapter 1.

Beyond the novelty of the AJP method, we made another step further in Chapter 6: the MAPbI<sub>3</sub> was printed on graphene sheet, which could tremendously amplify the sensitivity of the X-ray detection. This heterostructure is shown in Figure 5a, b and the X-ray module in Figure 5c. This structure demonstrated record-high sensitivity values, which could lead to a new generation of X-ray detectors for medical imaging, using a thousand times less radiation doses than conventional X-ray machines, strongly reducing the health hazard.

In Part 2 of this thesis (Chapters 5 and 6) everything comes together:

- material science: to elaborate a novel deposition technique by AJP;

- fundamental research:
  - the structural transformation of the material during the flight from the reservoir to the substrate, which prevents the spreading of the droplet;
  - understanding how graphene could improve the sensitivity of the device;
- applied research: the design of an X-ray detector unit;
- the task of an engineer: to test the device in real conditions, calculate, estimate the dose, the sensitivity, etc.
- last but not least, this device could have a noble outcome: better protection of the patients during X-ray imaging.

I learnt all these during my PhD, and it considerably helped me to appreciate the full spectrum of my profession as a physicist.



# **Hybrid organic-inorganic perovskites and relative compounds**

**Part I**





# 1 Methylammonium lead halide compounds

## 1.1 Crystal structure

### 1.1.1 General perovskite structure

Perovskites have a structure with general formula  $AMX_3$ . In this structure, the A- and M-site are occupied by two cations of different sizes, and X is an anion that binds to both. The A cations fill the space between  $MX_6$  octahedra, balancing the charge of the entire network, as sketched in Figure 1.1. The perovskite crystal structure can accommodate a wide variety of cations, which allows the development of many materials. The Goldschmidt's tolerance factor,  $t$ , and an octahedral factor,  $\mu_o$ , are used to determine the level of distortion in the system from a perfectly packed perovskite [14, 15].

$$t = \frac{R_A + R_X}{\sqrt{2}(R_M + R_X)}$$

$$\mu_o = \frac{R_M}{R_X}$$

where  $R_A$ ,  $R_M$  and  $R_X$  are the ionic radii of A, M and X, respectively. A stable cubic perovskite structure can be formed, when  $t$  is in the range of 0.8-1.0 and  $\mu_o$  is between 0.44 and 0.9 [15]. In case of lower  $t$  values the compound is yielding a tetragonal or orthorhombic system of lower symmetry.

Furthermore, the dimensionality can be tuned depending on the characteristics of the organic cation A. The  $[MX_6]^{4-}$  octahedra can form chains, layers or 3D networks. For instance, if the

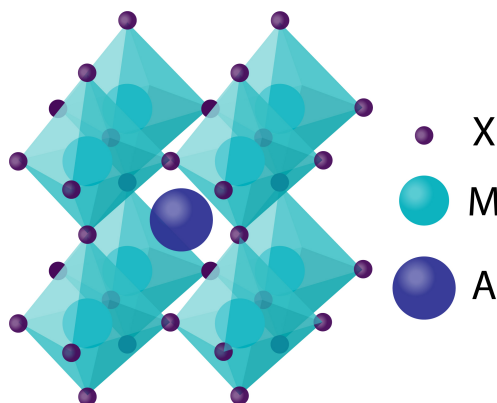


Figure 1.1 – Schematic crystal structure of the perovskite,  $AMX_3$ .

Temperature (K)	Crystal System	Space group	Lattice parameters (Å)
> 327.4	Cubic	$Pm\bar{3}m$	$a = 6.3285$
162.2-327.4	Tetragonal	$I422$	$a = 8.855, c = 12.659$
< 162.2	Orthorhombic	$Pna2_1$	$a = 8.886, b = 8.858, c = 12.62$

Table 1.1 – Temperature dependent crystallographic characteristic of MAPbI<sub>3</sub>.

cation radius,  $R_A$ , is bigger than 2.6 Å, low-dimensional perovskite can be obtained.

The central subject of this thesis is methylammonium lead iodide, CH<sub>3</sub>NH<sub>3</sub>PbI<sub>3</sub> (hereafter, MAPbI<sub>3</sub>). This compound is promising for a variety of applications due to the high light harvesting properties.

### 1.1.2 Structural transition

The structure of an organic-inorganic perovskite strongly depends on the temperature [16].

At low temperature, MAPbI<sub>3</sub> has an orthorhombic structure, but transforms into a tetragonal and cubic structure with temperature increase. These phase transitions are both driven by the organic cation positional disorder, which increases upon heating from 100 to 350 K [17]. The types of disorders can be classified by the behavior of the C–N axis of the MA. At high temperatures, the tetrahedrally coordinated C and N atoms show random distribution. In this case, the symmetry of the structure requires to have eight identical positions. Therefore, MAPbI<sub>3</sub> has a cubic symmetry above 330 K.

The transition to the tetragonal phase is accompanied by a slight distortion of the PbI<sub>6</sub> octahedra around their  $c$ -axis. The MA cation cannot be fixed there, either.

Finally, at low temperatures the disorder of MA is reduced and the system has an orthorhombic symmetry.

A detailed study of the phase transitions is described in Chapter 2; their crystallographic characteristics are shown in Table 1.1 [16].

## 1.2 Electronic structure

Organic compounds (carbon-based materials, like fullerene, anthracene, pentacene) offer a number of useful properties, including structural diversity, ease of processing, and efficient luminescence. On the other hand, inorganic materials (Si, GaAs, GaN) have a distinct set of advantages, including good electronic mobility, bandgap tunability (enabling tuning of the absorption and emission), mechanical, chemical and thermal stability. Organic–inorganic hybrids offer an important opportunity to combine useful properties of both.

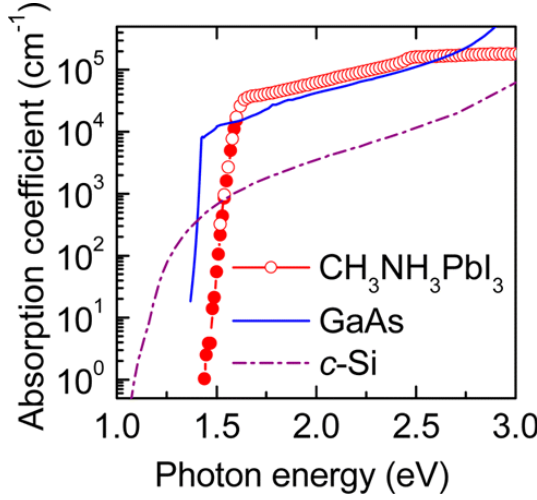


Figure 1.2 – The optical absorption coefficient at room temperature of a MAPbI<sub>3</sub> thin film compared with other typical photovoltaic materials. The plot is reproduced from publication [19].

### 1.2.1 Electronic bandgap

There is a fundamental limit for the maximum theoretical solar conversion efficiency of a single absorbing layer [18]. This efficiency is related to the bandgap ( $E_g$ ) of the semiconductor.

If  $E_g$  is very narrow then the material absorbs all light of the spectrum, generating high current. However, it will not generate high voltage, as all generated carriers relax to the bandgap energy. On the other hand, if  $E_g$  is as wide as 3 eV, then only UV wavelength is absorbed. This leads to optimal values of the bandgap between 1.3- 1.5 eV, which results in the maximum of 30 % efficiency [18].

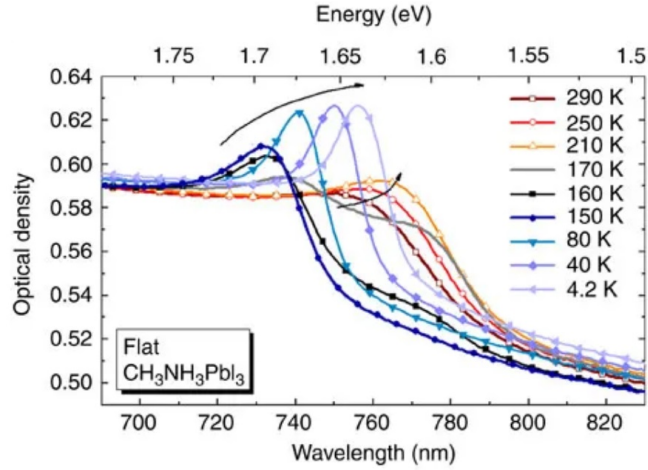
The absorption coefficient of a MAPbI<sub>3</sub> thin film compared with other typical photovoltaic materials, including GaAs and crystalline silicon (c-Si), is presented in Figure 1.2. It can be seen that MAPbI<sub>3</sub> exhibits a remarkably steep absorption onset at a photon energy of ~1.5 eV, with a rising absorption until a sharp shoulder appears at a photon energy near its reported bandgap, following which it saturates for photon energies above ~2.45 eV. The small Urbach tail and energy (16 meV) reflects the low density of sub-bandgap states near the band edge and therefore a high material quality [19].

MAPbI<sub>3</sub>-based devices have a remarkably high open-circuit photovoltage,  $V_{OC}$  (up to 1.13 V) compared with the bandgap of the absorber layer [20]. Besides the nature (amorphous vs. crystalline) and purity of a material, the  $V_{OC}$  also depends on the type of bandgap (direct vs. indirect), the absorber thickness. The bandgap increase, by mixing wider-bandgap materials, MAPbBr<sub>3-x</sub>Cl<sub>x</sub>, leads to even higher values of the  $V_{OC}$  (over 1.5 V) [21]. The high values of  $V_{OC}$  also points out that the non-radiative recombination rate in the material is low [19].

### 1.2.2 Charge carriers

At the core of any optoelectronic device lies electronic charge transport. First of all, it needs to be determined whether the primary photoexcited species are bound excitons or free carriers

Figure 1.3 – Temperature dependence of the absorption spectra of a MAPbI<sub>3</sub>. The plot is reproduced from the publication [25].



( $e^-$  and  $h^+$ ). In order to answer this question, the exciton binding energy,  $E_B$ , should be found. The absorption onset in the materials is quantified by the optical gap, which is defined as the lowest photon energy needed to create e-h pair, known as an exciton [22]. The photogenerated electrons and holes attract each other electrostatically, and the resulting  $E_B$  renders the optical gap smaller than the fundamental bandgap. For efficient charge carrier separation in the material,  $E_B$  must be small, compared to  $k_B T$ . At room temperature, the linear absorption spectrum of MAPbI<sub>3</sub> shows two absorption peaks located at 760 nm and 480 nm [23]. Whereas the low-energy peak is attributed to the direct bandgap transition [24]. In Figure 1.3 the absorption spectra around this peak of a polycrystalline MAPbI<sub>3</sub> film in temperature is shown. A sharp peak at 765 nm emerges at low temperatures ( $< 40$  K) is attributed to an excitonic transition. At 170 K, a second excitonic peak emerges at 740 nm. Upon further temperature increase, the latter peak gains strength in intensity and monotonically shifts to longer wavelengths, whereas the first peak disappears due to the low-temperature phase transition of MAPbI<sub>3</sub>.

The exciton binding energy in the tetragonal phase has been theoretically determined to be below 50 meV. And in the orthorhombic phase the lowest-energy exciton in MAPbI<sub>3</sub> has 37-50 meV binding energy [26]. However, these calculations assume a dielectric constant of 6.5, but the effective dielectric constant is much larger, due to screening effect of the Coulomb interaction between electrons and holes by optical phonons and collective rotational motion of the organic cations [27, 24]. This leads to exciton binding energies to be as low as 1-10 meV in the room-temperature phase, yielding free carriers [4]. At low temperatures the effective dielectric constant is larger due to screening induced by vibrations. In case of an effective dielectric constant equal to 11, the binding energy drops down to 18-24 meV at 5 K [24]. Nevertheless, even for the upper bound of  $\sim 50$  meV, free charges are generated spontaneously following light absorption, as opposed to a large population of bound excitons. Ultrafast spectroscopy indicates that exciton dissociation occurs on a timescale of 2 ps after photoexcitation [28].

### 1.2.3 Carrier mobility and lifetime

Transport of charge carriers in semiconductors is directly related to the electronic band structure. The electron and hole effective masses  $m_{e,h}^*$  are inversely proportional to the curvature ( $\frac{d^2E}{dk^2}$ ) of the relevant bands in the electronic band structure.

The carrier diffusion length,  $L_D$ , is a measure of how far carriers diffuse on average before recombining. MAPbI<sub>3</sub> has high diffusion length, in the single crystal  $L_D > 175 \mu\text{m}$  for both electrons and holes [29]. In case of the polycrystalline form,  $L_D$  is on the order of 100 nm [23]. The electron-hole diffusion length of a material is directly determined by the mobility,  $\mu$ , and lifetime,  $\tau_r$ , of the charge carriers:  $L_D = \sqrt{\frac{k_B T \mu \tau_r}{e}}$ .

The carrier lifetime of MAPbI<sub>3</sub> can be as long as 100 ns for polycrystalline films and even more than 1  $\mu\text{s}$  for a single crystal. These results indicate the lack of non-radiative recombination centers and trap states in the single crystals [22].

The carrier mobility is ambiguous for a determination. Depending on the assumptions and measuring technique values vary from 1  $\text{cm}^2\text{V}^{-1}\text{s}^{-1}$  (field-effect transistor measurements [30]) to 66  $\text{cm}^2\text{V}^{-1}\text{s}^{-1}$  (Hall-effect measurements [31]). At room temperature, values of  $\mu \approx 30 \text{ cm}^2\text{V}^{-1}\text{s}^{-1}$  are typically found [32].

A good agreement between theoretical and experimental values can be achieved if spin-orbit coupling (Rashba effect) associated with the presence of heavy atoms in MAPbI<sub>3</sub> is included in the picture [33]. The inorganic atoms' spin and orbit degrees of freedom are coupled with the electric field generated by organic cation. This results in the electronic band splitting for different spins and leads to an effectively indirect bandgap and prolonged lifetime. The spin-orbit coupling reduces the bandgap by 1 eV [34]. In this case, the density functional theory calculations give the values for the effective masses of photogenerated electrons and holes in MAPbI<sub>3</sub>  $m_e^* = 0.23 m_0$  and  $m_h^* = 0.29 m_0$ , which are smaller than without spin-orbit coupling, i.e.  $m_e^* = 0.32 m_0$ ,  $m_h^* = 0.36 m_0$  [33].

Within the Drude model, the free charge carrier motion is characterized by the scattering time,  $\tau$ , and the effective mass:  $\mu = e\tau / m^*$  [35]. As the effective mass is low, then the modest mobility values must be due to scattering. The scattering time is limited primarily by phonon scattering, and thus depends on temperature.

Taking into account the Rashba effect, the carrier mobility below 100 K follows  $\mu \propto T^{-1}$ , limited by the acoustic-phonon scattering [36]. Between 130 and 300 K optical phonon scattering is dominant and  $\mu \propto T^{-1.5}$ .

Traps are critical to the carrier lifetime in the material. The polycrystalline film MAPbI<sub>3</sub> has significant trap-density values,  $2 \times 10^{15} \text{ cm}^{-3}$ , while for the single crystal this value is extremely low at  $3.6 \times 10^{10} \text{ cm}^{-3}$  [29]. The suppressed trap density results in the increased diffusion length for the single crystal as discussed above.

### 1.2.4 Ionic transport

Diffusion of intrinsic ionic defects in  $\text{MAPbX}_3$  has important implications in terms of the long-term stability and performance of devices. As discussed in the previous section, the e-h transport properties indicate moderate carrier mobility and long diffusion lengths. Due to ion migration, hysteresis is observed during a photocurrent–voltage scan on the device. The mobile ionic species in the solid state are associated with some type of vacancy or interstitial defect.

It was shown that ionic conductivity in  $\text{MAPbI}_3$  is mainly due to iodine vacancies [37]. An increase of iodine partial pressure leads to the decrease of the ionic conductivity, while electronic conductivity increases. This identifies the mobile ionic defect as iodine vacancies, whose concentration decreases due to  $\text{I}_2$  incorporation from the gas phase [37].

The activation energy ( $E_A$ ) characterizes how easily an ion migrates in the material and defines the migration rate as  $\propto e^{-\frac{E_A}{k_B T}}$  [38]. In case of iodine  $E_A$  is the lowest, 0.58 eV, suggesting favourable vacancy-assisted diffusion of iodide ions. A higher activation energy of 0.84 eV is found for  $\text{MA}^+$  migration, which involves motion through the unit cell face or bottleneck comprising four  $\text{I}^-$  ions.  $\text{Pb}^{2+}$  vacancy migration has a high energy barrier (2.31 eV), resulting in an immobile Pb sublattice. At 320 K, the diffusion coefficient is  $10^{-12} \text{ cm}^2\text{s}^{-1}$  for  $\text{I}^-$  ions, which is four orders of magnitude higher than the value of  $10^{-16} \text{ cm}^2\text{s}^{-1}$  for  $\text{MA}^+$ , suggesting negligible diffusion of  $\text{MA}^+$  ions.

The diffusion length of an iodide vacancy on the timescale of a photocurrent relaxation at room temperature (around 10 s) is of the order of 30 nm.

Therefore, hybrid halide perovskites are mixed ionic–electronic conductors with iodide ions as the majority ionic carriers.

### 1.2.5 Tuning the electronic properties by chemical engineering

The structure of the organic-inorganic perovskite offers the possibility to tune the electronic properties of the material (e.g. bandgap or carrier mobility) by varying cationic and anionic components.

#### Halide and metal substitution

In an ionic material, the valence band (VB) is dominated by electronic states of the anion, while the conduction band (CB) is dominated by the electronic states of the cation. In accordance to this, the band structure of hybrid perovskites,  $\text{AMX}_3$ , is strongly depended on its inorganic components, M and X [39]. It was shown that for  $\text{MAPbI}_3$  the VB consists mostly of I states with some admixture of Pb states (I  $p$ -states and antibonding I  $p$ - and Pb  $p$ -states) and the CB consists primarily of Pb states ( $p$ -states) [40].

With a halide as the X anion, the metal (M) is generally expected to be a divalent cation that can adopt an octahedral coordination (e.g.  $\text{Cu}^{2+}$ ,  $\text{Mn}^{2+}$ ,  $\text{Co}^{2+}$ ,  $\text{Cd}^{2+}$ ,  $\text{Ge}^{2+}$ ,  $\text{Sn}^{2+}$ ,  $\text{Pb}^{2+}$  or  $\text{Eu}^{2+}$ )

Compound	Bandgap (eV)
MAPbI <sub>3</sub>	1.51
MAPbBr <sub>3</sub>	2.22
MAPbCl <sub>3</sub>	2.94

Table 1.2 – Bandgap of MAPbX<sub>3</sub> systems, X = Cl, Br, I [46].

[41]. The angle between the metal cation and the halide anions (X–M–X) has been attributed to have the greatest impact on tuning the bandgap of the material [42]. In the case of AMI<sub>3</sub>, where M = Ge, Sn, Pb, as the bridging angles decreases (Ge(166.27°) > Sn(159.61°) > Pb(155.19°)), so does the covalent character of the M–X bond, because the difference in electron-negativity between M and X increases [43]. As a consequence, the bandgap follow the trend of  $E_g(\text{AGeI}_3) < E_g(\text{ASnI}_3) < E_g(\text{APbI}_3)$  [44].

With anion substitution in MAPbX<sub>3</sub> systems, with X = Cl, Br, I, bigger anions (Cl < Br < I) have lower electron-negativity, resulting in an increase of the covalent character of the Pb–X bond [45]. Therefore, the compound with the biggest anion, MAPbI<sub>3</sub> has the smallest bandgap (Table 1.2), resulting in a red-shift of the optical absorption edge.

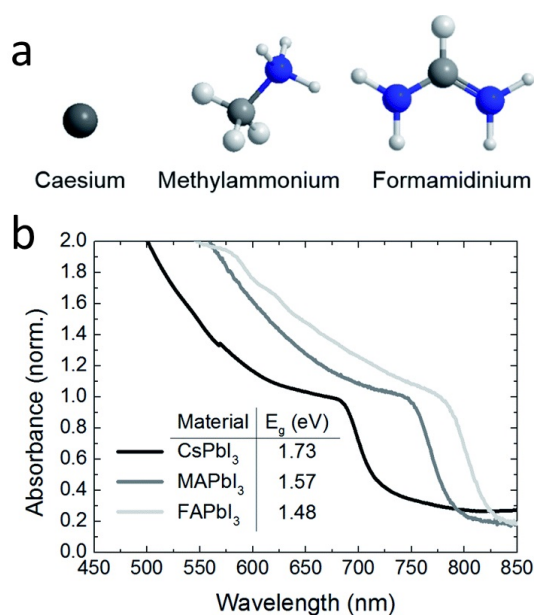
The incorporation of iodide with bromide or bromide with chloride allows continuous tuning of the bandgap and the optical absorption in order to cover almost the entire visible (VIS) spectrum [44]. Even if there is no obvious change in the bandgap by mixing iodide with chloride, small addition of chloride ions to MAPbI<sub>3</sub> results in a increase in both electron and hole diffusion lengths up to 1  $\mu\text{m}$  [47].

### Organic cation substitution

The size variation of an organic cation causes the MX<sub>6</sub> octahedron network deformation. This results in changes of the M–X bond length, which is an important factor in the determination of the bandgap [42]. A shorter M–X–M will directly increase the bandgap. Indeed, the size and polarity of the organic cation is capable of changing the M–X–M angles, and it has been theoretically shown that the bandgap of APbI<sub>3</sub> can be altered between 1.1–1.9 eV when organic molecules of different sizes are placed in the octahedral cavity [48]. There is a relatively small size range allowed for the organic cation to fit between the corner-sharing metal halide octahedra. If it is too large, the 3D perovskite structure is unfavourable and lower-dimensional perovskites will be formed [41]. By lowering the dimensionality of PbI<sub>6</sub> networks from 3D to 0D isolated octahedra, binding energy and bandgap increase, and charge transport becomes limited [26]. For instance, the binding energy of an exciton can be enhanced up to four times if it is confined in 2D [26].

In order to maintain cubic symmetry in APbI<sub>3</sub>, the organic cation's radius should be smaller than 2.6 Å [44]. Therefore, small monovalent cations, like formamidinium FA<sup>+</sup> (CHNH<sub>3</sub>), MA<sup>+</sup>, Cs<sup>+</sup>, K<sup>+</sup> and Rb<sup>+</sup> can form a 3D framework with the PbI<sub>6</sub> network [49, 50]. In Figure 1.4a the structures of three cations are presented. As the A cation decreases its effective ionic radius

Figure 1.4 – Tuning perovskite bandgap by replacing the A cation. (a) The atomic structure of the three cations. (b) UV-VIS spectra for the  $\text{APbI}_3$  perovskites formed, where A cation is either caesium (Cs), methylammonium (MA) or formamidinium (FA). The figure is reproduced from [51].



( $\text{FAPbI}_3 > \text{MAPbI}_3 > \text{CsPbI}_3$ ) the structural symmetry is reduced because the Pb–I–Pb bridging angles gradually deviate from the ideal linear conformation, resulting in an increase in orbital overlap of Pb–I. This corresponds to a widening of the bandgap, Figure 1.4b [31].

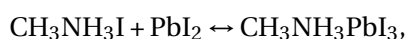
Therefore, by mixing  $\text{FA}^+$  and  $\text{MA}^+$ , the optical-absorption onset of  $\text{MA}_x\text{FA}_{1-x}\text{PbI}_3$  can be red-shifted compared to that of  $\text{MAPbI}_3$  [51].

Although the organic group is not directly involved in the formation of the band structure, the cation influences it by interacting with the inorganic  $\text{PbI}_6$  octahedron through the rotational degrees of freedom [52]. Therefore, the behavior of the cation also influences the electrical properties of the material in temperature.

### 1.2.6 Stability

There are four key factors causing decomposition of the perovskite into  $\text{PbI}_2$ : oxygen, moisture, solution processing and thermal effects [53]. These factors all lead to rapid device degradation.

In case of solution processing the reaction is



which can go in the positive direction for the synthesis of  $\text{MAPbI}_3$ . However, if the reaction is in the negative direction,  $\text{MAPbI}_3$  is decomposed.

Decomposition can also happen either when  $\text{PbI}_2$  and/or  $\text{MAI}$  combines with other components (then the chemical equilibrium can drive reaction in the negative direction) or the perovskite can directly degrade into other chemicals under certain conditions [53].



As the degradation of organic–inorganic halide perovskite is quite sensitive to moisture and oxygen. MAPbI<sub>3</sub> started to decompose at a humidity of 55%, which could be observed by a remarkable color change from dark brown to yellow [42]. It was shown, that upon moisture ingress the strong absorption onset of the material shifts from ~1.6 to almost 2.4 eV, where the shape of the absorbance spectrum demonstrates a compositional change of the deposited material [19]. This indicates that HI and MA are soluble in water [54].

The stability can be improved by modification of the MAPbI<sub>3</sub> surface to avoid contact of the perovskite with ambient air and prevent leakage of volatile products from the perovskite. For instance, the spin-coated phosphoric acid ammonium additive acts as crosslink between neighbouring grains in the perovskite structure, creating passivating and moisture protection layer [55]. Or through ionic compositional engineering - "cation cascade" can be build [56]. The small and oxidation-stable rubidium cation (Rb<sup>+</sup>) can be embedded into APbI<sub>3</sub> (A = MA, FA, Cs).

Exposure to elevated temperatures also causes the conversion of MAPbI<sub>3</sub> into PbI<sub>2</sub>. After annealing at 373 K for 30 min under vacuum, no diffraction peaks indicating Pb<sub>2</sub> were present, however, annealing at 413 and 433 K caused the decomposition to PbI<sub>2</sub> [57].

## 1.3 Crystallization process

MAPbX<sub>3</sub> can be prepared in a single crystal or a polycrystalline form (the details of the syntheses are in the Appendix B.1).

A common method to grow a single crystal involves the dissolution of a precursor salt into an acid (HI, HBr or HCl). A solution is held for several hours and then slowly cooled, at a rate of around 1 - 2 K/hr. Crystals precipitate out of solution and can be harvested, or placed in a fresh solution as seed crystals and grown to larger sizes.

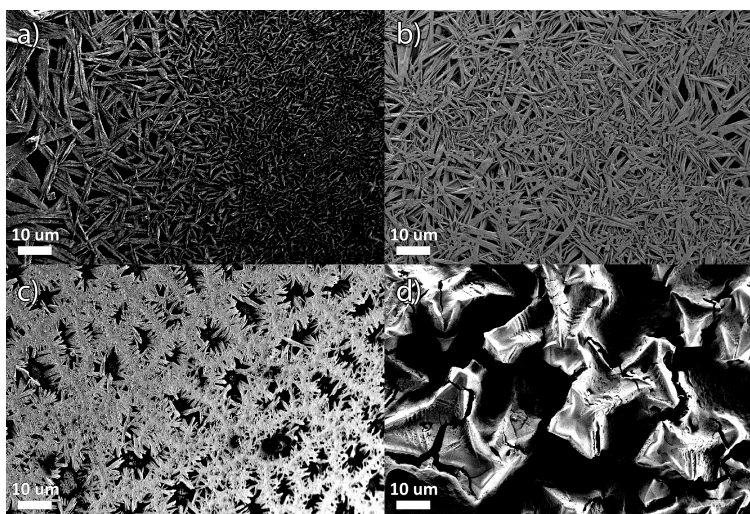
Methods of hybrid perovskite film fabrication include one-step precursor solution deposition [58], two-step sequential deposition [59], dual-source vapor deposition [60] and vapor-assisted solution process [61]. Additionally, for perovskite nanoparticles fabrication template-assisted [62] and template-free [63] methods have been developed.

A major advantage for perovskite films is the ability to be processed from solution in more cost-effective ways.

### One-step precursor deposition

One-step precursor solution deposition is the most popular method for producing a perovskite film [64]. It is carried out by dissolving the organic and inorganic species into an organic solvent and depositing onto the substrate. More precisely, the precursor solution is prepared by mixing the powder of an organic halide salt, RX (R: methyl, formamidine) and a metal salt PbX<sub>2</sub> (X: I, Br, Cl) at 1:1 (stoichiometric) or 3:1 (non-stoichiometric) mole ratio (mol %) in high boiling point polar aprotic solvents (typically dimethylacetamide (DMA), dimethylformamide (DMF), dimethyl sulfoxide (DMSO), and  $\gamma$ -butyrolactone (GBL)). This solution is then used for the in-situ formation of organometal halide perovskite by spin-coating or drop-casting [65]. Af-

Figure 1.5 – SEM images of the crystallized MAPbI<sub>3</sub> from (a) DMF, (b) DMA, (c) DMSO, (d) GBL solvents.



terwards, an annealing process is needed for the complete transformation of the precursor to the crystalline perovskite film.

### Sequential deposition and other methods

In a typical two-step processing [66] the metal halide salt (PbI<sub>2</sub>) is first spin-coated from solution in DMF, followed by dipping into a solution of MAI [67]. As in the one-step method during the annealing step MAPbI<sub>3</sub> is formed. In many cases a downside of the sequential deposition approach is incomplete conversion of PbI<sub>2</sub> to MAPbI<sub>3</sub>.

The crystallization process from solvated precursors determines most of the physical and electronic properties of the polycrystalline film. Crystallized wire-shaped MAPbI<sub>3</sub> causes pinholes in perovskite films. Vapor deposition provides uniform thin films, however this process is quite energy-intensive and limited in substrate choice. For obtaining homogeneous layers with the solution-based approaches the amount of MAI in DMF solutions of MAPbI<sub>3</sub> could be increased [68]. An other approach is the introduction of supramolecules to enhance PbI<sub>2</sub> solubility [69] or the low-temperature gas-solid crystallization method in which the intermediates, which lead to wire-shaped crystals are avoided [70].

### 1.3.1 Intermediate phases

The Scanning Electron Microscope (SEM) images of the polycrystallized films after one-step deposition of the 30%w saturated solution of DMF, DMSO, DMA and GBL with MAI and PbI<sub>2</sub> (1:1 mol %) are presented in Figure 1.5. As can be seen from these images, the choice of the solvent strongly influences the process of the crystallization. The composition and crystal structures of the adducts depend on the coordination and binding ability of the solvents and the ratio of the precursors [71].

In 2014 Horvath et al.[9] showed that some solvents induce highly anisotropic crystallization

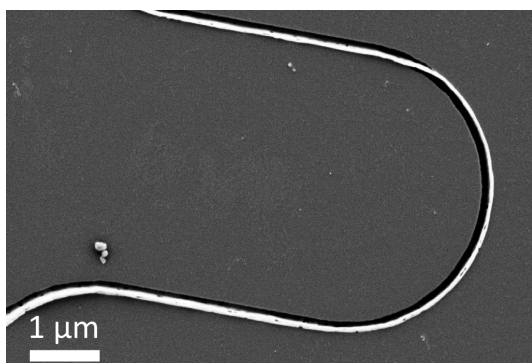


Figure 1.6 – SEM image of the MAPbI<sub>3</sub> nanowire in the channel.

of MAPbI<sub>3</sub>. Upon the fast solvent (for instance, DMF) evaporation yellow micron-long wires appear first. This phase is relatively stable in air and converts slowly to black MAPbI<sub>3</sub> upon further DMF evaporation, Figure 1.5a. The resulting perovskite film inherits the morphology of intermediate adduct phases that the crystal went through. Similar to MAPbI<sub>3</sub>·DMF, MAPbI<sub>3</sub>·DMA and MAPbI<sub>3</sub>·DMSO solution result in the black wire-shaped crystals, Figure 1.5b, c. Meanwhile, the film from MAPbI<sub>3</sub>·GBL consists of only cube-shaped clusters, Figure 1.5d [72]. This difference in the morphology can be explained by the analysis of the intermediate phases.

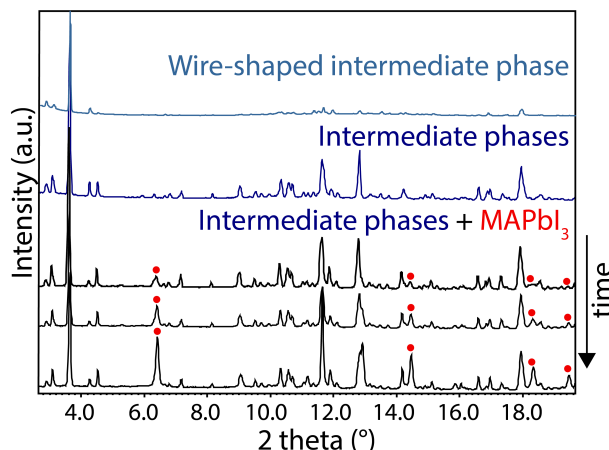
In case of PbI<sub>2</sub> excessive adduct (MA)<sub>2</sub>(solvent)<sub>2</sub>Pb<sub>3</sub>I<sub>8</sub> is formed. For solutions with DMF and DMSO it was identified that (MA)<sub>2</sub>(DMSO)<sub>2</sub>Pb<sub>3</sub>I<sub>8</sub> and (MA)<sub>2</sub>(DMF)<sub>2</sub>Pb<sub>3</sub>I<sub>8</sub> [73] are one of the intermediate phases, While MAPbI<sub>3</sub> does not form such adducts with GBL under the same conditions. In contrast to DMSO and DMF, GBL weakly interacts with lead ions and can not split a layered lattice of PbI<sub>2</sub> [71], which is one of the reasons for the difference in final crystal shape.

Moreover, the wire-shaped MAPbI<sub>3</sub> is not only an interesting subject for research. By guiding the high aspect-ratio perovskite nanowires growth a precise control over the physical properties and their location are gained. When the MAPbI<sub>3</sub>·DMF solution is applied in the fabricated channel, the nanowires follow the solvent evaporation-induced crystallization [74] and fill the channel. The crystal growth of existing nuclei continue until all the solute is consumed. One of the approaches is to fabricate a channel in a resist layer or PDMS mold [74, 75]. It also can be done with etched trenches in an SiO<sub>2</sub> substrate. By narrowing the channel down to 300 nm, there is a higher probability that there are less nucleation centers created in the channel. Thus, a single crystallite can be separated from the rest of the polycrystalline nanowire net. When an optimized curvature radius the nanowire can be bended, as can be seen in Figure 1.6. An ability to bend the nanowires gives an opportunity to use them in flexible optical sensors and wearable electronic devices [75].

### 1.3.2 Structure refinement

To understand the crystallization process of the wire-shaped MAPbI<sub>3</sub> in depth, the MAPbI<sub>3</sub>·DMF solution was applied on a glass capillary and XRD data were recorded during evaporation of the solvent (conditions are described in Appendix A.2).

Figure 1.7 – The XRD experimental patterns recorded during crystallization. The reflections related to MAPbI<sub>3</sub> and not to any of the intermediate phases are indicated by red dots.



Structure	Space group	Lattice parameters (Å)
MAPbI <sub>3</sub>	<i>I</i> 422	<i>a</i> = 8.88375(18), <i>c</i> = 12.7010(3)
(MA)(DMF)PbI <sub>3</sub>	<i>P</i> 2 <sub>1</sub> / <i>c</i>	<i>a</i> = 4.5647(9), <i>b</i> = 25.446(5), <i>c</i> = 12.119(2)
(MA)(DMF)Pb <sub>3</sub> I <sub>8</sub>	<i>Pn</i> <i>n</i> <i>m</i>	<i>a</i> = 17.165(4), <i>b</i> = 21.955(4), <i>c</i> = 4.5549(9)

Table 1.3 – MAPbI<sub>3</sub>, (MA)(DMF)PbI<sub>3</sub> and (MA)<sub>2</sub>(DMF)<sub>2</sub>Pb<sub>3</sub>I<sub>8</sub> crystal structure details.

The profile analysis in PXRD gives a lot of information about the material. For instance, the peak position tells us about the number of phases and the metrics of their unit cells if they mix. The intensity of the peaks gives information on the phase ratio and on the unit cell content for each of them. More information about structural refinement could be found in the Appendix A.1.

The XRD profiles in Figure 1.7 show the formation process of the MAPbI<sub>3</sub> from the (MA)(DMF)PbI<sub>3</sub>. Initially, in solution, a soft framework of the inorganic species is developed, surrounded by the organic ions. As there is no periodicity in the mixture (amorphous structure) the XRD profile consists of the background only. With the solvent evaporation intermediate phases with a distinctive character of a low angle ( $2\theta < 10^\circ$ ) reflections appear [70]. In Figure 1.7, it can be seen how the MAPbI<sub>3</sub> structure (indicated on the bottom profiles) emerges and grow with time from the mixture of two intermediate phases - (MA)(DMF)PbI<sub>3</sub> and (MA)<sub>2</sub>(DMF)<sub>2</sub>Pb<sub>3</sub>I<sub>8</sub>.

Reference XRD patterns and information for MAPbI<sub>3</sub> and the corresponding intermediate phases, with and without preferable orientation, are given in Figure 1.8 and Table 1.3. The first intermediate phase, (MA)(DMF)PbI<sub>3</sub>, has a double-chain motif, where the inorganic PbI<sub>3</sub><sup>-</sup> chain is surrounded by the MA<sup>+</sup> cations, which are strongly H-bonded to a DMF molecule [70]. The second intermediate phase is (MA)<sub>2</sub>(DMF)<sub>2</sub>Pb<sub>3</sub>I<sub>8</sub>, which is an PbI<sub>2</sub>-excessive adduct, this structure consists of triple-chains of edge-sharing lead iodide octahedra [76].

During the fast crystallization, (MA)(DMF)PbI<sub>3</sub> is the main intermediate phase for the formation of the wire-shaped MAPbI<sub>3</sub>. This can be concluded from Figure 1.9, as the (MA)(DMF)PbI<sub>3</sub> contribution is decreasing with simultaneously increased MAPbI<sub>3</sub> fraction (Appendix A.9).

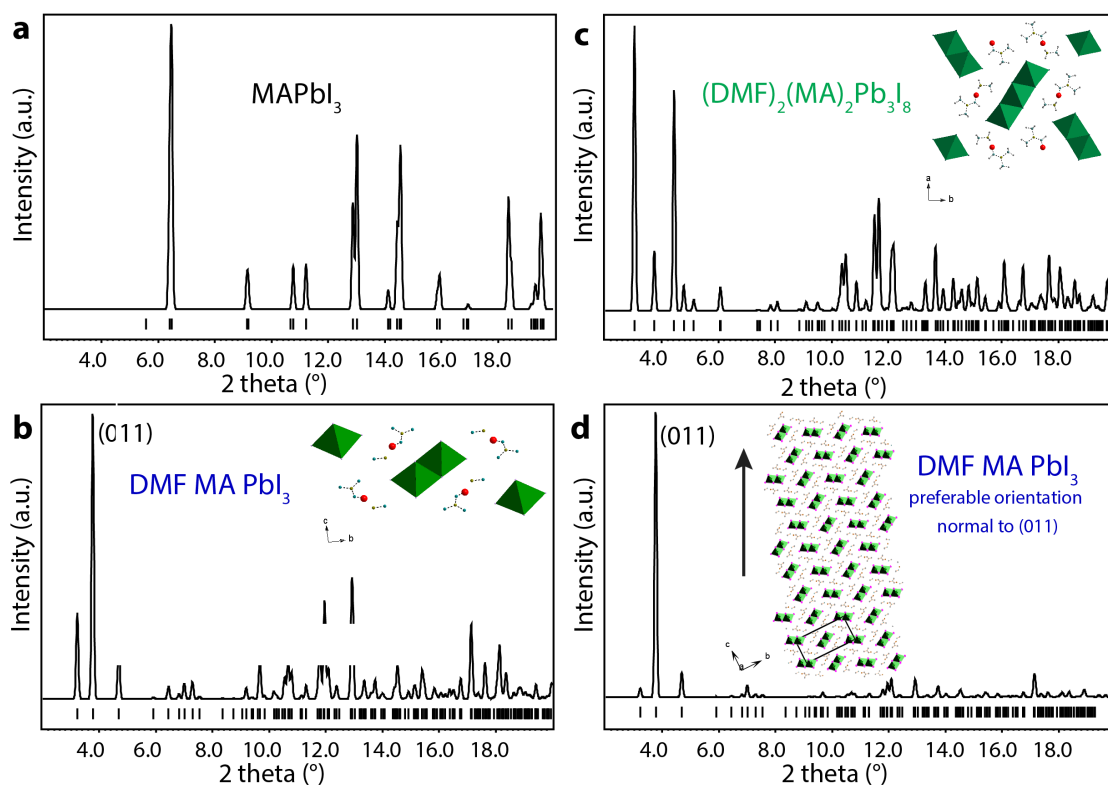


Figure 1.8 – XRD profiles of MAPbI<sub>3</sub> and intermediate phases. (a-c) Calculated standard XRD profiles of MAPbI<sub>3</sub> and (MA)(DMF)PbI<sub>3</sub>, (MA)<sub>2</sub>(DMF)<sub>2</sub>Pb<sub>3</sub>I<sub>8</sub> intermediate phases. (d) XRD profile of (MA)(DMF)PbI<sub>3</sub> calculated with the preferable grain orientation normal to the (011) planes.

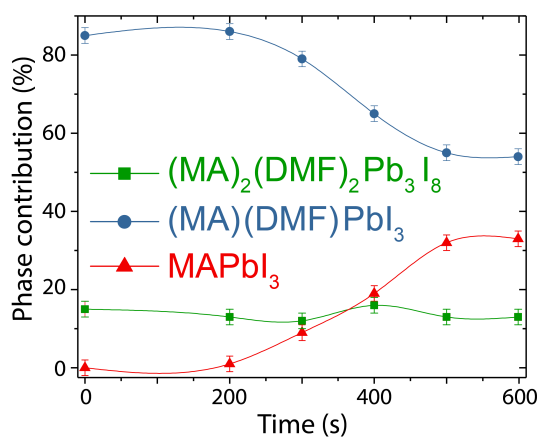


Figure 1.9 – Phase contributions in time of crystallization during heating.

Therefore, resulting wire-shaped MAPbI<sub>3</sub> inherited its morphology from the (MA)(DMF)PbI<sub>3</sub> intermediate phase [76, 77].

A strongly dominant single reflection at  $2\theta = 3.7^\circ$ , observed at the first stage of the crystallization in Figure 1.7, univocally indicates the direction of an elongation of the wire-shaped grains of (MA)(DMF)PbI<sub>3</sub>. This reflection, indexed as (011) for the (MA)(DMF)PbI<sub>3</sub> phase, signifies a

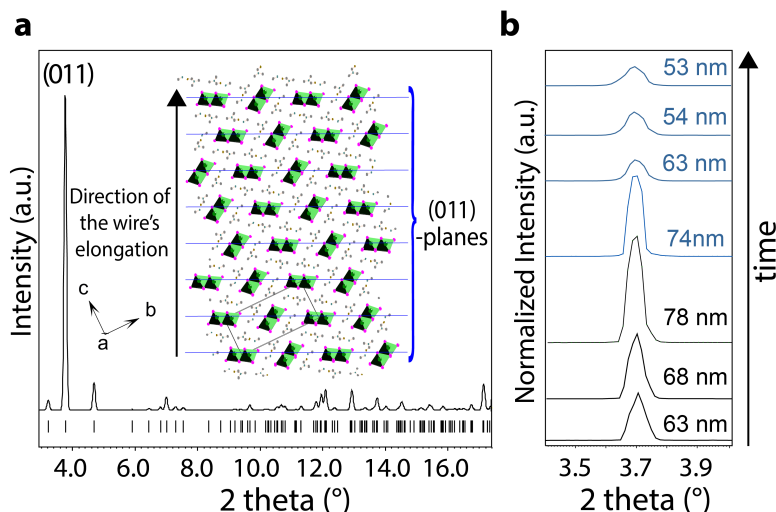


Figure 1.10 – (a) Simulation of the XRD pattern applying preferable growing of (MA)(DMF)PbI<sub>3</sub> in the direction normal to (011). The bottom ticks indicate positions of the Bragg reflections. (b) Evolution of the relative intensity of (011) reflection and the mean size of grains for the intermediate phase (MA)(DMF)PbI<sub>3</sub> in the direction of the grain elongation. Black-colored peaks correspond to room temperature measurements, while blue-colored data was recorded during a gradual temperature increase up to 337 K.

preferred growth of the wire-shaped grains in the direction normal to the stack of (011) planes, as shown in Figure 1.10a (the time has been set to zero at the moment of MAPbI<sub>3</sub> formation).

During the crystallization, the (011) reflection changes its relative intensity and width over time. The peak width tells us about the crystallite size (Appendix A.1.3). It is possible to estimate the mean size of the wire-shaped grains in the direction of their elongation using Scherrer's equation [78]:  $p = \frac{K\lambda}{\Gamma \cos\theta}$ , where  $p$  is the mean size of ordered domains,  $K$  is a shape factor,  $\Gamma$  - width of the diffraction peak (corrected for instrumental broadening), given in radians. The estimation of the normalized intensity and the mean size is depicted in Figure 1.10b. The intensity of the reflection represents the quantity of the wire-shaped grains, while its width defines the mean size of the grains in the indicated direction. The increase of both the reflection intensity and the mean size of the wire-shaped grains at room temperature, confirms their progressive formation and growth.

After stabilization of the intermediate phases at room temperature, the sample was heated to 337 K, during which the intensity of the (011) reflection and the mean size of the wire-shaped grains decreases. Both effects are associated with the transformation of the (MA)(DMF)PbI<sub>3</sub> phase into MAPbI<sub>3</sub> within the wire-shaped grains as it has been described by Guo et al. [77].

The possible way of the transformation (MA)(DMF)PbI<sub>3</sub> into MAPbI<sub>3</sub> is presented in Figure 1.11. Under DMF evaporation (Step 1) PbI<sub>6</sub>-octahedra change their connection from shared edges to shared vertices (Step 2). Following further DMF release the structure condenses into MAPbI<sub>3</sub> (Step 3). However, depending on the DMF diffusion kinetics, the transformation starts on the

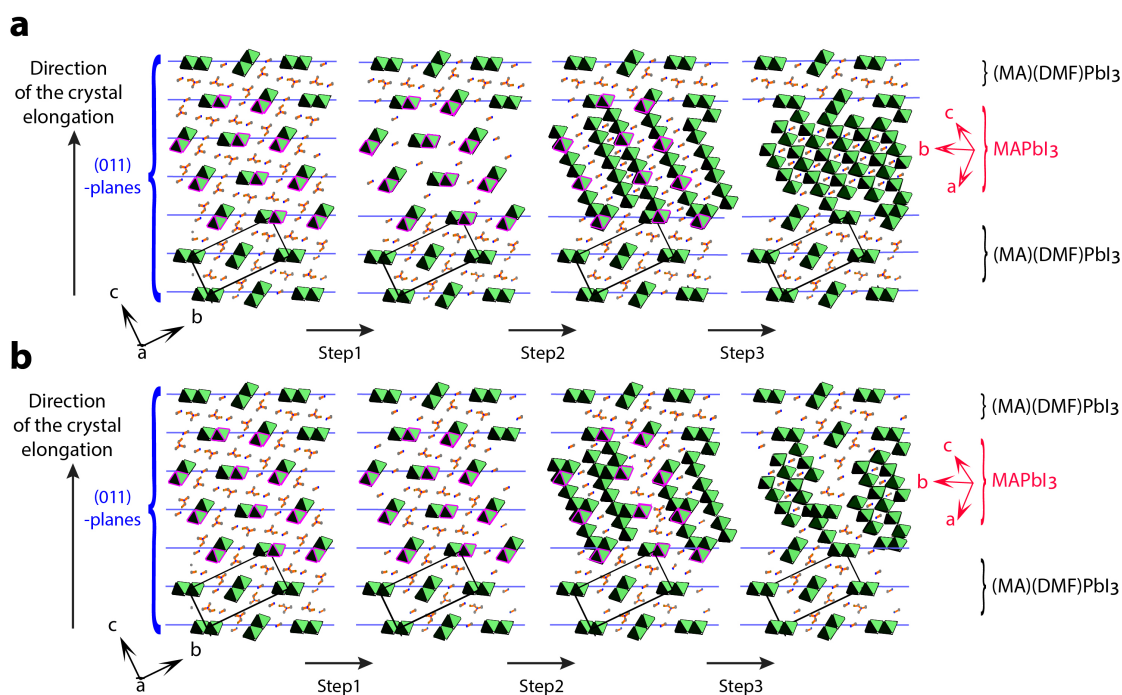


Figure 1.11 – Possible ways of converting intermediate phase to wire-shaped  $\text{MAPbI}_3$ . (a) Formation of the single crystal  $\text{MAPbI}_3$  under slow solvent evaporation. (b) Formation of the polycrystalline  $\text{MAPbI}_3$  under fast solvent evaporation.

surface or in the core of the  $(\text{MA})(\text{DMF})\text{PbI}_3$  single-crystal grain. Under the rapid crystallization conditions, the  $\text{MAPbI}_3$  formation is faster than migration of DMF molecules from the core of the intermediate phase to the surface, Figure 1.11b. Therefore, the solvent can be trapped in the crystal. And to release the solvent from the system the temperature should be further elevated. Additionally, this scheme could explain the difference in the formation of the  $\text{MAPbI}_3$  single-crystal and polycrystalline structure depending on the evaporation rate of the solvent.

For these experiments to exclude the concern of the structure modification due to the long X-ray exposure time, the data from two spots on the sample was probed after the measurements. Comparing profiles of the spot, which was exposed for half an hour, and an unexposed one on the sample, Figure 1.12 demonstrates the absence of radiation damage. The crystallized  $\text{MAPbI}_3$  phases from both spots have the same structure. This demonstrates that the X-ray radiation does not influence the crystallization process or cause any damage.

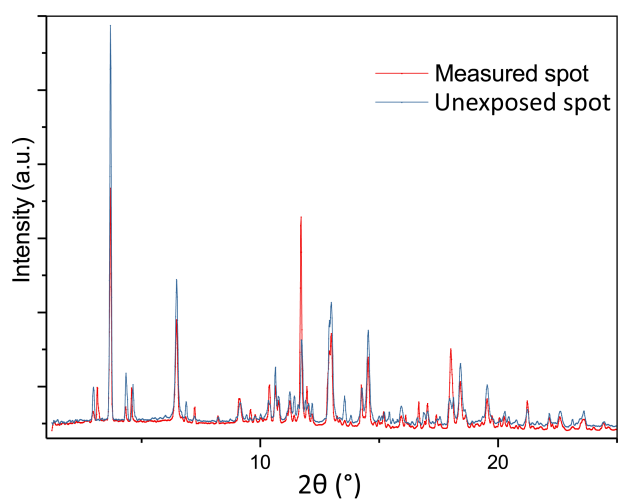


Figure 1.12 – XRD profiles of the MAPbI<sub>3</sub> nanowire from the measured and unexposed spots.



## 2 Effect of thermal cycling on structural evolution

### 2.1 Structural transformations of MAPbX<sub>3</sub> in temperature

Working perovskite devices are exposed to various conditions at ambient temperatures. Therefore, exploring the properties of hybrid organic-inorganic perovskites over a wide range of temperature is not only of fundamental interest but also aims to identify the practical applications of the devices based on these perovskites.

It is shown that the temperature profoundly affects the optoelectronic properties of MAPbI<sub>3</sub> across both the orthorhombic-tetragonal phase transition (160 K) and the tetragonal-cubic phase transition (330 K) [79]. For instance, below 80 K the transport behavior deviates a lot from ideal Drude, pointing to the charge-carrier localization and it is consistent with the emergence of excitonic effects at temperatures below the phase transition [79]. In Figure 2.1a it can be seen that the charge-carrier mobility decreases with increasing temperature. Carrier mobility is defined by charge interaction with the lattice (phonons) and material imperfections (lattice disorder, impurities). And in Figure 2.1b, the diffusion length decreases with increased temperature mostly due to the domination of the charge trapping term in the recombination dynamics [79].

Regarding the optical properties, for conventional semiconductors (Si, GaAs, etc.) the bandgap decreases with increasing temperature. However, the bandgap of MAPbI<sub>3</sub> increases with lattice temperature around 160 K and 300 K, as illustrated in Figure 2.2. This unusual behaviour was suggested to be explained by phonon modes and electron-phonon coupling (polarons) [80, 81].

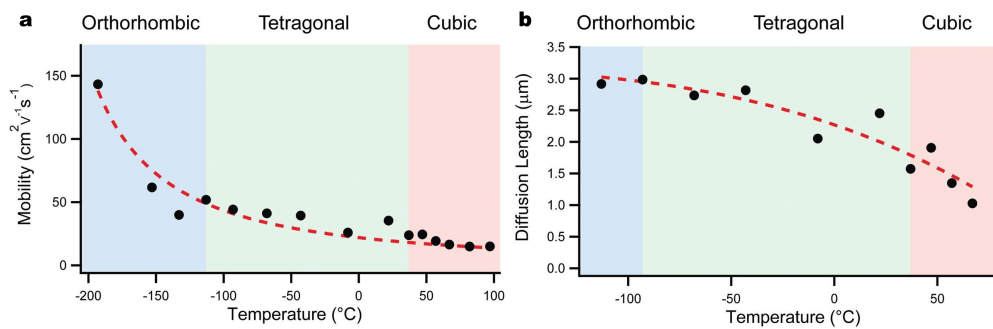
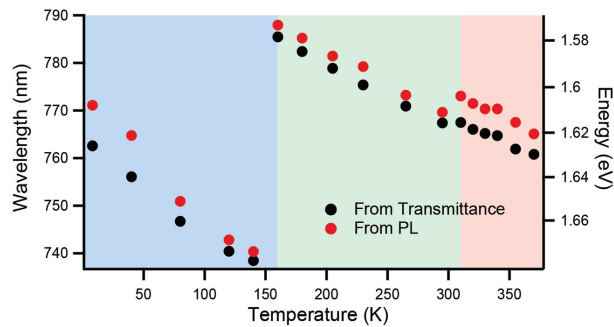


Figure 2.1 – (a) Mobility determined from optical-pump-THz probe measurements. The red dash is  $T^{-3/2}$  dependence. (b) Diffusion lengths at possible cell working temperatures. The plot is reproduced from [79].

Figure 2.2 – Absorption band-edge wavelength (energy) as a function of temperature. The plot is reproduced from [79].



An increased electron scattering on the lattice vibrations leads to the decrease in mobility. The phonon mode population is assigned to the Pb-I-Pb angular bending vibration. And as the position of CB and VB in a semiconductor is governed by phonon populations, it defines the bandgap of the material.

While most research concentrates on a single sweep across the temperature range, MAPbI<sub>3</sub> in a well-encapsulated solar panel can easily reach temperatures over 360 K under operating conditions [82]. Consequently crossing the high-temperature phase transition at least twice a day. Thus, a detailed investigation of the MAPbI<sub>3</sub> transformations while repeatedly crossing the phase transition temperature is needed. In this Chapter, it is shown that after thermal cycling around either phase transition temperature, MAPbI<sub>3</sub> does not return to the initial state. Instead, the material approaches an equilibrium state with specific electronic properties for each phase transition.

## 2.2 The low-temperature tetragonal to orthorhombic phase transition

First, we will take a look at MAPbI<sub>3</sub> at low temperatures. Below 130 K, MAPbI<sub>3</sub> is in the orthorhombic phase. In this phase the organic cations are fully ordered, the orientation of the C–N axis of MA<sup>+</sup> relative to the principal orthorhombic axes is restricted to two directions. This restriction is due to hydrogen bonds between the NH<sub>3</sub> group and the nearest I atoms, which also prevents the axial rotation of MA<sup>+</sup> [83]. Upon heating, above 130 K, the cation starts to adopt 90°-separated orientations. From 130 K up to 160 K the tetragonal and orthorhombic phases coexist [84]. By the temperature of 181 K, all four equivalent directions of the tetragonal unit cell become equally preferred. The organic cation remains in this disordered state with four possible alignments up to room temperature. In the tetragonal phase, the organic cation and the PbI<sub>6</sub> octahedra are rotated around the *c*-axis in an alternating manner. Such MA order–disorder transformation induces a transition from tilted to non-tilted PbI<sub>6</sub> octahedron [85].

## 2.2. The low-temperature tetragonal to orthorhombic phase transition

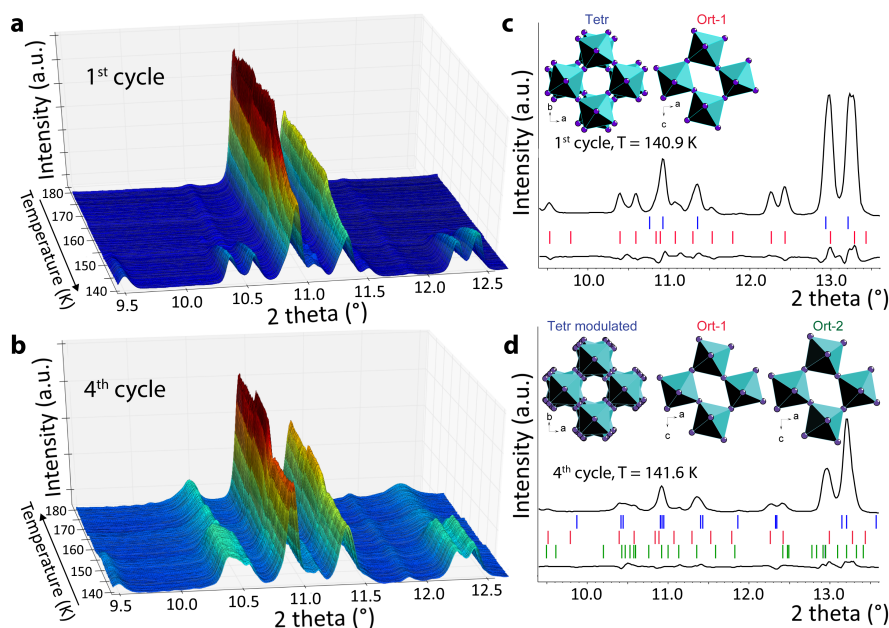


Figure 2.3 – Temperature-dependent XRD profiles recorded upon (a) cooling during the first and (b) heating during the fourth thermal cycles around 160 K. (c) A part of the XRD profile for the two-phase state at 140.9 K in the first thermal cycle. (d) A part of the XRD profile for the three-phase state at 141.6 K in the fourth thermal cycle (full XRD profile, Appendix Figure A.11). The blue, red, and green ticks below the profiles mark reflections of Tetr, Ort-1, and Ort-2 phases, respectively. The black lines below the ticks refer to the difference between the observed and calculated profiles.

### 2.2.1 X-ray data

The effect of thermal cycling between 180 and 140 K on the  $\text{MAPbI}_3$  structure was examined by powder XRD (PXRD) experiment (see Appendix A.2 for details). The XRD profiles obtained during the first thermal cycle upon cooling down and the fourth cycle upon warming up are shown in Figure 2.3. The data recorded over four thermal cycles enabled the identification of three distinct crystal structures: one tetragonal and two orthorhombic phases. Furthermore, the quantitative analysis of the phase composition at a given temperature showed an evolution of the amounts of the different phases in the sample with the number of cycles. For the first and fourth cycles, the temperature dependence of the calculated contribution of the phases and their unit cell volumes are shown in Figure 2.4, and changes in the unit cell parameters of each phase are presented in Figure 2.5.

#### First cycle

Upon cooling from 180 to 140 K, only a tetragonal (Tetr) phase is present down to a temperature of 157 K, below which the orthorhombic (Ort-1) phase appears, as can be seen from the peak appearance and splitting in Figure 2.3a. The result that Tetr and Ort-1 phases coexist down to 140 K is in accordance with previous reports [86, 87]. Their coexistence can be seen in the

Figure 2.4 – Temperature dependence of the phase composition and the unit cell volume of MAPbI<sub>3</sub> in the first and fourth thermal cycles around 160 K. (a, b) The coefficients  $k_1$ ,  $k_2$ , and  $k_3$  define the contribution of Tetr, Ort-1, and Ort-2 phases at each temperature. (c, d) The average unit cell volume,  $V(\text{avr})$ , was calculated using these coefficients.

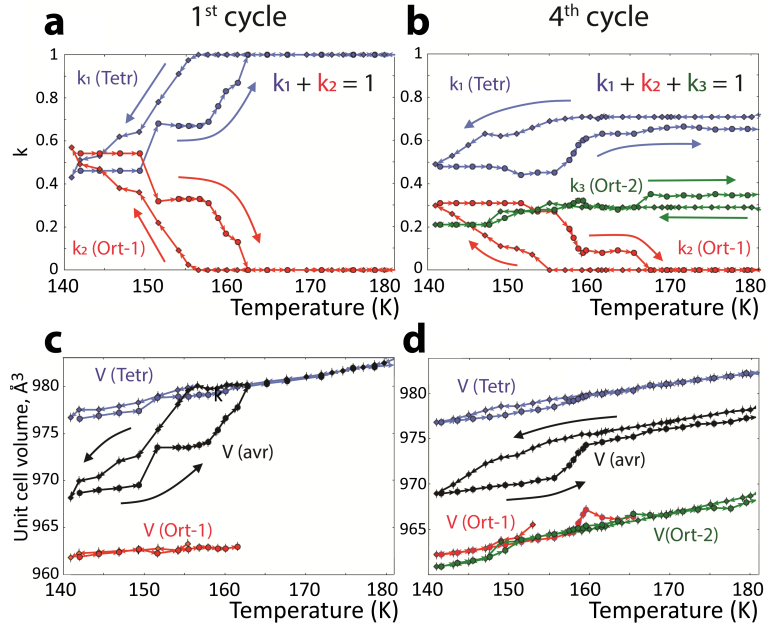
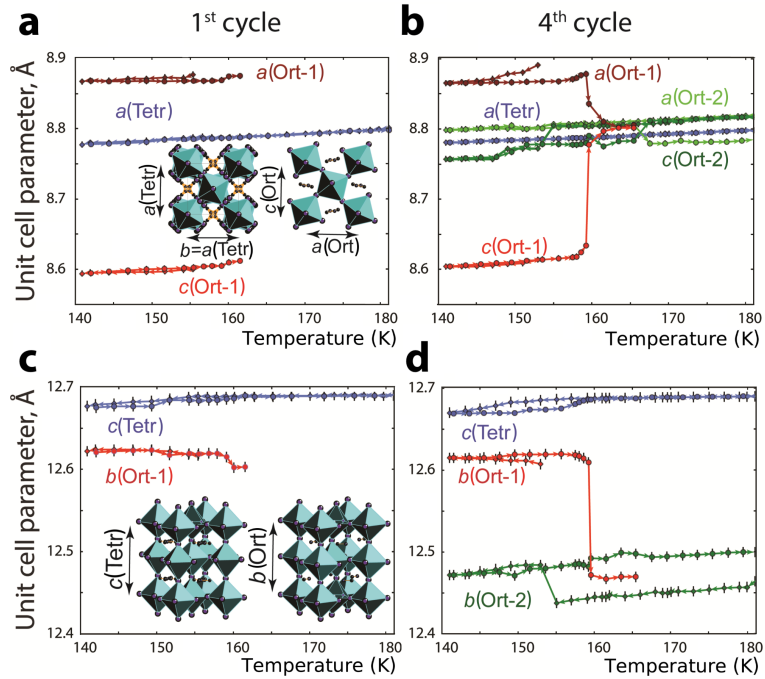


Figure 2.5 – Temperature dependence of the unit cell parameters of the Tetr, Ort-1, and Ort-2 phases revealed in the first and fourth thermal cycle around 160 K. The directions of the temperature sweeps are indicated by arrows between dots in the plots.



XRD profile at 140.9 K in Figure 2.3c. From structural refinement at each temperature the phase contribution can be found, Figure 2.4a, (with the coefficients  $k_1$  for the Tetr and  $k_2$  for the Ort-1 phase). From the plot, we can see the coexistence region and also notice that upon heating and cooling the transition to pure tetragonal phase shifts.

#### Fourth cycle

## 2.2. The low-temperature tetragonal to orthorhombic phase transition

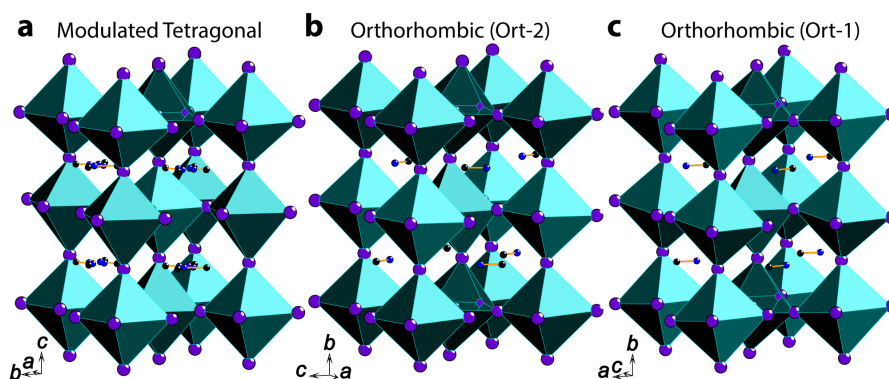


Figure 2.6 – Crystal structure of (a) the modulated tetragonal, (b) the orthorhombic boundary phase and (c) the orthorhombic phase at 141.6 K in the fourth thermal cycle around 160 K.

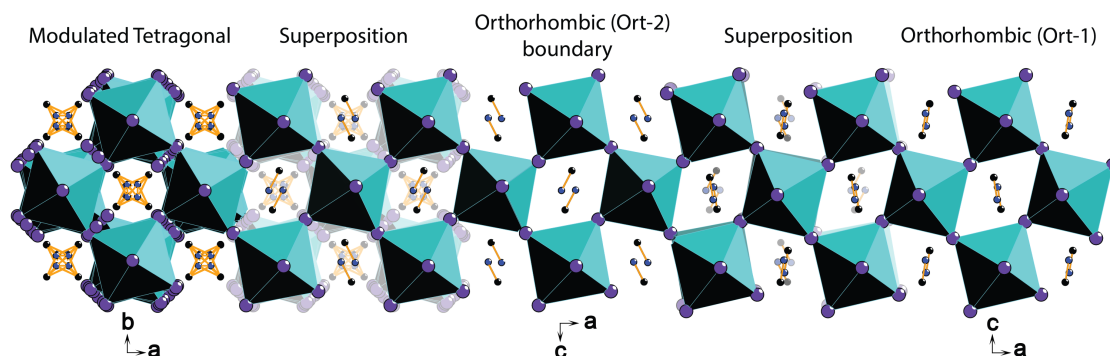


Figure 2.7 – Stacking of the modulated tetragonal (Tetr) and orthorhombic (Ort-1) phase through a boundary phase (Ort-2) at 141.6 K in the fourth thermal cycle around 160 K.

The XRD data plotted in Figure 2.3b indicate a more complex system in the fourth thermal cycle. A different orthorhombic phase, Ort-2, is now present over the full temperature range of 140–180 K. The numerous weak diffraction peaks, shown in Figure 2.3d, point to a modulation of the tetragonal phase, which is accounted for in the structure refinement process (the fitted PXRD profile is in Appendix, Figure A.11).

The modulated Tetr structure, represented in Figure 2.3d, accommodates a slight rotation of the  $\text{PbI}_6$  octahedra around the fourfold axis.

Figure 2.5b shows that independent of the temperature the two unit cell parameters of the Ort-2 ( $a \approx c$ ) phase are close to the parameters of the Tetr phase ( $a = b$ ). This fact suggests an epitaxial intergrowth between the Tetr and Ort-2 phases. Indeed, the coefficients of the phase contribution,  $k_1 \neq 0$  for Tetr and  $k_3 \neq 0$  for Ort-2 in Figure 2.4b, indicate the coexistence of the Ort-2 and Tetr phases at all temperatures between 140 and 180 K. In addition, Ort-1 and Ort-2 phases, as shown in Figure 2.3d and Figure 2.6, are topologically similar and differ only by the orientations of the  $\text{MA}^+$  cations. Hence, the Ort-2 phase can be considered as a boundary phase linking the Tetr and Ort-1 domains, as sketched in Figure 2.7.

Similarly to the observation during the first cycle, the hysteresis in the contributions of the phases Tetr ( $k_1$ ) and Ort-1 ( $k_2$ ) in Figure 2.4b confirms the first-order nature of the phase transition [87]. However, a comparison of Figure 2.4c and d shows a significant smoothing of the hysteresis, leading to the average unit cell volume,  $V(\text{avr})$ , as a result of thermal cycling. This smoothing is due to the presence of the boundary phase Ort-2. It can be expected that the hysteresis of  $V(\text{avr})$  would disappear with more thermal cycles. From Figure 2.4d can be seen that the unit cell volumes of the Ort-1 and Ort-2 phases are practically identical, making them thermodynamically equivalent. Consequently, it suggests that with thermal cycling, the Ort-1 phase could be partially or completely replaced by the Ort-2, thus bringing the system to a state of thermodynamic equilibrium characterized by the coexistence of only two mutually intergrown phases, Tetr and Ort-2.

To summarize the structural refinement for the thermal cycling of  $\text{MAPbI}_3$  between 140 and 180 K, the results indicate that the first-order phase transition, accompanied by the coexistence of the Tetr and Ort-1 phases, gives rise to domain formation [88, 89]. In addition, repeatedly crossing the phase transition leads to a gradual reduction and smoothing of the jump in the average unit cell volume  $V(\text{avr})$ , which is thermodynamically favorable. The changes throughout the thermal cycling occur due to the formation of the Ort-2 phase — a boundary state between the Tetr and Ort-1 phases.

### 2.2.2 Resistivity measurements

The contribution of the Tetr phase at the lower end of the explored temperature range (140 K) remains constant throughout the whole experiment (Figure 2.4a, b), and the boundary phase Ort-2, which is absent in the first sweep, comes from the Ort-1-Ort-2 transformation as a result of thermal cycling. Given that the contribution of Ort-2 scales up with the number of cycles ( $k_3 = 0$  in the first thermal cycle and  $k_3 = 0.25 \pm 0.05$  during the fourth thermal cycle), a growth of the number of domains is expected. This statement is supported by the electrical resistance of  $\text{MAPbI}_3$  single crystal (Figure 2.8, Appendix B.3), which shows at a given temperature, there is a continuous increase over the six successive thermal cycles. The complex temperature dependence of the resistivity has previously been discussed by Pisoni et al., [90], where the peak in the resistivity at 160 K is explained by the enhanced scattering of electrons due to increasing number of domain boundaries.

It has been pointed out that the efficiency of the charge-carrier trapping sharply decreases in the vicinity of the boundary phase [88]. The apparent transition temperature fluctuates slightly throughout multiple cycles because it is strongly dependent on the local properties of the material and, in particular, on the type and density of structural and chemical defects. Indeed, the Ort-1 and Tetr phases have different symmetries, and the actual symmetry of the defects can encourage the formation of either structures; hence, the transition temperature can increase or decrease.

## 2.2. The low-temperature tetragonal to orthorhombic phase transition

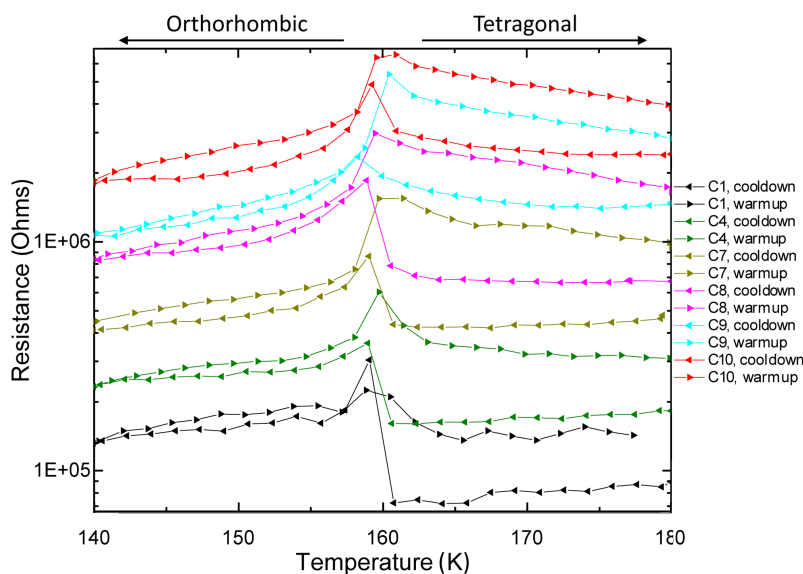


Figure 2.8 – Temperature dependence of the electrical resistance of MAPbI<sub>3</sub> during thermal cycling around 160 K.

### 2.2.3 Heat capacity measurements

Measurements of heat capacity at a constant pressure,  $C_p$ , were carried out on single crystals of MAPbI<sub>3</sub> using the thermal relaxation technique (Appendix B.6).

The heat capacity data of MAPbI<sub>3</sub> single crystal for the low-temperature transition shown in Figure 2.9 (calculated entropy change is in Appendix, Figure B.6) substantiate the XRD results and suggest a jump in the structural order parameter. The structural transition is reflected in the heat capacity data as a sharp peak. In agreement with the resistivity measurements, the existence of a hysteresis indicates that the transition is first order [89]. Also, the decrease of the heat capacity peak value with thermal cycling reflects the substitution of Ort-1 phase for Ort-2. At 330 K transition preserves the disordered character of the MA<sup>+</sup> cation and at 160 K an orthorhombic symmetry reduces the disordering MA occupation. The transition from tetragonal to orthorhombic symmetry reveals an important fact because in all cases there is a transition from centrosymmetric to non centrosymmetric space group which enables the

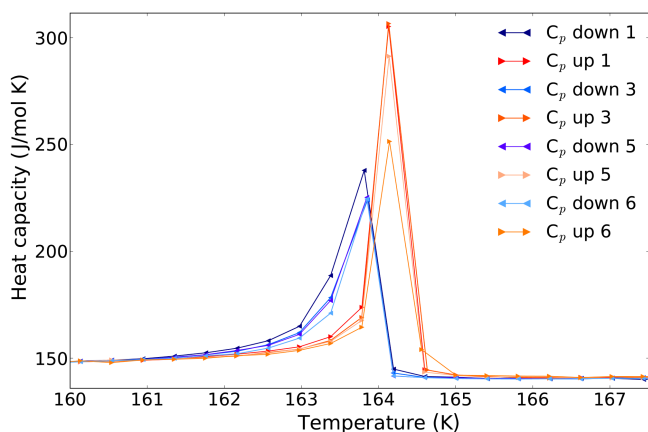


Figure 2.9 – Temperature dependence of the heat capacity of MAPbI<sub>3</sub> during thermal cycling around 160 K. Cycles 2 and 4 have been omitted for clarity.



ferroelectric or antiferroelectric phenomena in the material [91].

### 2.3 The high-temperature tetragonal to cubic phase transition

As the crystal is warmed up toward and past room temperature, the hydrogen bond between MA and iodine in the tetragonal phase of MAPbI<sub>3</sub> is progressively weakened. Thus, the cation starts to tumble inside the inorganic framework [92]. The rotation angle of the octahedra in the tetragonal phase decreases monotonically with increasing temperature, and simultaneously, the lattice constants  $c$  and  $a$  become equal, resulting in the high-temperature cubic phase above 330 K [93].

It has been suggested that the structural change is accompanied by a ferroelectric to paraelectric transition [94], which is plausible, given that the tetragonal (space group  $I422$ ) and cubic ( $Pm\bar{3}m$ ) phases, respectively, lack and possess an inversion symmetry [95]. The high-temperature transition results in the reduction of the unit cell in the  $c$ -direction and could be driven by an instability of the crystal with respect to the emergence of a particular phonon mode. This hypothesis is supported by the theoretical work of Saidi and Choi [96], in which the stabilization of the cubic phase is explained through vibrational energy and entropy considerations.

#### 2.3.1 X-ray data

In-situ powder XRD experiments were conducted on grounded MAPbI<sub>3</sub> crystals during six thermal cycles between 310 and 350 K. The lattice structure and the unit cell parameters were refined across the explored temperature range for the first and sixth cycles. The XRD profiles shown in Figure 2.10a indicate a gradual transition between the tetragonal and cubic phases in the first cycle, whereas those in Figure 2.10b imply the occurrence of an incommensurately modulated phase in the sixth cycle. Incommensurately modulated crystals are often encountered at phase transitions [97], however here it stabilized with thermal cycling. In Appendix A.1.4 more information on the incommensurately modulated structure definition and understanding is provided.

All the structural changes upon thermal cycling around 330 K are described in terms of a single tetragonal (3 + 3)-dimensional superspace group generated from the space group  $P4/mmm$  [98], which is applied to the pseudocubic unit cell with  $a \approx c \approx 6.3$  Å. The modulation vectors are  $\mathbf{q}_1 = \alpha \mathbf{a}^* + \alpha \mathbf{b}^*$ ,  $\mathbf{q}_2 = -\alpha \mathbf{a}^* + \alpha \mathbf{b}^*$ , and  $\mathbf{q}_3 = \gamma \mathbf{c}^*$ , where  $\alpha = (0.5 - \Delta_1)$  and  $\gamma = (0.5 - \Delta_2)$  can be either rational if the parameters  $\Delta_1$  and/or  $\Delta_2$  are 0, or irrational otherwise. If  $\Delta_1 = \Delta_2 = 0.5$ , then  $\alpha = \gamma = 0$  and the space group describes the 3D pseudocubic structure. In the  $a = c$  case, the structure acquires the cubic symmetry of the  $Pm\bar{3}m$  supergroup. Using this structural representation, only three atoms, located in fixed positions (Pb: 1a (000); I1: 1b (00½); I2: 2f (½00)), define the inorganic framework. The lattice parameters  $a$  and  $c$  were refined using only the main diffraction reflections indexed with only  $\mathbf{a}^*$ ,  $\mathbf{b}^*$ , and  $\mathbf{c}^*$  in the reciprocal lattice. Figure 2.11 shows these parameters as a function of temperature for the first and sixth thermal cycles. The coefficients  $\alpha$  and  $\gamma$  of the modulation vectors were refined using the whole set of reflections, including the significantly weaker satellites that can be indexed only if  $\alpha$  and  $\gamma$  differ from 0. Figure 2.11 shows



### 2.3. The high-temperature tetragonal to cubic phase transition

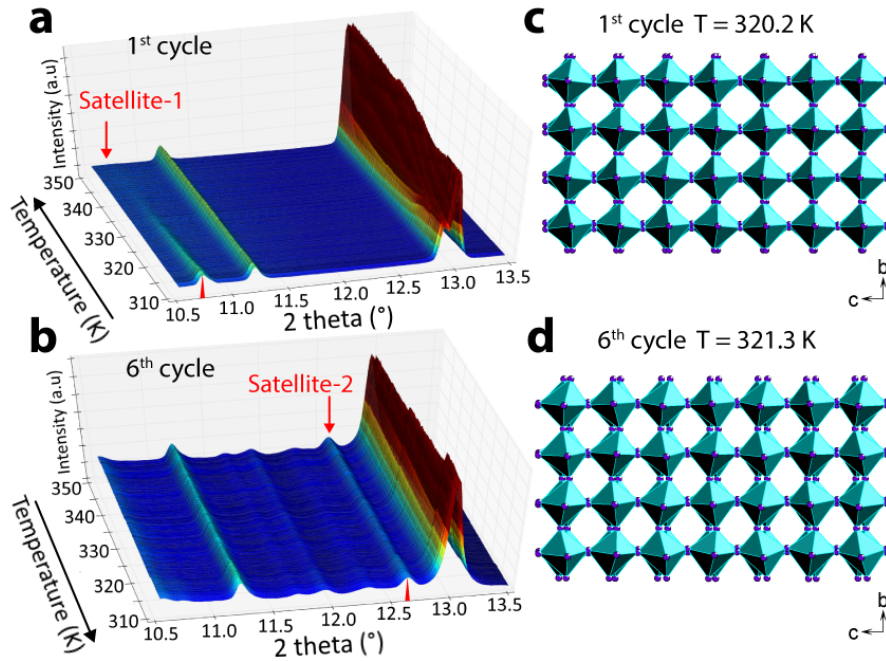


Figure 2.10 – Temperature-dependent XRD profiles recorded upon (a) heating during the first and (b) cooling during the sixth thermal cycles around 330 K. (c) The (*bc*) projection of a portion of the incommensurately modulated tetragonal structure in the first thermal cycle at 320.2 K. (d) The projection of a portion of the incommensurately modulated tetragonal structure in the sixth thermal cycle at 321.3 K.

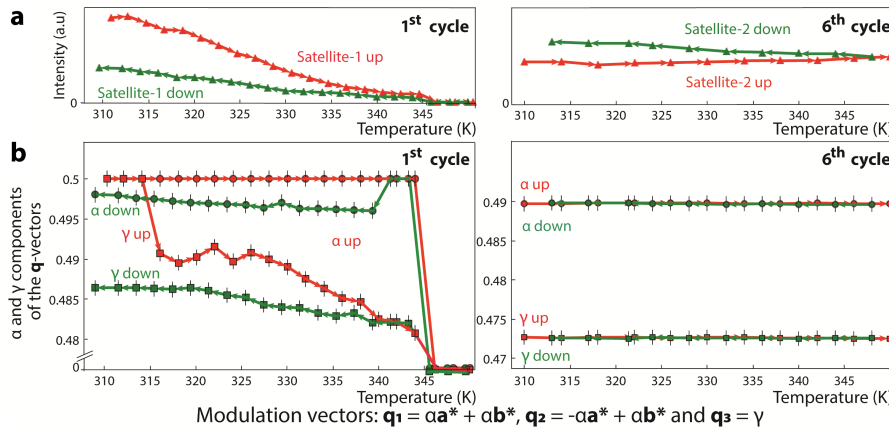


Figure 2.11 – Temperature dependence of the crystallographic characteristics for the incommensurately modulated structure of MAPbI<sub>3</sub> in the first and sixth thermal cycles around 330 K. (a) The integrated intensity of the strongest satellite. (b) Coefficients of the indicated modulation vectors. In the sixth thermal cycle, the weak temperature dependence of the quantities indicates the stabilization of the modulated phase, whereas an increase in the intensity of the satellite indicates the evolution of this phase toward an amplification of displacements of atoms from their average position.

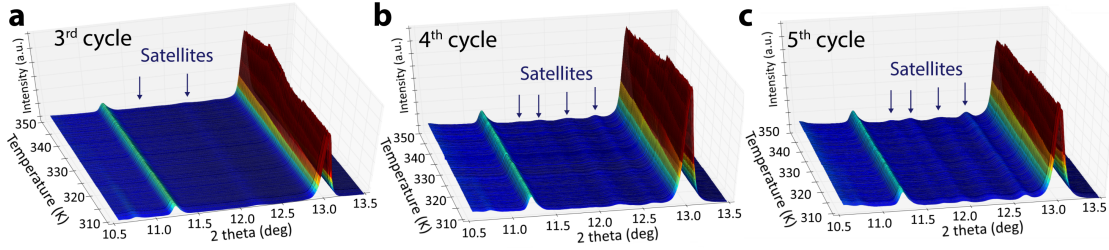


Figure 2.12 – Temperature-dependent XRD data obtained from 310 K to 350 K during (a) the third, (b) fourth and (c) fifth thermal cycles. Changes in the unit cell parameters and the increased intensity of the satellite reflections can be seen from the third to fifth thermal cycles.

the temperature dependence of their integrated intensity as well as the change in the  $\alpha$  and  $\gamma$  coefficients for the modulation vectors. The existence of the satellites (highlighted in Figure 2.12) indicates the presence of modulation waves of atomic displacements. The stronger intensities of satellites and the larger displacements are expected. Consequently, the absence of satellites denotes a primitive, non-modulated structure with the unit cell parameters mentioned above and atomic positions in accordance with the tetragonal space group  $P4/mmm$ . The  $Pm\bar{3}m$  super-group, which is characteristic of the cubic phase, requires identity of  $a$  and  $c$  lattice parameters.

### First cycle

On the first heating stage, in Figure 2.11 a, the intensity of the strongest satellite decreases to zero above 346 K, indicating that at this temperature only the cubic phase is expected [96]. However, in conformity with Tyson et al. [99], a pseudocubic unit cell in the whole 310–350 K range is observed. Another degenerate case, when  $\alpha = \gamma = 0.5$ , was observed below 315 K during the first thermal cycle heating stage. These rational values correspond to the room temperature tetragonal unit cell. Indeed, the vectors  $\mathbf{q}_1 = 0.5\mathbf{a}^* + 0.5\mathbf{b}^*$  and  $\mathbf{q}_2 = -0.5\mathbf{a}^* + 0.5\mathbf{b}^*$  define the tetragonal basis of the cell as  $\mathbf{a}_{tetr} = \mathbf{a} + \mathbf{b}$  and  $\mathbf{b}_{tetr} = -\mathbf{a} + \mathbf{b}$  ( $a_{tetr} = b_{tetr} = a\sqrt{2} \approx 8.9 \text{ \AA}$ ), and the vector  $\mathbf{q}_3 = 0.5\mathbf{c}^*$  defines the doubling of the  $c$  parameter,  $\mathbf{c}_{tetr} = 2\mathbf{c}$  ( $c_{tetr} = 2c \approx 12.6 \text{ \AA}$ ). The clear changes in the unit cell parameters, modulation vectors, and intensity of the strongest satellite reflections indicate that the structural transformation from the room temperature tetragonal phase directly into the pseudocubic phase occurs only in the first thermal cycle. In accordance with a previous report [99], the presence of an intermediate phase is confirmed, in the temperature range of 315–346 K between tetragonal and cubic phases.

The crystal structure of the intermediate phase has been refined by the Rietveld method for 320.2 K (Appendix Figure A.12, section A.1.2). The I atoms are primarily displaced due to the structural modulations.

A portion of the structure shown in Figure 2.10c shows that these displacements result in a wave of tilted  $\text{PbI}_6$  octahedra around the  $a$  and  $b$  axes, whereas one would rather expect a rotation around the  $c$ -axis, which is typical for the tetragonal phase. This “tilt wave” results in the crystal spatially alternating between the two types of regions: without (pseudocubic)

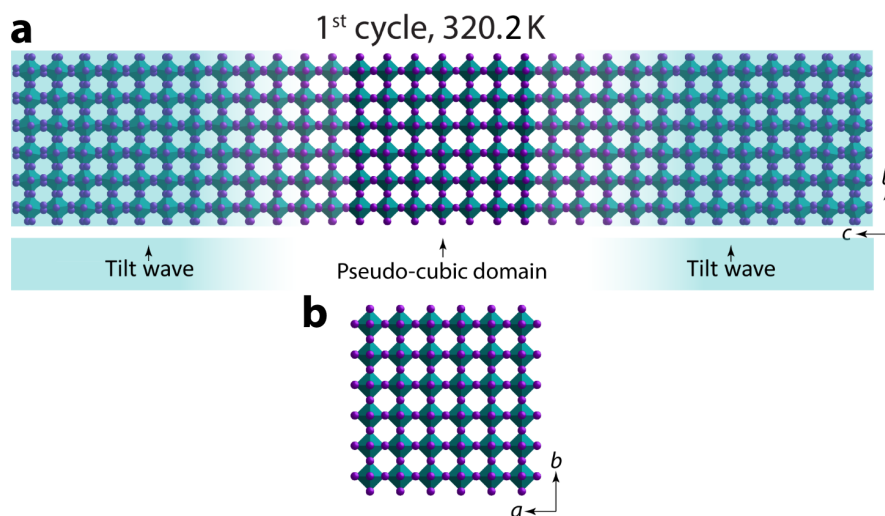


Figure 2.13 – Ordering in the distribution of the PbI<sub>6</sub> octahedra in the intermediate structure of MAPbI<sub>3</sub> at 320.16 K in the first thermal cycle. (a) Alternation of the non-tilted (pseudo-cubic) and the wave-tilted domains along the *c*-axis. (b) No rotation of the PbI<sub>6</sub> octahedra around the tetragonal *c*-axis is observed in the structure projection along the tetragonal *c*-axis.

and with periodically modulated tilt of the octahedra along the *c*-axis (see Figure 2.13). Figure 2.11a shows that the intensity of the strongest satellite continuously decreases with increasing temperature and is completely suppressed when the pseudocubic phase sets in. This behavior indicates that the average size of the pseudocubic region grows, and the mean magnitude of the displacements of I atoms becomes smaller.

#### Sixth cycle

In the sixth thermal cycle, a single stable phase is present. It is characterized by the irrational temperature-independent modulation coefficients  $\gamma \approx 0.473$  and  $\alpha \approx 0.490$  (Figure 2.11), which point to an aperiodicity of the crystal along the *c*-axis as well as in the (*ab*) plane. The unit cell parameters change linearly with temperature, as shown in Figure 2.14. Their values for both the warm-up and cool-down are now identical, suggesting that the system has settled into a thermodynamically stable state. A crystal structure estimation for the phases present in the sixth thermal cycle at 350.2, 321.3, and 310.2 K (Rietveld refinements in Figure A.13, Appendix A.1.2) shows that the “tilt wave” occurs along lattice axes in agreement with irrational values of the  $\alpha$  and  $\gamma$  components in the modulation vectors (Figure 2.11). The Figure 2.10d shows the variation of the tilt of the octahedral.

Despite the fact that each octahedron is tilted, the degree of tilt varies within a coherent area. Less tilted octahedra form pseudocubic structure regions, which smoothly turn into tetragonal, consisting of more tilted octahedra. With such a change from one unit cell to another, only an approximate boundary between these regions and, accordingly, an approximate size of the pseudocubic regions can be discussed. Due to incommensurability in three axes (three independent **q**-vectors of modulation), even the approximate size of the regions is varied de-

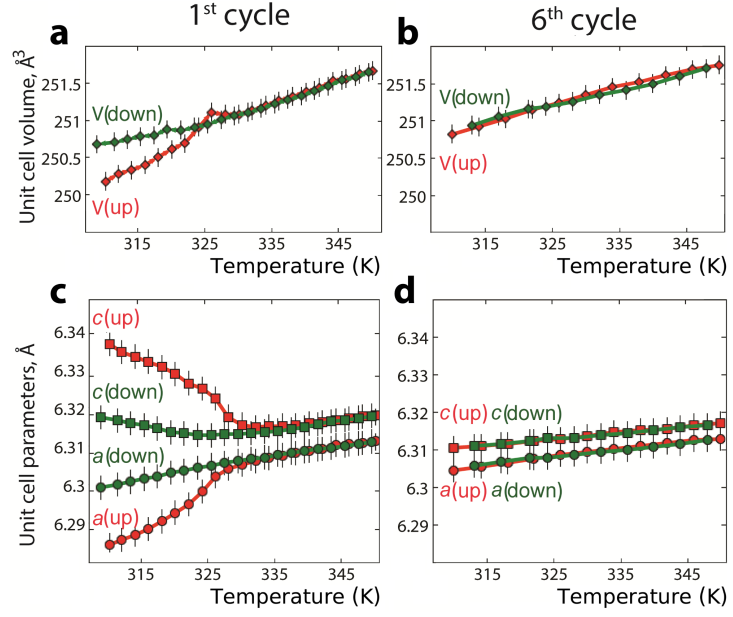


Figure 2.14 – Temperature-dependent variation of (a, b) the tetragonal unit cell volume and (c, d) its  $a$  and  $c$  parameters in the first and sixth thermal cycle around 330 K. In the sixth thermal cycle, the phase has been stabilized with respect to the plotted parameters.

pending on a portion taken from the aperiodic structure. However, the reconstruction of an identical portion of the structure taken at different temperatures can illustrate the temperature dependence of the size. Such illustration and details of the reconstruction are given in Figure 2.15 for a structure portion of  $14a \times 14b \times 5c$  ( $10 \times 10 \times 3$  nm). Temperature dependence of the incommensurately modulated structure, appearing as a result of thermal cycling around 330 K.

The main and expected temperature dependence concerns the approximate size of pseudocubic regions, which increases with increasing temperature from 310.2 to 350.2 K. The estimation of their exact size is quite a challenging task because of the following reasons. First, it is necessary to define “pseudo-cubic” regions, i.e. to define limits of deviations from the “cubic” arrangement. Some deviations are always present in the incommensurate structure owing to the structure modulation. A magnitude of the deviations is generally defined by a sum of the whole set of satellite reflection intensities, which is a complicated task to estimate. Second, owing to incommensurability in three axes (three  $q$ -vectors of the incommensurability, two of them are in the  $(\mathbf{a}^*\mathbf{b}^*)$ -plane and the third is along  $\mathbf{c}^*$  axes), even the approximate region size is varied depending on a portion taken from the aperiodic structure. However, using an opportunity to reconstruct an identical portion of the structure taken at different temperatures with the same parameters (numbers of average unit cells and the  $(t_0, v_0, u_0)$  origin of the modulation waves), it is possible to illustrate the temperature dependence of the size, Figure 2.15. After the size ( $14a \times 14b \times 5c$ ) of the portion has been selected, the origin for the modulation waves have been fixed as  $t_0 = 0, v_0 = 0, u_0 = 0$ . Then positions of all atoms (Pb and I) within the selected area have been calculated as in the unit cell defined by the selected area with  $P1$  symmetry. In the selected area, the approximate size of pseudocubic regions increases with increasing temperature from 310.2 to 350.2 K, indicating a transformation from “mainly tetragonal” to “mainly pseudocubic”.

Any dynamic distortion in a crystal can be described in terms of a complete set of normal

### 2.3. The high-temperature tetragonal to cubic phase transition

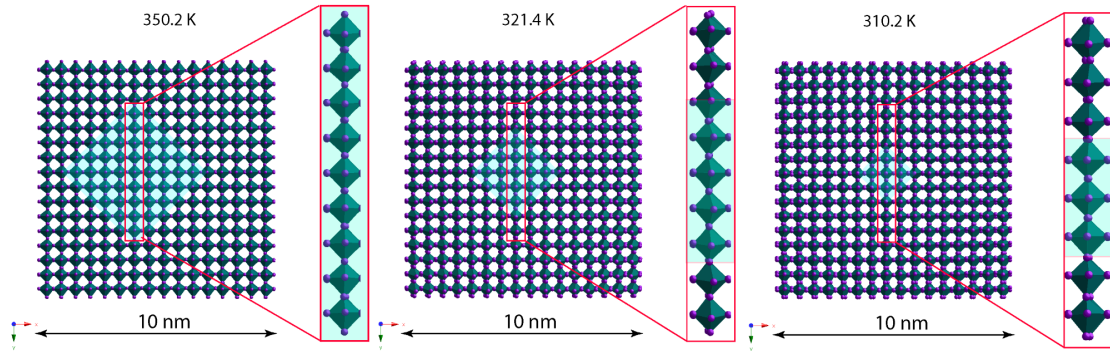


Figure 2.15 – A portion of the tetragonal modulated structure in the sixth thermal cycle at different temperatures. The (xy) projection is shown for a portion of  $14a \times 14b \times 5c$  unit cells. Cyan background indicates the approximated part of the structure, which is similar to the cubic phase. The size of this part decreases with lowering temperature indicating an evolution of the structure toward the tetragonal phase.

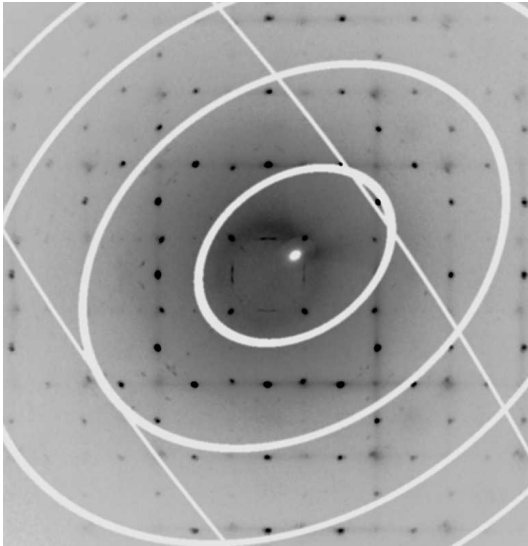


Figure 2.16 – XRD pattern of a single crystal taken in the (0.5 k l) plane after the sixth thermal cycle at 340 K.

vibrational modes. When a solid undergoes a structural phase transition, the process is often described in terms of anomalous behavior of a single mode, characterized by its displacement eigenvector, frequency, and wavelength. For the phase transitions the formation of the incommensurately modulated phase is also frequently driven by a soft phonon mode showing up at high temperature that condenses at the modulation wavevector [100]. If the space group of one phase is a subgroup of that of the other phase, the transition may proceed via a continuous distortion of the unit cell, i.e., the transition is of second order [101].

Within this framework, as the high-temperature pseudocubic phase is approached, the frequency of a particular low-energy phonon mode grows. In Figure 2.16, one can see the diffuse scattering in the diffraction pattern. In case of modulation in the crystal the pattern consists of the main and satellite reflections. Static and dynamic disorder in the system are seen on

the XRD patterns as the diffuse scattering. In this study a disorder diffuse scattering is present, as the diffuse lines around the Bragg reflection gradually increased with thermal cycling. The disorder diffuse scattering covers effects due to static occupational or displacive alterations of the crystal structure that are present only on a local scale [102], which corresponds to the final system. For the broad diffuse maxima, the periodicity of superspace must be disrupted [102]. This can be done with an enhancement of the vibrational energy of the lattice. The existence of transverse and longitudinal acoustic phonon modes as well as one transverse optical branch in the inorganic framework at 350 K has been shown by Beecher et al. [103]. Due to the low-energy modes associated with the inorganic lattice, phonons provide a major contribution to stabilize the cubic phase at a high temperature. From the structural refinement, we see the “tilt wave”; however, a proper mapping of the phonon modes to the structure modulations will require an additional study.

To summarize, the structural refinements for the thermal cycling around the high-temperature tetragonal–cubic phase transition show that the sharp change of the unit cell parameters at 330 K occurs only in the first thermal cycle. During the same initial pair of temperature sweeps, the change in the mobility of the  $\text{PbI}_6$  octahedra from rotation to tilt relative to the tetragonal  $c$ -axis underlies the 315 K second-order phase transition, and the first-order phase transition accompanied by a  $(3 + 3)$ -dimensional symmetry transformation into a 3D symmetry is observed at 345 K. Thermal cycling results in the occurrence of a  $(3 + 3)$ -dimensional incommensurately modulated phase, which consists of pseudocubic and pseudotetragonal regions as a result of the “tilt-wave” modulation of the octahedra orientations.

### 2.3.2 Resistivity measurements

To further explore the effect of thermal cycling around the high-temperature transition on the electronic properties of  $\text{MAPbI}_3$  the resistance of a single crystal between 310 and 350 K was measured. It can be seen from Figure 2.17 that in contrast to what was observed around the low-temperature transition, here the resistivity peak, just below 330 K, disappears after multiple thermal cycles. This supports the detected structural transformations.

Indeed, the change in sample resistance observed between the third and fifth cycles can be attributed to the stabilization of the incommensurately modulated phase that contains both the cubic-like and the tetragonal-like regions. The more progressive variation in the sample resistance during the fifth and seventh thermal cycles can be associated with the evolution of the incommensurate phase, which is inferred from the increased intensity of satellite reflections presented in Figure 2.11 and Figure 2.12.



## 2.3. The high-temperature tetragonal to cubic phase transition

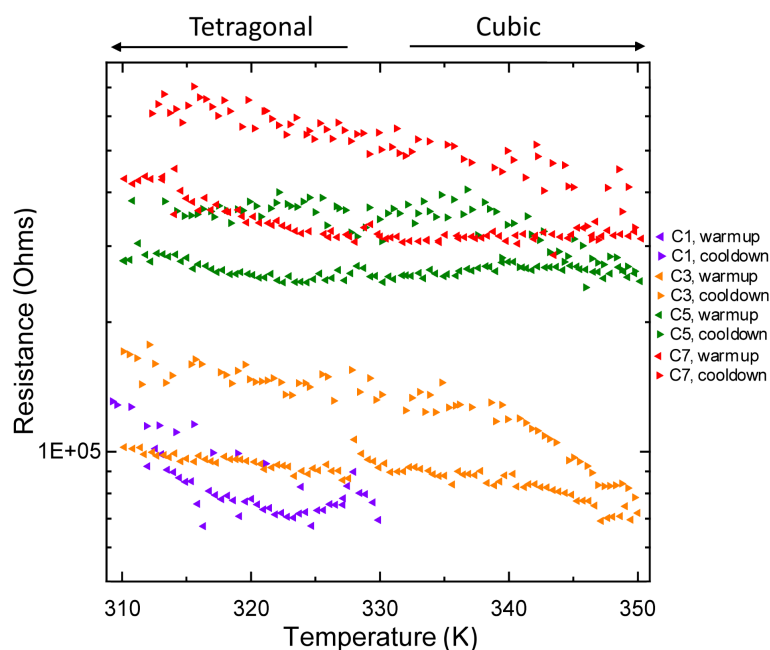


Figure 2.17 – Temperature dependence of the electrical resistance of MAPbI<sub>3</sub> during thermal cycling around 330 K. Cycles 2, 4, and 5 have been omitted for clarity.

### 2.3.3 Heat capacity measurements

Both the high- and low-temperature phase transitions of MAPbI<sub>3</sub> are technically of first order. However, the high-temperature transition is close to being of second order [104]. In addition to the fact that both the tetragonal and the pseudocubic phases can be described by one super-space group, the heat capacity data shown in Figure 2.18 (consistent with those in the literature [99]) support this statement. There is no apparent hysteresis, and the broad peak more closely resembles a power law divergence rather than a delta function. Changes in entropy ( $\Delta S$ ) are shown in Figure B.7, Appendix B.6. The jump in entropy is smoother for the high-temperature transition than for the low-temperature one (Appendix Figure B.6).

What stands out from the data in Figure 2.18 is the fact that the heat capacity value is higher

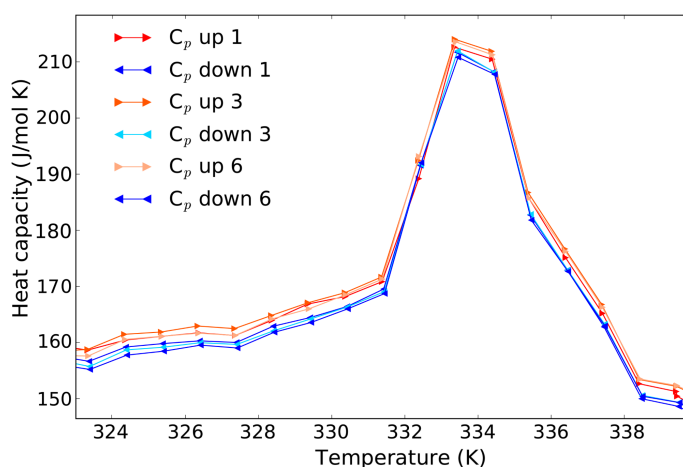


Figure 2.18 – Temperature dependence of the heat capacity of MAPbI<sub>3</sub> during thermal cycling around 330 K. Cycles 2, 4, and 5 have been omitted for clarity.

below the transition than above it. Onoda-Yamamuro et al. [104] attributed an excess heat capacity in the region below the transition to the associated latent heat smeared out toward the low-temperature side. Moreover, the results indicate that the phase transition exists even after six thermal cycles. The structural characteristics of the crystal can explain the behavior of the heat capacity during the thermal cycling. At the start of the first cycle, the strongest diffraction peak indicating the tetragonal phase (Satellite-1 in Figure 2.10a) continuously vanishes with increasing temperature. The highest rate of this disappearance (Figure 2.11a) coincides with the sharp rise in heat capacity (Figure 2.18) around 330 K. Starting from 335 K, both the intensity and the heat capacity value fall more smoothly. Therefore, the observed changes in the heat capacity are attributed to the cubic–tetragonal transition. This transformation is clearly a characteristic of the first thermal cycle. As discussed in Section 2.3.1 (Figure 2.15), a similar transformation is observed in the sixth thermal cycle, however, within the evolution of a single incommensurately modulated phase from “mainly cubic” to “mainly tetragonal”.

## 2.4 Conclusions

To investigate the effect of thermal cycling through the low- and high-temperature structural transitions on the crystal structure and electronic properties of MAPbI<sub>3</sub> crystals XRD, electrical resistivity, and heat capacity measurements were performed at temperatures covering each phase transition.

In case of the tetragonal–orthorhombic phase transition (160 K):

- Repeatedly crossing the phase transition generates an increase in the concentration of the domains of different phases.
- After four cycles, the new orthorhombic phase is present above and below the transition and acts as a boundary phase, which with temperature sweeps progressively replaces the low-temperature orthorhombic phase.
- This change correlates with the reduction in photoconductance as a result of thermal cycling [105].

In case of the tetragonal–cubic phase transition (330 K):

- An incommensurately modulated tetragonal phase emerges, which stabilizes the structure with successive transitions. This suggests that there is no boundary phase between the cubic and tetragonal regions, as both belong to the same incommensurately modulated structure.
- Series of phase transformations are described within the single (3 + 3)-dimension super-space group generated from the space group  $P4/mmm$  and applied to the pseudocubic tetragonal unit cell with  $a \approx c \approx 6.3$  Å.



- The coefficients  $\alpha$  and  $\gamma$  of the modulation vectors  $\mathbf{q}_1 = \alpha \mathbf{a}^* + \alpha \mathbf{b}^*$ ,  $\mathbf{q}_2 = -\alpha \mathbf{a}^* + \alpha \mathbf{b}^*$ , and  $\mathbf{q}_3 = \gamma \mathbf{c}^*$  determine the temperature- and the cycling-dependent state of the structure.



### 3 Pressure-induced transformation of $\text{CH}_3\text{NH}_3\text{PbI}_3$

Pressure variation adds a new dimension to crystal-structure analyses. Pressure is highly efficient for generating phase transitions, new phases and chemical reactions in soft material as  $\text{MAPbI}_3$  [106].

The high-pressure set-up consists of two opposed-diamond-anvils cell (DAC), an example of which is shown in Figure 3.1a. Diamond is the most suitable material for high-pressure XRD measurements due to the material's hardness and low absorption of short wavelengths. Synchrotron X-ray beams can be collimated down to a few micrometres, reducing the problem of the beam shadowing by the gasket [106]. However, the data for the low-symmetry samples can be incomplete due to the limited window opening, as illustrated in Figure 3.1b. As can be concluded from this issue, in case of a high-pressure XRD experiment, additional corrections to the limited data should be applied, which complicates the crystallographic calculation overall.

The  $\text{MAPbI}_3$  crystal structure is flexible due to a large space inside the inorganic framework (the void volume is  $\approx 211 \text{ \AA}^3$ ), where the small ( $\approx 36 \text{ \AA}^3$ ) cation is located. The strength and conformation of the hydrogen bonds between the  $\text{PbI}_6$  octahedra and the organic cation can be influenced by external factors, for instance, pressure or temperature.

There are two major pressure-induced structural transformations in  $\text{MAPbI}_3$ : a phase transition and amorphization. In DAC with helium pressure-transmitting medium (PTM) the applied pressure induces octahedral rotations and bond compression in the inorganic layers of  $\text{MAPbI}_3$  [107]. The material undergoes a phase transition at 0.3 GPa and amorphization at pressures above 2.7 GPa. It was shown that the resistivity of  $\text{MAPbI}_3$  decreases by 3 orders of magnitude between 30 and 51 GPa [107]. Reduction of the activation energy for conduction down to 13 meV under

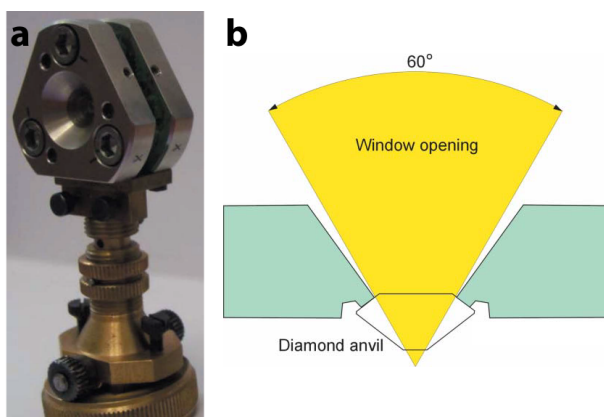


Figure 3.1 – (a) Photograph of the diamond-anvil cells mounted on goniometer head. (b) The effective access to the sample for XRD measurements, the crown facets of the anvil are supported on the edges of the window in the steel backing plate. The pictures are reproduced from [106].

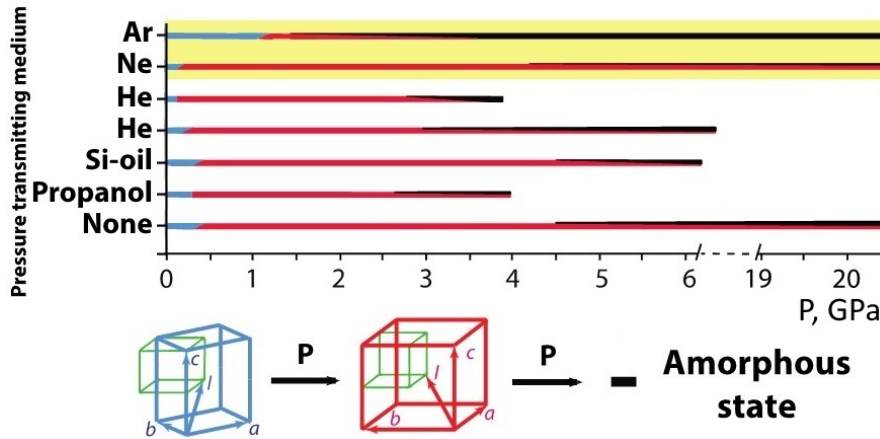


Figure 3.2 – Overview of the  $\text{MAPbI}_3$  pressure-induced transformation at room temperature. Top panel: influence of the PTM on the transformation. Bottom panel: the relations between the unit cells of different phases - the primitive perovskite cubic cell (green line), the tetragonal body-centred cell (blue), the body-centred (pseudo)cubic cell (red) and amorphous phases. The data are reproduced from: He [108, 107], no PTM (None) [109, 110], silicon oil (Si-oil) [110], propanol [111]. Data corresponding to Ar and Ne (highlighted in yellow) are from the present study.

Cubic	$a_{pr} \approx 6.4 \text{ \AA}$	ambient conditions
Tetragonal	$a = b \approx a_{pr} \sqrt{2} \approx 8.8 \text{ \AA}$ $c \approx 2a_{pr} \approx 12.7 \text{ \AA}$	ambient conditions
Pseudocubic	$a \approx b \approx c \approx 2a_{pr} \approx 12.3 \text{ \AA}$	high pressure

Table 3.1 – The unit cell parameters of different  $\text{MAPbI}_3$  phases under ambient and high-pressure conditions.

high pressure, suggested that the perovskite is approaching a metallic state at 51 GPa [107].

In Figure 3.2 a pressure-induced transformation of  $\text{MAPbI}_3$  in different PTM is presented. At low pressures (0.1–0.3 GPa), a first-order phase transition from the tetragonal body-centred to the body-centred (pseudo) cubic unit cell takes place (Figure 3.2, blue to red lines, Table 3.1). The amorphization of the compound occurs at higher pressure after the structural phase transition (Figure 3.2, black line).

It can be seen, that in different experiments the amorphization has been observed under different pressures. The PTM could be considered as one of the major factors affecting the pressure-induced transformation of  $\text{MAPbI}_3$ .

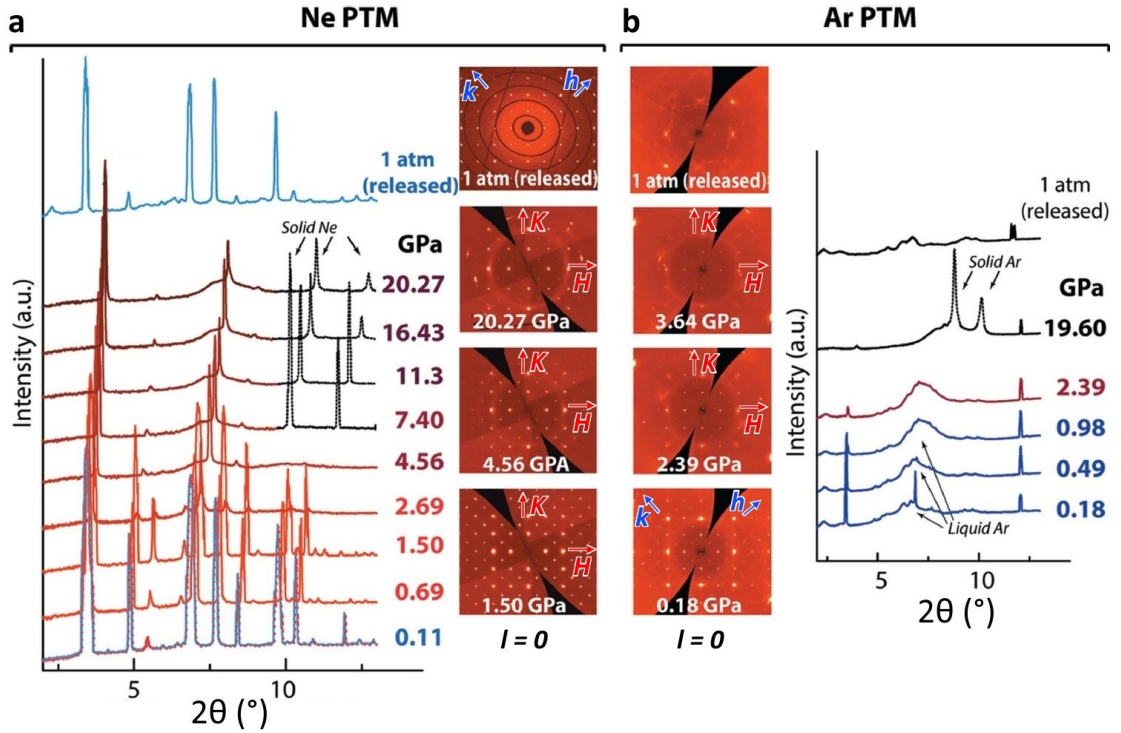


Figure 3.3 – The XRD patterns during the pressure-induced transformation of MAPbI<sub>3</sub> with (a) Ne and (b) Ar as PTM. Sections of the reciprocal space are shown for  $l=0$ . The axes  $h$  and  $k$ , which are specific for the tetragonal (pseudocubic) modification are emphasized in blue (red).

	pristine 1 atm	released 1 atm	0.69 GPa	20.27 GPa
$\Delta\rho$ without MA and Ne, eÅ <sup>-3</sup>	-0.20 - 1.41	-0.32 - 1.58	-1.44 - 1.97	-1.13 - 1.86
$\Delta\rho$ with MA and Ne, eÅ <sup>-3</sup>	-0.3 - 0.51	-0.27 - 0.23	-1.06 - 1.07	-0.54 - 0.56

Table 3.2 – The residual electron density calculated for two structure models at indicated pressures.

### 3.1 Single-crystal XRD experiments

The XRD data were collected at room temperature (293 K) under high pressure (up to 20.27 GPa). DACs were used with rhenium gaskets and Ne or Ar gases as the PTM. These noble gases have distinct atomic radii: 0.38 Å for Ne and 0.71 Å for Ar. Experimental details of the XRD measurements under pressure and release are illustrated in Figure 3.3.

From the XRD profiles it can be seen that under high pressure both Ar and Ne were incorporated into the structure. In the case of a Ne medium, the pressure-induced phase of Ne<sub>0.97</sub>MAPbI<sub>3</sub> remained stable and highly crystalline after decompression.

The general scheme of the structure determination of the Ne incorporation is illustrated in Figure 3.4. The starting (pristine) and the released (after exposure to 20.27 GPa) crystals are

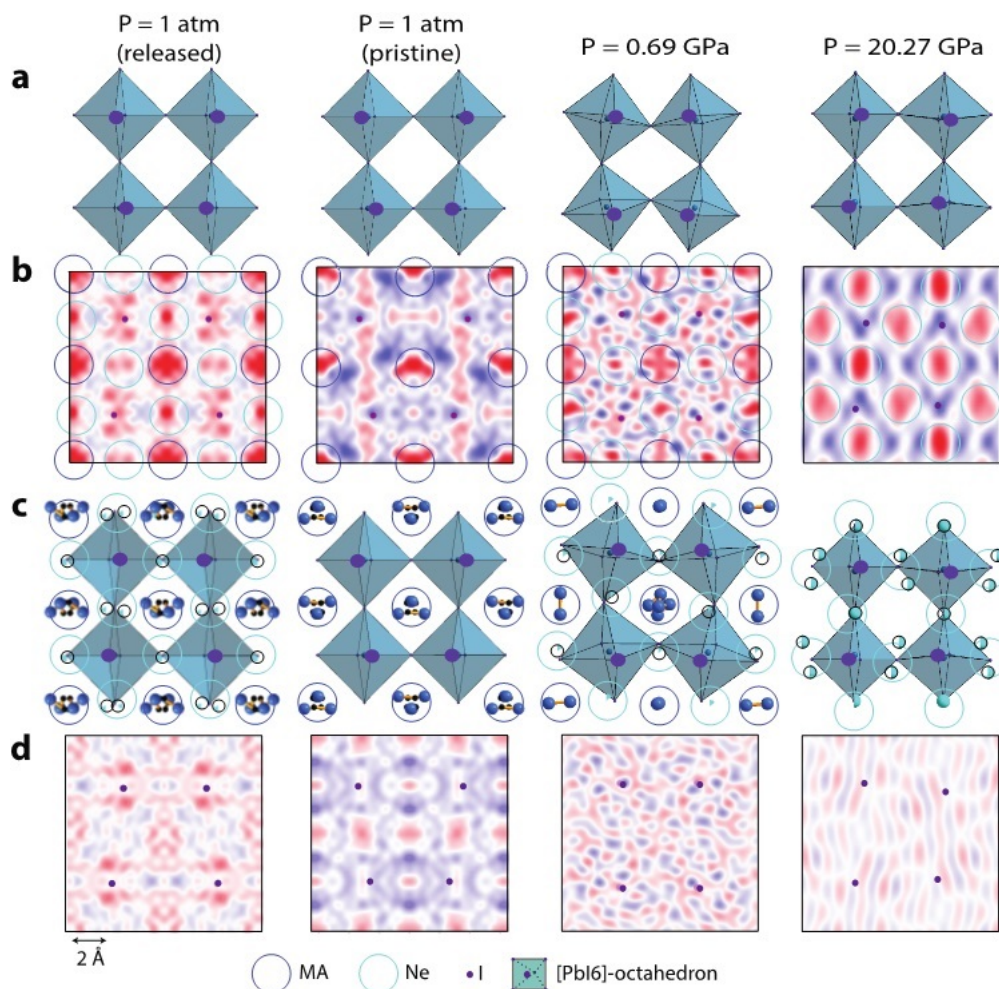


Figure 3.4 – Determination of the MA and Ne positions in the  $\text{MAPbI}_3$  crystal structure. Projections of the relevant fragments of the structure onto the  $(ac)$  plane are in (a) and (c). Purple dots indicate I atoms in the plane of the difference electron density ( $\Delta\rho$ ) maps in (b) and (d) with positive (red) and negative (blue) areas. (b) The residual electron density maps calculated using only Pb and I atoms. The maxima of  $\Delta\rho$  are identified with MA cations (dark-blue circles) and Ne atoms (cyan circles). (d) The residual electron density maps calculated using all atoms of the structure.

shown next to each other for comparison. After the refinement of the Pb and I atomic positions, Figure 3.4a, the difference electron density ( $\Delta\rho$ ) maps were calculated for each case, Figure 3.4b. As can be seen from Table 3.2,  $\Delta\rho$  varies from  $-0.32$  to  $1.58 \text{ e}\text{\AA}^{-3}$  for the released crystal at 1 atm pressure and from  $-0.20$  to  $1.41 \text{ e}\text{\AA}^{-3}$  at 1 atm for the pristine crystal. In the pristine crystal the maxima of  $\Delta\rho$  indicate the MA positions, it is represented by the dark-blue circles in Figure 3.4b. It is important to note, that these maxima are also perfectly identified at 0.69 GPa and for the released crystal, but they are absent at 20.27 GPa.

These strong and more localized maxima (shown as cyan circles in Figure 3.4b) are clearly visible

for each pressure, with the exception of the initial (pristine) case. By placing Ne atoms in these additional maxima the model is dramatically enhanced. The schematic diagrams of the crystal structure for each pressure value after including MA and Ne in the refined structure are shown in Figure 3.4c.

As can be seen in Figure 3.4d and Table 3.2, when all atoms are involved in the calculation maxima essentially decrease from 1.58 to 0.23  $\text{e}\text{\AA}^{-3}$  for the released crystal and from 1.41 to 0.51  $\text{e}\text{\AA}^{-3}$  for the pristine crystal at 1 atm. Within this model also  $\Delta\rho$  values at 0.69 GPa and 20.27 improved. At 20.27 GPa, the usual MA positions show nearly zero electron density and only the Ne-attributed maxima are observable. The residual electron density maps calculated included Ne atoms have values close to zero (Figure 3.4d), supporting the Ne-incorporation model.

A similar procedure for the structure determination was used for Ar PTM. The Ne and Ar inclusion in the structure has a varying effect on the symmetry and the bulk modulus at different pressures. The resulting structures made it possible to determine the interatomic distances, and consequently the nature and hierarchy of interactions between various components of each structure. The basic crystallographic information with Ne and Ar as the PTM at different pressures is provided in the Appendix (Tables A.4 and A.5) and is visualized in Figure 3.5.

It should be noted that, despite the reflections-to-parameters ratio (5.6 and 4.1 for the Ne-containing crystal at 16.43 and 20.27 GPa, respectively), the criteria  $R, wR = 0.051, 0.057$  for 16.43 GPa and 0.043, 0.064 for 20.27 GPa, and the residual electron density  $\rho_{max}, \rho_{min} = 0.58, -0.60 \text{ e}\text{\AA}^{-1}$  for 16.43 GPa and 0.56,  $-0.54 \text{ e}\text{\AA}^{-1}$  for 20.27 GPa shows that the corresponding structure solutions are valid. These structures obtained at the highest pressures are essential for understanding the Ne intercalation, which is also confirmed by the presence of Ne in the released crystal under ambient conditions.

#### 3.1.1 The high-pressure $\text{NeMAPbI}_3$ compounds

The crystal structure at room temperature was determined for 0.69, 1.5, 2.69, 4.56, 7.4, 16.43 and 20.27 GPa pressure values and for ambient pressure after decompression (Table A.4). In case of Ne PTM above 4 GPa an amorphous phase appears, coexisting with the crystalline one. This amorphous contribution slowly grows upon further increase of pressure and completely disappears after the pressure is released. The XRD data obtained at 0.11 GPa indicate the coexistence of two phases: a tetragonal phase, characteristic of ambient pressure, and a pseudo-cubic phase, which is typical for higher pressures. This is consistent with the first-order phase transition, which was reported for  $\text{MAPbI}_3$  between 0.3 GPa and 0.4 GPa [108, 111]. However, for the pseudo-cubic phase, the space group is  $R\bar{3}$ , which differs from the cubic  $Im\bar{3}$  and orthorhombic  $Imm2$  reported previously by [111] and [108], respectively.

Between 2.69 and 4.56 GPa the second phase transformation appears, which is in a good agreement with the literature value of 2.5 GPa [111] and 2.7 GPa [112]. In contrast to the reported space group  $Im\bar{3}$  [111], only its orthorhombic subgroup,  $Im2m$ , was found to describe the symmetry of the phase above 4.56 GPa.



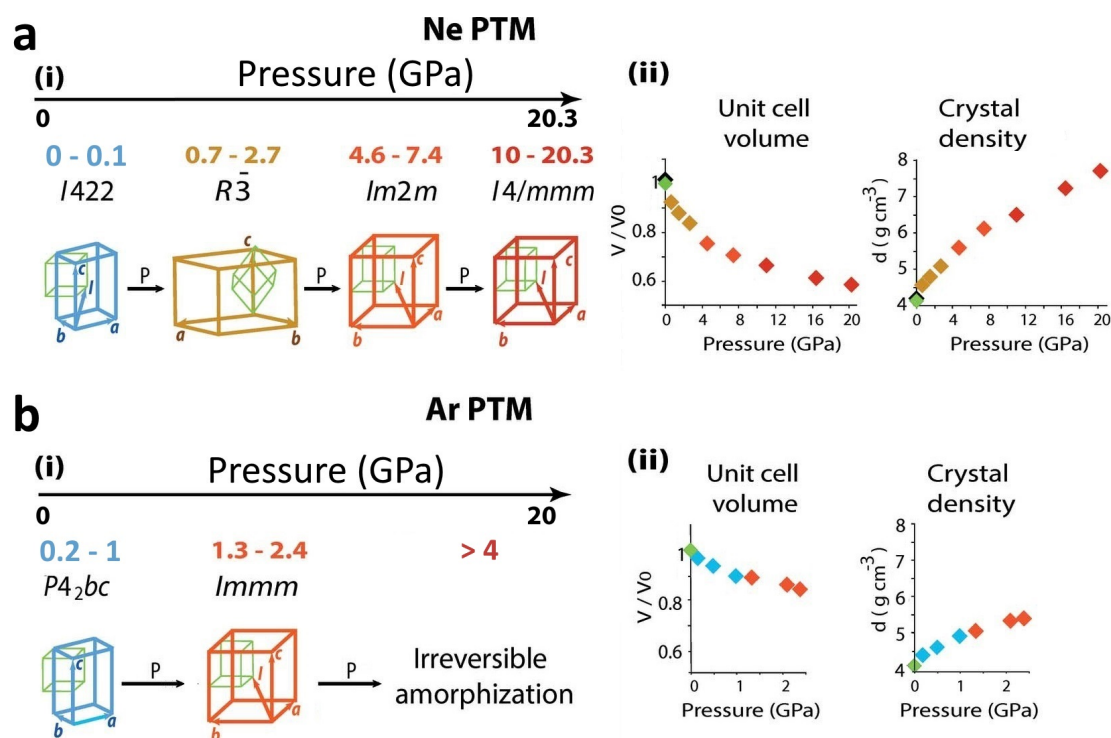


Figure 3.5 – Evolution of crystallographic characteristics of  $\text{MAPbI}_3$  under pressure with (a) Ne and (b) Ar PTM. (i) The symmetry transformation of the unit cell. Unit cells are shown in different colours for different crystallographic systems in relation to a primitive perovskite cube (green line). (ii) The pressure-dependence of the unit-cell volume and crystal density. The points in the diagrams are coloured according to the symmetries in panels (i). Green and black points correspond to the pristine and released crystals, respectively.

Furthermore, the third transformation is observed, from the orthorhombic to a tetragonal phase (space group  $I4/mmm$ ), between 7.4 GPa and 16.43 GPa. The unit cells and space groups corresponding to each phase are shown in Figure 3.5a(i).

This difference in the symmetry, the presence of a third phase transition and the lack of amorphization up to 20 GPa can be explained by the intercalation of Ne atoms at high pressure. Figure 3.6 illustrates the evolution of the  $\text{NeMAPbI}_3$  structure under compression. With an increase in the pressure Ne content in the compound composition grows, while MA is gradually disappearing from its position (i.e. period over a long range), Figure 3.6b.

The intercalated Ne atoms are located in the voids of the inorganic framework, more precisely at the faces of the primitive perovskite cube (surrounded by the four neighboring I atoms, Figure 3.6a), with a gradual increase in the occupancy of these sites upon compression (Figure 3.6d). The average occupancy of Ne sites starts at  $\approx 1/3$  in the low-pressure phases and goes up with pressure, eventually approaching 1 when Ne atoms sit at each face. At 20.27 GPa, Ne sites are fully occupied at four faces and the remaining two are half occupied. Therefore, one can expect that higher pressure is required in order to achieve the full occupancy of all faces. The corresponding



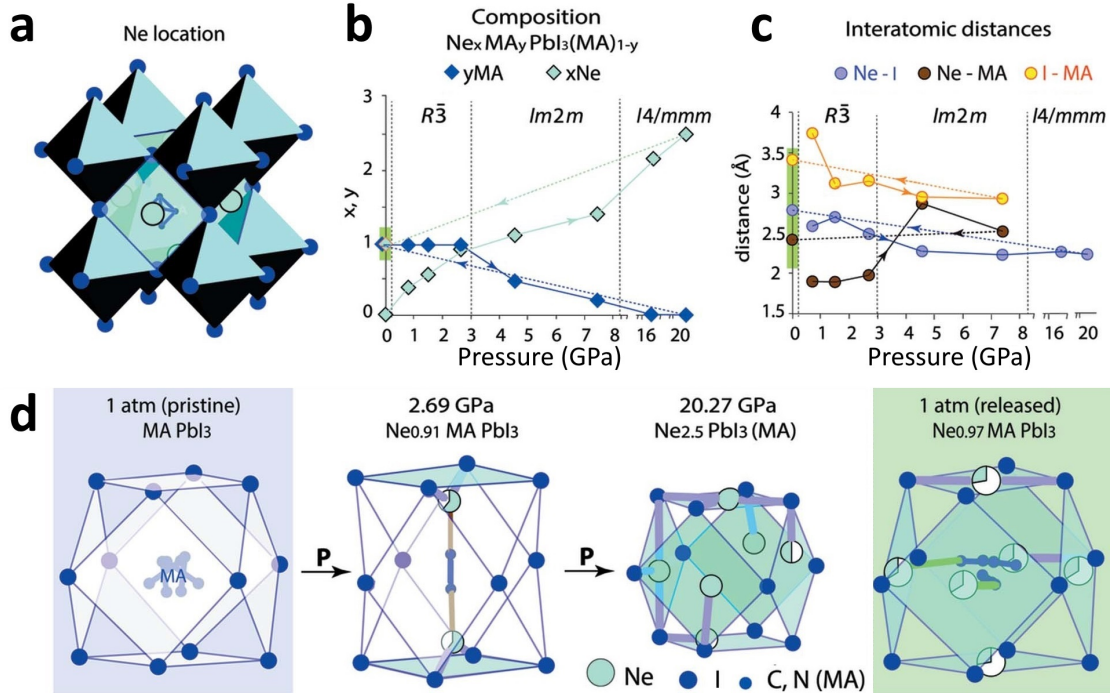


Figure 3.6 – NeMAPbI<sub>3</sub> structure evolution under compression and after the release. (a) The arrangement of Ne atoms at the faces (cyan squares) of the primitive perovskite cubic unit cell. Depending on pressure, some of the Ne sites can be empty or partially occupied. (b) Pressure-induced change of the crystal composition. In the chemical formula, y and (1 - y) refer to MA at the long-range-ordered and the non-localized (non-periodic) positions, respectively. (c) The shortest interatomic distances for Ne-I, Ne-MA and I-MA under different pressures. (d) Main trend of the pressure-induced structure evolution, a gradual increase in the number and occupancy of Ne sites, indicated in (a).

composition, Ne<sub>3</sub>PbI<sub>3</sub>(MA), reflects the maximum possible Ne content in the structure.

A reversible transformation, which restores all the long-range ordered positions of MA in the released crystal at ambient pressure (Figure 3.4), indicates that this cation can be in two different states in the high-pressure crystal: the long-range ordered state (i.e. periodic) and the randomly distributed one (i.e. non-periodic). In order to emphasize these two states of MA, the Ne<sub>x</sub>MA<sub>y</sub>PbI<sub>3</sub>(MA)<sub>1-y</sub> designation for the chemical formula, where indices y and (1 - y) denote the relative quantities of the long-range-ordered and randomly distributed MA, respectively. The presence of two states for the MA cation is a direct confirmation that the long-range ordering of MA is violated under high pressure, which was proposed before [109, 108, 111].

According to this assumption, a lack of long-range ordering of MA leads to the destruction of the inorganic framework, which is kept by the I-MA periodic interactions. Indeed, a decrease in the amount for long-range-ordered MA leads to a huge increase in ADP for I atoms (Figure 3.7), which is a sign of the inorganic framework destruction. Destruction of the inorganic framework leads to compound amorphization. However, in the Ne PTM the crystal structure is still periodic up to 20 GPa. The reasons of this can be understood from the analysis of the Ne-I, Ne-MA

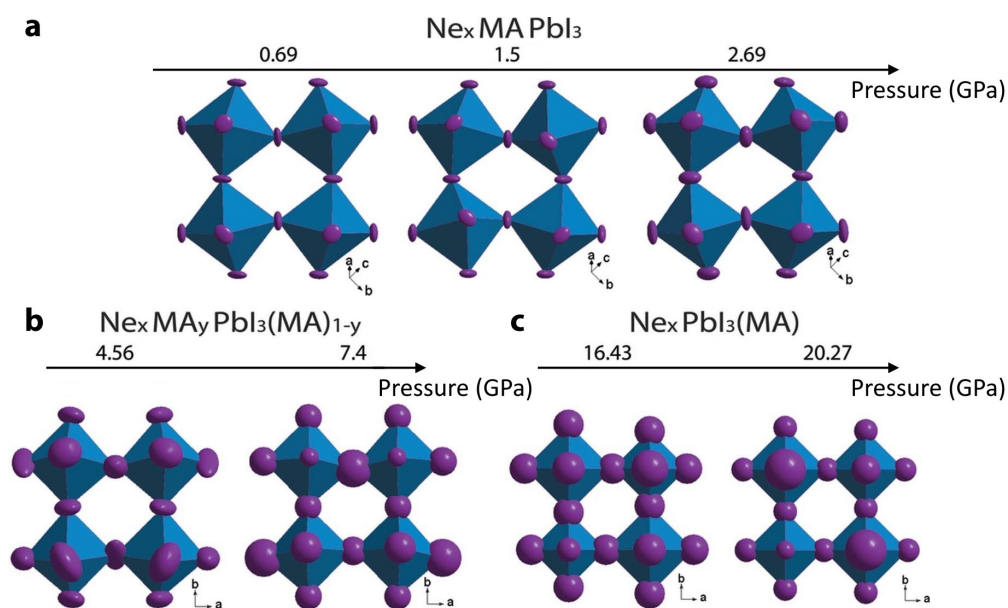


Figure 3.7 – Pressure-dependent ADP of I atoms of the inorganic framework. (a) The fragment under three pressure values with the long-range-ordered MA cation. (b) The fragment under two pressure values with the partially long-range ordered MA cation. (c) The fragment corresponding to the absence of the long-range-ordered MA cation. The ADP ellipsoids are shown with 50% probability for each pressure.

and I–MA interatomic distances found for the long-range-ordered MA cation (Figure 3.6c). The short distances MA–Ne of  $\approx 1.9$  Å indicating the corresponding interaction at pressure below 3 GPa can be recognized as unstable with respect to pressure, since the content of the long-range-ordered MA rapidly reduces from 0.5 (at 4.56 GPa) to 0.25 (at 7.4 GPa) per chemical formula, and the long-range-ordered MA is no longer observed for pressure above 16.3 GPa. As the expected rapid amorphization does not appear, it means the (Pb,I)-framework is stabilized by Ne atoms. Indeed, for pressures above 4 GPa, the loss of the long-range order for more than 50% of MA switches the shortest interatomic distance (i.e. the strongest interaction of Ne) from Ne–MA to Ne–I, as shown in Figure 3.6c.

Consequently, the Ne–I interactions can be considered as the cause of the framework stabilization, preventing the amorphization.

The stabilizing role of Ne under high pressure is also confirmed by the distortions observed in the (Pb,I)-framework. The minimal distortions (the I–Pb–I angle  $88.4$ – $90.3^\circ$  instead of the ideal  $90^\circ$  and the Pb–I–Pb angle  $178$ – $180^\circ$  instead of the ideal  $180^\circ$ ) were found in tetragonal structures at the highest pressure, when the long-range MA order is lost and the content of Ne is maximal. Thus, the progressive intercalation of Ne is the general trend in the pressure evolution of the  $\text{NeMAPbI}_3$ . The phenomenon is driven by the Ne–I interaction, which is substantially enhanced above 4 GPa.

Surprisingly, the occupation of Ne sites in all directions is preserved in the released structure

under ambient pressure, but with a much smaller probability of  $\approx 1/3$  (Figure 3.6d). The mean Ne–MA and Ne–I distances in the released structure are very similar, 2.83 Å and 2.78 Å, respectively (Figure 3.6c). The minimum Ne–MA distance ( $\approx 2.3$  Å) in the released crystal can be responsible for this stabilization. However, this is the distance between partially occupied Ne and MA sites, thus it is difficult to know for sure whether such separation is indeed realized. In the 0–20 GPa pressure range the bulk modulus  $B_0$ , calculated using the Birch–Murnaghan model [113], varies from 5.3 GPa at the lowest to 10.6 GPa at the highest pressure. These numbers fall within the spread of values in the literature [108, 107].

#### 3.1.2 The high-pressure ArMAPbI<sub>3</sub> compounds

The structure was determined at pressures of 0.18, 0.49, 0.98, 1.34, 2.1, and 2.39 GPa at room temperature (details in Table A.5). Above 1.34 GPa an amorphous phase appears, coexisting with the crystalline one. The amorphous contribution grows rapidly with increasing pressure until no crystalline phase can be observed above 3.6 GPa. This amorphization is irreversible in the experiments.

The tetragonal unit-cell parameters for the ambient conditions are identified in the ArMAPbI<sub>3</sub> structure up to 1 GPa (Table A.5 and Figure 3.5b(i)). The space group  $P4_2bc$  is the best fit in the 0.18–0.98 GPa pressure range. Only one transformation of this unit cell is detected for ArMAPbI<sub>3</sub>, occurring between 1 GPa and 1.3 GPa. The pseudo-cubic orthorhombic unit cell (Figure 3.5b(ii)) and the  $Immm$  space group are characteristic for the lattice for pressure above 1 GPa (Table A.5). No distortion in the long-range order is detected for the MA cation. In comparison to NeMAPbI<sub>3</sub>, an Ar-content increase as a function of pressure is 5.5 times larger, reaching the composition Ar<sub>1.4</sub>MAPbI<sub>3</sub> at 1.34 GPa. In the case of Ne PTM, the nearly equivalent composition, Ne<sub>1.41</sub>MA<sub>0.25</sub>PbI<sub>3</sub>(MA)<sub>0.75</sub>, occurs at 7.4 GPa (Tables A.4 and A.5). This result indicates stronger interaction between MAPbI<sub>3</sub> and Ar than with Ne.

The pressure-induced structural evolution of ArMAPbI<sub>3</sub> (Figure 3.8) is associated with a gradual growth in the Ar content. As can be seen in Figure 3.8c, this process is accompanied by the contraction of the Ar–I and Ar–MA distances. For pressure below 1 GPa, the MA cations, Ar and I atoms are arranged into chains, which polymerize in two dimensions upon further compression, Figure 3.9. Influence of the lattice contraction on the chain geometry is illustrated in Figure 3.10.

The shortest interatomic distances of  $\approx 2$  Å found for Ar–I and Ar–N (MA) at pressures above 2 GPa. The value for the Ar–N separation of 1.84 Å was theoretically predicted for ambient pressure [114]. Such values can be considered as a reasonable approximation if ADP are taken into account. Large and prolate ADP ellipsoids of the I atoms imply an anharmonic character. Therefore, the actual Ar–I distances are longer than the centers of the ellipsoids. Nevertheless, the dramatic reduction of the minimum Ar–MA and Ar–I distances at pressures above 2 GPa (circled in red, Figure 3.8c) is considered as a trigger for the complete and irreversible structure amorphization. In fact, a crystalline state at the time of its destruction was recorded.

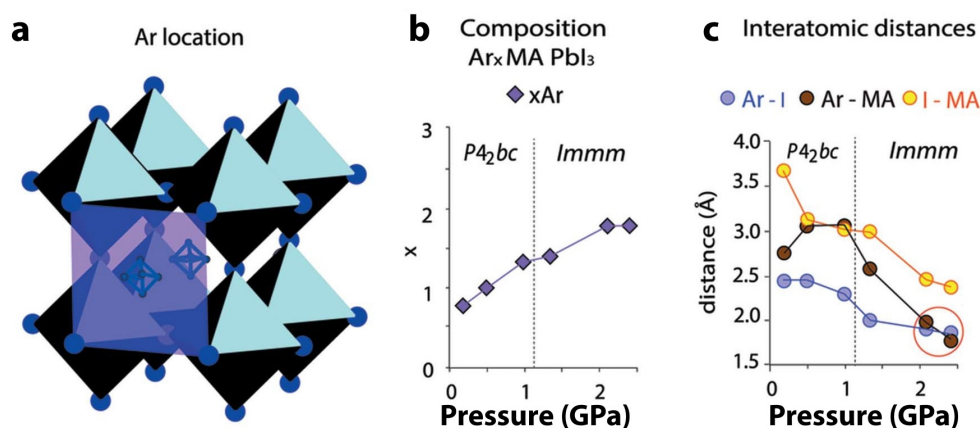


Figure 3.8 – Pressure-induced transformation of the tetragonal  $\text{ArMAPbI}_3$  phase. (a) Ar location in the (Pb,I)-framework. (b, c) Deformation of the group configuration and its connection to I atoms. Violet-coloured segments indicate the occupancies of the Ar sites.

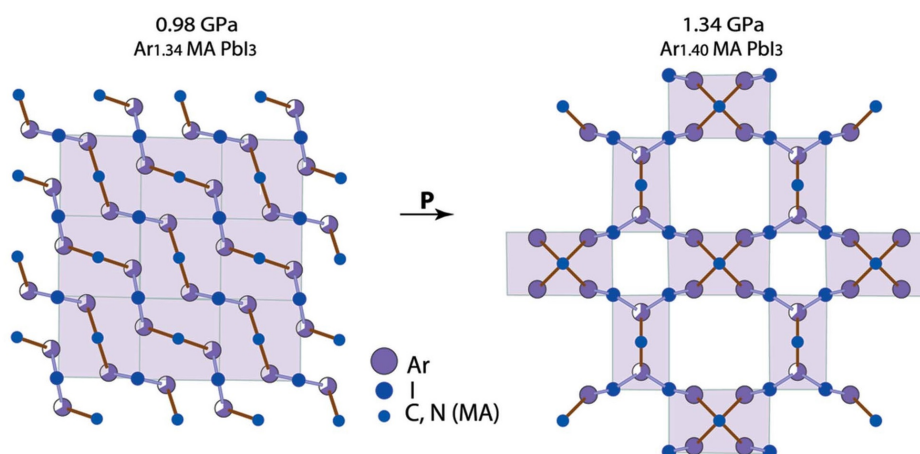


Figure 3.9 – Pressure-induced transformation of  $\text{Ar}_x\text{MAPbI}_3$  from tetragonal to orthorhombic phase.

Thus, the pressure-induced formation of the stable I–Ar–MA–Ar– chains and their polymerization (Figure 3.9) is at the origin of the structural evolution and amorphization of  $\text{ArMAPbI}_3$ .

### 3.2 Impact of Ne and Ar pressure transmitting medium

The present results show that both Ne and Ar interact with  $\text{MAPbI}_3$ , but in different ways.

Interactions between Ne and I atoms stabilize the inorganic framework up to 20 GPa and suppress amorphization of the crystal, despite the vanishing of the long-range ordering of MA. Therefore, Ne serves as a structural stabilizer instead of MA for pressures higher than 4 GPa.

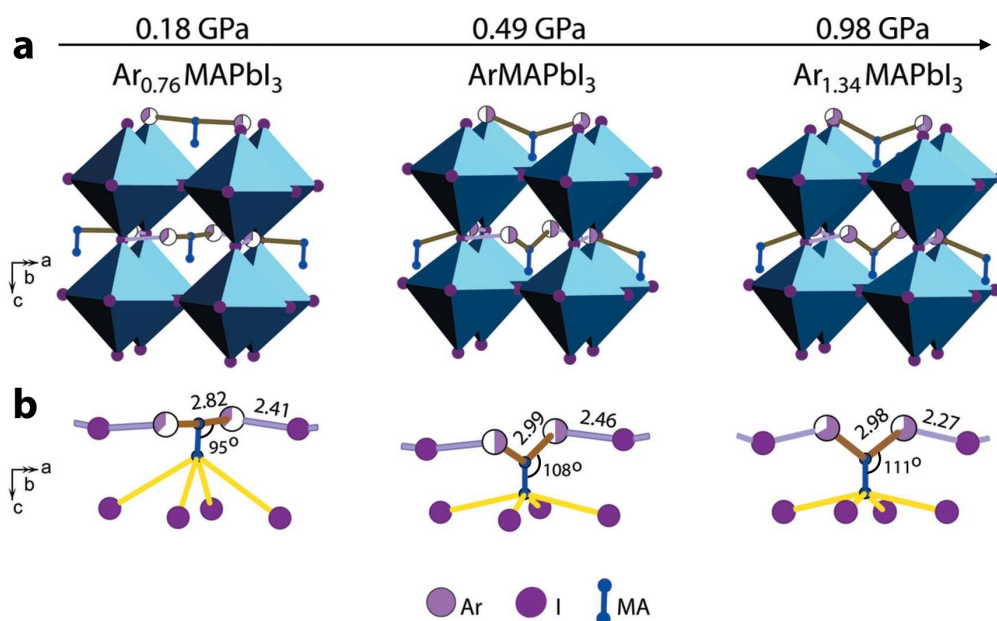


Figure 3.10 – Pressure-induced transformation of the tetragonal  $\text{ArMAPbI}_3$  phase. (a) Position of the  $\text{I-Ar-MA-Ar-}$  group within the  $(\text{Pb,I})$ -framework. (b) Deformation of the group configuration and its connection to I atoms. The MA–Ar and Ar–I interatomic distances are given in Å.

Unlike Ne PTM, Ar interacts with both I and MA even under low pressure of 0.18 GPa. These interactions accelerate the irreversible amorphization, which starts at 2 GPa.

The difference between the influences of Ne and Ar PTM is clearly related to the difference in their chemical activities, which are defined by their electronic configurations, i.e. their atomic radii being 0.38 Å for Ne and 0.71 Å for Ar.

### 3.2.1 Influence of Ne and Ar on the MA cation mobility

The role of the mobility of the MA cation in the structural transformation of  $\text{MAPbI}_3$  is often discussed [115, 109, 108, 111]. And the high-pressure amorphization is also directly linked to this phenomenon.

According to previous reports [109, 108, 111], the strong pressure-induced interaction between the MA cations and I atoms is considered as a template for the  $(\text{Pb,I})$ -framework stability. Following this interpretation, the results support the following scenarios of the influence of Ne and Ar on the MA cation behaviour.

In both cases, Ne–MA and Ar–MA interactions minimize the MA mobility by fixing the position of the MA dumbbell (the long-range-ordered form of MA). In particular, this explains the absence of cubic symmetry for the high-pressure phases.

In the case of Ne–PTM, up to  $\approx 3$  GPa, MA interacts with both Ne and I, which stabilizes its long-range ordering. For pressure above 3 GPa, intensifying interaction between MA and I

neighboring I atoms forces the organic cation to lose its long-range periodicity, first partially (for  $3 \text{ GPa} < P < 8 \text{ GPa}$ ) and then completely (for  $P > 8 \text{ GPa}$ ). However, the Ne–I interaction becomes sufficiently strong to stabilize the (Pb,I)-framework. This prevents amorphization and maintains the crystalline state up to 20.27 GPa. Such pressure-induced Ne–I interactions remain even after decompression of the crystal.

In the case of Ar PTM, MA cations interact with Ar to form –I–Ar–MA–Ar– chains as Ar enters the crystal. Formation of the chains prevents strong interaction between MA and I and, consequently, stabilizes the long-range periodicity of MA. At 1.34 GPa, a part of the cations still exist outside of the chains, they stimulate additional absorption of Ar by the crystal. All MA cations are involved in the polymerized chains at 2.39 GPa, but some of the Ar–MA and Ar–I distances are too short. On the one hand, it points to strong MA–Ar interactions, which benefit from the competition with the MA–I. On the other hand, the I–Ar–MA–Ar– chains get dense in the restricted space between the  $\text{PbI}_6$  octahedra and destroy the structure.

This scenario can explain both the small observed contribution of the crystalline phase at 2.39 GPa and the rapid irreversible amorphization upon further pressure increase.

### 3.3 Conclusions

Using single-crystal synchrotron diffraction data, the crystal structure of  $\text{MAPbI}_3$  was studied under high pressure with Ne and Ar gases as pressure transmitting media.

The following main conclusions have been drawn from the study:

- In the case of  $\text{MAPbI}_3$  compression up to 20.3 GPa, the noble gas atoms of the pressure transmitting media are not inert, but rather they form  $\text{NeMAPbI}_3$  and  $\text{ArMAPbI}_3$  high-pressure-induced compounds.
- Ne mainly interacts with I atoms, preventing amorphization and stabilizing the high-pressure crystalline state up to 20.27 GPa, despite the migration of MA cations to non-periodic positions. This means a loss of the long-range ordering of MA within the crystal lattice. Such high-pressure transformation is reversible and the  $\text{Ne}_{0.97}\text{MAPbI}_3$  compound is stable at ambient conditions after decompression.
- Ar interacts with both MA and I, thus forming chains and driving their pressure-induced polymerization up to  $P = 2.39 \text{ GPa}$ . Compression of the (Pb, I)-framework destroys the polymerized structure and the framework itself, initiating the irreversible and rapid amorphization of the compound.
- The difference between the pressure-induced impacts of Ne and Ar is related to the difference in their atomic radii and, consequently, their propensity towards interatomic interactions in the restricted space between the  $\text{PbI}_6$  octahedra.

## 4 Influence of the cation disorder on the crystal properties

The bandgap, optical and magnetic properties of MAPbI<sub>3</sub>, are mainly determined by the inorganic framework [116], as was already discussed in Section 1.2. The organic cation orientation on the other hand, influences the long carrier lifetime in MAPbI<sub>3</sub>, the formation of large polarons, Rashba effect, ferroelectric domains [117]. For instance, it was shown that the screening of band-edge charge carriers by organic cation rotation can have a major contribution to the prolonged carrier lifetime [117]. As the recombination of the photoexcited electrons and holes is suppressed by the screening, leading to the formation of polarons and thereby extending the lifetime.

Another interesting study regarding the cation influence is the comparison of MAPbI<sub>3</sub> and FAPbI<sub>3</sub>. The most important difference between these compounds is in the electrical moments of the organic cations. The MA<sup>+</sup> cation has a strong electric dipole moment (0.48 eÅ) and a weaker quadrupole moment (-0.37, -0.37, 0.75) eÅ<sup>2</sup>, while the FA<sup>+</sup> cation has a strong quadrupole moment (-3.8, 2.58, 1.21) eÅ<sup>2</sup> and a weak dipole moment (0.05 eÅ) [117]. This results in different interaction with the inorganic framework and phase transitions. As described in Chapter 2, upon cooling, MAPbI<sub>3</sub> undergoes cubic-tetragonal-orthorhombic transitions. While the FAPbI<sub>3</sub> phase transitions are different and depend on the cooling process [117]. If FAPbI<sub>3</sub> is cooled from RT, the structure becomes hexagonal, and if it is cooled from the high-temperature cubic phase the hexagonal structures are entirely avoided.

Because of their different electrical moments, MAPbI<sub>3</sub> and FAPbI<sub>3</sub> have different molecular rotational entropy. As MA has preferential orientations and FA has non-preferential orientations, the FA cation has a much higher rotational entropy [117]. The band-edge carrier lifetimes in both FAPbI<sub>3</sub> and MAPbI<sub>3</sub> increase when the systems enter from a structural phase with lower rotational entropy to another phase with higher entropy. For instance, the lifetime in FAPbI<sub>3</sub> dramatically changes from 30 to 300 ns as, upon heating, the system enters into its cubic phase with high rotational entropy. The photoexcited charge carriers are screened by cations, resulting in formation of large polarons that prolongs the charge carrier lifetime.

The choice of the cation defines the interactions between the inorganic and organic constituents, determining the dimensionality of the structure [118, 119].

In the interaction between inorganic framework and organic cation the weak hydrogen bond play the most important role. It appears that the cation rotation in 3D perovskites changes the bandgap from direct to indirect affecting the lifetime of charge carriers (i.e. diffusion and absorption lengths) [115]. Duan et al. reported that the orientation disorder of the organic



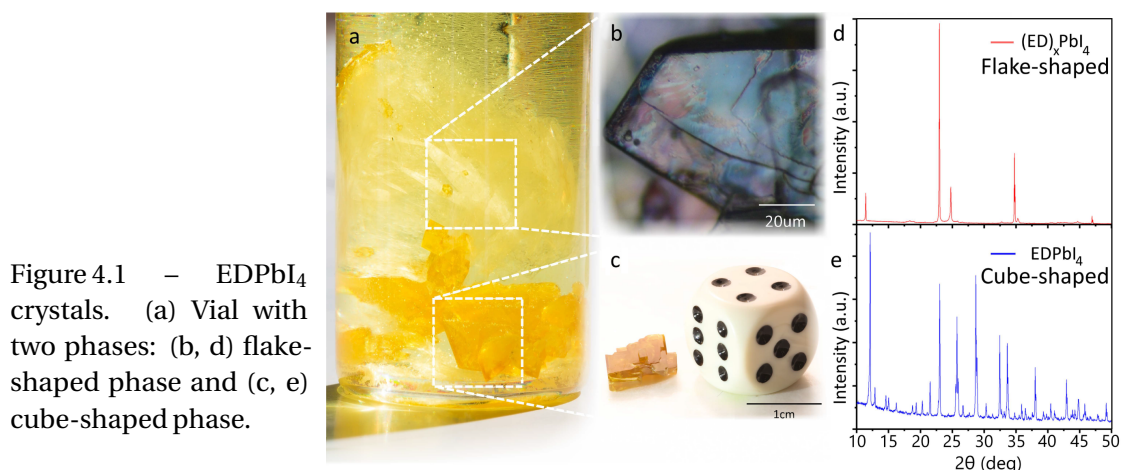


Figure 4.1 – EDPbI<sub>4</sub> crystals. (a) Vial with two phases: (b, d) flake-shaped phase and (c, e) cube-shaped phase.

cation strongly influences the dielectric and emission features [120].

Such cation disorder characteristic is directly related to the ADP, which can be found from a precise crystal structure determination. Therefore, the combination of the PV characteristic measurements with a precise crystal structure determination of two compounds differing by only the state of the organic cation is a challenging study, which is presented in this Chapter.

Ethylenediammonium lead iodide (NH<sub>3</sub>CH<sub>2</sub>CH<sub>2</sub>NH<sub>3</sub>)PbI<sub>4</sub> (EDPbI<sub>4</sub>) has been obtained in its pristine and thermally treated (1 hour at 423 K followed by cooling) state. The thermal treatment results in stabilization of additional N–H •• I hydrogen bonds. These bonds facilitate both the splitting of the ethylenediammonium (ED) cation and increased mobility of the carbon atoms. In turn, the current density–voltage characteristics (J–V curves) of the both pristine and thermally treated crystals mean that the increase of the ED leads to an improvement of the photoconductivity in the thermally treated crystal.

## 4.1 Crystallization of ethylenediammonium lead iodide

Ethylenediammonium lead tetraiodide, EDPbI<sub>4</sub>, crystals were synthesized by solution growth method, 3.3 mmol lead (II) acetate trihydrate (PbI<sub>2</sub>·x·3H<sub>2</sub>O, >99.9%) was reacted with a 6 ml saturated HI solution (57 wt% HI in H<sub>2</sub>O). The solution of PbI<sub>2</sub> at 278 K reacts with the respective amount of the ethylenediamine solution (3.30 mmol). Small, submillimetre-sized crystals are immediately precipitated and recrystallized to larger millimetre and centimetre sized crystals at 323 K for 7 days. After harvesting, the crystals are wiped with laboratory wipes and dried at room temperature. As can be seen in Figure 4.1a there are two distinct types of crystals in the vial. At the colder part of the vial flake-shaped, translucent colour crystals are grown (Figure 4.1b), while at the warmer part of the solution large bright yellow cube-shaped crystals are grown (Figure 4.1c). PXRD patterns confirm their difference (Figure 4.1d, e and full profile in the Appendix, Figure A.14).

In this Chapter, the detailed analysis of the cube-shaped crystals with different post-heat treat-



## 4.1. Crystallization of ethylenediammonium lead iodide

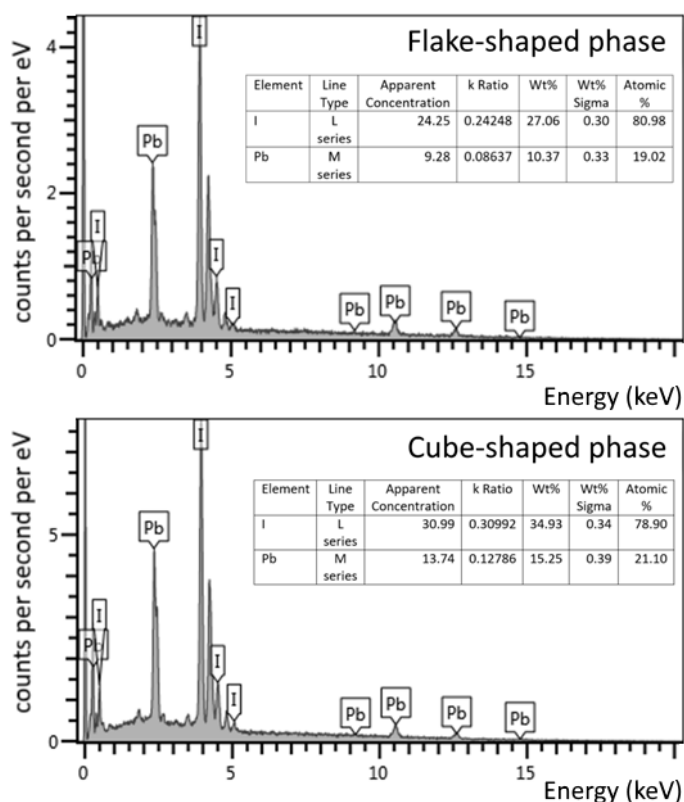


Figure 4.2 – EDX spectra of the flake- and cube-shaped phases of EDPbI<sub>4</sub> crystal. The atomic ratio for both phases is the same.

ment is presented. All EDPbI<sub>4</sub> crystals were annealed at 323 K for one hour in air, these ones will be noted as the **pristine**, and a part of the crystals, which were further heated at 423 K for one more hour in air, are **thermally treated** crystals.

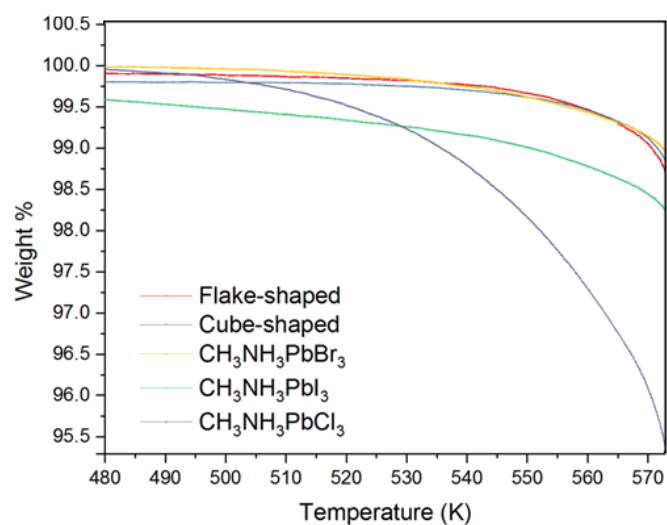
### 4.1.1 Chemical composition

One of the techniques for the chemical characterization of the crystal is energy dispersive X-ray (EDX) spectroscopy. By the stimulated emission of characteristic X-rays (from the excited to the ground state) of a specimen the amount of the elements in the crystal can be restored. In the EDX spectra in Figure 4.2, the ratio Pb : I = 1 : 4 confirms of PbI<sub>4</sub> for both phases. Further confirmation of the ED cation presence has been done by the single-crystal structure determination.

### 4.1.2 Thermogravimetry

To get more information on the physical and chemical characteristics, thermogravimetric analysis (TGA) is done (details on the equipment are in the Appendix B.5). By monitoring the mass of the sample over the time as the temperature changes phase transitions, absorption or thermal decomposition can be observed. For this TGA analyses, EDPbI<sub>4</sub> was investigated in the temperature range from 313 to 573 K. The TGA curves of both shapes of EDPbI<sub>4</sub> are shown in Figure 4.3.

Figure 4.3 – TGA of the flake- and cube-shaped phases in comparison with TGA of well-studied MAPbI<sub>3</sub>, MAPbBr<sub>3</sub>, MAPbCl<sub>3</sub> crystals.



It has been reasoned that the thermal stability of 3D organic–inorganic lead halide perovskites is similar to the perovskites containing shorter chain amines, e.g. MA or FA cation [121]. As can be concluded, regardless of the shape, EDPbI<sub>4</sub> crystal behaves the same to MAPbBr<sub>3</sub> compound in TGA measurements. These hybrid perovskites start to lose the organic components (EDI<sub>2</sub>, MAI, MABr, MACl) under 573 K and continues on at the isothermal 573 K.

## 4.2 Single crystal XRD

The main details on the experimental data and crystallographic characteristics of pristine and thermally treated EDPbI<sub>4</sub> crystals are given in Table 4.1. The further experimental details are available as a CIF file by CSD-numbers 434179 and 434178 in the database.

### 4.2.1 Structure solution and refinement

The arrangement of the PbI<sub>6</sub>-octahedra is found in the space group  $R\bar{3}c$  and is identical for the pristine and thermally treated crystals. Superposition of the pristine and thermally treated crystal structures is shown in two projections in Figure 4.4.

Within the  $R\bar{3}c$  space group, 57 and 63 independent reflections with  $I > 3\sigma(I)$  violate the  $c$ -glide plane for the pristine and thermally treated crystals, respectively. Correspondingly, the space groups  $R32$ ,  $R\bar{3}$  and  $R3$  have been tested. The best results of the structure determination and refinement have been obtained in  $R\bar{3}$  for both types of crystals. Further lowering of the symmetry to  $R3$  decreases the reliability index from 3.14 and 3.98 down to 2.9 and 3.7%, respectively, for the pristine and thermally treated crystal. However, this decrease is associated with the essential increase of a number of refined parameters and does not influence the main observations, which concern the atomic displacements in the ED cation.

Hence, the  $R\bar{3}$  space group is used for both the pristine and thermally treated crystals. Positions

	Pristine crystal	Thermally treated crystal
Chemical formula	$\text{I}_4\text{Pb} \cdot \text{C}_2\text{H}_{10}\text{N}_2\text{O}_{0.042(4)}$	$\text{I}_4\text{Pb} \cdot \text{C}_2\text{H}_{10}\text{N}_2\text{O}_{0.042(5)}$
Formula weight	777.60	777.60
Space group	Trigonal, $R\bar{3}$	Trigonal, $R\bar{3}$
Temperature (K)	293	293
$a, c$ (Å)	14.5906(1), 32.7775(5)	14.5645(1), 32.7195(4)
$V$ (Å <sup>3</sup> )	6043.00(14)	6010.75(13)
$Z$	18	18
Wavelength (Å)	0.7129	0.7129
Crystal size	$0.03 \times 0.02 \times 0.003$	$0.03 \times 0.02 \times 0.003$
$R_{int}$	4.2	3.8
No. of measured, independent and observed reflections	21 957 3078 2372	12 312 2998 2450
$(\sin \theta / \lambda) \text{min} (\text{Å}^{-1})$	0.676	0.677
$R[F^2 > 2\sigma(F^2)], wR, S$	0.032, 0.038, 1.49	0.040, 0.049, 1.89

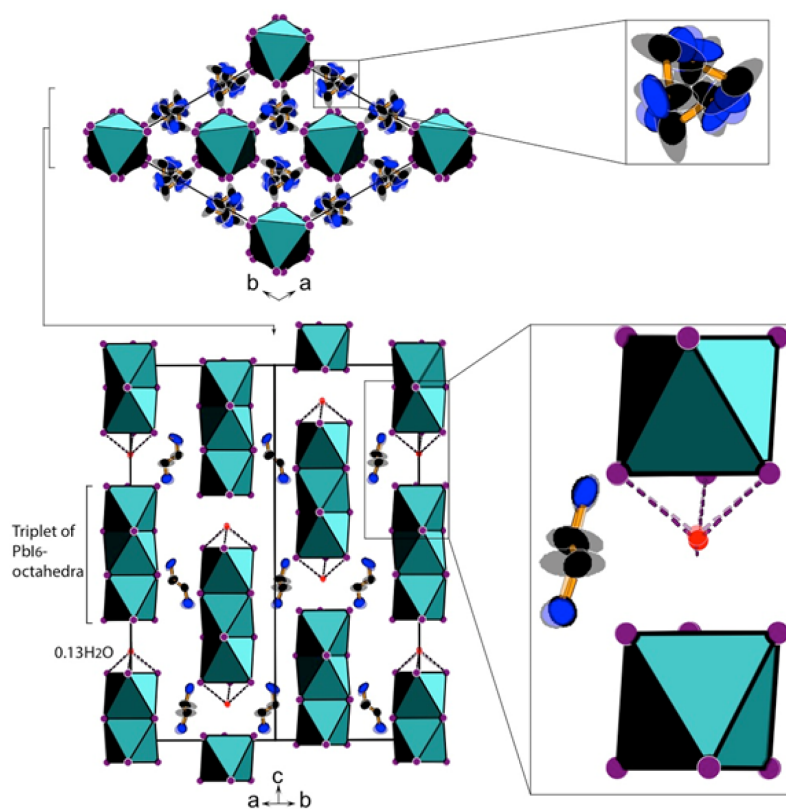
Table 4.1 – Crystallographic data of EDPbI<sub>4</sub> crystal.

Figure 4.4 – Crystal structure of EDPbI<sub>4</sub>. The thermally treated crystal is drawn with the 50% opacity. Topology of the crystal structures is identical. The difference mainly concerns atomic displacement parameters of N and C in the organic cation, here, is shown for the dynamic model of the C and N atoms disorder.

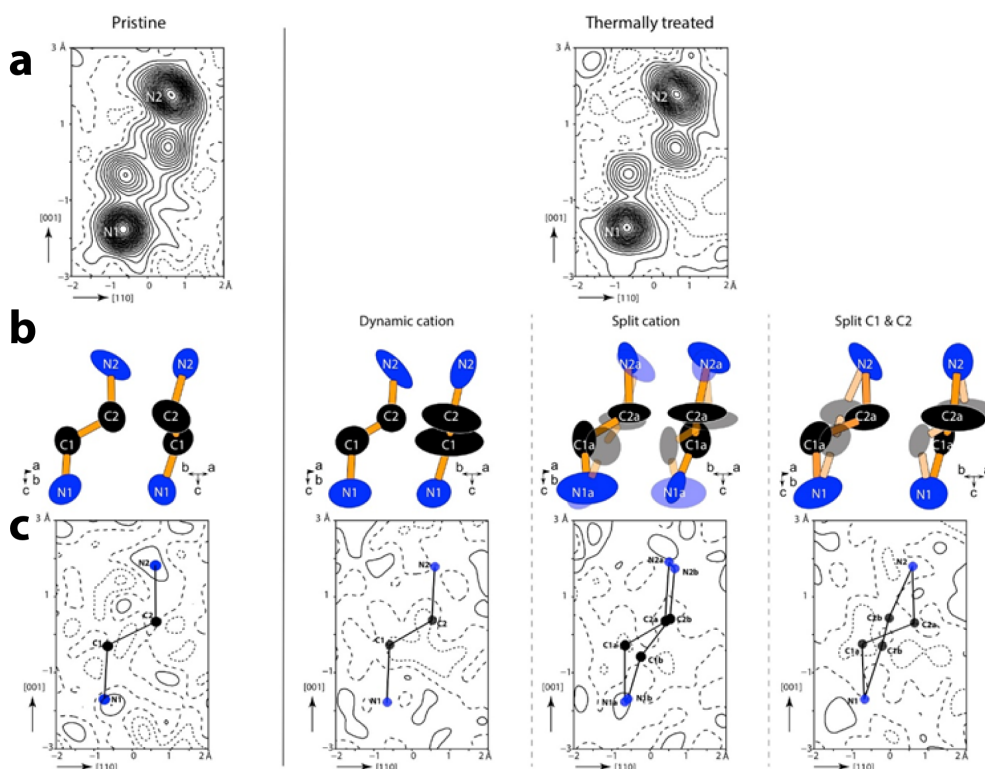


Figure 4.5 – ED organic cation localization with the difference electron density mapping in the pristine and thermally treated crystals. (a) The starting positions of the N and C atoms are determined from the maps calculated after the refinement of Pb and I atoms. (b) Two projections of the cation obtained after refinement of Pb, I, N and C atoms. ADP ellipsoids for the split cations are shown with 100% and 50% opacity. (c) The maps obtained after refinement of Pb, I, N and C atoms. The residual electron density is indifferently low in all three models of the cation disordering in the thermally treated crystal. In (a) and (c), the solid dashed and striped lines correspond to positive, negative and zero contours, respectively, drawn with a step of  $0.2 \text{ e } \text{\AA}^{-1}$ .

of N and C atoms are found from the difference electron density calculated after localization of Pb and I atoms (Figure 4.5a). For every atom there are three coordinates ( $x, y, z$ ) and one (isotropic) or six (anisotropic) displacement parameters. It is reasonable to assume that atoms move anisotropically, i.e. with different amplitudes in different directions. Therefore, instead of describing an atom as a sphere, it is described as an ellipsoid. The elements of the matrix describing the ellipsoid are called ADP. The size of the ellipsoids is chosen so that the ellipsoid includes 50% electron density of the atom type in the model.

Three models of the cation disorder in the thermally treated crystal are considered:

### Dynamic model

In this model, the positions of N and C atoms are fixed and ADP parameters are refined. Within this model, it is assumed that the atoms have a large oscillation amplitude. Refinement of Pb,

		Thermally treated		
	Pristine	Dynamic model	Split model	Split C1 & C2 model
N1-C1 dist.(Å)	1.432(15)	1.51(2)	1.41(4)	1.48(3) & 1.49(3)
C1-C2 dist.(Å)	1.449(13)	1.29(2)	1.43(5)	1.40(7) & 1.50(5)
C2-N2 dist.(Å)	1.508(16)	1.43(2)	1.52(4)	1.60(7) & 1.39(7)
$\Delta$ C1 dist.(Å)	—	—	0.90(9)	0.86(3)
$\Delta$ C2 dist.(Å)	—	—	0.51(9)	0.77(3)
$\Delta$ N1 dist.(Å)	—	—	0.25(7)	—
$\Delta$ N2 dist.(Å)	—	—	0.34(9)	—
N1-C1-C2 (°)	114.4(10)	120.5(18)	110(3)	113(3) & 108(3)
C1-C2-N2 (°)	111.3(9)	119.3(17)	116(3)	108(4) & 117(3)
Deviation of C2 from the N1C1N2 cation plane (Å)	0.13(3)	0.03(5)	0.15(9)	(i) N1C1aN2: C2a – 0.15(5), (ii) C2b – 0.45(4); (ii) N1C1bN2: (ii) C2a – 0.52(2), C2b – 0.18(3)

Table 4.2 – Geometry characteristics of the ED cation.

I, N and C atoms reveals unusually elongated ADP ellipsoids for N and C in the structure of the thermally treated crystal (Figure 4.4 and dynamic model in Figure 4.5b).

#### Split cation model

The split cation model is describing the static disorder of the cation. Instead of big dynamic, there are two equivalent positions of N and C atoms in the crystal. Two ED positions of 0.5 occupancy are refined along with atomic parameters of all atoms, N1, N2, C1 and C2, constituted the cation (split cation in Figure 4.5b).

#### Split C1 and C2 model

The last model is splitting of only for C-positions. This is considered due small splitting of N-atoms (0.2 Å) in the split cation model (split C1 & C2 in Figure 4.5b).

The residual electron density is indifferently low in all three models of the cation disordering in the thermally treated crystal (Figure 4.5c). Positions of hydrogen atoms are in the 1.2 Å vicinity of the carbon and nitrogen atoms and then constructed according to expected geometry of the cation,  $\text{NH}_3\text{CH}_2\text{CH}_2\text{NH}_3$ . The hydrogen positions are restricted to 0.96 Å distance and to a tetrahedron configuration relative to the corresponding carbon and nitrogen atoms, while taking torsion angles into account. The structure refinement details appear very similar for all three models.

Geometry characteristics of the ED are listed in Table 4.2 for the pristine and three models of the thermally treated crystal. Characteristics of atomic positions and interatomic geometry

are available from the CIF files and in the Appendix, Tables A.6 and A.7. Based on consideration of the cation geometry in Table 4.1 split cation model is presented as preferable.

After refinement of both crystals, the calculated residual electron density shows additional weak maxima of about  $1 \text{ e}\text{\AA}^{-3}$ . These maxima are associated with the presence of a small amount of water. Placing the corresponding oxygen position gives about 13(2)% occupation for both crystals. This occupation corresponds to 0.042(4) and 0.042(5)  $\text{H}_2\text{O}$  per a chemical formula of the pristine crystal and thermally treated crystal, respectively (Table 4.1).

### 4.3 Photocurrent measurements

In order to characterize the photoconductivity response of the  $\text{EDPbI}_4$  single crystals, two-point electrical resistivity measurements (current density vs. voltage,  $J$ - $V$ ) are performed in the dark and under UV light illumination (see Methods in the Appendix B.4).

All measurements were performed under ambient conditions at room temperature. Gold wires connected with Dupont 4929 silver epoxy are used as electrical leads. The photocurrent characteristics were obtained under illumination from a UV light source (365 nm) with an intensity of  $0.055 \text{ mW mm}^{-2}$ . The voltage was swept from 0 V to +10 V/-10 V and back with a scanning speed of  $1 \text{ V s}^{-1}$ . All measurements were performed with crystalline samples of approximately equivalent size. Recalculation from current flow to current density are done by measuring the geometric factor of the sample and considering the absorption depth of the photon with an energy of 4 eV in the material [122].

### 4.4 Influence of the organic cation disorder on photoconductivity

As shown in Figure 4.4, the crystal structure of the cube-shaped  $\text{EDPbI}_4$  is topologically identical for the pristine and thermally treated crystals. The  $\text{PbI}_6$ -octahedra share a common face to form three-octahedra segments of a chain along the hexagonal  $c$ -axis. The segments are separated from each other by a distance of about 8.2 Å between the Pb atoms along the chain and about 8.4 Å between their axes. The trigonal prismatic cavity separating two segments of octahedra is not completely empty. A small amount of  $\text{H}_2\text{O}$  (about 13% occupation in both crystals) is found in the three-fold axis closer to the face of one of the octahedra ( $\text{O-I} \approx 3.2$  and 3.7 Å). The ED cations are distributed between the  $\text{PbI}_6$  chains, as can be seen in Figure 4.4.

Each organic cation is connected by  $\text{N-H}\cdots\text{I}$  hydrogen bonds to  $\text{I}^-$  anions forming  $\text{PbI}_6$  octahedra. These H-bonds are different in pristine and thermally treated crystals.

In the thermally treated crystal, hydrogen bonds are calculated according to a model of the atomic ordering in the ED cation (Figure 4.6 and Appendix Table A.7). The selection of the correct model needs a special discussion, which is in the following section.

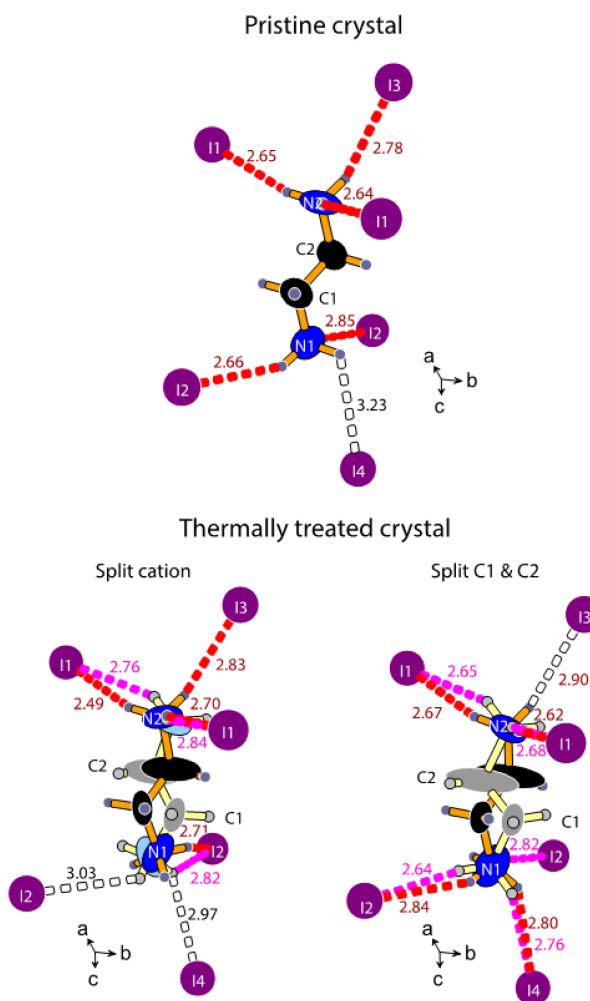


Figure 4.6 – Comparison of the N–H...I interactions in the pristine and thermally treated crystals of EDPbI<sub>4</sub>. The ED cation, H<sub>3</sub>N1–C1H<sub>2</sub>–C2H<sub>2</sub>–N2H<sub>3</sub>, and surrounding I atoms are shown in the identical perspective projection for each model. The distances N–H < 2.85 Å are emphasized: (top panel) by red for the pristine crystal; (bottom panel) by red and pink split positions of the ED cation in the thermally treated crystal are indicated.

#### 4.4.1 Disorder of the organic cation in the thermally treated crystal

Criteria of the quality of structure refinement cannot help to select the preferable model of the ED cation disorder among three of them described as dynamic, split cation and split C atoms (Figure 4.5). Each of the models is characterized by the identically low R-factors of 0.04 and reasonably low residual electron density of  $-2.5 < \Delta\rho < 1.4$ , which is located at about 1 Å from the Pb atoms.

Therefore, the geometry of the ED cation (Table 4.2) and ADP of C and N atoms constituting this structural unit (Figure 4.7) are considered to resolve this question.

From Table 4.2, it can be seen that in the dynamic model the distance C1–C2 = 1.29 Å is too short, while angles N–C–C of about 120° instead of the expected 108° are too large. Additionally, in Figure 4.7 ADP ellipsoids of both C1 and C2 are flattened. These factors show that the dynamic model with thermal atomic vibrations is not suitable.

On the other hand, the minimum deviation of the N and C atoms from their common plane (0.03(5) Å, Table 4.2) appears to be represented exactly in the dynamic model of disorder. This

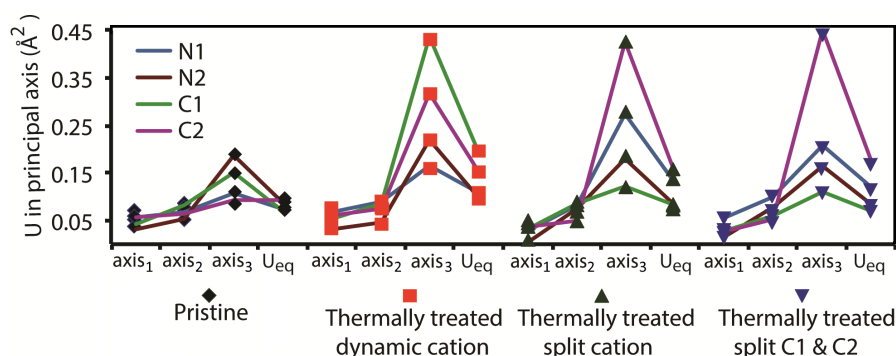


Figure 4.7 – Comparison of the displacement parameters of C and N atoms of ED cation in the pristine crystal and three models of the thermally treated crystal. The values of the principal axes of ADP ellipsoid and  $U_{eq}$  are displayed for each atom in each indicated model. The  $U_{eq}$  values are systematically lower in the pristine crystal.

means the improved geometry of ED cation causes deviations from the plane. Which is exactly observed in both the split cation and split C atoms models.

They are characterized by an essentially better geometry of the cation ( $N-C = 1.4-1.6$ ,  $C-C = 1.4-1.5$  Å, angles  $N-C-C = 108-117^\circ$ , Table 4.2) with the cost of  $0.15(5)-0.18(3)$  Å deviation of C2 from the  $N1N2C1$  plane. The deviation of C atoms from the ED plane can be regarded as the reason for their “pedal-like” [123] oscillations around positions inside the plane. Note that the deviation of  $0.13(3)$  Å from the plane is also observed for C2 in the pristine crystal structure, which is characterized by a good geometry of the ED cation (Table 4.2). This can be a reason for the stabilization of the thermally treated crystal under the ambient conditions: heating creates the oscillation in the unstable state of the pristine crystal.

It can be seen that in both split models, the virtually undistorted ADP ellipsoid of C1 (Figure 4.6 and 4.7) can be adopted in both static and dynamic types. However, the strongly enlarged ellipsoid of C2 (Figure 4.6 and 4.7) unambiguously indicates the contribution of the dynamic type. Considering possible  $N-H \cdots I$  interactions in two split models (Figure 4.6), one can say that two split positions of ED cation are perfectly bonded to the same I atoms.

This means that static and dynamic disorder types of ED cation can be stabilized by the very similar  $N-H \cdots I$  hydrogen bond interactions. Taken into account the more reasonable distances and angles within ED cation (Table 4.2), the split cation model is considered as the best approximation. However, some contribution of the “pedal-like” oscillation of carbon atoms cannot be completely excluded [123].

Summarizing this analysis, it can be concluded that despite the selection of the atomic disorder model in ED cation, the organic cation is certainly disordered in the thermally treated crystal. It is important to note that, in average, the  $U_{eq}$  atomic displacement parameters of C and N atoms are systematically larger in comparison to the pristine crystal (Figure 4.7). Thus, disorder of ED increases in the thermally treated crystal.



## 4.4. Influence of the organic cation disorder on photoconductivity

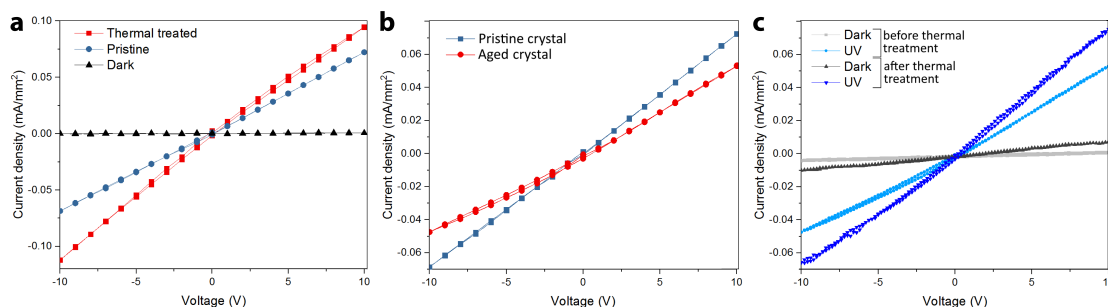


Figure 4.8 – The current density–voltage curves of EDPbI<sub>4</sub> crystal. (a) Comparison of the freshly prepared pristine and thermally treated crystals. (b) Comparison of the freshly prepared and aged pristine crystal. (c) Comparison of the aged crystal before and after thermal treatment, current density increased by 36%.

### 4.4.2 Correlation between the organic cation disorder and photoconductivity

In general, lower dimensional lead iodide structures display wider optical bandgaps [124]. Accordingly, the J–V curves (Figure 4.8a) show that the photocurrent is more than one order of magnitude weaker than in the commonly used MAPbX<sub>3</sub> material (for comparison in Appendix Figure B.4 shows J–V for MAPbCl<sub>3</sub> [125]) for both the pristine and thermally treated crystals. One of the benefits of low-dimensional perovskites is reduced ion migration, as can be seen from the J–V curves, the hysteresis is negligible. This is assumed to be due to the discontinuous PbI<sub>6</sub> chains, as iodine is the main migrating ion.

Despite the identical amount of water both in crystals (Table 4.1), the thermally treated crystal shows higher photoconductivity.

As discussed above, the main difference between these two types of treatment of the crystals concerns the ED cation disorder. It has been reported that for MAPbI<sub>3</sub> the CB minimum and VB maximum are mainly created by lead and iodine states and the contribution of the organic part does not affect the bands directly [126]. However, an interaction between the organic cation and the inorganic components of the structure plays an important role. Through the hydrogen bonding, the dynamic of the organic cation can change the bandgap [122]. Therefore, the organic cation position and mobility changes of the electron band structure and might be the origin for the increase of the carrier diffusion length and, consequently, better photoconductivity of the crystal with higher mobility of ED cation [115, 127].

### 4.4.3 Stability of crystals against moisture

The PV properties of the pristine crystal were studied once again ten months after it was synthesized. The crystal had been held at ambient conditions throughout this period. In Figure 4.8b is shown that the current density of this aged crystal decreased by 40% in comparison to its fresh state. The J–V curves were measured at 293 K in the dark and under UV light illumination (365 nm).

Next, the crystal was annealed for 10 minutes at 423 K. After 30 minutes of cooling, the measurements were repeated for this thermally treated aged crystal was measured.

Comparison of the measurements before and after heating of the aged crystal (Figure 4.8c) demonstrates almost identical increase of the current density induced by the thermal treatment. However, the aged crystal has degraded and its photoconductivity decreased by 40% in comparison to the freshly prepared pristine crystal (Figure 4.8b). Therefore, the degradation is mainly associated with incorporation of water that is typical for other lead iodide perovskite related compounds [95].

### 4.5 Conclusions

In this chapter  $\text{NH}_3\text{CH}_2\text{CH}_2\text{NH}_3\text{PbI}_4$  compound was synthesized with different post heat treatments. The results of the structural studies and electrical measurements are:

- After thermal treatment ethylenediammonium lead iodide,  $\text{NH}_3\text{CH}_2\text{CH}_2\text{NH}_3\text{PbI}_4$ , crystals possessing an arrangement of the  $\text{PbI}_6$  octahedra identical to the pristine crystals, but increased ethylenediammonium cation disorder.
- A link between the increased disorder of ethylenediammonium cation in the thermally treated crystal and its photoconductivity is observed.
- Measurements of the current–voltage curves revealed that after the thermal treatment the photoconductivity of the material improves by 36%.

These results highlight the fragility and delicate structural–property of  $\text{NH}_3\text{CH}_2\text{CH}_2\text{NH}_3\text{PbI}_4$  to thermal treatment, which might be a general characteristic of all organic–inorganic low-dimensional halide perovskites-related compounds.

## **Photodetector fabrication Part II**



## 5 3D Aerosol jet printing of hybrid halide perovskites

As mentioned in the Introduction, there are different deposition methods to synthesize  $\text{MAPbI}_3$  (for instance, solution or vapor based). Integration of the material in electrical circuits and miniaturization down to chip-scale is an important requirement for device application. Therefore, the capability to deposit PV material on a wide range of substrates with good spatial control is highly desirable.

In the prevalent patterning methods for  $\text{MAPbI}_3$ , mask fabrication is compulsory. For instance, for vertical growth of the  $\text{MAPbI}_3$  in nanopillars, a nanoimprinting crystallization technique has been developed [128]. In this method, the solution is pressed with prefabricated mold, shaping the crystallization process in the desired direction.

However, using the direct writing the pattern could be altered without excessive fabrication steps. One of the most used direct writing methods is ink-jet printing, which found applications in a variety of fields (such as photonics, medicine and biology [129, 130, 131]). The introduction of the ink-jet printing technique led to low-cost production of sensing electronics [132].

Many functional materials can be deposited with this method simply by varying the composition of the ink [133], including perovskites. Wei et al. developed the two-step process to pattern  $\text{MAPbI}_3$  by ink-jet printing MAI on a spin-coated lead iodide ( $\text{PbI}_2$ ) layer [134]. This approach gives a good resolution, but the full coverage of the surface in  $\text{PbI}_2$  is definitely a disadvantage for many applications.

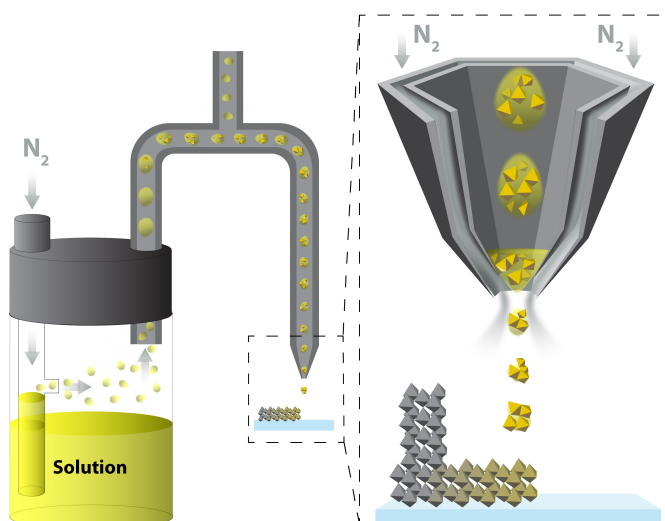
This Chapter provides an overview of a new approach based on aerosol jet printing (AJP) for  $\text{MAPbX}_3$  integration into electric circuits. AJP enables the precise patterning and unlimited layering of a functional material, with the possibility to create arrays of elements on various substrates. The success of this technique in writing well-defined 3D structures is linked to the formation of the intermediate phases of  $\text{MAPbX}_3$  during deposition.

### 5.1 Aerosol jet printing deposition

AJP has introduced new possibilities for direct writing through its use of a focused aerosol stream [135]. An overview of the AJP system is presented in Figure 5.1.

An aerosol is generated using either an ultrasonic or a pneumatic atomiser. The interplay between the surface tension, viscosity, volatility, and density of the solution for aerosolization presents challenges in the process development.

Figure 5.1 – Schematic of the AJP system. During the time-of-flight intermediate  $\text{MAPbX}_3$  is formed. By the time the solution reaches the substrate, the solvent is almost completely evaporated.



An advantage of the AJP method is an ability to work with viscous solutions, depending on the atomisation method, it is possible to generate an aerosol from inks with viscosities ranging from 1 to 1000 cP [136]. This presents opportunities beyond competing ink-jet technologies, which are often limited to viscosities below 20 cP. Ultrasonication also produces aerosols from low-viscosity (1–10 cP) solutions. While the pneumatic approach has a wider range of viscosities, it enables the atomisation of materials with a viscosity up to 1000 cP, but sacrifices the uniformity.

### Ultrasonic atomiser

An ultrasonic transducer produces highly uniform aerosols. The transducer is submerged within a transfer medium (water), where it oscillates at high frequency (> MHz). This pressure wave propagates through the transfer medium to a vial with the solution suspended above the transducer. Within the vial, a standing wave is formed on the surface and the superposition of consecutive waves results in the formation of large peaks. Local shear at the top of these peaks produces small droplets which are ejected from the rest of the solution. Aerosols generated using this technique are typically of low dispersity, with droplet sizes ranging from 2 to 5  $\mu\text{m}$  [135].

### Pneumatic atomiser

To generate aerosol the carrier gas collides with the ink surface, creating a sheared series of droplets. If within this stream the droplet is large, then due to high inertia, it is impacted on the side wall of the reservoir and returns to the rest of the ink. While lower inertia droplets remain as an aerosol and are transported further in the system.

In our system the aerosol is generated using a pneumatic atomiser.

After a suitable aerosol is produced, a carrier gas ( $\text{N}_2$ ) transports it to the nozzle. With the  $\text{N}_2$  jet and physical narrowing of the nozzle the aerosol is focused and deposited on the substrate. In the zoom in Figure 5.1 the shaping of the deposition with the secondary  $\text{N}_2$  flow is illustrated. This sheath flow gives unique characteristics to the AJP method, that is the collimation of the

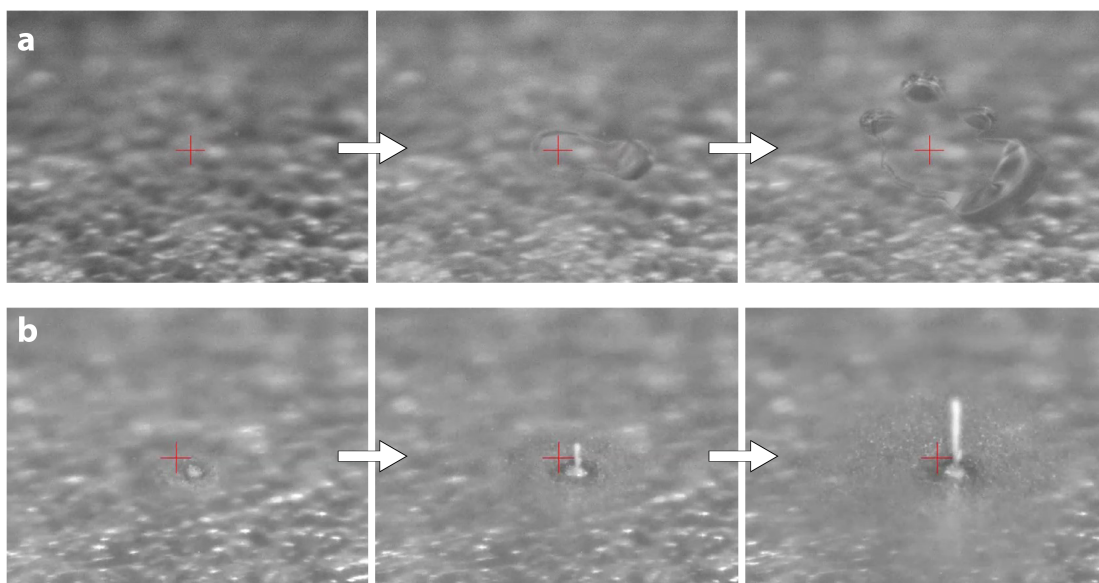


Figure 5.2 – Printing and 3D printing conditions. Time-lapse images illustrating typical (a) non-optimal and (b) optimal conditions of AJP.

aerosol flow and consistent deposition at a fixed distance [136].

Finally, AJP is a promising approach to make use of  $\text{MAPbI}_3$  intermediate phases [9] as they crystallize during the aerosol transfer. With this crystallization process it is possible to create 3D structures of  $\text{MAPbI}_3$ .

## 5.2 Solution preparation and 3D printing

During the ink preparation,  $\text{MAPbI}_3$  and  $\text{MAPbBr}_3$  crystals are stabilized as soluble complexes in DMF (see Methods in Appendix B.1). These solutions of  $\text{MAPbI}_3$  and  $\text{MAPbBr}_3$  (10 ml) are loaded in the vial. Aerosol jet printing was performed using a commercial Aerosol Jet Printer, Optomec AJ-300.

AJP requires control over numerous parameters, including the flow rate of the carrier and sheath gases, temperature and speed of the stage. The distance between the nozzle tip ( $150\ \mu\text{m}$  diameter) and the substrate was kept constant at 0.92 mm. The speed stage was 1 mm/s. The sheath gas flow was fixed at 693.7 sccm, while the carrier gas flow was varied.

During the flight, the solvent starts to evaporate, leading to the homogenous nucleation and crystallization of perovskite intermediate phases already in the nozzle. Exactly this process of crystallization under fast-solvent evaporation conditions is described in Chapter 1.3 (the first observable phases is presented in Appendix Figure A.10). When the droplet reaches the substrate, the solvent is mostly evaporated, thus reducing the spatter of the solution and improving spatial precision, as demonstrated in Figure 5.2.

At a carrier gas flow rate of 29.4 sccm and stage temperature at  $19.6\ ^\circ\text{C}$ , the intermediate phases

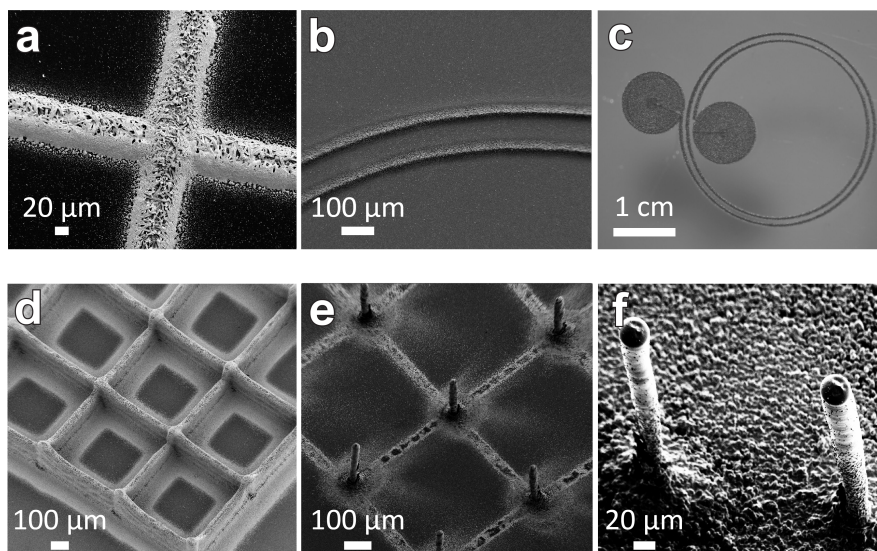


Figure 5.3 – SEM and optical images of 3D MAPbI<sub>3</sub> aerosol-jet-printed patterns.

were not formed during the time-of-flight of AJP micro-droplets, the carrier gas induces significant spreading of the MAPbI<sub>3</sub>·DMF solution on the substrate's surface, as shown in Figure 5.2a. This points out that the solution lands on the substrate in a liquid state. And under optimized conditions (the carrier gas flow rate - 59.4 sccm and stage temperature at 45°C), when the homogenous nucleation of intermediate phase crystallization is achieved during the time-of-flight, no spreading of the MAPbI<sub>3</sub>·DMF solution on the surface is observed, Figure 5.2b. The solution droplets land on the substrate as a crystalline solid (solvatomorph phase).

Moreover, preventing dissolution of the previously-deposited layers allows the creation of 3D patterns. For example, layer by layer deposition of high-aspect-ratio pillars and other features as illustrated in Figure 5.3a-f. Printed patterns are created by translating the deposition head with respect to the substrate in XY directions using a path generated from a CAD file. An average optimized spot size of  $48.7 \pm 2.8 \mu\text{m}$  is attained, substantially below the previously-achieved minimal spot size from MAPbI<sub>3</sub> ink of  $75 \mu\text{m}$ , demonstrated by Mathies et al. [137].

As can be seen from SEM images at high magnification, in AJP MAPbI<sub>3</sub> the number of grain boundaries is large. More boundaries in the material results in the increase of charge trapping. This leads to the trap-induced photoconducting gain effect, which helps in obtaining higher detector sensitivity [138], as we will see in the next Chapter.

The saturated solution was deposited on the substrate with the help of an N<sub>2</sub> jet and aligned the position by placing a nozzle at the location of interest. Over the multiple passes of the nozzle, the spread of the material around the 3D feature is growing. After 40 repetitions, a line with a width of  $45 \mu\text{m}$  is broadened to  $250 \mu\text{m}$ . After 120 repetitions the width is increased to  $585 \mu\text{m}$ . Thus, the minimum achievable width of a feature increases with the number of passes required for printing. Nevertheless more optimization could be done to decrease the spread, which was outside the scope of this thesis work.



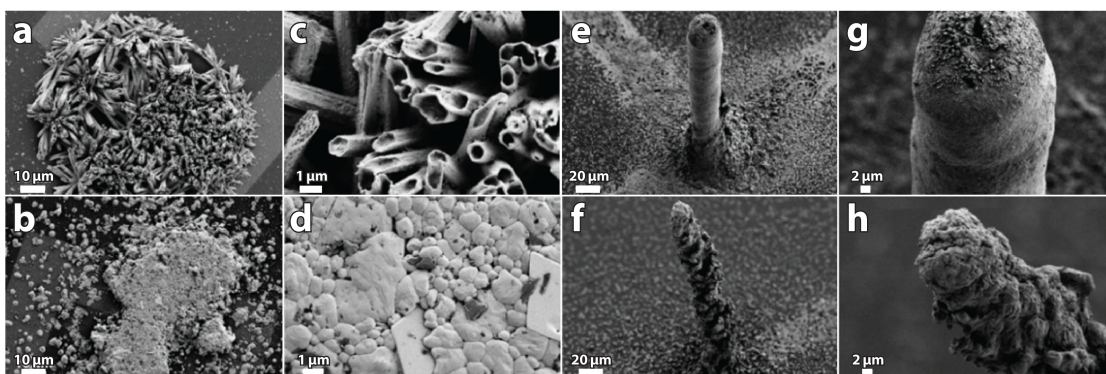


Figure 5.4 – SEM images of aerosol-jet-printed MAPbI<sub>3</sub> and MAPbBr<sub>3</sub>. (a, b) AJP MAPbI<sub>3</sub> and MAPbBr<sub>3</sub> sports on the metal pads with the zoom (c) and (d), respectively. (e, f) AJP MAPbI<sub>3</sub> and MAPbBr<sub>3</sub> pillars with the zoom (g) and (h), respectively.

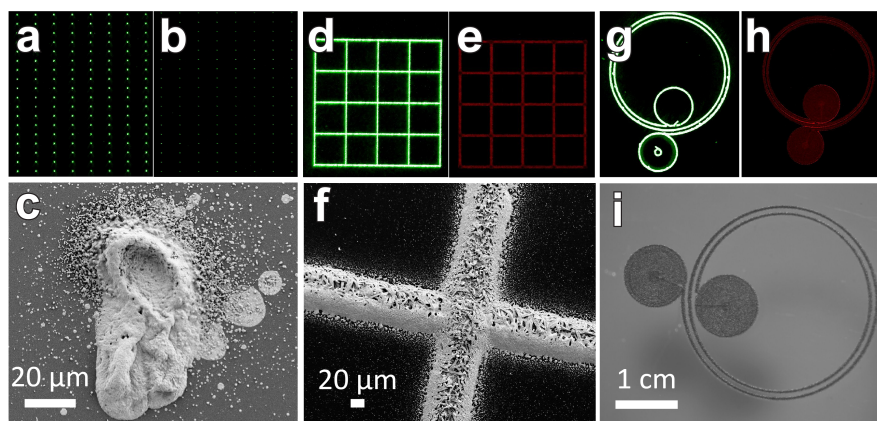


Figure 5.5 – Fluorescence of aerosol-jet printed (a-d, g, i) MAPbBr<sub>3</sub> and (e, f, h) MAPbI<sub>3</sub>, their (c, f) SEM and (i) optical microscope images.

### 5.2.1 Fluorescence

Excellent morphology and uniformity of the polycrystalline AJP-deposited MAPbX<sub>3</sub> are crucial for a final device performance. The morphology strongly depends on the solution saturation and the substrate temperature during the deposition process [139]. The AJP spots and pillars of MAPbI<sub>3</sub> and MAPbBr<sub>3</sub> have distinguished morphologies, as only MAPbI<sub>3</sub> is forming wire-shaped intermediates, Figure 5.4.

Arrays of MAPbBr<sub>3</sub> emitters with diameters of 93 μm and 48 μm have been deposited and examined by fluorescence imaging and SEM (Figure 5.5). The homogeneous fluorescence emission intensity indicates a good optical quality and structural reproducibility of the deposits.



## 6 Characterization of aerosol-jet-printed MAPbI<sub>3</sub> photodetectors

A photodetector is a device that converts light into an electrical signal. This can be achieved by separation of photogenerated charge carriers in a photoconductor under an external bias voltage ( $V_D$ ), as shown in Figure 6.1. When a photon with energy  $E > E_g$  is absorbed, an e-h pair is generated in the semiconductor. If an electric field strong enough to split the two charges is applied to the material, the charge carriers can contribute to the current of the device. Depending on the application, there are different requirements to the device regarding spectral response, sensitivity, response time, stability, etc.

### 6.1 X-ray imaging

X-rays with high photon energies have a short wavelength between 0.03 and 0.2 nm, that is similar to the size of atoms, which allows to use them for crystal structure determination (see Appendix A.1).

On the other hand, due to the low absorption of X-rays in many materials, they are widely used to image the inside of objects. Most notably in medical imaging, X-ray techniques enable the detection and characterization of cancers, cardiovascular diseases, osteoporosis, bone fracture, neurological diseases and many others. In this market, Computed Tomography (CT) remains highly popular as it is cheap, fast and robust in comparison to MRI [140, 141, 142]. However,

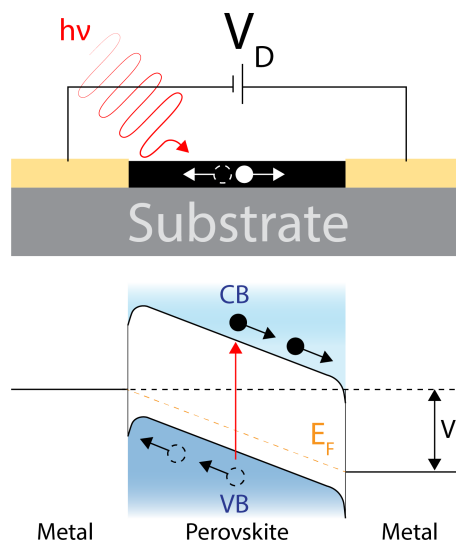


Figure 6.1 – Sketch of the photoconductor and its energy band diagram.

X-ray photons carry enough energy to ionize atoms and disrupt molecular bonds. Therefore, such radiation exposure is harmful to the human body and remains a major concern and a crucial limitation of CT's utility. The medical imaging industry is seeking new ways to reduce a radiation dose in CT as a key opportunity for growth. A typical CT scan exposes the patient to 2-16 mGy, which is the equivalent of one to eight years of background radiation [143, 144]. It is estimated that these radiation levels contribute to 1-3% of cancers [145] due to mutations induced by X-ray photons, hence the strong motivation to search for novel, more efficient photosensitive materials which can retain good image quality at a much lower photon flux.

Today's most common X-ray detectors are based on an indirect approach, where scintillating phosphors convert X-ray into visible photons, which can be detected by silicon photodiodes [146, 147]. The light emitted from the scintillator propagates isotropically from the point of generation. This causes optical cross-talk between adjacent pixels and results in a low resolution. Additionally, the detectors resolution is also limited by pixel size and electrical cross-talk [148].

A better approach is to convert X-ray radiation directly into an electrical signal. Direct-conversion detectors consist of a semiconductor material which provides a high intrinsic X-ray absorption coefficient [149]. Because charges are generated directly inside the semiconductor, these photodetectors have almost no optical cross-talk.

Photodetectors are a good example how AJP can integrate functional materials such as MAPbX<sub>3</sub> in device fabrication. For X-ray applications, a key material characteristic is the stopping power of photogenerated carriers, expressed as the energy loss per unit distance. Several processes determine the stopping power. A collision (ionization) term represents the interaction between charged particles and atomic orbital electrons and is proportional to the atomic number,  $Z$ . A radiative term stems from the interaction of charged particles with atomic nuclei,  $\propto Z^2$ . Due to the high atomic numbers of Pb, I and Br, lead halide perovskites have a suitable stopping power for X-rays [11, 12]. Additionally, it was shown that MAPbI<sub>3</sub> exhibits long-term stability even to high radiation doses [13, 150], making it a promising material for operationally-stable X-ray detectors.

Therefore, it is promising to implement the AJP deposition method for fabrication of a MAPbX<sub>3</sub>-based photodetector.

### 6.2 Photocurrent measurements under VIS

MAPbI<sub>3</sub> of different geometries (dots and pillars) was printed on electrodes (process flow is explained in Appendix C). Then the device response was tested under visible-light illumination. The photocurrent is composed of the photogenerated e-h pairs and is defined as  $I_{ph} = I_{light} - I_{dark}$ , where  $I_{light}$  is the total current through the device under illumination and  $I_{dark}$  is the value in the dark.

The 3D printed geometry (pillar shape) showed an increased charge carrier collection compared to its 2D counterpart (dot shape, Figure 6.2a), as illustrated in Figure 6.3. As visible light is ab-

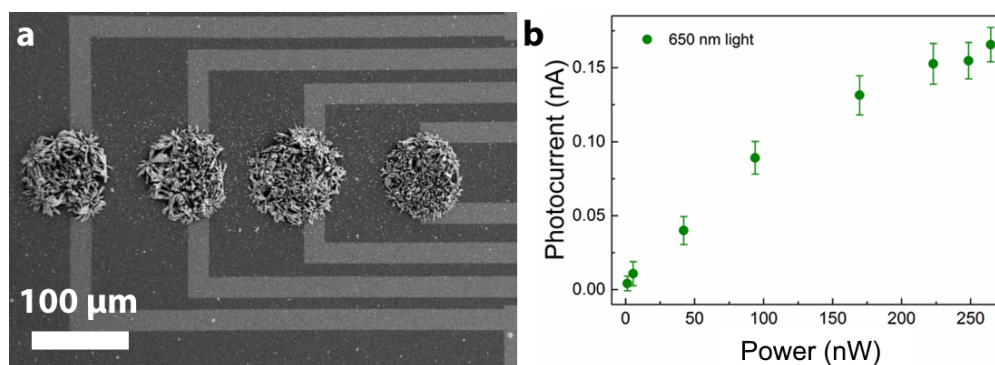


Figure 6.2 – MAPbI<sub>3</sub> aerosol-jet printed dot on the electrodes: (a) SEM image and (b) photocurrent dependence on the illumination intensity. The detection is possible down to 31.4 μW/cm<sup>2</sup>.

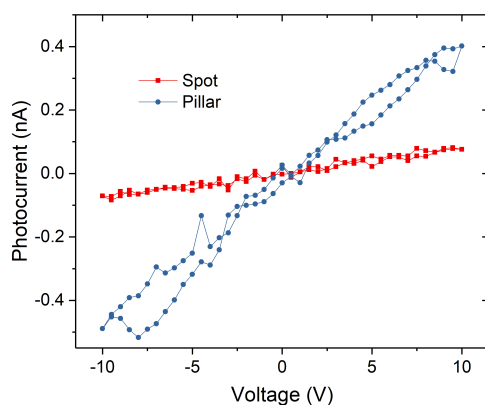


Figure 6.3 – Comparison of the pillar vs. dot device photocurrent under VIS light illumination.

sorbed near the surface, the difference in photocurrent could be explained by the larger volume and bigger surface area of the pillar compared to the dot pattern. Hence, the 3D geometry generates more carriers and gives a higher photocurrent.

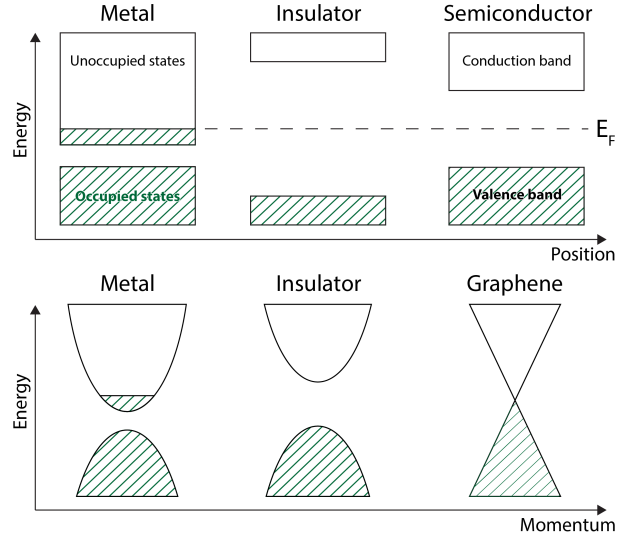
As many organic-inorganic perovskites, MAPbI<sub>3</sub> experiences ion migration, which results in current-voltage hysteresis. Both 2D and 3D geometries enabled detection of low light intensities, down to 31.4 μW/cm<sup>2</sup> under continuous wave (CW) illumination ( $\lambda = 650$  nm, Figure 6.2b).

## 6.3 Heterostructures based on aerosol-jet-printed MAPbX<sub>3</sub>

### 6.3.1 Graphene

Graphene consists of a single layer of hexagonally bonded carbon atoms. In the layer each carbon atom possesses three electrons which form a bond with the nearest-neighbor atom and the fourth electron is delocalized over the whole graphene sheet, allowing the conduction of an electrical current. This results in one of the most interesting aspect about graphene, its electronic properties, it has a particularly high electron mobility at room temperature [151],

Figure 6.4 – Band structure sketch of different type of materials.



which can reach  $170000 \text{ cm}^2 \text{ V}^{-1} \text{ s}^{-1}$  on hBN [152].

In Figure 6.4 the difference between the band structures of metals, insulators and semiconductors is illustrated.

In a semiconductor, the conduction and valence bands are separated by a band gap,  $E_g$ , which is small enough so thermal excitations or dopants can create electrons in the CB or holes in the VB. In the other case, the material is considered an insulator. Metals have a Fermi level in the middle of a band, resulting in occupied and available states in close proximity, and hence an easy electric conduction.

When the electron energy is plotted as a function of the momentum, the bands can be described as  $E = \frac{p^2}{2m^*}$  and presented as parabolas near the band edge extremum. In the case of graphene, the energy dispersion of electrons is linear and represented as two cones touching at the tips. As there is no gap, the behavior is unlike the insulators, and as there is no partially filled band as in metals, this zero-gap semiconductor obtains unique properties. Due to this band structure, the electrons in graphene have the same velocity and no inertia  $E = vp$ , as if they would have no mass. Which mimics relativistic particles traveling at the speed of light  $E = cp$ .

Relativistic particles in the limit of zero-rest mass follow the Dirac equation, therefore charge carriers in graphene are called massless Dirac fermions. Graphene exhibits an astonishing electronic quality. Its electrons can cover submicrometer distances without scattering, even in samples placed on an atomically rough substrate at room temperature.

### 6.3.2 MAPbX<sub>3</sub>-graphene interface

To further increase charge collection of halide perovskite light sensors, photodetectors based on AJP MAPbI<sub>3</sub> and graphene were fabricated. The process flow for the samples with etched graphene sheet and thermally evaporated contacts is described in Appendix C.

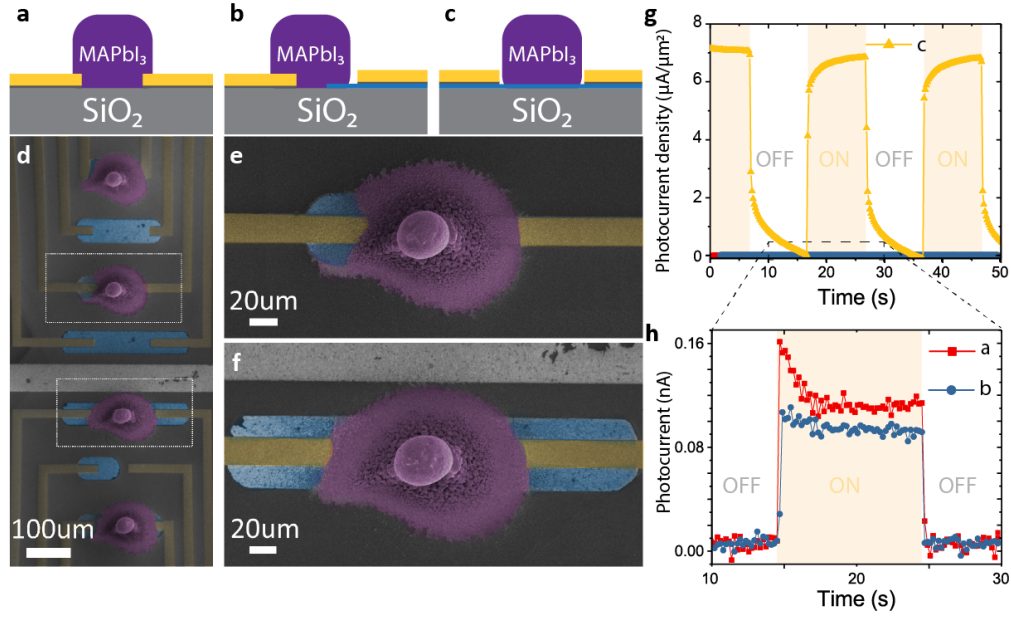


Figure 6.5 – Different configurations of AJP MAPbI<sub>3</sub> pillars. (a-c) Schematic of the devices: (a) resistor, (b) diode and (c) heterojunction types. (d-f) False-colored SEM images of AJP MAPbI<sub>3</sub> (purple) on the graphene layer (blue) with electrodes (yellow): (e) diode-like and (f) heterojunction configurations. (g, h) Transient photoresponse on-off characteristics of the photodetector under white light illumination for the three device architectures, (h) measurements of (a, b) types at 5 V bias, while for (c) device only 10 mV bias was applied.

Graphene has a low light absorption of 2.3% [153], so by itself is not ideal for photodetection. But due to its band structure (the zero band-gap character [154]) it can amplify the effect of photoelectrons created in MAPbX<sub>3</sub> in the following way. The light-induced excitons in the perovskite have low binding energy [4], and due to the difference in chemical potential and bias voltage they are transferred through the interface to graphene. It is likely that the remaining electrons in the perovskite exercise field-effect gating on the graphene, further amplifying the output [155].

It was shown in the visible range that the MAPbI<sub>3</sub>-based photodetector exhibits responsivities as high as 3.5 A/W with ITO/PET, which can be increased up to 180 A/W when graphene is used [156, 157]. The responsivity is enhanced even further, up to  $2.6 \times 10^6$  A/W when a hybrid structure with wire-shaped MAPbI<sub>3</sub> and graphene is used [155].

This increase in charge collection is explained in Section 6.4.

### 6.3.3 Photodetector architecture

In order to determine the optimal pixel design and sensing configuration, several possible architectures and operation modes have been tested (resistor, Au/MAPbI<sub>3</sub>/Graphene diode-like, and heterostructure, as illustrated in Figure 6.5a-c). The measurement details are provided in Appendix B.4. The best performance was found for MAPbI<sub>3</sub> pillars printed on a graphene layer



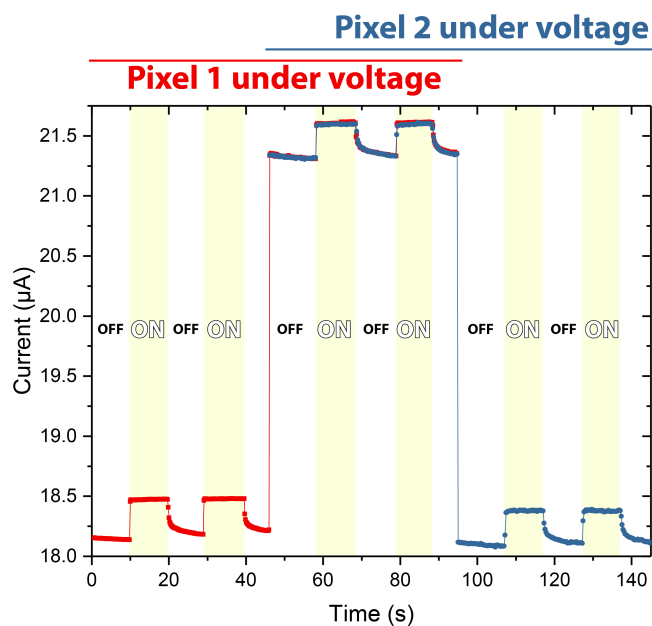


Figure 6.6 – Cross-talk measurements of neighboring pixels under white light illumination. Photocurrent measurements under 10 mV.

covering the whole distance between the gold electrodes (Figure 6.5c, f). In the case of resistor and diode-like configuration, the current is conducted through a highly resistant MAPbI<sub>3</sub> material, whereas in heterostructure, the current is governed by graphene, and MAPbI<sub>3</sub> plays a role of dopant in the system. This results in the increased photocurrent signal at significantly lower bias voltages.

As the device demonstrated good detection characteristics even for low bias voltages, it makes it compatible with low-power electronics (Figure 6.5g). This structural unit represents one pixel in the detector.

An alternative design for an X-ray detector consists of a non-microstructured graphene below the microelectrodes, and 3D printed lead halide perovskite. In order to assess, whether or not the non-microstructured graphene sheet is suitable for imaging purposes, the degree of cross-talk, of neighboring pixels should be characterized.

The cross-talk measurement was performed under white light illumination, Figure 6.6.

For this kind of measurements, the whole surface of the integrated chip is exposed. A voltage of 10 mV is applied to pixel 1 in time, while turning the light on and off. After two on-off cycles, the same bias voltage is applied to the neighboring pixel, no. 2, simultaneously. Two additional on-off cycles are recorded. Lastly, the applied voltage is stopped on pixel 1, while it is maintained on pixel 2, to record two more on-off cycles.

The baseline changes at the moments the additional bias voltage is applied. This current is governed by the graphene, as an additional electric field is applied to it. In a future commercially available device, one single bias voltage could be applied through the whole graphene sheet, powering the individual pixels. What is important for the study of the cross-talk, is that the photocurrent signals of a pixel do not change in value whether or not its neighboring signal



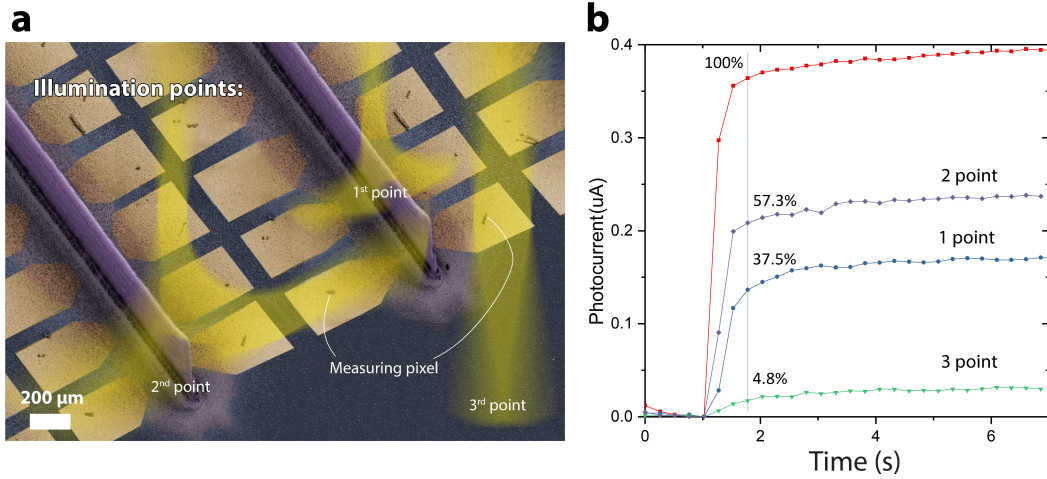


Figure 6.7 – (a) False-colored SEM image with illustration how VIS light scatters on PDMS. (b) Photocurrent drop measured under 10 mV at indicated points.

is under operation. Therefore, from these measurements, there is no observable crosstalk between neighboring pixels and the architectural design of the integrated chip will be suitable for imaging purposes in the future.

In a second series of measurements, different individual pixels are illuminated by a collimated white light source with an active area of  $0.2 \text{ mm}^2$ , while measuring the photocurrent signal of a reference pixel (Figure 6.7). When illuminating the neighboring pixel on the same MAPbI<sub>3</sub> wall ridge (point 1), the photocurrent response drops to 37.5% of the reference value. This is already a substantial decrease in value, however, the remaining contribution is due to the white light scattering on the PDMS which is encapsulating the device from ambient conditions. This is even more pronounced when illuminating the neighboring pixel in the same column but in a different line (point 2). As the PDMS layer is at an angle, following the wall shape of the printed perovskite, the light scatters even more towards the measured pixel. Nevertheless, there is an almost 50% decrease in the signal. Even if the light is moved completely out of the structure (point 3), a weak signal is visible due to the scattered light and high sensitivity of the device. Therefore, the layout without etching graphene layer still gives a good image contrast and is used for the final device.

## 6.4 X-ray photodetector

For this work, the X-ray detection performance of the devices is investigated using a standard fine-focus copper X-ray tube (CuK $\alpha$ ). X-ray photon intensities (dose-rates) are selected by varying tube voltage and current in the range of 15 - 45 kV and 5 - 40 mA, respectively. The calibration of the beam and description of the dose-rate calculation can be found in the Appendix B.2.

For X-ray photons with a specific energy, the X-ray attenuation efficiency ( $\epsilon$ ) can be calculated

Figure 6.8 – Attenuation efficiency of CdTe, MAPbI<sub>3</sub>, MAPbBr<sub>3</sub>, MAPbCl<sub>3</sub> and Si to 50 keV X-ray photons vs. thickness. The plot is reproduced from [158].

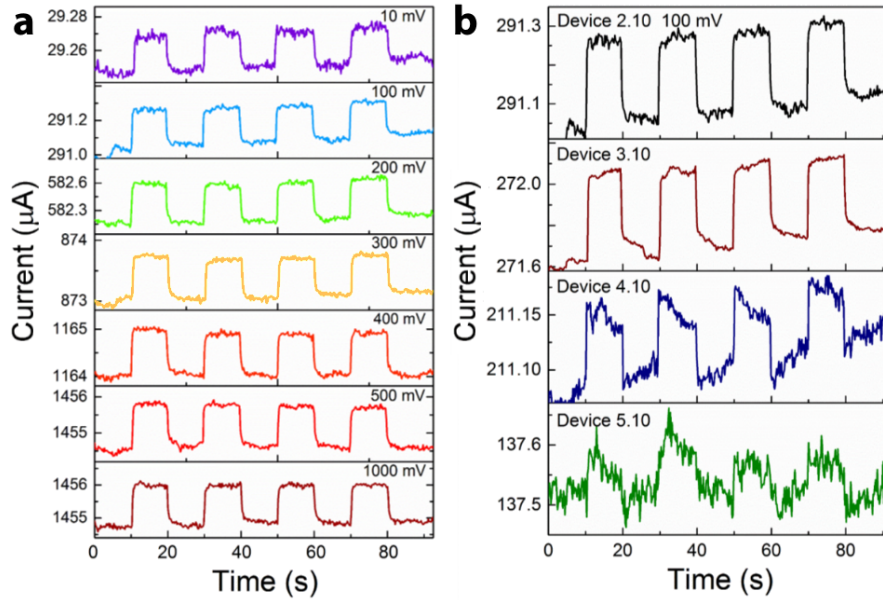
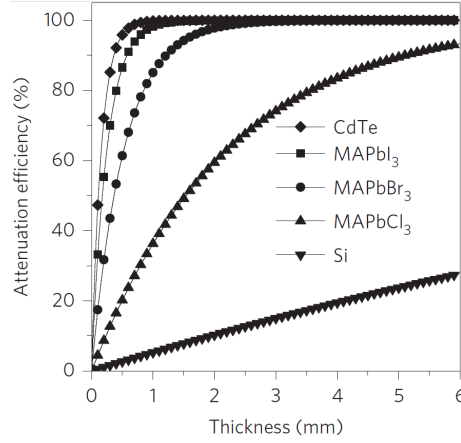


Figure 6.9 – Dependence of the photocurrent on the AJP MAPbI<sub>3</sub> dot on graphene under 358  $\mu\text{Gy/s}$  X-ray illumination (a) on applied voltage and (b) dot size (no.2 is the biggest dot and no.5 is the smallest). The parameters of the dots are provided in Table B.1.

as  $\epsilon = 1 - e^{-\alpha_a x}$ , where  $x$  is the thickness and  $\alpha_a$  is the absorption coefficient of the sample. An example of  $\epsilon$  for different materials for a 50 keV X-ray source is presented in Figure 6.8. As can be concluded from this plot, the heavy Pb and I atoms are much more efficient in absorbing highly energetic X-rays compared to lighter elements such as Si. For visible light, 1 - 2  $\mu\text{m}$  of MAPbI<sub>3</sub> is sufficient to absorb all light, while for a conventional CuK $\alpha$  X-ray tube source (8 keV) approximately 30  $\mu\text{m}$  is needed [138].

Therefore, due the difference in the photon absorption conditions for high energetic X-rays and for visible light [13], the impact in the smallest MAPbI<sub>3</sub> dot size gives a weaker response under X-ray illumination, Figure 6.9 (VIS in Appendix Figure B.5).

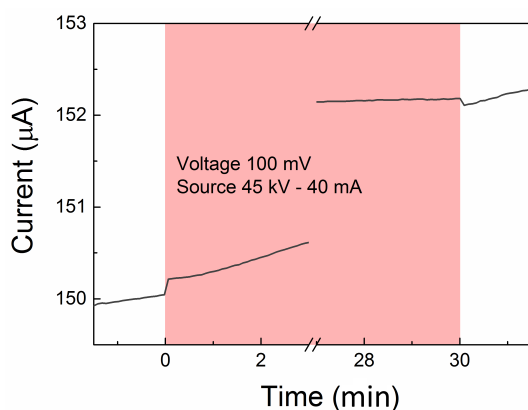


Figure 6.10 – Operational stability of the AJP MAPbI<sub>3</sub> device under X-ray exposure.

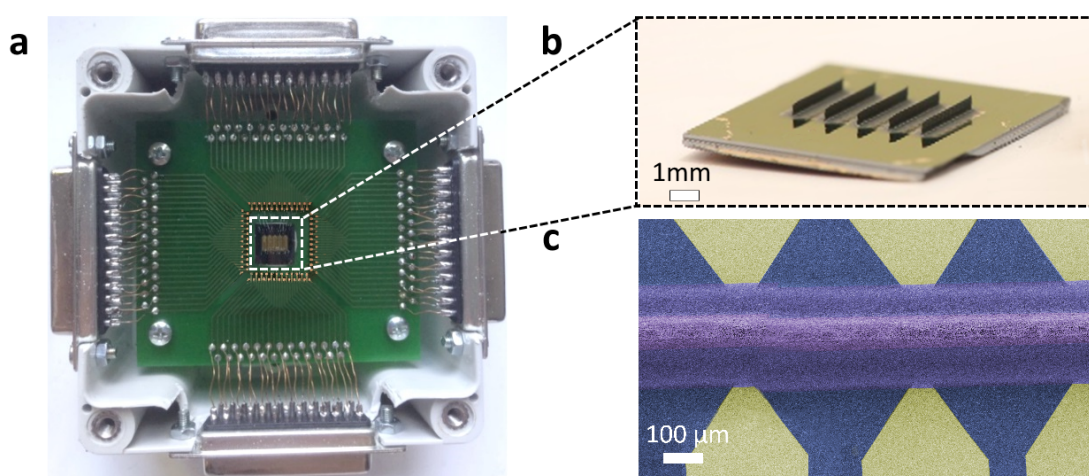


Figure 6.11 – (a) Photograph of the fully integrated X-ray detector. (b) 1 cm<sup>2</sup> sensing chip with 3D printed MAPbI<sub>3</sub> walls of about 600 μm height. (c) False-colored top view SEM image of the 3D printed MAPbI<sub>3</sub> wall on the Ti/Au electrodes (graphene in blue, MAPbI<sub>3</sub> in purple and metal electrodes in yellow).

The operational stability of the AJP MAPbI<sub>3</sub> dot on graphene was tested for 30 minutes under a constant voltage and a 358 μGy/s dose-rate, Figure 6.10. The sample showed no degradation during or after the long-term test. However, the signal experienced a drift of 1.5 μA over the 30 min, which is probably due to ion migration [38].

In order to collect all photons, devices with a high wall of MAPbI<sub>3</sub> were fabricated, as illustrated in Figure 6.11 a-c. The electrodes were wire-bonded to the PCB and the chip was encapsulated in PDMS to protect it from dust and moisture. The module was placed in front of the X-ray beam for further characterization.

The pair of neighboring pixels (the same pair as in Figure 6.5) was measured to evaluate the cross-talk between them under X-ray exposure, Figure 6.12. Pixel 1 performs among the best in the array and neighboring pixel 2 has an average signal. This could be due to the better interface between the printed material and the graphene, and because of the quality of the graphene

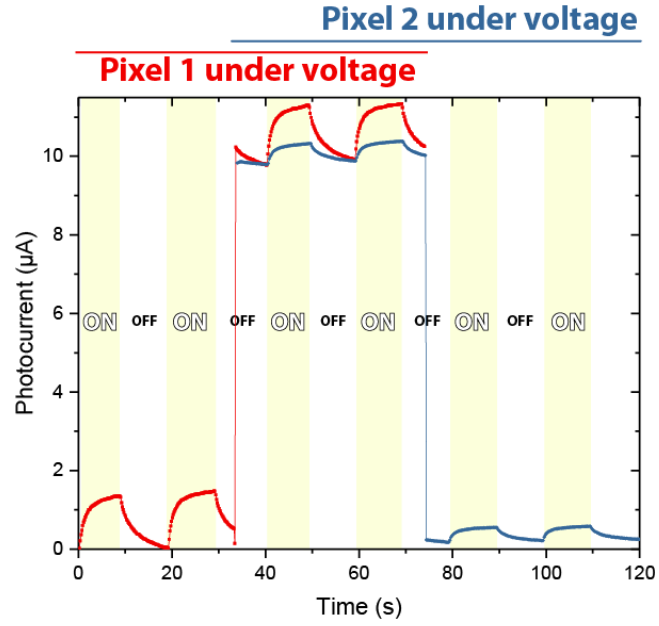


Figure 6.12 – Cross-talk measurements of neighboring pixels under X-ray exposure. Photocurrent is measured under 10 mV bias voltage.

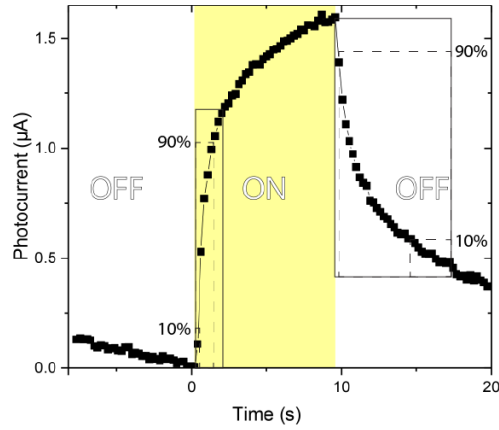


Figure 6.13 – Rise and fall photoresponse times of AJP MAPbI<sub>3</sub> on graphene.

(there could be cracks in the film). However, with advanced electronics this difference could be taken into account for the integration of a picture. The results are similar as under white light illumination, adjacent pixels do not influence each others amplitude in the photoresponse.

The photoresponse times of the heterostructure are defined as follows: the rise time as the time required to reach 90% from 10% of the amplitude (“On-state” after 2 seconds), while the fall time is the time needed to reach 10% from 90% of the same amplitude in the “Off-state”, Figure 6.13. The device exhibits a rise time of  $1.45 \pm 0.13$  s, while the fall time is  $2.8 \pm 1.7$  s at 100 mV for dose-rates below  $90 \mu\text{Gy/s}$ . The fast-rising component represents the signal induced by the originally produced carriers [155]. The slow part of the fall time is a characteristic of the detrapping process of carriers [159]. The trap density in single crystal is much lower than in the polycrystalline structures, as can be seen from Figure 6.14.

However, as the device exhibits high photocurrent, for an actual application the signal at subsecond times of the rise and fall would be at the sufficient signal-to-noise level. To further

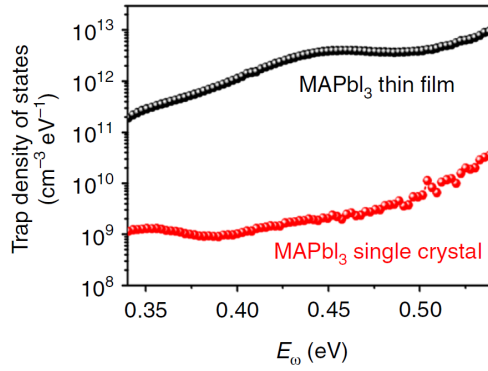


Figure 6.14 – Trap density of states of the MAPbI<sub>3</sub> single crystal and polycrystalline thin film measured by thermal admittance spectroscopy at room temperature. The plot is reproduced from [160].

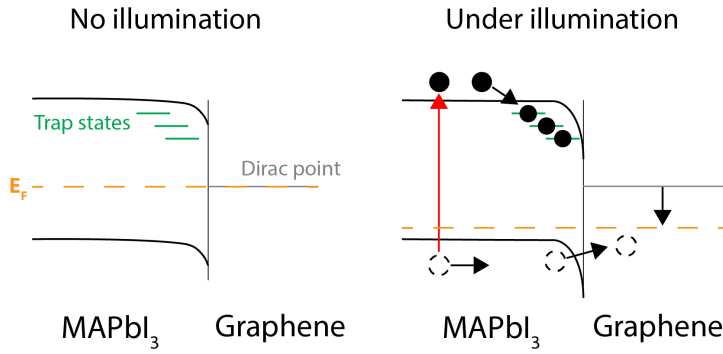


Figure 6.15 – Band diagram of the MAPbI<sub>3</sub> and graphene heterostructure in the dark and under illumination. Trapped electrons give a rise to the photogain.

enhance the signal-to-noise ratio a pulsed-voltage bias could be applied as is done in other publications [138]. When the voltage is applied every 0.5 s, the current is simultaneously measured across the detector. In that configuration, the baseline current drift would be drastically suppressed and a stable signal can be detected.

The high value of the photocurrent consists of two main contributions: impact ionization and photoconducting gain [138]. The former appears when the carrier with an excessive energy (binding energy of a valence electron to the atom) colliding with the atom breaks a covalent bond and produces an e-h pair. These energized electrons and holes can on their turn generate more free carriers. However, the effect of photoconducting gain plays a main role in these devices. The high gain is a result of the very high defect density in the MAPbI<sub>3</sub> deposited with AJP, as explained in Figure 6.15. Under illumination, photogenerated electrons near the MAPbI<sub>3</sub>-graphene interface are trapped in these defect states, which causes charging and band bending in this region [161], pushing the Fermi level in the graphene downwards from the Dirac level. On the other hand, the photogenerated holes can still transfer to the graphene, further lowering the Fermi level. This results in so-called photogating, as the lowered Fermi level causes a large increase in the electronic states which contribute to current conduction, resulting in a drastic increase in current through the graphene [162]. Overall the high photogain is obtained as a small amount of photogenerated e-h pairs cause orders of magnitude more carriers to pass through the graphene.

In Figure 6.16a, the most sensitive pixels are further exposed to dose-rates from 0.12  $\mu\text{Gy/s}$  to 358  $\mu\text{Gy/s}$  while opening and closing the shutter in front of the 8 keV X-ray source for periods



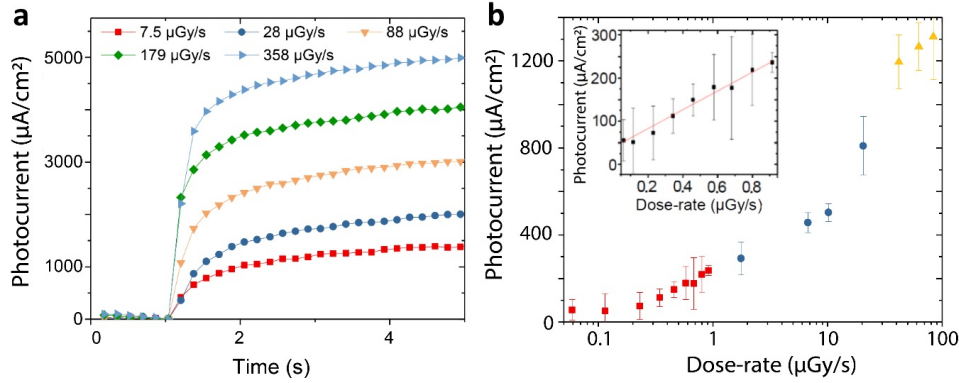


Figure 6.16 – X-ray detector measurements. (a) X-ray illumination-induced photocurrent response as a function of time for several X-ray dose-rates at 100 mV bias voltage. (b) Photocurrent density as a function of X-ray dose-rate, region below 1 μGy/s is in the inset.

of 10 s. High photocurrents of up to 4 mA/cm<sup>2</sup> are measured at 358 μGy/s dose-rate.

The X-ray detection limit is found to be at a 0.12 μGy/s dose-rate, below which the signal could not be distinguished from the background noise. Which is an outstanding value for MAPbI<sub>3</sub>-based detectors, but, for instance, MAPbBr<sub>3</sub>-based X-ray detectors have demonstrated a detection limit around 0.036 μGy/s [12].

### 6.4.1 Sensitivity

#### Theoretical considerations

In the following, we are going to estimate the maximum number of e-h pairs which could potentially be generated in a semiconductor when absorbing X-ray radiation. As such, we will consider that all X-ray energy will be transformed into e-h pairs.

As the absorbed X-ray dose in a material can not be directly measured, physical quantities such as particle and energy fluence are used to describe a monoenergetic beam of ionizing radiation. The photon fluence of our 8 keV X-ray source is  $7.5 \times 10^{11} \frac{\text{photons}}{\text{cm}^2 \text{R}}$ . In the idealized case where all photons are absorbed, a total absorbed energy  $E_{ab} = 6 \times 10^{15} \frac{\text{eV}}{\text{cm}^2 \text{R}}$ . Since a single e-h pair has an energy of  $E_g = 1.6 \text{ eV}$ , then the maximum number of generated e-h pairs is  $N_{ehp} = \frac{E_{ab}}{E_g} = 3.75 \times 10^{15} \frac{1}{\text{cm}^2 \text{R}}$ . Which results in a collected charge of  $Q_c = N_{ehp} \times e = 6.01 \times 10^2 \frac{\mu\text{C}}{\text{cm}^2 \text{R}}$ .

For an ideal semiconductor, a dose of 1 R corresponds to 0.001032 Gy. Therefore, for an ideal semiconductor, the total charge could reach  $Q_c = 5.8 \times 10^5 \mu\text{C Gy}^{-1} \text{cm}^{-2}$ .

This dependence of the photocurrent on the dose-rate is also called sensitivity,  $S_x$ .

#### Experimental results

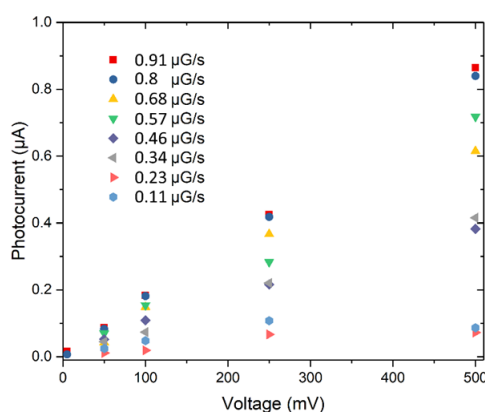


Figure 6.17 – Photocurrent vs. voltage bias under X-ray of different photon energy.

$S_x$  was calculated at 100 mV bias for three regions by linear fitting  $I_{light} = I_{dark} + S_x \cdot D$  to the experimental data, where  $D$  is the X-ray dose-rate. At dose-rates below  $1 \mu\text{Gy/s}$ , the sensitivity of the device is the largest, reaching  $S_x = 2.2 \times 10^8 \mu\text{C Gy}^{-1} \text{cm}^{-2}$ . It is important to point out that this is a sensitivity of the pixel on the chip with an estimated surface of  $0.075 \text{ mm}^2$ . For dose-rates above  $1 \mu\text{Gy/s}$ , the photocurrent begins to saturate (Figure 6.16b), yielding a sensitivity of  $S_x = 2.5 \times 10^7 \mu\text{C Gy}^{-1} \text{cm}^{-2}$  for a dose-rate of up to  $40 \mu\text{Gy/s}$  and finally,  $S_x = 2.9 \times 10^6 \mu\text{C Gy}^{-1} \text{cm}^{-2}$  was found from  $40$  to  $100 \mu\text{Gy/s}$ . A linear dependence of the response to voltage was measured (Figure 6.17).

However, we are observing sensitivities which are 3 orders of magnitude larger than the upper limit for an ideal semiconductor. This is a result of the long carrier lifetime, and large number of surface interface states at the MAPbI<sub>3</sub>/graphene interface, which drastically increase the graphene conductivity (Figure 6.15). As such, a single photogenerated e-h pair allows many thousands of extra electrons to flow through the graphene.

One of the major obstacles preventing perovskite-based optoelectronic devices from being commercialized is their long-term stability. Gradual decomposition of MAPbI<sub>3</sub> is observed in air and scales with increasing humidity [95]. Water molecules replace MA<sup>+</sup> cations, leading to PbI<sub>2</sub> nucleation. Thus, the active layer should be protected from water vapour present in ambient air. This also applies to the X-ray detector unit.

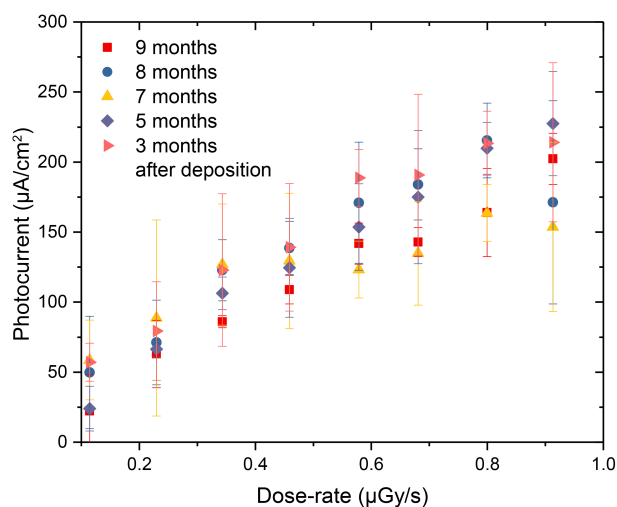
The shelf-life stability was tested and the operational reproducibility checked monthly after assembling the detector unit. It has shown satisfactory stability since, in a time period of nine months, no degradation in performance of the PDMS-encapsulated device has been observed (Figure 6.18).

## 6.5 Conclusions

The last two Chapters described the fabrication and characterization of aerosol-jet-printed MAPbI<sub>3</sub>-based X-ray photodetectors. In these Chapters:

- A rapid and cheap printing technique, the aerosol jet printing, was optimized for MAPbX<sub>3</sub>

Figure 6.18 – Shelf stability of the device. Monthly low dose-rate measurements during a storage. Fit of all measurements gives  $10^8$  value of the sensitivity.



integration in an electrical circuit.

- An aerosol-jet-printed X-ray detector unit, based on MAPbI<sub>3</sub> on graphene, was structured and tested.
- The X-ray detector shows a record sensitivity of  $2.2 \times 10^8 \mu\text{C Gy}^{-1}\text{cm}^{-2}$ , four orders of magnitude higher than the state-of-the-art perovskite devices.

As for one of the applications, this approach could allow significant lowering of the radiation doses required for X-ray imaging, resulting in safer and more affordable CT imaging systems.



# Conclusions

Within this thesis a lot of information about MAPbI<sub>3</sub> material properties and applications was covered.

The influence of environmental factors, such as temperature and pressure, and role of cation disorder has been investigated in the First Part.

It was shown that MAPbI<sub>3</sub> structure does not returned to its initial state upon thermal cycling. And each of the phase transition (low and high temperature) introduces different effects on the material. These structural modifications are important and should be considered in the engineering of the perovskite-based devices.

Furthermore, the pressure-induced phase transitions could be modified with the medium. This discovery is significant for the fundamental science, as it demonstrate how with applying high pressure noble gases activate and intercalate in the soft structure of MAPbI<sub>3</sub>. And for the practical application it could open a new path for the stabilization of the organic-inorganic perovskites.

An interesting link between the organic cation disorder and conductivity is the next step in understanding of the hybrid perovskites. With the separation of the octahedra on the clusters in lower-dimensional perovskites the ion migration is prevented. Therefore, we are able to see a pure influence of the dynamic and disorder of the cation on the structure. These results could help to explain the enhance in the performance of the perovskite-based devices after an annealing process.

Also this work covers an analysis of the intermediate phases of the wire-shaped MAPbI<sub>3</sub>. In solar cell application most of the effort is concentrated on the homogenizing of the perovskite film. Whereas here we demonstrate how these derivatives of the material can find an application in photodetection. With an aerosol jet printing fast anisotropic crystallization enables creation of highly crystalline 3D structures. This creates a unique combination of the material engineering and technological approach to create an X-ray detector with record values of sensitivities.

As a result, in this thesis work, the material, MAPbI<sub>3</sub> was characterized under various conditions and even was implemented in the X-ray detector with promising properties for the future application.



# Outlook

This thesis was dedicated to the study of methylammonium lead iodide, which exhibits various intriguing properties. The present work investigates the interaction between organic and inorganic parts of this mixed-conduction material and explains its links to the observed properties. It was demonstrated how external factors such as temperature and pressure modify this soft material. However, future work should check if a thermally cycled MAPbI<sub>3</sub> crystal indeed reaches the monophasic state with increased number of cycles around 330 K and if this phonon-governed phase persists after thermal cycling. Also questions regarding the long-term stability and electrical properties of the Ne-incorporated crystals are open for further investigation.

It is of great importance to understand the crystallization process in detail, in order to control solution preparation and develop new deposition methods. Such analysis has been done here for the wire-shaped methylammonium lead iodide. Methylammonium lead iodide gives outstanding optoelectronic efficiencies, which is promising for applications in a wide range of devices. To underline this, wire-shaped intermediates were used in a novel 3D aerosol jet printing method for fabrication of an X-ray detector. The final device based on a perovskite/-graphene heterostructure demonstrates record sensitivity values. However, the spreading of the material during the deposition could be optimized in the future for obtaining cleaner structure confinement on the wafers. For future work on these X-ray detectors, the readout electronics and image processing should be improved and real tests in the hospital should be performed.

An overall downside of the present material itself is its lead content. Even if the amount of lead in perovskite devices is no more dangerous than other lead-containing electronics, the production of lead itself is harmful. Before the industrial revolution, lead was nearly entirely absent in the top layers of the earth's crust, but after two centuries of mining activities, current values of lead concentration on the surface are up to 36.3 mg kg<sup>-1</sup> [163]. A comparison of MAPbI<sub>3</sub> and PbI<sub>2</sub> soil contamination showed that the organic cation influences the pH of the soil and has a substantial impact of lead bioavailability. Which leads to higher vegetal lead uptake [163]. And, in turn, plants transfer heavy metals from the soil to the food chain and thus the human body. Therefore, ideally lead should be substituted in MAPbI<sub>3</sub> with non-toxic or rapidly oxidizing (low solubility in water) elements.

Another issue is related to toxic solvents used during synthesis. In this work most of the crystals were produced using dimethylformamide at relatively high temperatures, which is suboptimal at best. One of the developing methods of the substitutional growth use alcohols (methanol, ethanol, 2-propanol) for MAPbI<sub>3</sub> synthesis [164]. Thus, the incorporation of new solvents could be one of the next steps for this research area.



# A Appendix: X-ray diffraction

## A.1 XRD experiments background

The periodicity of the crystal structure distinguishes crystalline from non-crystalline solids. In the case of a crystal a structural unit of atomic arrangement is periodically repeated in 3D. Therefore, the crystal lattice gives a 3D framework in space with the cell parameters, shown in Figure A.1. These  $a, b, c, \alpha, \beta, \gamma$  are called **unit-cell parameters**. The variation in the crystal lattices is classified into the seven "crystal systems", Table A.1.

It is possible to investigate the crystal structure by studying diffraction, which results from scattering on and interference from the material. The interference is the interaction between the periodic lattice ( $hkl$ ) with incoming waves. Bragg's law relates the periodically re-occurring

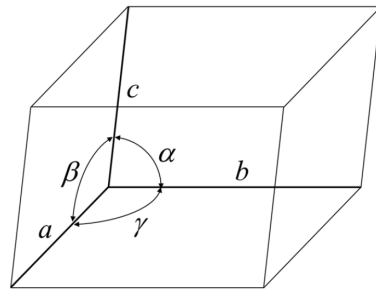


Figure A.1 – Sketch of the unit-cell parameters.

Crystal system	Restrictions on unit-cell parameters	Parameters to be determined
Triclinic	None	$a, b, c, \alpha, \beta, \gamma$
Monoclinic	$\alpha = \gamma = 90^\circ$ or $\alpha = \beta = 90^\circ$	$a, b, c, \beta$ $a, b, c, \gamma$
Orthorhombic	$\alpha = \beta = \gamma = 90^\circ$	$a, b, c$
Tetragonal	$a = b, \alpha = \beta = \gamma = 90^\circ$	$a, c$
Trigonal	Hexagonal: $a = b, \alpha = \beta = 90^\circ, \gamma = 120^\circ$ Rhombohedral: $a = b = c, \alpha = \beta = \gamma$	$a, c$ $a, \alpha$
Hexagonal	$a = b, \alpha = \beta = 90^\circ, \gamma = 120^\circ$	$a, c$
Cubic	$a = b = c, \alpha = \beta = \gamma = 90^\circ$	$a$

Table A.1 – Crystal systems and relationships of unit-cell parameters.

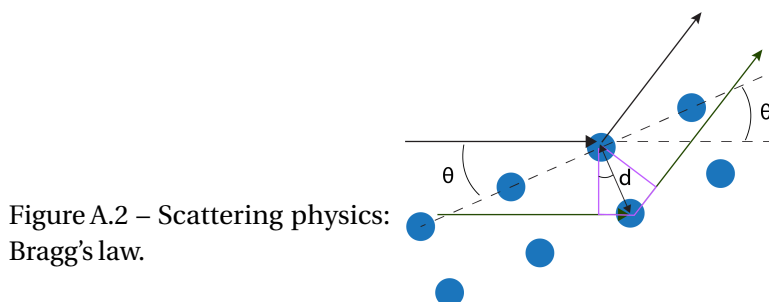


Figure A.2 – Scattering physics:  
Bragg's law.

distances of lattice planes (***d*-spacings**):  $2d \sin(\theta_B) = n\lambda$ , where  $d$  is the distance between lattice planes,  $\theta_B$  - Bragg angle (Figure A.2). This is because the beam reflected from consecutive planes must be in phase (forms a difference in optical path equal to  $n\lambda$ ) for constructive interference. As the angle between the incident beam and the lattice planes, and the angle between diffracted beam and the lattice planes, are equal to the Bragg angle  $\theta_B$ . Thus, the diffraction angle under which a reflection is observed is two times the Bragg angle, i.e.  $2\theta_B$ .

For a given crystal structure, there is a number of possible lattice plane sets (*d*-spacings). However, these *d*-spacings are not all independent, but result from a maximum of six lattice parameters ( $a, b, c, \alpha, \beta, \gamma$ ) describing the size and shape of the unit cell. As a convenience it was decided to select the smallest repeating unit of the crystal lattice. The number of independent unit cell parameters depends on the crystal symmetry. For the lowest symmetry (triclinic), there are six independent parameters as shown above. For the highest symmetry (cubic), there is only a single parameter  $a$ .

As in the unit cell usually there is more than a single atom, then sub-lattices, based on different atoms, can be created, which can be imagined to diffract independently. However, all sub-lattices have the same periodicity, and thus the same *d*-spacings. While the incident beam is a coherent wave, the diffracted (sub-)waves will have phase shifts relative to each other, depending on the positions of the atoms in the unit cell. Each atom type has a different scattering power, hence the diffracted (sub-)waves may also have different amplitudes. Due to these phase shifts and different amplitudes, various degrees of positive and negative interference between the diffracted sub-waves will result in an intensity modulation for the resulting total of the diffracted beam. As a result, the information about the unit cell's content is coded in the relative intensities of the diffraction peaks for a given crystalline phase.

### Lattice plane

For understanding the "*d*-spacing", we can take a look at the NaCl example as it is a simple cubic system. In Figure A.3a four red lines passing through pairs of two points (O and A, B, C, and D). This represents the planes perpendicular to the page. Any lattice point can be chosen instead of O, because the same structural unit is infinitely repeated in the crystal. Thus, as there is a plane passing through O and B, the plane with the same direction will be present in a specified interval (in this case the next plane could be EC), Figure A.3b. In the crystal, a number of planes in the same direction are infinitely repeated at a regular spacing. These planes are called "lattice

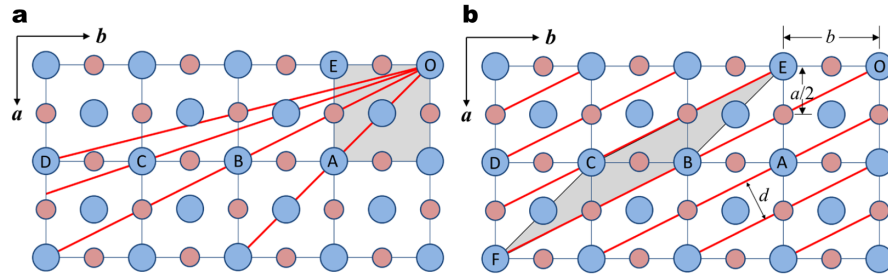


Figure A.3 – Lattice planes. (a) Lattice planes in different directions and (b) repeated plane in the same direction. The pictures are reproduced from [165].

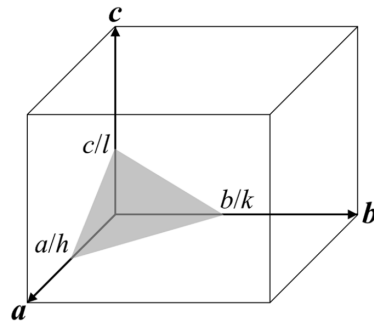


Figure A.4 – Lattice plane in 3D structure. The picture is reproduced from [165].

planes", the distance between a lattice plane and an adjacent plane is called the "*d*-spacing".

All lattice planes in the same direction pass through the points positioned at regular intervals. In case of Figure A.3b, it is  $a/2$  in *a*-axis and  $b$  in the *b*-axis. For other cases in Figure A.3a it would be  $a$ ,  $a/3$  and  $a/4$  in the *a*-axis. In general the plane in 3D is described as  $\frac{a}{A} + \frac{b}{B} + \frac{c}{C} = \text{constant}$ . Taking constant for 1, we can rewrite this equation as  $BCa + ACb + ABc = ABC$ . Introducing a new notation, it becomes:  $ha + kb + lc = \text{constant}$ , then for the closest to the origin plane constant = 1 and as in the Figure A.4 it intersects with the axes at three points,  $a/h$ ,  $b/k$ ,  $c/l$ . The set of integers  $hkl$  allows to define a specific plane. Therefore,  $(hkl)$  are called the plane or **Miller indices**. Thus, our planes from Figure A.3 would be (110), (210), (310) and (410). As all these planes are parallel to the *c*-axis there is no intersection with the latter, and  $l = 0$ . For the planes in other quadrants, negative values of the indices are used, the notation is  $\bar{l} = -l$ .

With these basic knowledge we can understand what is going on in an XRD experiment.

### A.1.1 X-ray data

Since X-ray diffractions occurs in those directions where subsequent reflections by the lattice plains interfere constructively, the lattice planes have to be perfectly oriented with respect to the X-ray source. When using a single crystal, this can be satisfied by rotating the crystal, which renders the crystal perfectly oriented for every possible diffraction during a short instant. When using a powder sample, the fine crystalline particles are oriented randomly. Therefore there is no need to rotate the crystal, as the Bragg's law will always hold for some lattice planes

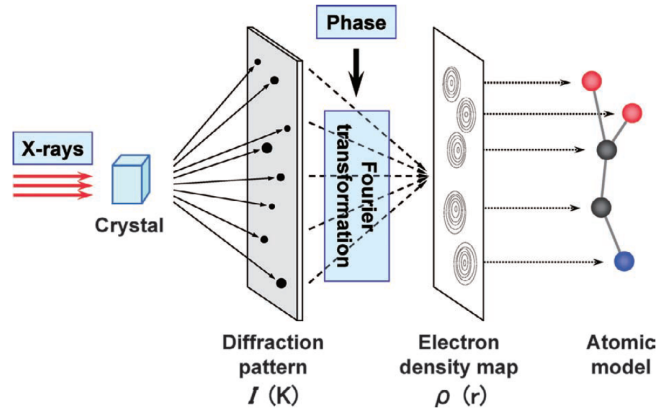


Figure A.5 – A scheme of X-ray measurements and analysis. The picture is reproduced from [167].

in a statistical sense.

### Electron density maps

During XRD experiment, the medium which interacts with X-rays (the wave vector  $\mathbf{k}_0$ , in crystallography  $\lambda = \frac{1}{|\mathbf{k}_0|}$  is the convention) is the electron density,  $\rho(\mathbf{r})$ , periodically distributed in a crystal with periodicity vectors  $\mathbf{a}$ ,  $\mathbf{b}$  and  $\mathbf{c}$ . Maxima of  $\rho(\mathbf{r})$  in a single unit cell correspond to atoms located in positions determined by the vectors  $\mathbf{r} = (x, y, z)$ .

Reciprocal space is used to describe diffraction phenomena and relates to sets of scattering planes with Miller index  $hkl$  in real space. Each diffraction reflection in reciprocal space is characterized by a scattering vector  $\mathbf{K}(hkl) = h\mathbf{a}^* + k\mathbf{b}^* + l\mathbf{c}^*$ , where  $\mathbf{a}^*$ ,  $\mathbf{b}^*$  and  $\mathbf{c}^*$  are the lattice parameters in the reciprocal space ( $\mathbf{a}^* \perp (\mathbf{bc})$ ;  $\mathbf{b}^* \perp (\mathbf{ac})$ ;  $\mathbf{c}^* \perp (\mathbf{ab})$ ).

The electron density as a function of the  $\mathbf{r}$  (Figure A.5) can be calculated by the Fourier transformation of the structure factors  $F_{hkl}$ :  $\rho(\mathbf{r}) = \int_V F_{hkl} e^{-2\pi i(\mathbf{K} \cdot \mathbf{r})} d\mathbf{v}_{\mathbf{r}}$ , where  $V$  is the unit cell volume and the structure factor  $F_{hkl}$  is a function describing the amplitude and phase of a wave diffracted from the  $(hkl)$  crystal lattice planes.

The structure factor can be expressed as  $F_{hkl} = |F_{hkl}| e^{i\phi_{hkl}}$ ,  $F_{hkl}$  is the structure amplitude and  $\phi_{hkl}$  is the phase of the diffraction wave with  $\mathbf{K}(hkl)$  vector.

Directly from the diffraction measurements we obtain the intensities of the diffraction reflection,  $I_{hkl}$ , for each  $\mathbf{K}(hkl)$ . This diffraction intensity is proportional to the square of the amplitude,  $I_{hkl} = |F_{hkl}|^2$ .

Based on this, several different electron density maps ( $e/\text{\AA}^3$ ) can be built.

$F_o$  map - an electron density calculated using observed structure amplitudes combined with phases from the atomic model. This map shows the observed electron density.

$F_c$  map - an electron density calculated from structure amplitudes and phases from the atomic model. This map shows the electron density according to the model only.



The difference between them,  $F_o - F_c$  map, has close-to-zero values for parts of the model that are consistent with the experimental density, large positive values at places where the model should have an atom, but does not, and large negative values at places where the model has an atom, which should not be there. In case of weaker positive or negative values in the  $F_o - F_c$  map could point to wrongly assigned atom types.

The structure solution algorithm reveals the position of the atoms which is used to create a model of the structure. The structure factor based on this model can thus be compared to the measured one and the difference between both can be minimized by least-squares refinements.

Better phases can be calculated from the atomic positions, which allow re-determining of the electron density function with a higher precision. From the new electron density map, more accurate atomic positions can be derived, which lead to even better phase angles, and so forth. In every such cycle, adjustments to the atomic model are made: atom types are changed, missing atoms are introduced, etc. When all atoms have been identified, the process is called **structure refinement** by least-squares.

Three main steps of structural refinement: Examination of the  $F_o - F_c$  map helps to introduce new atoms and remove unnecessary ones. Once all non-hydrogen atoms are found, the atoms can be refined anisotropically. Once the model is anisotropic, the hydrogen atom positions can be determined or calculated.

### Atomic displacement parameters

As the atoms in crystals oscillate around their equilibrium positions, the electron density is smeared. In order to take these effects (dynamic and static disorder) into account, the atomic displacement parameters (ADP) should be introduced. An isotropic model assumes equal (spherical) oscillation around the equilibrium position in all directions. It is usually used to describe the thermal vibrations of atoms. The anisotropic model requires six parameters per atom to define the general ellipsoid that describes the atomic motion.

### A.1.2 Reliability index

How to judge quality of the model? It could be done with the least-squares fit between the calculated and observed intensities for each measured point in the diffraction profile [168].

For that the "conventional"  $R$ -factor could be used [169]  $R = \frac{\sum |F_o - F_c|}{\sum |F_o|}$ . It is calculated during each cycle of least-squares structure refinement to assess progress and measure of model quality. The minimal  $R$  shows the discrepancy between the experimental,  $F_o$ , and the best calculated,  $F_c$ , structure factors (Fourier amplitudes) based on the complete set of diffracted intensities. Reflections with  $I < 2\sigma(I)$  were excluded from the least square refinement. According to the common practice,  $R_I$  factor is calculated for the reliable reflections with  $I > 2\sigma(I)$ , while  $R(all)$  factor is calculated for all reflections including weak ones with  $I < 2\sigma(I)$ .

Figure A.6 – A modulated chain and its diffraction. The picture is reproduced from [166].



Another calculated parameter is a profile  $R$ -factor, closely related to refinements against  $F^2$ :  $R_p = \sqrt{\frac{\sum (F_o - F_c)^2}{\sum F_o^2}}$ . A small  $R_p$  is simply a statement about quantity and means that the average number of counts in a profile is large—it bears no relationship to the quality of a profile fit [170].

More often used value for least-squares refinement is weighted  $R$ -factor, since the functions minimized are weighted according to estimates of the precision of the measured quantity [169]. The general term for a weighted residual is  $wR = \sqrt{\frac{\sum |w(F_o - F_c)|}{\sum |wF_o^2|}}$ , where  $w$  is a measure of the contribution of structure factor  $F$ .  $wR$  gives both the quality of the data and the quality of the fit to the data [170]. The minimization of  $wR$  is the result of the Rietveld refinement with refined parameters defined for each Fourier amplitude,  $F_c$ , depending on atomic coordinates.

Goodness of fit ( $GOF$ ) is supposed to be  $> 1.0$ :  $GOF = \sqrt{\frac{\sum |w(F_o - F_c)|}{(N_R - N_P)}}$ , where  $N_R$  is a number of independent reflections and  $N_P$  is a number of refined parameters.

### A.1.3 Peak width

In theory, the Bragg diffraction should yield infinitely sharp reflections. As a single wavelength diffracted at lattice planes with an exactly defined  $d$ -spacing would fulfill Bragg's law only for an exactly defined angle. However, all imperfections of the experiment and sample will contribute to the relaxation of Bragg's law, resulting in noticeable broadening of the observed peak profiles. Since the sample-related contribution to the peak profile contains information about the sample imperfections, like crystallite size, strain, stacking faults and other defects, a careful peak profile analysis should yield information about the nature and amount of such defects in the sample. Generally speaking, two important aspects of the peak profile are the profile shape and the peak width. The width of a peak profile can be described by different parameters, depending on the peak shape function used. Most commonly, the full width at half maximum (FWHM) is used to express peak width. The ambiguity of the baseline translates into the question where exactly half the height is, so that different baseline choices will alter width parameters for the same peak.

### A.1.4 Commensurated and incommensurated modulations

Mathematical models for periodic crystals show sharp Bragg peaks only. In the early 1960s more materials were found that could be described as a periodic lattice structure with some disturbance affecting this lattice periodicity [171]. This was observed by the occurrence of additional spots as a consequence of periodic variation [166]. In Figure A.6 the top line consists of an unmodulated chain, which results in single reflection. When we have a modulated chain the diffraction satellites appear next to the main reflection creating a **superstructure**.

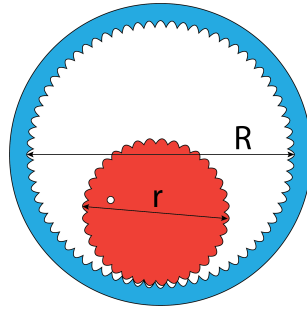


Figure A.7 – Sketch of the spirograph. By placing the pen in the inner gear's hole the pattern will be periodic after certain amount of loops.

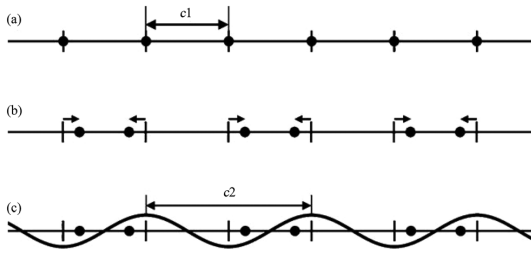


Figure A.8 – 1D modulated system. (a) Before modulation: all atoms lie equally spaced along a straight line. (b) After modulation: half the atoms shift to the left, and half to the right. (c) Modulation in (b) represented as a simple cosine function. The picture is reproduced from [172].

If the satellites are located at simple fractions of the reciprocal lattice vectors, the resulting symmetry is conserved within multiple unit cells. Such a modulation is called a **commensurate** superstructure. If the positions do not represent a simple fraction, the structure has lost all translational symmetry in a particular direction. This is called an **incommensurate** structure. A visualization for the commensurated structures is spirograph, Figure A.7. In this simple device the ratio of  $R/r$  is integer, therefore the internal gear will again arrive at the same point after a number of rotations. For an incommensurate structure, the ratio of the lattice period to the modulation period is irrational [100].

Aperiodic crystals are long-range ordered structures without 3D lattice translations and encompass incommensurately modulated phases, incommensurate composites and quasicrystals [100]. In the theory of superspace crystallography, by adding a supplementary dimension to the usual 3D space, allows for a deeper understanding of the atomic structure of aperiodic crystals. For instance, in case of a simple modulation in one direction: the periodicity is broken in  $c$ -direction (helical magnetism in the system) then diffraction peaks are found at positions  $\mathbf{H} = h\mathbf{a}^* + k\mathbf{b}^* + l\mathbf{c}^* + m\mathbf{q}$ , where  $\mathbf{q} = \alpha\mathbf{c}^*$ . Let  $\mathbf{n}$  be a lattice vector, then a displacement at a site  $\mathbf{n}$  is given by  $A\cos(2\pi\mathbf{q} \cdot \mathbf{n})$ , the periodicity is along  $\mathbf{q}$  with a period  $1/\alpha$ . However to be periodic,  $\alpha$  should be rational. In case  $\alpha$  is irrational, the crystal is aperiodic.

A great example of this has been shown in [172] in a 1D single atom chain: The unit cell is  $c_1$  as in Figure A.8a. In Figure A.8b, the arrows indicate the modulations of atomic positions, the hatch marks indicate the average atomic positions, and the small solid circles indicate the atom positions after modulation (real positions). In the alternative view, the arrows of Figure A.8b were replaced by simple sinusoidal wave with wavelength  $c_2$ , Figure A.8c. If the ratio  $\gamma = c_1/c_2$  is rational, the structure is commensurately modulated. If the ratio  $\gamma$  is irrational and the structure is incommensurately modulated. Such a modulated 1D atom system can be treated as a section through a  $(1 + 1)$ D superspace. In the 3D-case, if there is no basis  $\mathbf{a}_1^*, \mathbf{a}_2^*, \mathbf{a}_3^*$

## Appendix A. Appendix: X-ray diffraction

---

which allows integer indexing then modulation coefficients are irrational numbers. The phases were called incommensurate modulated phases and the idea was that these satellites were the consequence of a periodic modulation of the atomic positions, having a period not fitting the periodicity of the underlying lattice [171].

Modulated phases may also occur with more than one modulation wave-vector. In general the Fourier coefficients may be written as:  $F(\mathbf{H}) = \sum_n e^{2\pi i(\mathbf{H} \cdot (\mathbf{n} + \mathbf{A} \cos(2\pi \mathbf{q} \cdot \mathbf{n}))}$ . Therefore, in the case of the (3 + 3)-dimensional incommensurately modulated structures, the calculated structure factor is defined [173]:

$$F_c(\mathbf{H}) = \frac{1}{\Omega} \sum_{\mu} \int_{\Omega_{\mu}} f_{\mu}(\mathbf{H}, \mathbf{r}_I) e^{2\pi i \mathbf{H} \cdot \mathbf{r}_{\mu}(\mathbf{r}_I) + \mathbf{H} \cdot \mathbf{r}_I} d\mathbf{r}_I$$

where:  $\Omega = \sum_{\mu} \Omega_{\mu}$  is the volume of the projections of  $\mu$  atomic surfaces on the so called "internal space", corresponding to  $\mu$  atoms in the unit cell; when the structure is unmodulated the position of the  $\mu^{th}$  atom in the unit cell is  $\mathbf{r}_{\mu}(\mathbf{r}_I) = \mathbf{n} + \mathbf{r}_I$ , where  $r_I$  is a position of the corresponding atomic surface in the internal space. With the modulation it becomes  $\mathbf{r}_{\mu}(\mathbf{r}_I) = \mathbf{n} + \mathbf{r}_I + \mathbf{u}_I(\mathbf{q} \cdot \mathbf{n})$ ,  $\mathbf{u}_I$  are the modulation functions;  $f_{\mu}$  is an atomic scattering factor;  $f_{\mu}(\mathbf{H}, \mathbf{r}_I)$  defines occupation modulation (which is not applicable in our case).

Here, the wave-vector is  $\mathbf{H} = h\mathbf{a}^* + b^* + lc^* + m\mathbf{q}_1 + p\mathbf{q}_2 + t\mathbf{q}_3$ , where the reciprocal lattice vectors  $\mathbf{a}^*$ ,  $\mathbf{b}^*$  and  $\mathbf{c}^*$  correspond to the unit cell parameters  $a$ ,  $b$ ,  $c$  and  $\mathbf{q}_1$ ,  $\mathbf{q}_2$  and  $\mathbf{q}_3$  are the modulation vectors in the reciprocal space;  $\mathbf{H}_I$  is defined by the  $m$ ,  $p$ ,  $t$  indices. In the above expression of  $F_c(\mathbf{H})$  define a position for each of  $\mu$  atom as a function of both  $\mathbf{r}$  and  $\mathbf{r}_I$ . Details for derivation of the above expression can be found, for instance, in references [173] and [166], as well as the consistent presentation of the theory of diffraction in an aperiodic (quasiperiodic) systems with more than a hundred examples. Each reflection has been characterized not only by its experimental intensity but also with indices,  $hklmpt$ , according to the wave-vector  $\mathbf{H}$ .

### A.2 XRD measurements details

All synchrotron measurements were done at the European Synchrotron Radiation Facility, Grenoble, France. Crys-AlisPro software was used for the data processing of the experimental data for single crystal. Structural calculations were made with the JANA2006 software [174]. For PXRD experiments crystals were ground just before the experiment in a mortar and loaded into a quartz capillary. The XRD data for the Chapter 3 have been collected at the High Pressure Beamline (ID27). For all other Chapters the data were recorded at the Swiss–Norwegian Beam Lines (BM01A) with the PILATUS@SNBL diffractometer [175]. The PXRD raw data were preprocessed with BUBBLE software [175]. Then the reciprocal space maps were reconstructed with the CrysAlis software.

For the thermal cycling Chapter 2:

The synchrotron radiation PXRD data were collected as a function of temperature using a

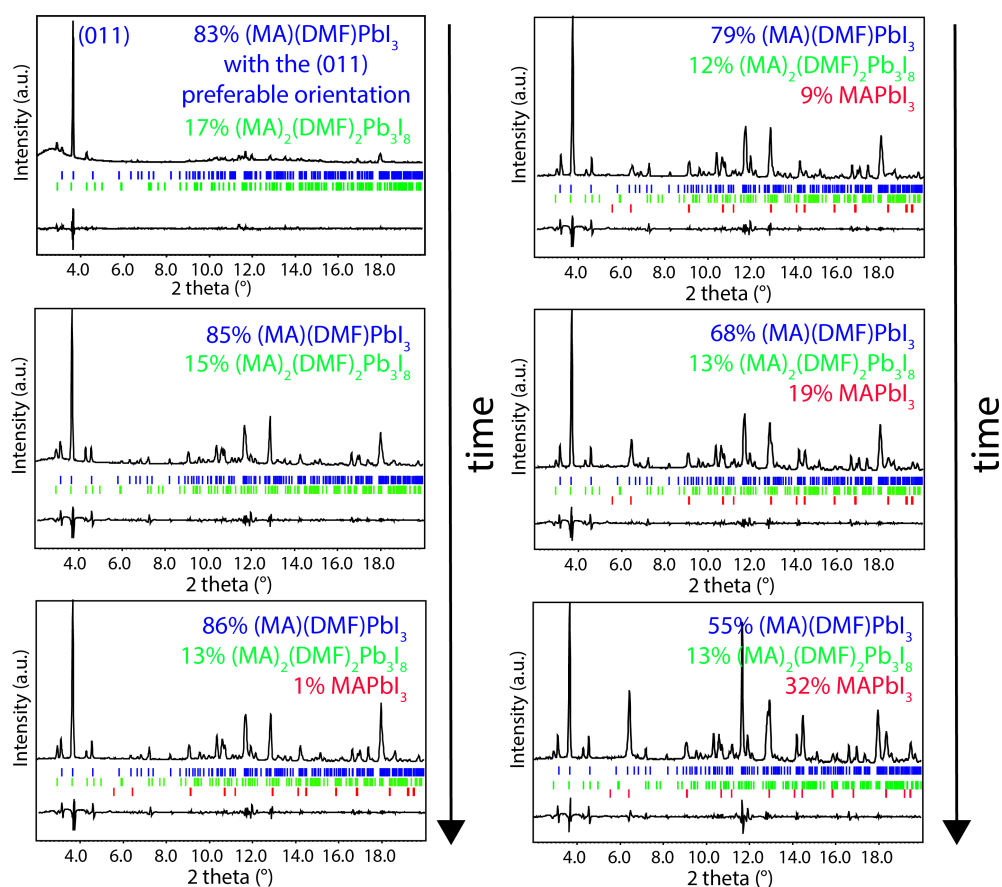


Figure A.9 – Analysis of the experimental XRD profiles.

wavelength  $\lambda = 0.7129 \text{ \AA}$  and 5 s of exposure time. The thermal sweeps across the transitions temperature took place at  $0.7 \text{ K min}^{-1}$  in both directions using an Oxford Cryostream 700+ nitrogen blower.

The formation of wire-shaped  $\text{MAPbI}_3$  in Chapter 1 were recorded at the following conditions: PXRD experiments were carried out under Oxford Cryostream 700+ nitrogen blower with  $\lambda = 0.71446 \text{ \AA}$  for an exposure time of 0.9977 s. After 24 minutes the intermediate phases were stabilized at room temperature and the sample was heated to 337 K to evaporate the trapped solvent. It has been documented that the formation of the intermediate adduct phases depends on the experimental conditions [71, 76, 95].

In Chapter 3 the X-ray wavelength was set to  $0.3738 \text{ \AA}$ . The minimal linear size of the crystals was about 10 nm. Diffraction data were recorded with a Mar165 CCD detector and the pressure was measured using the ruby fluorescence technique. After decompression, additional measurements were conducted on the Necontaining crystal to determine its structure under ambient conditions.

In Chapter 4, the data from the single crystal  $\text{EDPbI}_4$  were recorded at room temperature with

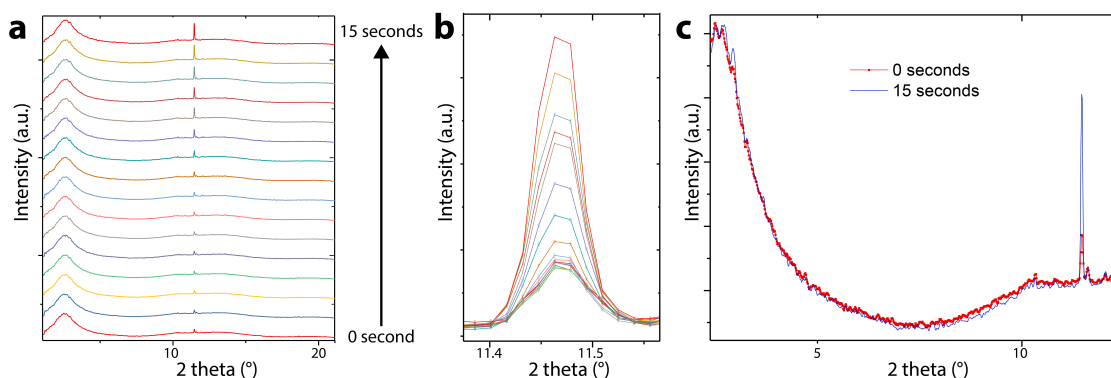


Figure A.10 – Nucleation and early stage of crystal growth of MAPbI<sub>3</sub> solvatomorph phases from DMF solution tracked via synchrotron XRD. (a) The growth of the first observable peak on the amorphous background for 15 seconds. (b) Evolution of the peak at  $2\theta = 11.48^\circ$ . (c) Nucleation and early stage crystallization of (MA)(DMF)PbI<sub>3</sub>.

wavelength  $\lambda = 0.7129\text{\AA}$ . For additional PXRD measurements for the pristine EDPbI<sub>4</sub> crystals an Empyrean system, equipped with a PIXcel<sup>-1D</sup> detector (Cu K $\alpha$ -radiation, Bragg–Brentano beam optics) was used at room temperature.

### A.3 Refinements details

#### Crystallization process

The first XRD pattern is recorded 50 seconds after the solution was pipetted on the quartz capillary. At the moment of recording the time is set to zero, frames are recorded each second. At this stage two broad peaks centered around  $2\theta$  3° and 12° can be observed, which presumably corresponds to an amorphous “gel” formed during the evaporation induced supersaturation. Interestingly, on the top of the amorphous background sharper peaks appear at  $2\theta$  2.94° and 11.48° Figure A.10.

Although, the origin of these reflections is unknown today, this first ordered structure can be considered as the nuclei of the intermediate phases of at a later stage of crystallization. According to the identification, these peaks presumably correspond to nucleation of (MA)(DMF)PbI<sub>3</sub>.

Initially, the size of this nuclei at one direction is 50 nm and during 15 seconds it grows to 75 nm. The FWHM is reduced and the peak intensity has quadrupled. At later stages, this peak disappears and the peaks of the two identified intermediate phases appear (Chapter 1.3.1).

#### Thermal cycling

For thermal cycling around the low-temperature (160 K) phase transition from Chapter 2.2.1 the profile recorded during the heating stage of the fourth thermal cycle is given in Figure A.11 ( $Rp = 0.0176$ ,  $wRp = 0.0218$ ,  $GOF = 1.68$ ) and the reliability factors in Table A.2.

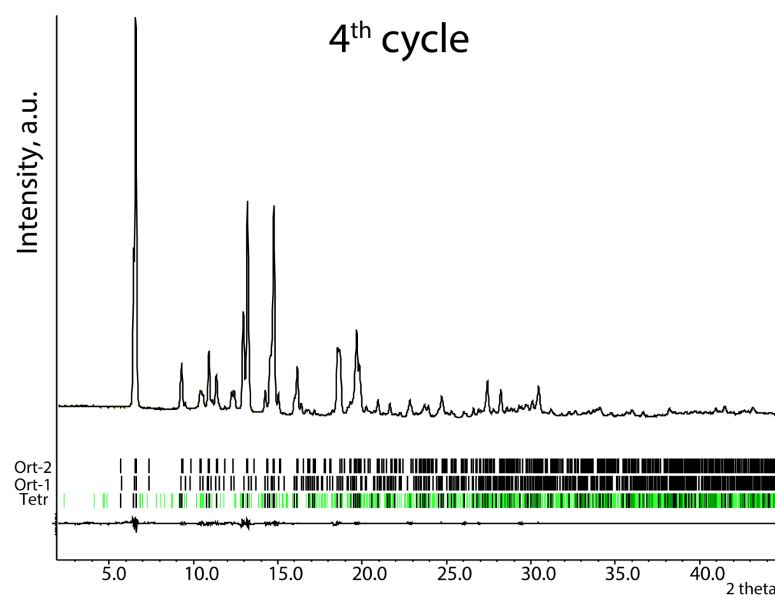


Figure A.11 – PXRD profile for the three-phase state of MAPbI<sub>3</sub> at 141.6 K after thermal cycling around low-temperature phase transition. The green ticks indicate the satellite reflections for the Tetr phase.

	Tetr	Ort-1	Ort-2
Space group	<i>I</i> 422(00g)000 [No. 97.1.21.1]	<i>Pnma</i>	<i>Pnma</i>
<i>a</i> , Å	8.7806(7)	8.8657(17)	8.795(5)
<i>b</i> , Å	= <i>a</i>	12.618(2)	12.474(4)
<i>c</i> , Å	12.6717(15)	8.6028(18)	8.765(4)
<b>q</b>	0.7213(2) <b>c</b> *		
<i>R</i> 1	0.0159	0.0233	0.0217
<i>wR</i> ( <i>all</i> )	0.0178	0.0283	0.0248

Table A.2 – Crystallographic data and reliability factors for low-temperature thermal cycling.

The three phases: tetragonal modulated (Tetr), orthorhombic (Ort-1) and boundary orthorhombic (Ort-2), were included into the Rietveld refinement (Table A.2). Coefficients of the phase contribution: Tetr - 49.7%; Ort-1 - 25.7%; Ort-2 - 24.6%.

For the high-temperature (330 K) phase transition from Chapter 2.3.1 the profile recorded during the heating stage of the first thermal cycle is in Figure A.12 (*Rp* = 2.44%, *wRp* = 3.88%) and the reliability factors are the following: *R*(*all*) = 6.32%; *wR*(*all*) = 8.50%; *R*1(*main*) = 4.12%; *wR*(*main*) = 6.80%. The profile is fitted with the tetragonal modulated structure solved in the (3 + 3)D superspace group *P*4/*mmm*( $\alpha$ 1, $\alpha$ 1,0)0s0s(- $\alpha$ 1, $\alpha$ 1,0)0s00(0,0, $\gamma$ 2)00ss [No. 123.3.174.104]. The unit cell parameters are: *a* = *b* = 6.2925(5), *c* = 6.3295(9) Å and the modulation vectors are: **q**<sub>1</sub> = 0.5**a**\* + 0.5**b**; **q**<sub>2</sub> = -0.5**a**\* + 0.5**b**\*; **q**<sub>3</sub> = 0.4902(8)**c**\*.

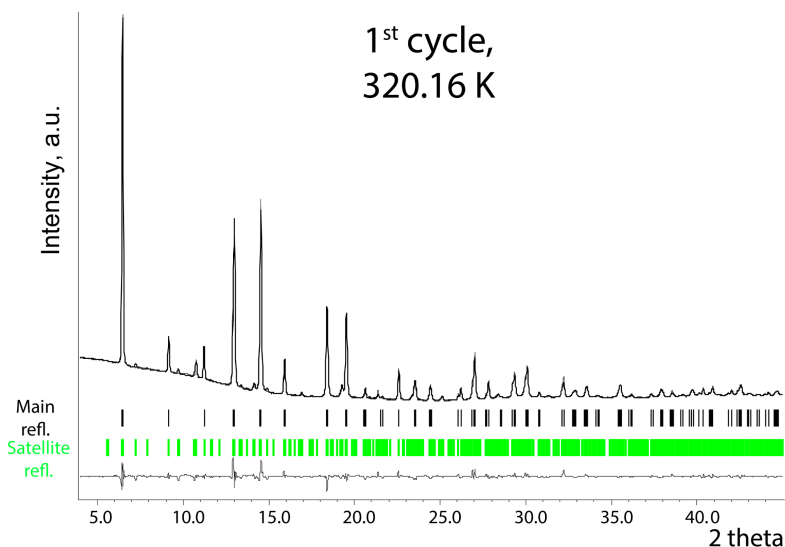


Figure A.12 – PXRD profile for the MAPbI<sub>3</sub> at 320.16 K at the first thermal cycle around high-temperature phase transition.

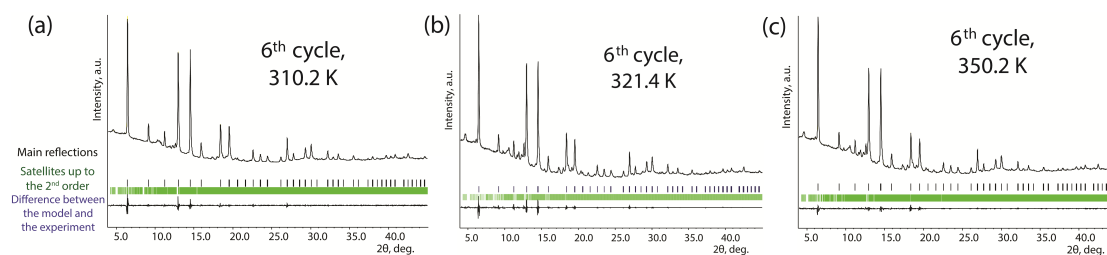


Figure A.13 – PXRD profiles for the incommensurately modulated structure at (a) 310.2 K, (b) 321.4 K and (c) 350.2 K recorded during the heating stage of the sixth thermal cycle around the 330 K transition.

The fit of the profiles during the sixth thermal cycle for three temperatures is in Figure A.13 and Table A.3: The profiles are fitted using the (3 + 3)D superspace group  $P4/mmm(\alpha 1, \alpha 1, 0)0s0s(-\alpha 1, \alpha 1, 0)0s00(0, 0, \gamma 2)00ss$  [No. 123.3.174.104] with the tetragonal unit cell parameters from Table A.3.



### A.3. Refinements details

Tetr phase	310.2 K	321.4 K	350.2 K
<i>a</i> , Å	6.303(2)	6.309(1)	6.3130(14)
<i>c</i> , Å	6.311(4)	6.3171(17)	6.322(4)
<b>q</b> <sub>1</sub>	0.4852(8) <b>a</b> *+0.4852(8) <b>b</b> *	0.4871(8) <b>a</b> *+0.4871(8) <b>b</b> *	0.4861(8) <b>a</b> *+0.4861(8) <b>b</b> *
<b>q</b> <sub>2</sub>	-0.4852(8) <b>a</b> *+0.4845(8) <b>b</b> *	-0.4871(8) <b>a</b> *+0.4871(8) <b>b</b> *	-0.4861(8) <b>a</b> *+0.4861(8) <b>b</b> *
<b>q</b> <sub>2</sub>	0.4742(8) <b>c</b> *	0.4686(8) <b>c</b> *	0.4676(8) <b>c</b> *
<i>R(all)</i>	9.98%	11.43%	11.51%
<i>wR(all)</i>	8.93%	11.08%	9.77%
<i>R1(main)</i>	4.73%	4.66%	5.24%
<i>wR(main)</i>	7.00%	6.93%	7.92%
<i>Rp</i>	1.56%	1.67%	1.33%
<i>wRp</i>	2.41%	2.30%	1.84%

Table A.3 – Crystallographic data for a Tetr phase and reliability factors at 310.2, 321.4 and 350.2 K during the sixth thermal cycle.

#### EDPbI<sub>4</sub>

In Chapter 4 the single-crystal refinement is presented. To confirm the structure and composition of the studied crystalline phase additional PXRD were made. The profile from PXRD experiment has been successfully fitted by the Rietveld refinement of the model obtained from the single crystal structure determination (Figure A.14). The whole set of atomic parameters has been refined again for the pristine crystal. No significant difference was found within two standard deviations.

XRD profile of a flake-shaped phase (Figure A.14a) can be fitted by le-Bail decomposition with the monoclinic unit cell parameters  $a = 21.82425$ ,  $b = 15.29009$ ,  $c = 34.49222$  Å and  $\beta = 96.3269^\circ$ . XRD profile of the cube-shaped phase (Figure A.14b) has been fitted by the Rietveld refinement of the model obtained from the single crystal structure determination of EDPbI<sub>4</sub> compound.

The structure has been solved using the Superflip program [176].

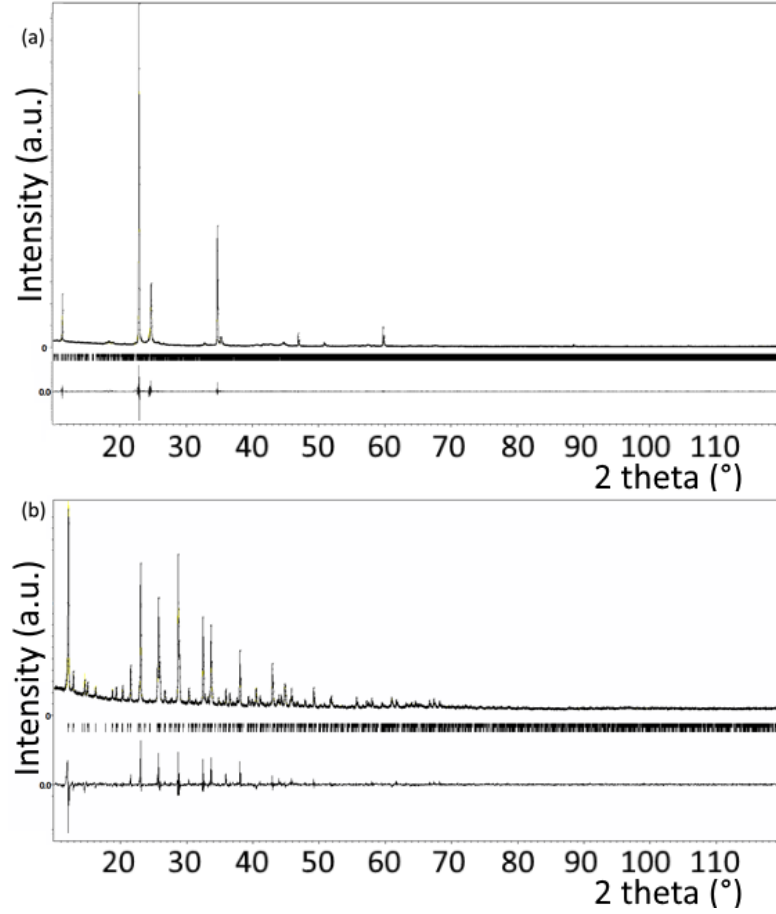


Figure A.14 – PXRD profiles of two simultaneously obtained phases of  $\text{EDPbI}_x$ : (a) a flake-shaped phase, (b) a cube-shaped phase.

#### A.4 Crystallographic tables

	$\text{Ne}_x\text{MAPbI}_3$	$\text{Ne}_x\text{MAPbI}_3$	$\text{Ne}_x\text{MAPbI}_3$	$\text{Ne}_{0.97}\text{MAPbI}_3$
P (GPa)	0.69 → 1.5 → 2.69	4.56 → 7.4	16.43 → 20.27	released
Crys. system	Trigonal	Orthorhombic	Tetragonal	Tetragonal
Sp. group	$R\bar{3}$	$Im2m$	$I4/mmm$	$I422$
$a$ (Å)	17.3128(9) → 17.0325(9) → 16.7757(9)	11.435(3) → → 11.196(3)	10.700(5) → → 10.538(5)	8.876(1)
$b$ (Å)	$=a$	11.437(3) → → 11.197(3)	$=a$	$=a$
$c$ (Å)	10.6019(5) → 10.4338(5) → 10.2267(5)	11.442(3) → → 11.201(3)	10.620(10) → → 10.3793(11)	12.672(1)
$x$ in $\text{Ne}_x$	0.42(1) → 0.60(1) → 0.91(1)	1.10(1) → 1.41(1)	2.17(1) → 2.50(1)	0.97

Table A.4 – Crystallographic data and composition for Ne-MAPbI<sub>3</sub> in the 0–20 GPa pressure range.

#### A.4. Crystallographic tables

	Ar <sub>x</sub> MAPbI <sub>3</sub>	Ar <sub>x</sub> MAPbI <sub>3</sub>
P (GPa)	0.18 → 0.49 → 0.98	1.34 → 2.10 → 2.39
Crys. system	Tetragonal	Orthorhombic
Sp. group	<i>P4<sub>2</sub>bc</i>	<i>Immm</i>
<i>a</i> (Å)	8.850(5) → 8.7468(15) → 8.7222(15)	12.1294(12) → 12.0192(10) → 11.900(11)
<i>b</i> (Å)	= <i>a</i>	12.1415(12) → 12.0195(10) → 11.990(1)
<i>c</i> (Å)	12.520(5) → 12.398(10) → 11.9979(15)	12.1734(15) → 12.0213(10) → 11.920(1)
<i>x</i> in Ar <sub>x</sub>	0.76(1) → 1.00(1) → 1.34(1)	1.40(1) → 1.78(1) → 1.75(1)

Table A.5 – Crystallographic data and composition for Ar-MAPbI<sub>3</sub> in the 0–2.4 GPa pressure range.

## Appendix A. Appendix: X-ray diffraction

Crystal	Pristine	Thermally treated
Chemical formula	$\text{I}_4\text{Pb}\cdot\text{C}_2\text{H}_{10}\text{N}_2\cdot\text{O}_{0.043(4)}$	$\text{I}_4\text{Pb}\cdot\text{C}_2\text{H}_{10}\text{N}_2\cdot\text{O}_{0.043(5)}$
Space group	$\text{R}\bar{3}$ (No. 148)	$\text{R}\bar{3}$ (No. 148)
Pb1 occupancy	1.0	1.0
Wyckoff symbol	3b: $00\frac{1}{2}$	3b: $00\frac{1}{2}$
x, y, z	0, 0, 0.5	0, 0, 0.5
$U_{eq}$	0.0573(11)	0.112(2)
Harmonic ADP		
U11	0.0590(14)	0.120(2)
U22	= U11	= U11
U33	0.0539(15)	0.097(4)
U12	= $\frac{1}{2}$ U11	= $\frac{1}{2}$ U11
Pb2 occupancy	1.0	1.0
Wyckoff symbol	3a: 000	3a: 000
x, y, z	0, 0, 0	0, 0, 0
$U_{eq}$	0.0457(7)	0.0876(17)
Harmonic ADP		
U11	0.0450(9)	0.090(2)
U22	= U11	= U11
U33	0.0472(12)	0.083(3)
U12	= $\frac{1}{2}$ U11	= $\frac{1}{2}$ U11
Pb3 occupancy	1.0	1.0
Wyckoff symbol	6c: 00z	6c: 00z
x, y, z	0, 0, 0.37520(4)	0, 0, 0.37529(9)
$U_{eq}$	0.0539(7)	0.0876(17)
Harmonic ADP		
U11	0.0573(9)	0.121(2)
U22	= U11	= U11
U33	0.0471(9)	0.089(2)
U12	= $\frac{1}{2}$ U11	= $\frac{1}{2}$ U11
Pb4 occupancy	1.0	1.0
Wyckoff symbol	6c: 00z	6c: 00z
x, y, z	0, 0, 0.12521(4)	0, 0, 0.12547(7)
$U_{eq}$	0.0522(7)	0.0869(13)
Harmonic ADP		
U11	0.0526(8)	0.0926(18)
U22	= U11	= U11
U33	0.0514(10)	0.0755(18)
U12	= $\frac{1}{2}$ U11	= $\frac{1}{2}$ U11
I1 occupancy	1.0	1.0
Wyckoff symbol	18f: x, y, z	18f: x, y, z
x, y, z	0.31267(15), 0.48181(13), 0.84578(5)	0.3167(3), 0.4846(3), 0.84583(8)
$U_{eq}$	0.0646(11)	0.110(2)
Harmonic ADP		
U11	0.0759(16)	0.116(3)
U22	0.0520(13)	0.106(3)
U33	0.0694(12)	0.110(2)
108 U12	0.0346(12)	0.058(2)
U13	-0.0037(10)	-0.014(2)
U23	0.0057(9)	-0.0045(18)

# A.4. Crystallographic tables

I2 occupancy	1.0	1.0
Wyckoff symbol	18f: x, y, z	18f: x, y, z
x, y, z	0.16482(18), 0.18431(14), 0.32086(6)	0.1654(4), 0.1875(4), 0.3214(9)
$U_{eq}$	0.0687(12)	0.117(2)
Harmonic ADP		
U11	0.0657(15)	0.131(3)
U22	0.0536(14)	0.117(3)
U33	0.0870(15)	0.105(2)
U12	0.0299(12)	0.064(2)
U13	0.0051(11)	0.011(2)
U23	0.0084(11)	0.013(2)
I3 occupancy	1.0	1.02(3)
Wyckoff symbol	18f: x, y, z	8g: x, y, z
x, y, z	0.18668(13), 0.02324(15), 0.44098(5)	0.1882(2), 0.0269(2), 0.44121(8)
$U_{eq}$	0.0678(11)	0.107(2)
Harmonic ADP		
U11	0.0505(13)	0.093(2)
U22	0.0907(15)	0.123(2)
U33	0.0641(11)	0.107(2)
U12	0.0367(12)	0.055(2)
U13	-0.0003(9)	-0.003(2)
U23	0.0019(9)	0.0039(19)
I4 occupancy	1.0	1.0
Wyckoff symbol	18f: x, y, z	18f: x, y, z
x, y, z	0.16387(14), -0.02183(16), 0.05836(5)	0.1671(3), -0.0168(4), 0.05834(9)
$U_{eq}$	0.0720(13)	0.128(3)
Harmonic ADP		
U11	0.0691(14)	0.138(3)
U22	0.1113(19)	0.174(4)
U33	0.0633(12)	0.099(2)
U12	0.0659(13)	0.098(4)
U13	0.0037(9)	-0.002(2)
U23	0.0102(11)	0.006(3)
C1 occupancy	1.0	(a) 0.5; (b) 0.5
Wyckoff symbol	18f: x, y, z	18f: x, y, z
x, y, z	0.6280(7), 0.5717(9), 0.5927(3)	(a) 0.622(3), 0.570(3), 0.5938(8); (b) 0.629(5) 0.634(5) 0.5982(12)
$U_{eq}$	0.072(5)	0.128(3)
Harmonic ADP		
U11	0.058(5)	0.107(14)
U22	0.080(7)	0.028(6)
U33	0.073(6)	0.099(12)
U12	0.030(5)	0.023(8)
U13	-0.003(5)	0.005(12)
U23	0.011(5)	-0.001(7)

## Appendix A. Appendix: X-ray diffraction

C2 occupancy	1.0	(a) 0.5; (b) 0.5
Wyckoff symbol	18f: x, y, z	18f: x, y, z
x, y, z	0.7078(9), 0.6671(8), 0.5727(3)	(a) 0.708(3), 0.655(4), 0.5726(8); (b) 0.709(4) 0.624(5) 0.5779(10)
$U_{eq}$	0.092(6)	0.13(3)
Harmonic ADP		
U11	0.106(9)	0.061(9)
U22	0.048(6)	0.26(4)
U33	0.086(7)	0.044(8)
U12	0.013(6)	0.05(2)
U13	0.020(6)	-0.004(7)
U23	-0.005(5)	-0.005(17)
N1 occupancy	1.0	(a) 0.5; (b) 0.5
Wyckoff symbol	18f: x, y, z	18f: x, y, z
x, y, z	0.6053(8), 0.5870(9), 0.6339(3)	(a) 0.612(2) 0.603(2) 0.6332(5); (b) 0.610(4) 0.588(5) 0.6373(9)
$U_{eq}$	0.078(6)	0.11(3)
Harmonic ADP		
U11	0.069(6)	0.199(18)
U22	0.091(9)	0.16(2)
U33	0.085(6)	0.072(7)
U12	0.048(6)	0.17(2)
U13	-0.005(5)	-0.015(10)
U23	-0.011(5)	0.001(13)
N2 occupancy	1.0	(a) 0.5; (b) 0.5
Wyckoff symbol	18f: x, y, z	18f: x, y, z
x, y, z	0.7202(9), 0.6467(12), 0.5285(3)	(a) 0.720(4) 0.635(4) 0.5277(8); (b) 0.729(5) 0.658(6) 0.5334(10)
$U_{eq}$	0.095(8)	0.095(7)
Harmonic ADP		
U11	0.086(7)	0.060(7)
U22	0.166(12)	0.066(9)
U33	0.078(6)	0.099(9)
U12	0.097(8)	-0.014(10)
U13	0.051(5)	0.057(7)
U23	0.066(7)	-0.021(10)
O (H <sub>2</sub> O) occupation	0.127(2)	0.127(2)
Wyckoff symbol	6c: 0,0,z	6c: 0,0,z
x, y, z	2/3, 1/3, 0.5717(10)	2/3, 1/3, 0.6236(18)
$U_{eq}$	0.003(3)	0.033(12)

Table A.6 – Positional and displacement parameters of non-hydrogen atoms in the pristine and the thermally treated crystals of EDPbI<sub>4</sub>.

#### A.4. Crystallographic tables

	Pristine	Thermally treated
Distances in PbI <sub>6</sub> octahedra		
Pb1 - I3	3.2176(19)	3.208(4) x6
Pb2 - I4	3.200(2)	3.197(7) x6
Pb3 - I2	3.118(2)	3.130(6) x3
- I3	3.355(2)	3.353(5) x3
Pb4 - I1	3.110(2)	3.087(5) x3
-I4	3.374(2)	3.376(6) x3
Distances in ED cation		
N1 - C1	1.432(15)	(a) 1.41(4); (b) 1.41(6)
C1 - C2	1.445(13)	(a) 1.43(5); (b) 1.43(5)
C2 - N2	1.508(16)	(a) 1.52(4); (b) 1.52(5)
Angles in ED cation		
N1 - C1 - C2	115.5(10)	113.6(19)
C1 - C2 - N2	112.7(9)	117.5(16)
O - I distances		
O1 - I1	3.23(4) x3	-
O1 - I2	-	3.22(4)

Table A.7 – Selected interatomic distances (Å) and angles (°) in the pristine and the thermally treated crystals.





## B Appendix: Experimental details

### B.1 Synthesis

All of the chemical reagents were of analytical reagent grade purity and used without further purification. MAPbI<sub>3</sub> was synthesized using a slightly modified version [177] of the method described by Poglitsch and Weber [91]. The single crystals were prepared by precipitation from a concentrated aqueous solution of hydriodic acid (57 wt% in H<sub>2</sub>O, 99.99% Sigma–Aldrich) containing lead (II) acetate trihydrate (99.999%, Acros Organics) and the respective amount of CH<sub>3</sub>NH<sub>2</sub> solution (30 wt% in H<sub>2</sub>O, Sigma–Aldrich). A constant 328–315 K temperature gradient was applied to induce a continuous precipitation of the solute. Large (1 × 2 mm) silver-gray MAPbI<sub>3</sub> crystals were grown within 2 days.

These crystals were used for XRD, heat capacity and resistivity measurements.

The perovskite precursor PbI<sub>2</sub> and MAI/MABr (molar ratio 1:1) dissolved in DMF with a concentration of 30 wt% for MAPbI<sub>3</sub> and MAPbBr<sub>3</sub> were used for recording XRD data for wire-shaped MAPbI<sub>3</sub> crystallization. And 15 wt% solution was used for AJP process, Figure 5.4.

### B.2 Dose-rate calibration

The X-ray beam was first detected using a PIXcel<sup>1D</sup> detector. Counts were measured for each tube voltage and current used in our measurements, corresponding to different dose-rates of exposure, Figure B.1. A Cu attenuator (0.2 mm) was additionally inserted into the beam path

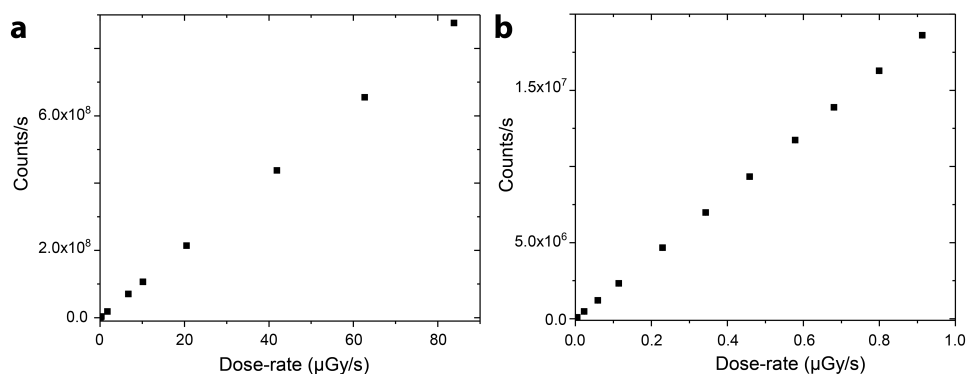


Figure B.1 – X-ray beam calibration: counts dependence on dose-rate.

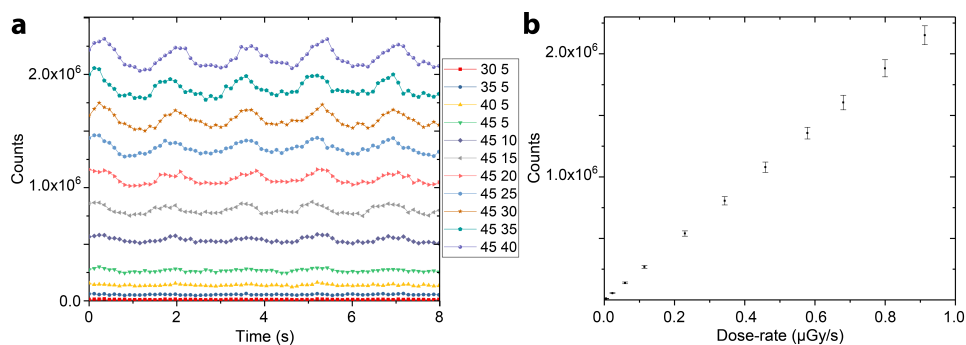


Figure B.2 – X-ray source intensity fluctuation in time. Legend in (a) corresponds to voltage (kV) and current (mA) of the tube.

to achieve even lower intensities, required to test the detection limit. The lowest dose-rate, obtained at 15 kV-5 mA voltage-current applied to the X-ray tube (with the Cu attenuator), was measured with a FLUKE Biomedical - VICTOREEN Advanced survey meter 990S and gave the value of 2.18 mSv/h. Taking into account the effect of the Cu attenuator, taken from the on-line X-ray Optics Calculator, and the area of the beam of 10 cm<sup>2</sup>, a final dose-rate per surface area was estimated: 2.725 Sv/h/cm<sup>2</sup>, for the 15 kV-5mA case (w/o the Cu attenuator).

The dose-rate for one pixel was then calculated by multiplying the dose-rate density and the wall cross-section (active area = 0.00075 cm<sup>2</sup>). The count values obtained for different applied voltage-currents, shown in Figure B.1a, were normalized to the lowest 15 kV-5 mA case to estimate all dose-rates for all experimental conditions.

To calculate the low dose-rate region (detection limit), counts were recorded as before, but this time with the Cu attenuator in the beam path. The measurements for the set of tube voltages and currents are shown in Figure B.1b. The 20 kV-5 mA count value without the Cu attenuator is the same as for the 45 kV-15 mA value with the attenuator. Therefore, the low-intensity dose-rates were calculated using this correlation. A standard deviation of the counts is below 6% for all the dose-rates (Figure B.2). For our calculations we assumed that the dose equivalent is equal to the absorbed dose, resulting in the dose-rates for the pixel in μGy/s. The photocurrent in Figure 6.16e is the mean photocurrent value after 2 seconds under X-ray exposure with a standard deviation error bar.

### B.3 Temperature dependent resistivity measurements

In Chapter 2 electrical resistivity data as a function of temperature were obtained in helium atmosphere using a standard four-point probe direct current (DC) method with a Keithley 220 current source and a Nanovoltmeter 2182. Gold wires were glued on the sample with carbon-containing paste to minimize the Schottky barrier at the interface [178]. The MAPbI<sub>3</sub> single crystal was illuminated by a red light (660 nm) produced by an ADL-66505TL AlGaInP visible laser diode and delivered to the sample via a 2 mm diameter polymer optical fiber (PMMA). The

#### B.4. Two-point resistivity measurements under VIS and X-ray illumination

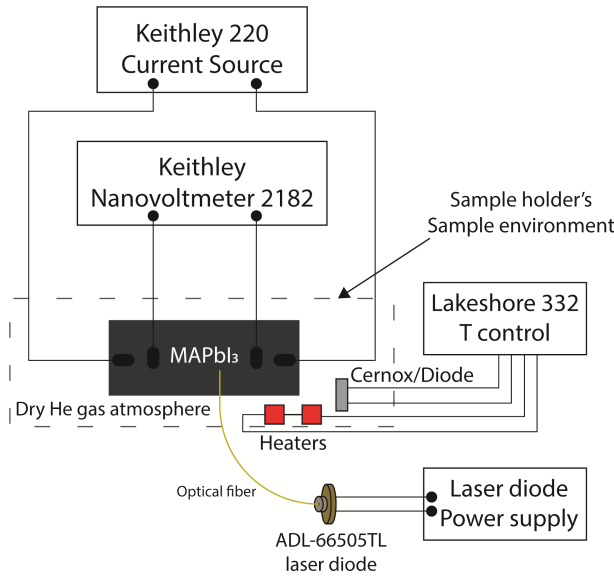


Figure B.3 – Schematic diagram of the resistivity measurement setup.

schematic diagram of the setup is shown in Figure B.3. The current polarity was periodically alternated to avoid the effects of charge accumulation.

#### B.4 Two-point resistivity measurements under VIS and X-ray illumination

All X-ray and VIS photocurrent measurements were performed under CW illumination. In Chapter 4 two-point J-V measurements was done using a Keithley 220 current source and a Nanovoltmeter 2182. In Chapter 6 the optimization of the device configuration (three types - resistor, diode and heterojunction) and photodetector were measured using Keithley 2400 SourceMeter in a two-terminal geometry under fixed DC-bias. The photocurrent experiments were performed in ambient atmosphere at 23 °C. Two-point resistivity measurements were performed under VIS light illumination from a halogen lamp coupled with a monochromator (at  $\lambda = 450$  nm, 550 nm, 650 nm) with a sweep in intensities from 0.48 to 293.71 nW.

X-ray detection properties of the devices were investigated using a standard fine-focus copper X-ray tube (CuK $\alpha$ ;  $\lambda = 1.541874$  Å) mounted in a PANalytical Empyrean diffractometer, energized from 15 to 45 kV and 5 to 40 mA.

For low intensity 0.2 mm Cu plate was used to attenuate the beam to reach 0.12  $\mu$ Gy/s dose-rate. All measurements of performances of the devices were done in ambient conditions at room temperature.

A Keithley 2400 source meter allowed us to measure the current with less than 0.1 nA resolution while tuning the applied bias voltage, in the dark and under white or X-ray irradiation.

For the samples in the Section 6.4 with the variation of the dot size on the graphene we obtained the parameters as in the Table B.1: The patten consists of an array  $5 \times 10$  AJP MAPbI<sub>3</sub> dots.

Figure B.4 – J-V curves of  $\text{CH}_3\text{NH}_3\text{PbCl}_3$  under UV illumination ( $\lambda = 365 \text{ nm}$ ) with an intensity of  $0.055 \text{ mW/mm}^2$ .

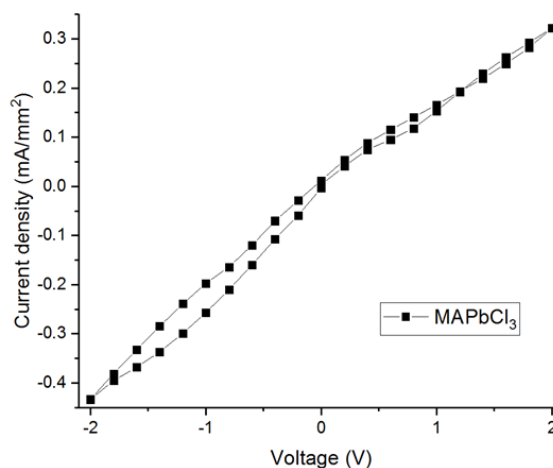
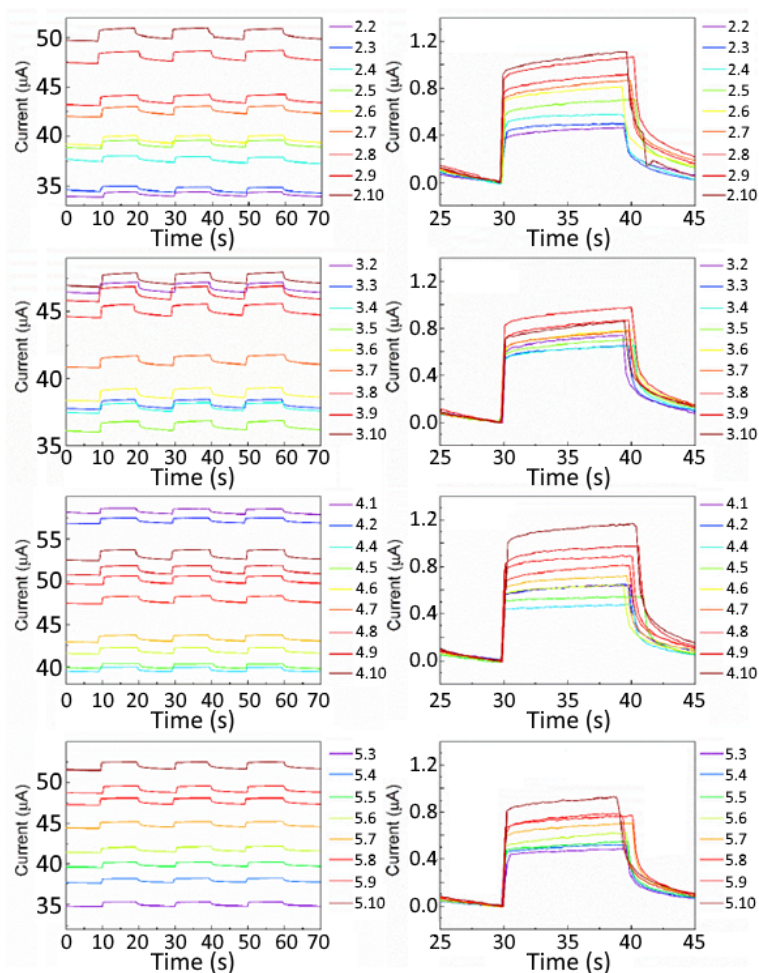


Figure B.5 – Dependence of the photocurrent of the AJP  $\text{MAPbI}_3$  spot size under VIS illumination ( $\lambda = 650 \text{ nm}$ ,  $265 \text{ nW}$ ). On the bottom (5.x) – the smallest spot on the top (2.x) the biggest. No size dependence is observed under light. The difference in photocurrent in each plot shows how the distance between the electrodes impacts it. The lowest step (x.2) represents the furthest distance and the biggest (x.10) the closest.



## B.5. Thermogravimetric analysis

Distance between electrodes, $\mu\text{m}$	x.1 150	x.2 140	x.3 130	x.4 120	x.5 110	x.6 100	x.7 90	x.8 80	x.9 70	x.10 60
Dot size, $10^{-3} \text{ mm}^2$	1.x 0	2.x 11	3.x 9.1	4.x 4.9	5.x 4.2					

Table B.1 – The distances between the electrodes and dot sizes of the AJP MAPbI<sub>3</sub> dots on the graphene. The variation of the row or column is denoted with "x".

## B.5 Thermogravimetric analysis

Thermogravimetric analysis is a method of thermal analysis in which the mass of a sample is measured over time as the temperature changes. It can be used to get an information about chemical reactions (oxidation, reduction) or thermal decomposition and so on. Such analysis helps to determine the mass loss behavior of the individual organic and inorganic components of MAPbI<sub>3</sub> as a function of temperature. The organic component, MAI, undergoes 100% weight loss in one step, which occurs at 397 K [179]. While the inorganic component, PbI<sub>2</sub> slowly losses 90% weight at 919 K, implying a thermal decomposition [179]. In this thesis the TGA analyses were done on a Perkin Elmer TGA 4000 system with an auto sampler in N<sub>2</sub> atmosphere with a heating rate of 10 K min<sup>-1</sup>.

## B.6 Heat capacity measurements

Measurements of heat capacity at a constant pressure,  $C_p$ , were carried out using the Quantum Design PPMS (Physical Property Measurement System) heat capacity option with the thermal relaxation technique. The measurements are performed by controlling the heat added to and removed from a sample while monitoring the resulting change in temperature. The sample weights for high-temperature measurements was 1.52 mg and for low-temperature measurements 1.37 mg. During a measurement, a known amount of heat is applied at constant power for a fixed time, and then this heating period is followed by a cooling period of the same time.

Figures B.6 and B.7 show the calculated changes in entropy,  $\Delta S$ .

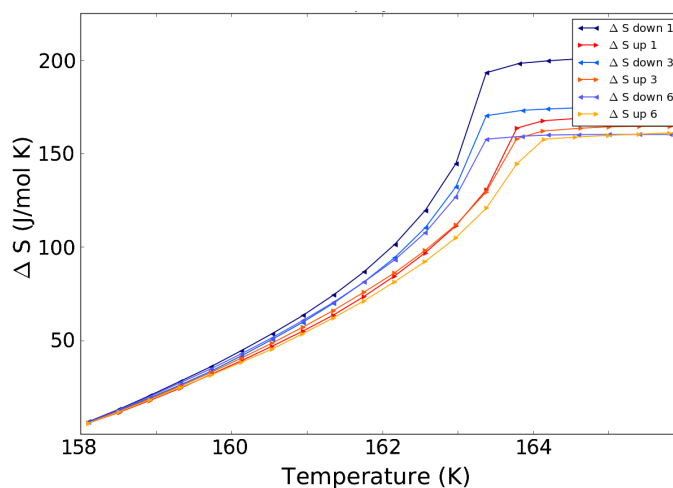


Figure B.6 – Temperature dependence of the entropy during thermal cycling around 160 K.

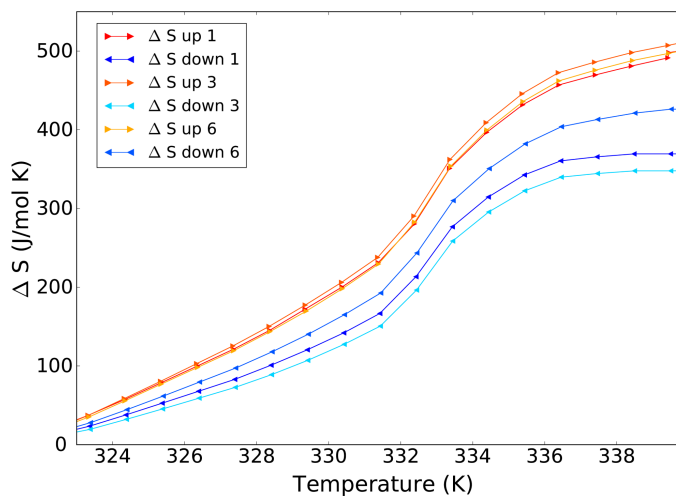


Figure B.7 – Temperature dependence of the entropy during thermal cycling around 330 K. The weak hysteresis visible in the first cycle tend to disappear with thermal cycling.

## C Appendix: Fabrication

The device fabrication was performed at CMi (Center of MicroNanoTechnology), EPFL. The substrates are 300 nm SiO<sub>2</sub> on Si. The monolayer graphene was produced by chemical vapor deposition (CVD) and transferred to a substrate by a wet transfer process.

During the CVD process graphene layer grows on both sides of a Cu foil. After protecting one of the sides with a layer of polymethyl methacrylate (PMMA) and etching the graphene on the other side with piranha solution (mixture of sulfuric acid (H<sub>2</sub>SO<sub>4</sub>) and hydrogen peroxide (H<sub>2</sub>O<sub>2</sub>)) or short oxygen plasma. After that, the Cu is etched with ferric chloride (FeCl<sub>3</sub>) or ammonium persulfate ((NH<sub>4</sub>)<sub>2</sub>S<sub>2</sub>O<sub>8</sub>) and the film of the graphene on PMMA is cleaned in deionized water. The final step is to fish the film onto the target substrate, bake it on the hotplate at the temperature around 70° C. Before further fabrication PMMA should be removed with an appropriate solvent.

### C.1 Electron beam lithography

Lithography is a commonly used technique for the creation of a 2D pattern on the surface of the substrate. For this purpose a electrosensitive resist is coated on the surface of the sample and is exposed by a highly focused electron beam to modify the solubility of the resist during a development step. As such, the exposed or unexposed areas (depending on the characteristics of the resist) are opened during the development for further steps. The first three fabrication steps related to e-beam lithography are illustrated in Figure C.1. The pattern for the diode-like structure and non-etched samples was made in this stage of an e-beam lithography. For fabrication of the isolated graphene areas only methyl methacrylate (MMA) resist was used and for the lift-off process a PMMA and MMA resist double-layer were spin-coated on the sample.

Resists with different contrasts give have different optimal doses. Therefore, using two resists with high-contrast (PMMA) on low-contrast (MMA) contrast, the resulting layers will have a sharp pattern on top of an overexposed area underneath (Figure C.2). This structure is commonly used for the lift-off process, as the deposited material through PMMA pattern lands on the substrate surface instead of the resist sidewalls.

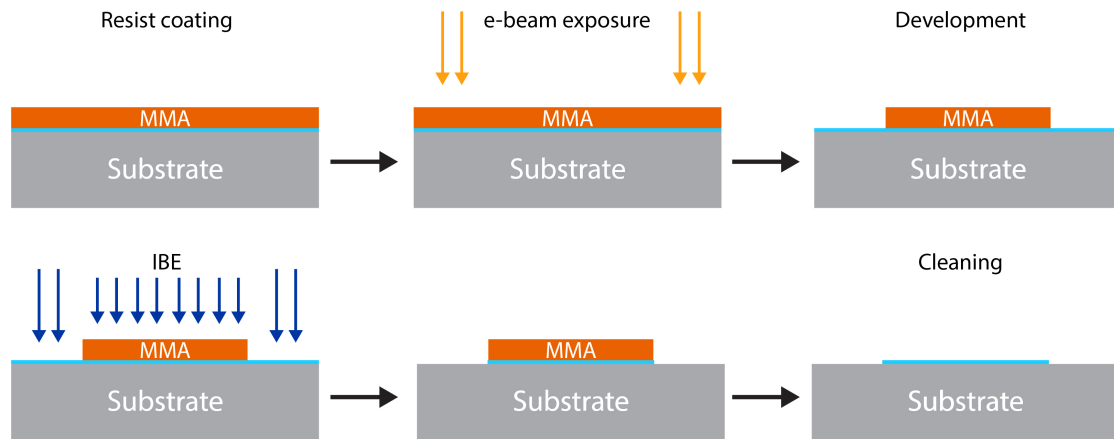


Figure C.1 – Process flow: graphene patten fabrication. The top panel illustrates the formation of the graphene pattern on the substrate with the e-beam lithography. The bottom panel shows the etching and cleaning fabrication steps.

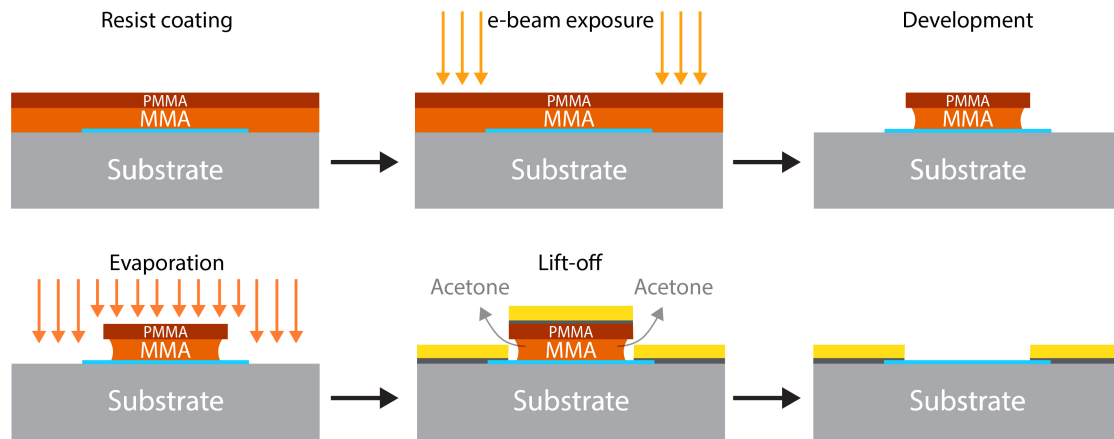


Figure C.2 – Process flow: electrodes fabrication. The top panel illustrates the formation of the electrodes pattern on the substrate with the e-beam lithography. The bottom panel shows the evaporation, lift-off and fabrication steps.

## C.2 Ion beam etching

An etching process allows us to remove the materials in a selective way by use of previously defined mask. One of dry etching process is Ion Beam Etching (IBE). After the first e-beam lithography the graphene pattern was etched, as illustrated in Figure C.1. Depending on the pattern the final device was without graphene - resistor mode, with the graphene covering the whole area - heterojunction, or partially etched - diode configuration. Argon ions are extracted from an ICP source, accelerated and directed to form a mono-energetic beam used to etch any materials by pure physical sputtering. The equipment possesses a large range energy capability from 50 to 800 V. A low acceleration voltage allows a low ion damage process, which is needed for etching the graphene layer.



### **C.3 Lift-off**

The gap between the electrodes has been varied from 60  $\mu\text{m}$  to 140  $\mu\text{m}$ . With the second aligned exposure (e-beam lithography) the electrodes were patterned, as shown in Figure C.2. After the development of the resist, 20 nm of Ti and 50 nm of Au were evaporated. The process of thermal evaporation consists of the vapor creation and material condensation on the substrate. This deposition method is more suitable than sputtering for a lift-off process. Due to interaction with the plasma, during sputtering the deposition is more randomized in the direction, leading to coverage of the resists sidewalls and eliminating the access of the solvent to the resist.

The remaining resist with the excess material is subsequently removed during a lift-off in acetone for 10 minutes. After that the sample with different configurations (resistor, diode and heterojunction) was ready to be AJP printed on, as described in Chapter 5.

For the X-ray detector the Ti-Au electrodes were evaporated as described above without graphene etching step.



# D Appendix: Humidity sensor based on methylammonium bismuth bromide

## D.1 Methylammonium bismuth bromide

Despite the great merits of  $\text{MAPbX}_3$ , the high concentration of lead reduces the enthusiasm for mass production with this material. As  $\text{MAPbX}_3$  compounds are highly soluble in water [180], there is a great need to find a non-toxic element to replace lead.

To save the properties of  $\text{MAPbI}_3$  the new compound should have a similar band structure. As the VB consists of halide  $p$ -states and Pb  $s$ -states, and the CB of empty Pb  $p$ -orbitals, to have the same  $\text{Pb}^{2+}$  electronic configuration, the elements below or above lead (Ge, Sn and Fl) could be considered. However, Ge and Sn are easily oxidized and Fl is radioactive. Therefore, the closest elements to Pb are Tl and Bi. But Tl is even more toxic than Pb, which makes  $\text{Bi}^{3+}$  one of the candidates for lead replacement.

As Bi has an extra charge, it forms lower-dimensional perovskites. One of them is an environmentally-friendly methylammonium bismuth bromide ( $\text{MA}_3\text{Bi}_2\text{Br}_9$ ).

The power conversion efficiency of  $\text{MA}_3\text{Bi}_2\text{Br}_9$  is lower in comparison to  $\text{MAPbI}_3$  and  $\text{MAPbBr}_3$  compounds. Therefore, a new possible application for this modification is studied.

Exposed to water  $\text{MA}_3\text{Bi}_2\text{Br}_9$  crystal does not incorporate it in the structure, but accumulate on the surface. This modification leads to the changes in the electrical resistivity of the material, thus making  $\text{MA}_3\text{Bi}_2\text{Br}_9$  a candidate for a promising humidity sensor.

In contrast, lead perovskites absorb water already at 55% relative-humidity (RH), which leads to the degradation of the sensing material [181]. The mixed chloride/iodide derivative is stable up to 90% RH, however such sensors have a slow response time of 24 s [182]. Finally, a 3D bismuth-based ( $\text{Cs}_2\text{BiAgBr}_6$ ) humidity sensor shows a very good performance and response time of 1.78s [183], giving a motivation for this work.

### D.1.1 Synthesis

A vial containing  $\text{Bi}(\text{NO}_3)_3 \cdot 5\text{H}_2\text{O}$  (4.85g) and concentrated HBr (10 ml) was placed in an ice bath. Methylamine solution (1.3 ml) was added drop-wisely over the course of 1 hour. The reaction was stirred until the formation of brown  $\text{NO}_2$  bubbles stopped (more than 24 hours). Afterwards, the mixture was kept at 277 K in the refrigerator for another 24 hours.

The flake-like shiny yellow crystals of  $\text{MA}_3\text{Bi}_2\text{Br}_9$  were harvested after gradual cooling down the reaction mixture over 24 hours (Figure D.1a).

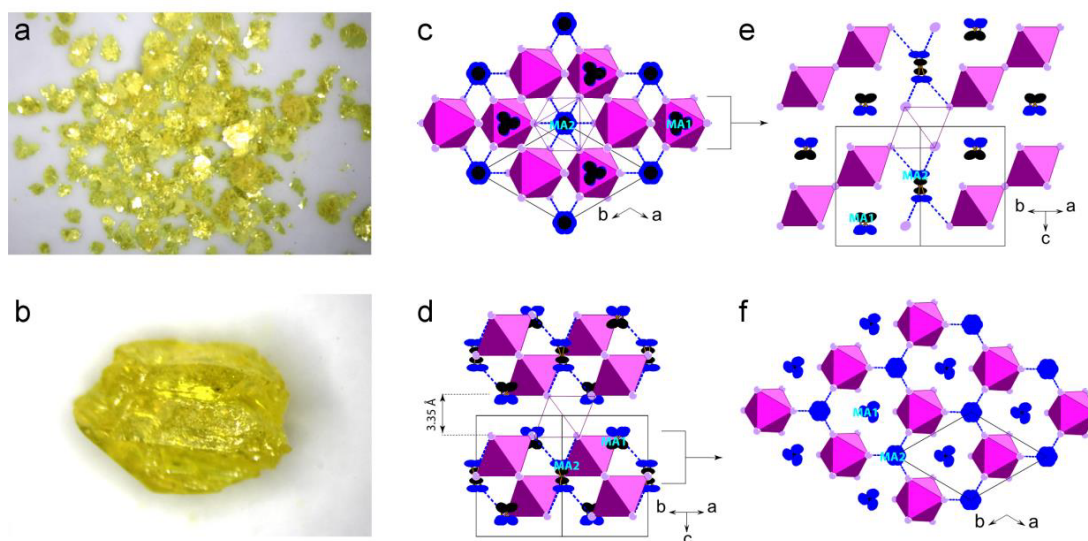


Figure D.1 –  $\text{MA}_3\text{Bi}_2\text{Br}_9$ : Photographs of (a) flakes and (b) single crystal. (c, d) Structure projection along the  $c$ -axis and the  $[110]$ -direction, respectively. (e) Representative section of the structure parallel to the  $c$ -axis. (f) Structure of one layer normal to the  $c$ -axis. Blue dashed lines indicate the donor-accepter hydrogen bonds of 3.08 Å. Violet lines show the empty  $\text{Br}_6$ -octahedron.

Three types of  $\text{MA}_3\text{Bi}_2\text{Br}_9$  are prepared: powder, single crystals and nanowires.

Single crystals of  $\text{MA}_3\text{Bi}_2\text{Br}_9$  (Figure D.1b) are prepared directly from the reaction solution. Preparation of larger single crystals is performed under similar conditions over a longer time, and by making a temperature gradient in the vial. After one week, macroscopic crystals are formed on the hot side (313 K) of the vial.

Nanowires are prepared by complete dissolution of  $\text{MA}_3\text{Bi}_2\text{Br}_9$  flakes in DMSO and recrystallization on a substrate by evaporation of solvent at room temperature. The formation an undesired side product of  $\text{BiOBr}$  is starting under solvent evaporation at temperatures above 350 K.

### D.1.2 Crystal structure

The synchrotron radiation XRD experiments were carried out with wavelength  $\lambda = 0.7129$  Å at 293 K for single crystal and  $\lambda = 0.64109$  Å at 276 K for powder samples at the SNBL, Grenoble. The main results of the experiment, crystallographic characteristics and quality of the structure refinement are given in Table D.1.

From the structural refinement it is shown that  $\text{MA}_3\text{Bi}_2\text{Br}_9$  belongs to the  $\text{A}_3\text{B}_2\text{X}_9$  family of 2D perovskites similar to the  $\text{Cs}_3\text{Sb}_2\text{I}_9$  structure type [184], which is characterized by the space group  $P\bar{3}m1$ . Arrangement of the  $\text{BiBr}_6$ -octahedra differs from the perovskite by missing every third layer of the octahedra along the 3-fold axis (Figure D.1d,e). Positions of N and C atoms of two MA cations are found from the difference electron density calculated after localization of Bi and Br atoms. Each N and C atom is statistically distributed in a site with higher multiplicity

Chemical formula	(CNH <sub>6</sub> ) <sub>3</sub> Bi <sub>2</sub> Br <sub>9</sub>
Space group	Trigonal, $P\bar{3}m1$
Temperature, K	293
$a, c$ (Å)	8.2301 (2), 10.0246 (3)
$V$ (Å <sup>3</sup> )	588.04 (4)
$\lambda$ , Å	0.7129
$R[F > 2\sigma(F)], wR(F), S$	0.020, 0.025, 1.99
$\Delta\rho_{max}, \rho_{min}$ (eÅ <sup>-3</sup> )	0.50, -0.87

Table D.1 – Experimental details for the single crystal MA<sub>3</sub>Bi<sub>2</sub>Br<sub>9</sub> structure determination and refinement

than one, so that the corresponding sites are partially occupied. Hence, similar to MAPbI<sub>3</sub> [95], MA cations are partially disordered in the structure (Figure D.1c-f). Essential disorder of N and C does not allow localization of the hydrogen positions.

## D.2 Sensor characterisation

Relative humidity (RH) is defined as the ratio of actual water vapor pressure to the saturated water vapor pressure at the ambient temperature. And one of the most common humidity sensors is the resistive type, which exhibits variation of the conductivity of the sensing layer upon water adsorption. In MA<sub>3</sub>Bi<sub>2</sub>Br<sub>9</sub> a strong variation of electrical current is observed with changing humidity level, suggesting the possible material application as an RH sensor.

As described in Section D.1.1, three forms of MA<sub>3</sub>Bi<sub>2</sub>Br<sub>9</sub> are prepared and tested for the device: powder, single crystal and nanowires.

Electrical properties of the sample with MA<sub>3</sub>Bi<sub>2</sub>Br<sub>9</sub> powder are measured by pressing the material into cylindrical pellets, together with graphite paper as an electrical contact. If we would place two carbon electrodes on opposite sides of the pellet, charging in the thus-created capacitor would tamper the measurements. Therefore, both graphite contacts are placed on the same side of the pellet, laterally separated by  $\approx 1$  mm. Gold wires are attached to the graphite paper using carbon paste and connected to a Keithley 2400 multimeter.

The hygrometer properties are measured under a stream of synthetic air (a mixture of N<sub>2</sub> and O<sub>2</sub> at volume ratio 78/22) with an initial water content < 3 ppm. The moisture content of the gas is defined in ppm by volume, which is proportional to the ratio of the water vapor partial pressure to the total system pressure. To achieve RH  $\approx 100\%$  the air stream is going through a saturated water solution of CuSO<sub>4</sub>  $\times$  5H<sub>2</sub>O. The stream of humid air is then reunited with the dry air stream in a controlled way to obtain the desired RH for the measurements. After that the steam is guided into the sealed desiccator equipped with an exhaust pipe and connectors to the multimeter.

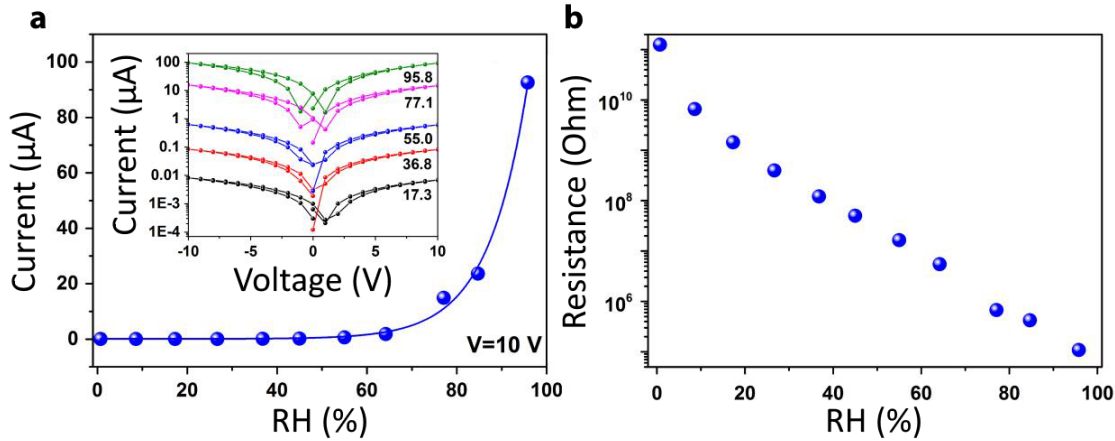


Figure D.2 – (a) Dependence of current on RH in the pressed powder  $\text{MA}_3\text{Bi}_2\text{Br}_9$  sensor at 10 V bias voltage. (b) Dependence of the resistance of  $\text{MA}_3\text{Bi}_2\text{Br}_9$  on RH.

### D.2.1 Detection range

With the described setup it is possible to control the humidity in the desiccator and achieve a reliable RH range from 0.7-95.8% measured by a commercial humidity sensor Sensirion SHT 31. The  $\text{MA}_3\text{Bi}_2\text{Br}_9$  is connected by wires and closed in the desiccator next to the commercial humidity sensor.

It is observed that the  $\text{MA}_3\text{Bi}_2\text{Br}_9$ -based sensor is operable at the full measuring range (0.7-95.8% RH). The rise in RH from 0.7% to 95.8% is accompanied by the increased current from  $10^{-4}$  to  $10^2 \mu\text{A}$ , as shown in Figure D.2a. The sensor response at different RH is represented in the inset in Figure D.2a as a set of I-V curves, from which the current values are extracted. As can be seen, the current value increases exponentially with higher relative humidity.

The  $\text{MA}_3\text{Bi}_2\text{Br}_9$  sensor demonstrates high selectivity towards water, as no change in resistivity is observed under exposure to  $\text{CO}_2$ , Ar,  $\text{N}_2$  and  $\text{O}_2$  gases.

For more precise measurements, the sensor is placed in a glovebox equipped with an Electro-Tech System (ETS) microprocessor humidification/dehumidification system model 5100, which allows the most precise control of the humidity. A linear trend in Figure D.2b is observed in the logarithmic scale as resistivity drops from  $10^{-5}$  to  $10 \mu\Omega$  when RH changes from 0.7% to 95.8% RH.

The normalized sensitivity of the humidity sensor reaches the value of  $S_h = |\Delta R|/R_0 = 9.5 \times 10^3$  at 10 V bias voltage, where  $\Delta R$  is the difference in the resistance under humidity exposure and  $R_0$  is the resistance before the exposure [185]. The value of  $S_h$  is substantially enough for humidity detection application.

While pellets show logarithmic trend in response over the whole RH measuring range, the single crystal demonstrates a plateau until 50% RH (Figure D.3) And the nanowires response to RH does not give unique value of the resistivity to RH values.

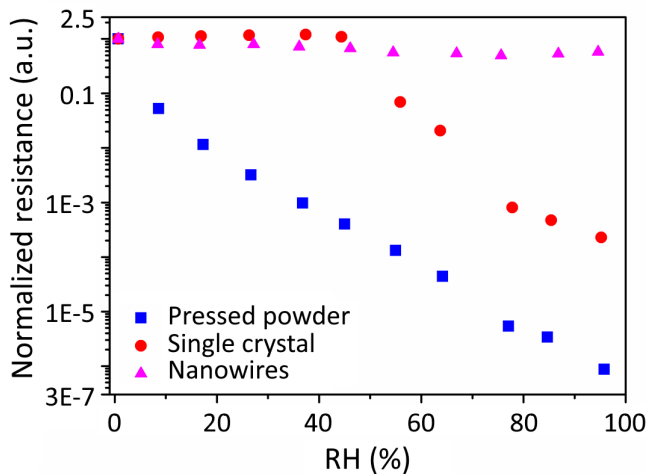


Figure D.3 – Resistivity measurements of three types of  $\text{MA}_3\text{Bi}_2\text{Br}_9$  sensor: powder pellets and single crystal at 10 V bias voltage and nanowires at 100 mV under different RH values.

### D.2.2 Stability

To test the sensor stability, measurements were repeated over a month. The sensor was stored at ambient conditions.

No change in the signal for powder pellets was observed, indicating that the sample has not degraded and no water inclusion has occurred during the storage. A slow degradation of sensing properties of the  $\text{MA}_3\text{Bi}_2\text{Br}_9$  nanowires was observed over time.

Generally, powder pellets are found superior to both, the single crystal and nanowires, in all characteristics.

### D.2.3 Humidity response time

The response and recovery periods are measured as the time required for the signal to reach a certain value as a response to external stimuli. Here, the response time,  $t_{res}$ , is the time at which 90% of current value  $\Delta I = I_p - I_b$  is reached, where  $I_p$  is the current at the peak of the signal at 55% RH and  $I_b$  is the average current at the baseline at 25% RH. In the same manner, the recovery time,  $t_{rec}$ , is the time required for the signal to return back to 10% of  $\Delta I$ .

Response times of all three types of  $\text{MA}_3\text{Bi}_2\text{Br}_9$  sensors are fast, ranging from 1.5-1.7 s, followed by recovery times ranging from 4.1-7.1 s to get from 25-55% RH (Figure D.4). For comparison the commercial Sensirion SHT 31 sensor is measured, which demonstrates response and recovery times  $t_{res}/t_{rec} = 3.4/13.8$  s in the same RH range. The best results are obtained with the powder pressed  $\text{MA}_3\text{Bi}_2\text{Br}_9$  in pellets,  $t_{res}/t_{rec} = 1.5/4.1$  s.

Differential thermogravimetric analysis shows that  $\text{MA}_3\text{Bi}_2\text{Br}_9$  is stable towards thermal decomposition up to 573 K. Therefore, an influence of the temperature on the humidity sensor was investigated. By gradual heating, it is possible to shorten the response times down to  $t_{res}/t_{rec} = 1.5/1.5$  s at 308 K for 30-65% RH interval (Figure D.5). The shorter response and recovery times at higher temperatures are accompanied by a weakening of the signal, albeit the signal-to-noise ratio is still large in the detection range, owing to the high sensitivity of the sample.

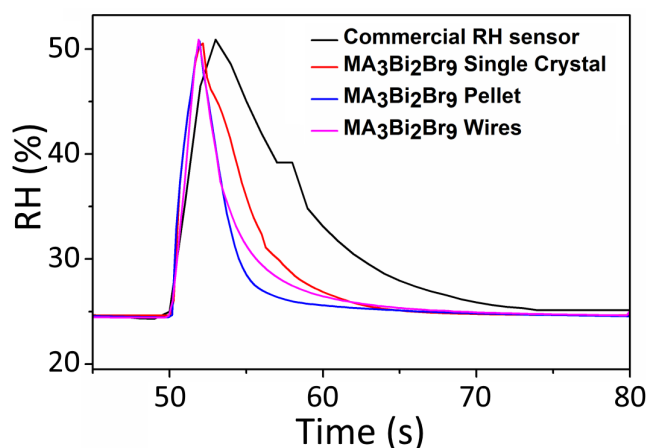


Figure D.4 – Comparison of humidity response between three types of  $\text{MA}_3\text{Bi}_2\text{Br}_9$  and a commercial sensor.

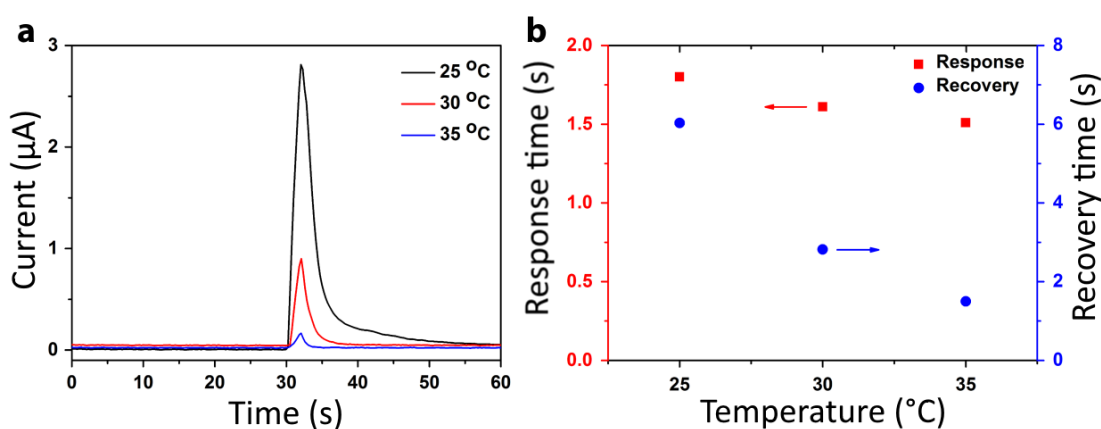


Figure D.5 – Temperature dependence of the  $\text{MA}_3\text{Bi}_2\text{Br}_9$  pellet (a) Response from 30% to 65% RH at 298, 303 and 308 K. (b) Response and recovery times shortening upon heating.

Dynamical measurements of humidity are performed by parallel exposures of the sensor to a short stream of humid air. Figure D.6 shows a comparison of  $\text{MA}_3\text{Bi}_2\text{Br}_9$  pellets sensor with the commercial one over several detection cycles. As can be seen from the measurements, response of the  $\text{MA}_3\text{Bi}_2\text{Br}_9$ -based sensor is faster than of the commercial sensor. Over a month after initial measurements, good reproducibility and stability of the device are demonstrated.

### Surface vs. bulk water absorption

In the following part it will be shown, that the change in the conductivity by exposure  $\text{MA}_3\text{Bi}_2\text{Br}_9$  to a humid atmosphere is only due to surface effects.

As for a single crystal the resistance value remains unchanged until  $\approx 50\%$  RH, then begins to follow a linear trend (similar to the microcrystalline sample, Figure D.3), it may be attributed to the conductivity of material without the contribution from the adsorbed water. Effectively, it makes this type of the detector unsuitable for low RH.

In contrast, a larger surface of polycrystalline sample (powder pellet) of comparable volume allows more water to be collected, resulting in drastically lower resistivity at the same RH. For



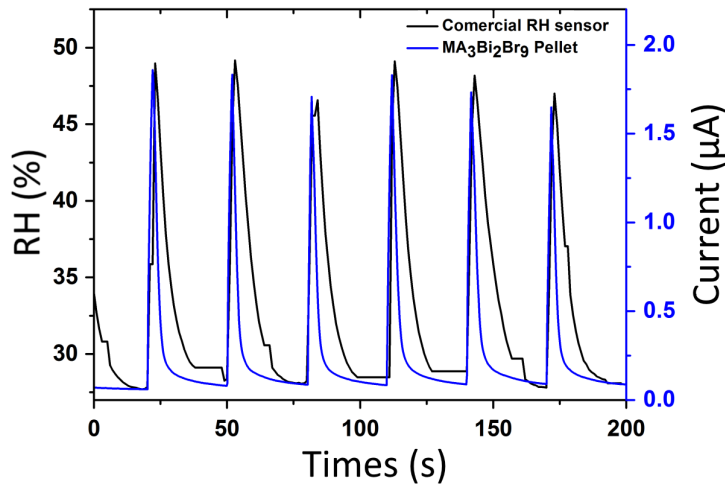


Figure D.6 – Response time measurements of powder pellets in comparison to the commercial sensor from RH 25-50%. The signals are scaled to normal.

	Pristine	Thermally treated
Chemical formula	(CNH <sub>6</sub> ) <sub>3</sub> Bi <sub>2</sub> Br <sub>9</sub>	(CNH <sub>6</sub> ) <sub>3</sub> Bi <sub>2</sub> Br <sub>9</sub>
Space group	Trigonal, $P\bar{3}m1$	Trigonal, $P\bar{3}m1$
Temperature, K	276	276
$a, c$ (Å)	8.2169(3), 10.0027(5)	8.2187(3), 10.0065(5)
$V$ (Å <sup>3</sup> )	584.88(4)	585.36(3)
$\lambda$ , Å	0.64109	0.64109
$R(obs), wR(obs), R(all), wR(all)$	0.018, 0.025, 0.018, 0.025	0.019, 0.026, 0.019, 0.026
$Rp, wRp$	0.017, 0.022	0.018, 0.024
$\Delta\rho_{max}, \rho_{min}$ (eÅ <sup>-3</sup> )	0.76, -1.6	0.78, -1.92

Table D.2 – Experimental details for the "wet" and "dry" powder MA<sub>3</sub>Bi<sub>2</sub>Br<sub>9</sub> sample structure determination and refinement

instance, at 50% RH, the resistance of single crystal is  $\approx 10^9 \Omega$ , while in pressed pellet it is only  $\approx 10^7 \Omega$ .

Moreover, in the polycrystalline sample the grain boundaries increase net resistance at lower RH, allowing to measure values below the threshold of the single crystal sample (up to  $\approx 10^{11} \Omega$  at 0.7% RH).

XRD measurements supports the suggestion that the conductivity of MA<sub>3</sub>Bi<sub>2</sub>Br<sub>9</sub> is a surface phenomenon. Two types of powder samples are sealed in glass capillaries: one at the 95.7% ("wet") RH and an other at 0.3% ("dry") RH. Structure refinement shows no difference between the "wet" and "dry" samples. Crystallographic characteristics and the main details of the structure refinement are listed in Table D.2 for the "wet" and "dry" samples. A slightly higher volume of the unit cell found for the "wet" sample,  $V_w = 585.36(3) \text{ Å}^3$ , in comparison to the pristine one,  $V_{pr} = 584.88(4) \text{ Å}^3$ , can be explained by the amount of adsorbed water on the surface of crystallites. The presence of water is also confirmed by a slightly higher background characteristic of the XRD profile for the "wet" sample.

Therefore, since no detectable change in XRD profiles is observed, it may be concluded that no water incorporates into the sample structure. An effect from humidity is confined to the surface of  $\text{MA}_3\text{Bi}_2\text{Br}_9$ , where a conductive effect happens in accordance to the Grotthuss mechanism [186], involving proton hopping between adsorbed water molecules.

### **D.3 Conclusion**

A lead-free perovskite-related material for humidity sensors was characterized and tested. Following the synthesis, detailed crystal structural refinement was performed for all the prepared forms of  $\text{MA}_3\text{Bi}_2\text{Br}_9$ , showing that the bulk crystal structure is stable and indifferent to water. Sensor properties were measured in both static and dynamic conditions of relative humidity. While the sensor is stable and active over the whole humidity range (0.7-95.8% RH), it is also faster than the commercial ones, with response/recovery time of 1.5s/4.1s.

# Bibliography

- [1] T. Barker, I. Bashmakov, L. Bernstein, J. Bogner, P. Bosch, R. Dave, B. Metz, and G. Naburs, "Contribution of Working Group III to the Fourth Assessment Report of the IPCC: Technical Summary," in *Climate Change 2007: Mitigation contribution of Working Group III to the Fourth Assessment Report of the Intergovernmental Panel on Climate Change*, Intergovernmental Panel on Climate Change, pp. 27–93, Cambridge University Press, 2009.
- [2] O. Morton, *A new day dawning?: Silicon Valley sunrise*. Nature Publishing Group, 2006.
- [3] "Best Research-Cell Efficiencies (NREL);," 2020.
- [4] S. D. Stranks and H. J. Snaith, "Metal-halide perovskites for photovoltaic and light-emitting devices," *Nature nanotechnology*, vol. 10, no. 5, p. 391, 2015.
- [5] L. Mazzarella, Y.-H. Lin, S. Kirner, A. B. Morales-Vilches, L. Korte, S. Albrecht, E. Crossland, B. Stannowski, C. Case, H. J. Snaith, and others, "Infrared Light Management Using a Nanocrystalline Silicon Oxide Interlayer in Monolithic Perovskite/Silicon Heterojunction Tandem Solar Cells with Efficiency above 25%," *Advanced Energy Materials*, vol. 9, no. 14, p. 1803241, 2019.
- [6] Z.-K. Tan, R. S. Moghaddam, M. L. Lai, P. Docampo, R. Higler, F. Deschler, M. Price, A. Sadhanala, L. M. Pazos, D. Credgington, and others, "Bright light-emitting diodes based on organometal halide perovskite," *Nature nanotechnology*, vol. 9, no. 9, p. 687, 2014.
- [7] S. Chen, K. Roh, J. Lee, W. K. Chong, Y. Lu, N. Mathews, T. C. Sum, and A. Nurmikko, "A photonic crystal laser from solution based organo-lead iodide perovskite thin films," *Acs Nano*, vol. 10, no. 4, pp. 3959–3967, 2016.
- [8] K. Mantulnikovs, A. Glushkova, M. Kollár, L. Forró, E. Horváth, and A. Sienkiewicz, "Differential response of the photoluminescence and photocurrent of polycrystalline  $\text{CH}_3\text{NH}_3\text{PbI}_3$  and  $\text{CH}_3\text{NH}_3\text{PbBr}_3$  to the exposure to Oxygen and Nitrogen," *ACS Applied Electronic Materials*, 2019.
- [9] E. Horváth, M. Spina, Z. Szekrényes, K. Kamarás, R. Gaal, D. Gachet, and L. Forró, "Nanowires of methylammonium lead iodide ( $\text{CH}_3\text{NH}_3\text{PbI}_3$ ) prepared by low temperature solution-mediated crystallization," *Nano letters*, vol. 14, no. 12, pp. 6761–6766, 2014.
- [10] W. Heiss and C. Brabec, "X-ray imaging: Perovskites target X-ray detection," *Nature Photonics*, vol. 10, no. 5, p. 288, 2016.
- [11] R. D. Evans and R. Evans, "The atomic nucleus," 1955.

## Bibliography

---

- [12] W. Wei, Y. Zhang, Q. Xu, H. Wei, Y. Fang, Q. Wang, Y. Deng, T. Li, A. Gruverman, L. Cao, and others, "Monolithic integration of hybrid perovskite single crystals with heterogenous substrate for highly sensitive X-ray imaging," *Nature Photonics*, vol. 11, no. 5, p. 315, 2017.
- [13] B. Náfrádi, G. Náfrádi, L. Forró, and E. Horváth, "Methylammonium lead iodide for efficient X-ray energy conversion," *The Journal of Physical Chemistry C*, vol. 119, no. 45, pp. 25204–25208, 2015.
- [14] V. Goldschmidt, "Crystal structure and chemical correlation," *Ber Deut Chem Ges*, vol. 60, pp. 1263–1296, 1927.
- [15] C. Li, X. Lu, W. Ding, L. Feng, Y. Gao, and Z. Guo, "Formability of ABX<sub>3</sub> (X= F, Cl, Br, I) Halide Perovskites," *Acta Crystallographica Section B: Structural Science*, vol. 64, no. 6, pp. 702–707, 2008.
- [16] A. Poglitsch and D. Weber, "Dynamic disorder in methylammoniumtrihalogeno-plumbates (II) observed by millimeter-wave spectroscopy," *The Journal of chemical physics*, vol. 87, no. 11, pp. 6373–6378, 1987.
- [17] M. T. Weller, O. J. Weber, P. F. Henry, A. M. Di Pumpo, and T. C. Hansen, "Complete structure and cation orientation in the perovskite photovoltaic methylammonium lead iodide between 100 and 352 K," *Chemical communications*, vol. 51, no. 20, pp. 4180–4183, 2015.
- [18] W. Shockley and H. J. Queisser, "Detailed balance limit of efficiency of p-n junction solar cells," *Journal of applied physics*, vol. 32, no. 3, pp. 510–519, 1961.
- [19] S. De Wolf, J. Holovsky, S.-J. Moon, P. Löper, B. Niesen, M. Ledinsky, F.-J. Haug, J.-H. Yum, and C. Ballif, "Organometallic halide perovskites: sharp optical absorption edge and its relation to photovoltaic performance," *The journal of physical chemistry letters*, vol. 5, no. 6, pp. 1035–1039, 2014.
- [20] M. M. Lee, J. Teuscher, T. Miyasaka, T. N. Murakami, and H. J. Snaith, "Efficient hybrid solar cells based on meso-superstructured organometal halide perovskites," *Science*, vol. 338, no. 6107, pp. 643–647, 2012.
- [21] E. Edri, S. Kirmayer, M. Kulbak, G. Hodes, and D. Cahen, "Chloride inclusion and hole transport material doping to improve methyl ammonium lead bromide perovskite-based high open-circuit voltage solar cells," *The journal of physical chemistry letters*, vol. 5, no. 3, pp. 429–433, 2014.
- [22] T. M. Brenner, D. A. Egger, L. Kronik, G. Hodes, and D. Cahen, "Hybrid organic—inorganic perovskites: low-cost semiconductors with intriguing charge-transport properties," *Nature Reviews Materials*, vol. 1, no. 1, p. 15007, 2016.
- [23] G. Xing, N. Mathews, S. Sun, S. S. Lim, Y. M. Lam, M. Grätzel, S. Mhaisalkar, and T. C. Sum, "Long-range balanced electron-and hole-transport lengths in organic-inorganic CH<sub>3</sub>NH<sub>3</sub>PbI<sub>3</sub>," *Science*, vol. 342, no. 6156, pp. 344–347, 2013.

- [24] J. Even, L. Pedesseau, and C. Katan, "Analysis of multivalley and multibandgap absorption and enhancement of free carriers related to exciton screening in hybrid perovskites," *The Journal of Physical Chemistry C*, vol. 118, no. 22, pp. 11566–11572, 2014.
- [25] V. D'innocenzo, G. Grancini, M. J. Alcocer, A. R. S. Kandada, S. D. Stranks, M. M. Lee, G. Lanzani, H. J. Snaith, and A. Petrozza, "Excitons versus free charges in organo-lead tri-halide perovskites," *Nature communications*, vol. 5, p. 3586, 2014.
- [26] T. Ishihara, "Optical properties of PbI<sub>2</sub>-based perovskite structures," *Journal of luminescence*, vol. 60, pp. 269–274, 1994.
- [27] J. Even, L. Pedesseau, J.-M. Jancu, and C. Katan, "DFT and k·p modelling of the phase transitions of lead and tin halide perovskites for photovoltaic cells," *physica status solidi (RRL)–Rapid Research Letters*, vol. 8, no. 1, pp. 31–35, 2014.
- [28] C. S. Ponseca Jr, T. J. Savenije, M. Abdellah, K. Zheng, A. Yartsev, T. Pascher, T. Harlang, Chabera, T. Pullerits, A. Stepanov, and others, "Organometal halide perovskite solar cell materials rationalized: ultrafast charge generation, high and microsecond-long balanced mobilities, and slow recombination," *Journal of the American Chemical Society*, vol. 136, no. 14, pp. 5189–5192, 2014.
- [29] Q. Dong, Y. Fang, Y. Shao, P. Mulligan, J. Qiu, L. Cao, and J. Huang, "Electron-hole diffusion lengths > 175 μm in solution-grown CH<sub>3</sub>NH<sub>3</sub>PbI<sub>3</sub> single crystals," *Science*, vol. 347, no. 6225, pp. 967–970, 2015.
- [30] Y. Mei, C. Zhang, Z. Vardeny, and O. Jurchescu, "Electrostatic gating of hybrid halide perovskite field-effect transistors: balanced ambipolar transport at room-temperature," *MRS Communications*, vol. 5, no. 2, pp. 297–301, 2015.
- [31] C. C. Stoumpos, C. D. Malliakas, and M. G. Kanatzidis, "Semiconducting tin and lead iodide perovskites with organic cations: phase transitions, high mobilities, and near-infrared photoluminescent properties," *Inorganic chemistry*, vol. 52, no. 15, pp. 9019–9038, 2013.
- [32] M. Karakus, S. A. Jensen, F. D'Angelo, D. Turchinovich, M. Bonn, and E. Canovas, "Phonon–electron scattering limits free charge mobility in methylammonium lead iodide perovskites," *The journal of physical chemistry letters*, vol. 6, no. 24, pp. 4991–4996, 2015.
- [33] G. Giorgi, J.-I. Fujisawa, H. Segawa, and K. Yamashita, "Small photocarrier effective masses featuring ambipolar transport in methylammonium lead iodide perovskite: a density functional analysis," *The journal of physical chemistry letters*, vol. 4, no. 24, pp. 4213–4216, 2013.
- [34] J. Even, L. Pedesseau, J.-M. Jancu, and C. Katan, "Importance of spin–orbit coupling in hybrid organic/inorganic perovskites for photovoltaic applications," *The Journal of Physical Chemistry Letters*, vol. 4, no. 17, pp. 2999–3005, 2013.

- [35] H. Oga, A. Saeki, Y. Ogomi, S. Hayase, and S. Seki, "Improved understanding of the electronic and energetic landscapes of perovskite solar cells: high local charge carrier mobility, reduced recombination, and extremely shallow traps," *Journal of the American Chemical Society*, vol. 136, no. 39, pp. 13818–13825, 2014.
- [36] Z.-G. Yu, "Rashba effect and carrier mobility in hybrid organic–inorganic perovskites," *The journal of physical chemistry letters*, vol. 7, no. 16, pp. 3078–3083, 2016.
- [37] A. Senocrate, I. Moudrakovski, G. Y. Kim, T.-Y. Yang, G. Gregori, M. Grätzel, and J. Maier, "The nature of ion conduction in methylammonium lead iodide: a multimethod approach," *Angewandte Chemie International Edition*, vol. 56, no. 27, pp. 7755–7759, 2017.
- [38] Y. Yuan and J. Huang, "Ion migration in organometal trihalide perovskite and its impact on photovoltaic efficiency and stability," *Accounts of chemical research*, vol. 49, no. 2, pp. 286–293, 2016.
- [39] E. Mosconi, A. Amat, M. K. Nazeeruddin, M. Grätzel, and F. De Angelis, "First-principles modeling of mixed halide organometal perovskites for photovoltaic applications," *The Journal of Physical Chemistry C*, vol. 117, no. 27, pp. 13902–13913, 2013.
- [40] M. H. Du, "Efficient carrier transport in halide perovskites: theoretical perspectives," *Journal of Materials Chemistry A*, vol. 2, no. 24, pp. 9091–9098, 2014.
- [41] D. B. Mitzi, "Synthesis, structure, and properties of organic-inorganic perovskites and related materials," *Progress in inorganic chemistry*, pp. 1–121, 1999.
- [42] J. H. Noh, S. H. Im, J. H. Heo, T. N. Mandal, and S. I. Seok, "Chemical management for colorful, efficient, and stable inorganic–organic hybrid nanostructured solar cells," *Nano letters*, vol. 13, no. 4, pp. 1764–1769, 2013.
- [43] J. L. Knutson, J. D. Martin, and D. B. Mitzi, "Tuning the band gap in hybrid tin iodide perovskite semiconductors using structural templating," *Inorganic chemistry*, vol. 44, no. 13, pp. 4699–4705, 2005.
- [44] P. Gao, M. Grätzel, and M. K. Nazeeruddin, "Organohalide lead perovskites for photovoltaic applications," *Energy & Environmental Science*, vol. 7, no. 8, pp. 2448–2463, 2014.
- [45] L.-y. Huang and W. R. Lambrecht, "Electronic band structure, phonons, and exciton binding energies of halide perovskites CsSnCl<sub>3</sub>, CsSnBr<sub>3</sub>, and CsSnI<sub>3</sub>," *Physical Review B*, vol. 88, no. 16, p. 165203, 2013.
- [46] T. Baikie, N. S. Barrow, Y. Fang, P. J. Keenan, P. R. Slater, R. O. Piltz, M. Gutmann, S. G. Mhaisalkar, and T. J. White, "A combined single crystal neutron/X-ray diffraction and solid-state nuclear magnetic resonance study of the hybrid perovskites CH<sub>3</sub>NH<sub>3</sub>PbX<sub>3</sub> (X= I, Br and Cl)," *Journal of Materials Chemistry A*, vol. 3, no. 17, pp. 9298–9307, 2015.

- [47] S. D. Stranks, G. E. Eperon, G. Grancini, C. Menelaou, M. J. Alcocer, T. Leijtens, L. M. Herz, A. Petrozza, and H. J. Snaith, "Electron-hole diffusion lengths exceeding 1 micrometer in an organometal trihalide perovskite absorber," *Science*, vol. 342, no. 6156, pp. 341–344, 2013.
- [48] M. R. Filip, G. E. Eperon, H. J. Snaith, and F. Giustino, "Steric engineering of metal-halide perovskites with tunable optical band gaps," *Nature communications*, vol. 5, p. 5757, 2014.
- [49] K. Yamada, T. Tsuritani, T. Okuda, and S. Ichiba, "Structure and Bonding of Two Modifications of  $\text{CsSnI}_3$  by Means of Powder X-Ray Diffraction, 127i NQR, AND DTA," *Chemistry Letters*, vol. 18, no. 8, pp. 1325–1328, 1989.
- [50] D. Trots and S. Myagkota, "High-temperature structural evolution of caesium and rubidium triiodoplumbates," *Journal of Physics and Chemistry of Solids*, vol. 69, no. 10, pp. 2520–2526, 2008.
- [51] G. E. Eperon, S. D. Stranks, C. Menelaou, M. B. Johnston, L. M. Herz, and H. J. Snaith, "Formamidinium lead trihalide: a broadly tunable perovskite for efficient planar heterojunction solar cells," *Energy & Environmental Science*, vol. 7, no. 3, pp. 982–988, 2014.
- [52] C. Motta, F. El-Mellouhi, S. Kais, N. Tabet, F. Alharbi, and S. Sanvito, "Revealing the role of organic cations in hybrid halide perovskite  $\text{CH}_3\text{NH}_3\text{PbI}_3$ ," *Nature communications*, vol. 6, p. 7026, 2015.
- [53] G. Niu, X. Guo, and L. Wang, "Review of recent progress in chemical stability of perovskite solar cells," *Journal of Materials Chemistry A*, vol. 3, no. 17, pp. 8970–8980, 2015.
- [54] J. M. Frost, K. T. Butler, F. Brivio, C. H. Hendon, M. Van Schilfgaarde, and A. Walsh, "Atomistic origins of high-performance in hybrid halide perovskite solar cells," *Nano letters*, vol. 14, no. 5, pp. 2584–2590, 2014.
- [55] X. Li, M. I. Dar, C. Yi, J. Luo, M. Tschumi, S. M. Zakeeruddin, M. K. Nazeeruddin, H. Han, and M. Grätzel, "Improved performance and stability of perovskite solar cells by crystal crosslinking with alkylphosphonic acid  $\omega$ -ammonium chlorides," *Nature chemistry*, vol. 7, no. 9, p. 703, 2015.
- [56] M. Saliba, T. Matsui, K. Domanski, J.-Y. Seo, A. Ummadisingu, S. M. Zakeeruddin, J.-P. Correa-Baena, W. R. Tress, A. Abate, A. Hagfeldt, and others, "Incorporation of rubidium cations into perovskite solar cells improves photovoltaic performance," *Science*, vol. 354, no. 6309, pp. 206–209, 2016.
- [57] D. Wang, M. Wright, N. K. Elumalai, and A. Uddin, "Stability of perovskite solar cells," *Solar Energy Materials and Solar Cells*, vol. 147, pp. 255–275, 2016.
- [58] H.-S. Kim, C.-R. Lee, J.-H. Im, K.-B. Lee, T. Moehl, A. Marchioro, S.-J. Moon, R. Humphry-Baker, J.-H. Yum, J. E. Moser, and others, "Lead iodide perovskite sensitized all-solid-state submicron thin film mesoscopic solar cell with efficiency exceeding 9%," *Scientific reports*, vol. 2, p. 591, 2012.

- [59] K. Liang, D. B. Mitzi, and M. T. Prikas, "Synthesis and characterization of organic-inorganic perovskite thin films prepared using a versatile two-step dipping technique," *Chemistry of materials*, vol. 10, no. 1, pp. 403–411, 1998.
- [60] M. Liu, M. B. Johnston, and H. J. Snaith, "Efficient planar heterojunction perovskite solar cells by vapour deposition," *Nature*, vol. 501, no. 7467, p. 395, 2013.
- [61] Q. Chen, H. Zhou, Z. Hong, S. Luo, H.-S. Duan, H.-H. Wang, Y. Liu, G. Li, and Y. Yang, "Planar heterojunction perovskite solar cells via vapor-assisted solution process," *Journal of the American Chemical Society*, vol. 136, no. 2, pp. 622–625, 2013.
- [62] A. Kojima, M. Ikegami, K. Teshima, and T. Miyasaka, "Highly luminescent lead bromide perovskite nanoparticles synthesized with porous alumina media," *Chemistry Letters*, vol. 41, no. 4, pp. 397–399, 2012.
- [63] L. C. Schmidt, A. Pertegás, S. González-Carrero, O. Malinkiewicz, S. Agouram, G. Minguez Espallargas, H. J. Bolink, R. E. Galian, and J. Pérez-Prieto, "Nontemplate synthesis of  $\text{CH}_3\text{NH}_3\text{PbBr}_3$  perovskite nanoparticles," *Journal of the American Chemical Society*, vol. 136, no. 3, pp. 850–853, 2014.
- [64] A. Kojima, K. Teshima, Y. Shirai, and T. Miyasaka, "Organometal halide perovskites as visible-light sensitizers for photovoltaic cells," *Journal of the American Chemical Society*, vol. 131, no. 17, pp. 6050–6051, 2009.
- [65] Z. Ku, Y. Rong, M. Xu, T. Liu, and H. Han, "Full printable processed mesoscopic  $\text{CH}_3\text{NH}_3\text{PbI}_3/\text{TiO}_2$  heterojunction solar cells with carbon counter electrode," *Scientific reports*, vol. 3, p. 3132, 2013.
- [66] D. B. Mitzi, "Thin-film deposition of organic-inorganic hybrid materials," *Chemistry of Materials*, vol. 13, no. 10, pp. 3283–3298, 2001.
- [67] J. Burschka, N. Pellet, S.-J. Moon, R. Humphry-Baker, P. Gao, M. K. Nazeeruddin, and M. Grätzel, "Sequential deposition as a route to high-performance perovskite-sensitized solar cells," *Nature*, vol. 499, no. 7458, p. 316, 2013.
- [68] K. Yan, M. Long, T. Zhang, Z. Wei, H. Chen, S. Yang, and J. Xu, "Hybrid halide perovskite solar cell precursors: colloidal chemistry and coordination engineering behind device processing for high efficiency," *Journal of the American Chemical Society*, vol. 137, no. 13, pp. 4460–4468, 2015.
- [69] S. Masi, F. Aiello, A. Listorti, F. Balzano, D. Altamura, C. Giannini, R. Caliandro, G. Uccello-Barretta, A. Rizzo, and S. Colella, "Connecting the solution chemistry of  $\text{PbI}_2$  and MAI: A cyclodextrin-based supramolecular approach to the formation of hybrid halide perovskites," *Chemical science*, vol. 9, no. 12, pp. 3200–3208, 2018.
- [70] F. Hao, C. C. Stoumpos, Z. Liu, R. P. Chang, and M. G. Kanatzidis, "Controllable perovskite crystallization at a gas-solid interface for hole conductor-free solar cells with steady



- power conversion efficiency over 10%,” *Journal of the American Chemical Society*, vol. 136, no. 46, pp. 16411–16419, 2014.
- [71] S. A. Fateev, A. A. Petrov, V. N. Khrustalev, P. V. Dorovatovskii, Y. V. Zubavichus, E. A. Goodilin, and A. B. Tarasov, “Solution Processing of Methylammonium Lead Iodide Perovskite from  $\gamma$ -Butyrolactone: Crystallization Mediated by Solvation Equilibrium,” *Chemistry of Materials*, vol. 30, no. 15, pp. 5237–5244, 2018.
- [72] B. Cai, W.-H. Zhang, and J. Qiu, “Solvent engineering of spin-coating solutions for planar-structured high-efficiency perovskite solar cells,” *Chinese Journal of Catalysis*, vol. 36, no. 8, pp. 1183–1190, 2015.
- [73] J. Cao, X. Jing, J. Yan, C. Hu, R. Chen, J. Yin, J. Li, and N. Zheng, “Identifying the molecular structures of intermediates for optimizing the fabrication of high-quality perovskite films,” *Journal of the American Chemical Society*, vol. 138, no. 31, pp. 9919–9926, 2016.
- [74] M. Spina, E. Bonvin, A. Sienkiewicz, B. Náfrádi, L. Forró, and E. Horváth, “Controlled growth of  $\text{CH}_3\text{NH}_3\text{PbI}_3$  nanowires in arrays of open nanofluidic channels,” *Scientific reports*, vol. 6, p. 19834, 2016.
- [75] Q. Zhou, J. G. Park, R. Nie, A. K. Thokchom, D. Ha, J. Pan, S. I. Seok, and T. Kim, “Nanochannel-assisted perovskite nanowires: from growth mechanisms to photodetector applications,” *ACS nano*, vol. 12, no. 8, pp. 8406–8414, 2018.
- [76] A. A. Petrov, I. P. Sokolova, N. A. Belich, G. S. Peters, P. V. Dorovatovskii, Y. V. Zubavichus, V. N. Khrustalev, A. V. Petrov, M. Grätzel, E. A. Goodilin, and others, “Crystal structure of DMF-intermediate phases uncovers the link between  $\text{CH}_3\text{NH}_3\text{PbI}_3$  morphology and precursor stoichiometry,” *The Journal of Physical Chemistry C*, vol. 121, no. 38, pp. 20739–20743, 2017.
- [77] Y. Guo, K. Shoyama, W. Sato, Y. Matsuo, K. Inoue, K. Harano, C. Liu, H. Tanaka, and E. Nakamura, “Chemical pathways connecting lead (II) iodide and perovskite via polymeric plumbate (II) fiber,” *Journal of the American Chemical Society*, vol. 137, no. 50, pp. 15907–15914, 2015.
- [78] P. Scherrer, “Bestimmung der inneren Struktur und der Größe von Kolloidteilchen mittels Röntgenstrahlen,” in *Kolloidchemie Ein Lehrbuch*, pp. 387–409, Springer, 1912.
- [79] R. L. Milot, G. E. Eperon, H. J. Snaith, M. B. Johnston, and L. M. Herz, “Temperature-dependent charge-carrier dynamics in  $\text{CH}_3\text{NH}_3\text{PbI}_3$  perovskite thin films,” *Advanced Functional Materials*, vol. 25, no. 39, pp. 6218–6227, 2015.
- [80] X.-Y. Zhu and V. Podzorov, *Charge carriers in hybrid organic–inorganic lead halide perovskites might be protected as large polarons*. ACS Publications, 2015.
- [81] H. Kim, J. Hunger, E. Cánovas, M. Karakus, Z. Mics, M. Grechko, D. Turchinovich, S. H. Parekh, and M. Bonn, “Direct observation of mode-specific phonon-band gap coupling

- in methylammonium lead halide perovskites,” *Nature communications*, vol. 8, no. 1, pp. 1–9, 2017.
- [82] W. L. Leong, Z.-E. Ooi, D. Sabba, C. Yi, S. M. Zakeeruddin, M. Graetzel, J. M. Gordon, E. A. Katz, and N. Mathews, “Identifying fundamental limitations in halide perovskite solar cells,” *Advanced Materials*, vol. 28, no. 12, pp. 2439–2445, 2016.
- [83] W. Huang, S. Yue, Y. Liu, L. Zhu, P. Jin, Q. Wu, Y. Zhang, Y. Chen, K. Liu, P. Liang, and others, “Observation of unusual optical band structure of  $\text{CH}_3\text{NH}_3\text{PbI}_3$  perovskite single crystal,” *ACS Photonics*, vol. 5, no. 4, pp. 1583–1590, 2018.
- [84] H. Wang, L. Whittaker-Brooks, and G. R. Fleming, “Exciton and free charge dynamics of methylammonium lead iodide perovskites are different in the tetragonal and orthorhombic phases,” *The Journal of Physical Chemistry C*, vol. 119, no. 34, pp. 19590–19595, 2015.
- [85] N. Onoda-Yamamuro, T. Matsuo, and H. Suga, “Dielectric study of  $\text{CH}_3\text{NH}_3\text{PbI}_3$  ( $\text{X} = \text{Cl}, \text{Br}, \text{I}$ ),” *Journal of Physics and Chemistry of Solids*, vol. 53, no. 7, pp. 935–939, 1992.
- [86] C. Wehrenfennig, M. Liu, H. J. Snaith, M. B. Johnston, and L. M. Herz, “Charge carrier recombination channels in the low-temperature phase of organic-inorganic lead halide perovskite thin films,” *Apl Materials*, vol. 2, no. 8, p. 081513, 2014.
- [87] A. Osherov, E. M. Hutter, K. Galkowski, R. Brenes, D. K. Maude, R. J. Nicholas, P. Plochocka, Bulović, T. J. Savenije, and S. D. Stranks, “The impact of phase retention on the structural and optoelectronic properties of metal halide perovskites,” *Advanced Materials*, vol. 28, no. 48, pp. 10757–10763, 2016.
- [88] A. Dobrovolsky, A. Merdasa, E. L. Unger, A. Yartsev, and I. G. Scheblykin, “Defect-induced local variation of crystal phase transition temperature in metal-halide perovskites,” *Nature communications*, vol. 8, no. 1, p. 34, 2017.
- [89] F. Brivio, J. M. Frost, J. M. Skelton, A. J. Jackson, O. J. Weber, M. T. Weller, A. R. Goni, M. Leguy, P. R. Barnes, and A. Walsh, “Lattice dynamics and vibrational spectra of the orthorhombic, tetragonal, and cubic phases of methylammonium lead iodide,” *Physical Review B*, vol. 92, no. 14, p. 144308, 2015.
- [90] A. Pisoni, J. Jacimovic, B. Náfrádi, P. Szirmai, M. Spina, R. Gaál, K. Holczer, E. Tutis, L. Forró, and E. Horváth, “Metallicity and conductivity crossover in white light illuminated  $\text{CH}_3\text{NH}_3\text{PbI}_3$  perovskite,” *arXiv preprint arXiv:1604.05637*, 2016.
- [91] A. Poglitsch and D. Weber, “Dynamic disorder in methylammonium trihalogeno-plumbates (II) observed by millimeter-wave spectroscopy,” *The Journal of chemical physics*, vol. 87, no. 11, pp. 6373–6378, 1987.
- [92] A. A. Bakulin, O. Selig, H. J. Bakker, Y. L. Rezus, C. Müller, T. Glaser, R. Lovrincic, Z. Sun, Chen, A. Walsh, and others, “Real-time observation of organic cation reorientation in methylammonium lead iodide perovskites,” *The journal of physical chemistry letters*, vol. 6, no. 18, pp. 3663–3669, 2015.

- [93] M. N. F. Hoque, N. Islam, Z. Li, G. Ren, K. Zhu, and Z. Fan, "Ionic and Optical Properties of Methylammonium Lead Iodide Perovskite across the Tetragonal–Cubic Structural Phase Transition," *ChemSusChem*, vol. 9, no. 18, pp. 2692–2698, 2016.
- [94] Y. Kutes, L. Ye, Y. Zhou, S. Pang, B. D. Huey, and N. P. Padture, "Direct observation of ferroelectric domains in solution-processed  $\text{CH}_3\text{NH}_3\text{PbI}_3$  perovskite thin films," *The journal of physical chemistry letters*, vol. 5, no. 19, pp. 3335–3339, 2014.
- [95] A. Arakcheeva, D. Chernyshov, M. Spina, L. Forró, and E. Horváth, " $\text{CH}_3\text{NH}_3\text{PbI}_3$ : precise structural consequences of water absorption at ambient conditions," *Acta Crystallographica Section B: Structural Science, Crystal Engineering and Materials*, vol. 72, no. 5, pp. 716–722, 2016.
- [96] W. A. Saidi and J. J. Choi, "Nature of the cubic to tetragonal phase transition in methylammonium lead iodide perovskite," *The Journal of chemical physics*, vol. 145, no. 14, p. 144702, 2016.
- [97] S. Van Smaalen, *Incommensurate crystallography*, vol. 21. Oxford University Press, 2007.
- [98] S. van Smaalen, B. J. Campbell, and H. T. Stokes, "Equivalence of superspace groups," *Acta Crystallographica Section A: Foundations of Crystallography*, vol. 69, no. 1, pp. 75–90, 2013.
- [99] T. Tyson, W. Gao, Y.-S. Chen, S. Ghose, and Y. Yan, "Large Thermal Motion in Halide Perovskites," *Scientific reports*, vol. 7, no. 1, p. 9401, 2017.
- [100] M. de Boissieu, "Ted Janssen and aperiodic crystals," *Acta Crystallographica Section A: Foundations and Advances*, vol. 75, no. 2, 2019.
- [101] P. A. Fleury, "The effects of soft modes on the structure and properties of materials," *Annual Review of Materials Science*, vol. 6, no. 1, pp. 157–180, 1976.
- [102] E. M. Schmidt and R. B. Neder, "Interpretation of diffuse scattering using superspace crystallography," *Physical Review B*, vol. 100, no. 5, p. 054201, 2019.
- [103] A. N. Beecher, O. E. Semonin, J. M. Skelton, J. M. Frost, M. W. Terban, H. Zhai, A. Alatas, J. S. Owen, A. Walsh, and S. J. Billinge, "Direct observation of dynamic symmetry breaking above room temperature in methylammonium lead iodide perovskite," *ACS energy Letters*, vol. 1, no. 4, pp. 880–887, 2016.
- [104] N. Onoda-Yamamuro, T. Matsuo, and H. Suga, "Calorimetric and IR spectroscopic studies of phase transitions in methylammonium trihalogenoplumbates (II)," *Journal of Physics and Chemistry of Solids*, vol. 51, no. 12, pp. 1383–1395, 1990.
- [105] E. M. Hutter, M. C. Gélvez-Rueda, A. Osherov, V. Bulović, F. C. Grozema, S. D. Stranks, and T. J. Savenije, "Direct–indirect character of the bandgap in methylammonium lead iodide perovskite," *Nature materials*, vol. 16, no. 1, p. 115, 2017.

## Bibliography

---

- [106] A. Katrusiak, "High-pressure crystallography," *Acta Crystallographica Section A: Foundations of Crystallography*, vol. 64, no. 1, pp. 135–148, 2008.
- [107] A. Jaffe, Y. Lin, C. M. Beavers, J. Voss, W. L. Mao, and H. I. Karunadasa, "High-pressure single-crystal structures of 3d lead-halide hybrid perovskites and pressure effects on their electronic and optical properties," *ACS central science*, vol. 2, no. 4, pp. 201–209, 2016.
- [108] F. Capitani, C. Marini, S. Caramazza, P. Postorino, G. Garbarino, M. Hanfland, A. Pisanu, P. Quadrelli, and L. Malavasi, "High-pressure behavior of methylammonium lead iodide (MAPbI<sub>3</sub>) hybrid perovskite," *Journal of Applied Physics*, vol. 119, no. 18, p. 185901, 2016.
- [109] T. Ou, J. Yan, C. Xiao, W. Shen, C. Liu, X. Liu, Y. Han, Y. Ma, and C. Gao, "Visible light response, electrical transport, and amorphization in compressed organolead iodine perovskites," *Nanoscale*, vol. 8, no. 22, pp. 11426–11431, 2016.
- [110] S. Jiang, Y. Fang, R. Li, H. Xiao, J. Crowley, C. Wang, T. J. White, W. A. Goddard III, Z. Wang, Baikie, and others, "Pressure-Dependent Polymorphism and Band-Gap Tuning of Methylammonium Lead Iodide Perovskite," *Angewandte Chemie International Edition*, vol. 55, no. 22, pp. 6540–6544, 2016.
- [111] M. Szafranski and A. Katrusiak, "Mechanism of pressure-induced phase transitions, amorphization, and absorption-edge shift in photovoltaic methylammonium lead iodide," *The journal of physical chemistry letters*, vol. 7, no. 17, pp. 3458–3466, 2016.
- [112] A. Francisco-López, B. Charles, O. J. Weber, M. I. Alonso, M. Garriga, M. Campoy-Quiles, T. Weller, and A. R. Goñi, "Pressure-induced locking of methylammonium cations versus amorphization in hybrid lead iodide perovskites," *The Journal of Physical Chemistry C*, vol. 122, no. 38, pp. 22073–22082, 2018.
- [113] F. Birch, "Finite elastic strain of cubic crystals," *Physical review*, vol. 71, no. 11, p. 809, 1947.
- [114] C. M. Novak and R. C. Fortenberry, "Theoretical rovibrational analysis of the covalent noble gas compound ArNH<sup>+</sup>," *Journal of Molecular Spectroscopy*, vol. 322, pp. 29–32, 2016.
- [115] C. Motta, F. El-Mellouhi, and S. Sanvito, "Charge carrier mobility in hybrid halide perovskites," *Scientific reports*, vol. 5, p. 12746, 2015.
- [116] D. B. Mitzi, "Templating and structural engineering in organic–inorganic perovskites," *Journal of the Chemical Society, Dalton Transactions*, no. 1, pp. 1–12, 2001.
- [117] T. Chen, W.-L. Chen, B. J. Foley, J. Lee, J. P. Ruff, J. P. Ko, C. M. Brown, L. W. Harriger, Zhang, C. Park, and others, "Origin of long lifetime of band-edge charge carriers in organic–inorganic lead iodide perovskites," *Proceedings of the National Academy of Sciences*, vol. 114, no. 29, pp. 7519–7524, 2017.
- [118] T. D. d. Morais, F. Chaput, K. Lahlil, and J.-P. Boilot, "Hybrid Organic–Inorganic Light-Emitting Diodes," *Advanced materials*, vol. 11, no. 2, pp. 107–112, 1999.

- [119] D. B. Mitzi, K. Chondroudis, and C. R. Kagan, "Organic-inorganic electronics," *IBM journal of research and development*, vol. 45, no. 1, pp. 29–45, 2001.
- [120] H.-B. Duan, S.-S. Yu, S.-X. Liu, and H. Zhang, "An inorganic–organic hybrid crystal with a two-step dielectric response and thermochromic luminescence," *Dalton Transactions*, vol. 46, no. 7, pp. 2220–2227, 2017.
- [121] W. Nie, H. Tsai, R. Asadpour, J.-C. Blancon, A. J. Neukirch, G. Gupta, J. J. Crochet, M. Chhowalla, S. Tretiak, M. A. Alam, and others, "High-efficiency solution-processed perovskite solar cells with millimeter-scale grains," *Science*, vol. 347, no. 6221, pp. 522–525, 2015.
- [122] M. A. Green, Y. Jiang, A. M. Soufiani, and A. Ho-Baillie, "Optical properties of photovoltaic organic–inorganic lead halide perovskites," *The journal of physical chemistry letters*, vol. 6, no. 23, pp. 4774–4785, 2015.
- [123] J. Harada and K. Ogawa, "Pedal motion in crystals," *Chemical Society Reviews*, vol. 38, no. 8, pp. 2244–2252, 2009.
- [124] O. J. Weber, K. L. Marshall, L. M. Dyson, and M. T. Weller, "Structural diversity in hybrid organic–inorganic lead iodide materials," *Acta Crystallographica Section B: Structural Science, Crystal Engineering and Materials*, vol. 71, no. 6, pp. 668–678, 2015.
- [125] M. Kollár, L. Ćirić, J. H. Dil, A. Weber, S. Muff, H. M. Ronnow, B. Náfrádi, B. P. Monnier, J. S. Luterbacher, L. Forró, and others, "Clean, cleaved surfaces of the photovoltaic perovskite," *Scientific reports*, vol. 7, no. 1, p. 695, 2017.
- [126] J. Ma and L.-W. Wang, "Nanoscale charge localization induced by random orientations of organic molecules in hybrid perovskite  $\text{CH}_3\text{NH}_3\text{PbI}_3$ ," *Nano letters*, vol. 15, no. 1, pp. 248–253, 2014.
- [127] T. Etienne, E. Mosconi, and F. De Angelis, "Dynamical origin of the Rashba effect in organohalide lead perovskites: A key to suppressed carrier recombination in perovskite solar cells?," *The journal of physical chemistry letters*, vol. 7, no. 9, pp. 1638–1645, 2016.
- [128] D. H. Chun, Y. J. Choi, Y. In, J. K. Nam, Y. J. Choi, S. Yun, W. Kim, D. Choi, D. Kim, H. Shin, and others, "Halide Perovskite Nanopillar Photodetector," *ACS nano*, vol. 12, no. 8, pp. 8564–8571, 2018.
- [129] L. Cui, Y. Li, J. Wang, E. Tian, X. Zhang, Y. Zhang, Y. Song, and L. Jiang, "Fabrication of large-area patterned photonic crystals by ink-jet printing," *Journal of Materials Chemistry*, vol. 19, no. 31, pp. 5499–5502, 2009.
- [130] S. Yoo, J. S. Hsieh, P. Zou, and J. Kokoszka, "Utilization of calcium carbonate particles from eggshell waste as coating pigments for ink-jet printing paper," *Bioresource technology*, vol. 100, no. 24, pp. 6416–6421, 2009.

## Bibliography

---

- [131] J. Sumerel, J. Lewis, A. Doraiswamy, L. F. Deravi, S. L. Sewell, A. E. Gerdon, D. W. Wright, and R. J. Narayan, "Piezoelectric ink jet processing of materials for medical and biological applications," *Biotechnology Journal: Healthcare Nutrition Technology*, vol. 1, no. 9, pp. 976–987, 2006.
- [132] S. J. Leigh, R. J. Bradley, C. P. Purcell, D. R. Billson, and D. A. Hutchins, "A simple, low-cost conductive composite material for 3d printing of electronic sensors," *PloS one*, vol. 7, no. 11, p. e49365, 2012.
- [133] M. Chen, J. Yang, Z. Wang, Z. Xu, H. Lee, H. Lee, Z. Zhou, S.-P. Feng, S. Lee, J. Pyo, and others, "3d Nanoprinting of Perovskites," *Advanced Materials*, p. 1904073, 2019.
- [134] Z. Wei, H. Chen, K. Yan, and S. Yang, "Inkjet printing and instant chemical transformation of a  $\text{CH}_3\text{NH}_3\text{PbI}_3$ /nanocarbon electrode and interface for planar perovskite solar cells," *Angewandte Chemie International Edition*, vol. 53, no. 48, pp. 13239–13243, 2014.
- [135] J. G. Tait, E. Witkowska, M. Hirade, T.-H. Ke, P. E. Malinowski, S. Steudel, C. Adachi, and P. Heremans, "Uniform Aerosol Jet printed polymer lines with 30  $\mu\text{m}$  width for 140 ppi resolution RGB organic light emitting diodes," *Organic Electronics*, vol. 22, pp. 40–43, 2015.
- [136] N. Wilkinson, M. Smith, R. Kay, and R. Harris, "A review of aerosol jet printing—a non-traditional hybrid process for micro-manufacturing," *The International Journal of Advanced Manufacturing Technology*, pp. 1–21, 2019.
- [137] F. Mathies, T. Abzieher, A. Hochstuhl, K. Glaser, A. Colsmann, U. W. Paetzold, G. Hernandez-Sosa, U. Lemmer, and A. Quintilla, "Multipass inkjet printed planar methylammonium lead iodide perovskite solar cells," *Journal of Materials Chemistry A*, vol. 4, no. 48, pp. 19207–19213, 2016.
- [138] S. Yakunin, M. Sytnyk, D. Kriegner, S. Shrestha, M. Richter, G. J. Matt, H. Azimi, C. J. Brabec, J. Stangl, M. V. Kovalenko, and others, "Detection of X-ray photons by solution-processed lead halide perovskites," *Nature photonics*, vol. 9, no. 7, p. 444, 2015.
- [139] S.-G. Li, K.-J. Jiang, M.-J. Su, X.-P. Cui, J.-H. Huang, Q.-Q. Zhang, X.-Q. Zhou, L.-M. Yang, and Y.-L. Song, "Inkjet printing of  $\text{CH}_3\text{NH}_3\text{PbI}_3$  on a mesoscopic  $\text{TiO}_2$  film for highly efficient perovskite solar cells," *Journal of Materials Chemistry A*, vol. 3, no. 17, pp. 9092–9097, 2015.
- [140] H. J. Choi, J. W. Roh, S.-S. Seo, S. Lee, J.-Y. Kim, S.-K. Kim, K. W. Kang, J. S. Lee, J. Y. Jeong, and S.-Y. Park, "Comparison of the accuracy of magnetic resonance imaging and positron emission tomography/computed tomography in the presurgical detection of lymph node metastases in patients with uterine cervical carcinoma: a prospective study," *Cancer*, vol. 106, no. 4, pp. 914–922, 2006.
- [141] L. A. Hunter, S. Krafft, F. Stingo, H. Choi, M. K. Martel, S. F. Kry, and L. E. Court, "High quality machine-robust image features: Identification in nonsmall cell lung cancer computed tomography images," *Medical physics*, vol. 40, no. 12, p. 121916, 2013.

- 
- [142] G. J. Davis, A. S. Kapatkin, L. E. Craig, G. S. Heins, and J. A. Wortman, "Comparison of radiography, computed tomography, and magnetic resonance imaging for evaluation of appendicular osteosarcoma in dogs," *Journal of the American Veterinary Medical Association*, vol. 220, no. 8, pp. 1171–1176, 2002.
- [143] M. Sohrabi, "The state-of-the-art on worldwide studies in some environments with elevated naturally occurring radioactive materials (NORM)," *Applied Radiation and Isotopes*, vol. 49, no. 3, pp. 169–188, 1998.
- [144] J. H. Hendry, S. L. Simon, A. Wojcik, M. Sohrabi, W. Burkart, E. Cardis, D. Laurier, M. Tirmarche, and I. Hayata, "Human exposure to high natural background radiation: what can it teach us about radiation risks?," *Journal of Radiological Protection*, vol. 29, no. 2A, p. A29, 2009.
- [145] R. Smith-Bindman, J. Lipson, R. Marcus, K.-P. Kim, M. Mahesh, R. Gould, A. B. De González, and D. L. Miglioretti, "Radiation dose associated with common computed tomography examinations and the associated lifetime attributable risk of cancer," *Archives of internal medicine*, vol. 169, no. 22, pp. 2078–2086, 2009.
- [146] M. Spahn, "Flat detectors and their clinical applications," *European radiology*, vol. 15, no. 9, pp. 1934–1947, 2005.
- [147] D. Pacella, "Energy-resolved X-ray detectors: the future of diagnostic imaging," *Reports in Medical Imaging*, vol. 8, no. 1, 2015.
- [148] M. Z. Kabir, S. Kasap, W. Zhao, and J. Rowlands, "Direct conversion x-ray sensors: Sensitivity, DQE and MTF," *IEE Proceedings-Circuits, Devices and Systems*, vol. 150, no. 4, pp. 258–266, 2003.
- [149] S. Kasap, J. B. Frey, G. Belev, O. Tousignant, H. Mani, J. Greenspan, L. Laperriere, O. Bubon, A. Reznik, G. DeCrescenzo, and others, "Amorphous and polycrystalline photoconductors for direct conversion flat panel X-ray image sensors," *Sensors*, vol. 11, no. 5, pp. 5112–5157, 2011.
- [150] S. Yang, Z. Xu, S. Xue, P. Kandlakunta, L. Cao, and J. Huang, "Organohalide Lead Perovskites: More Stable than Glass under Gamma-Ray Radiation," *Advanced Materials*, vol. 31, no. 4, p. 1805547, 2019.
- [151] K. S. Novoselov, A. K. Geim, S. V. Morozov, D. Jiang, Y. Zhang, S. V. Dubonos, I. V. Grigorieva, and A. A. Firsov, "Electric field effect in atomically thin carbon films," *science*, vol. 306, no. 5696, pp. 666–669, 2004.
- [152] H. Hirai, H. Tsuchiya, Y. Kamakura, N. Mori, and M. Ogawa, "Electron mobility calculation for graphene on substrates," *Journal of Applied Physics*, vol. 116, no. 8, p. 083703, 2014.
- [153] R. R. Nair, P. Blake, A. N. Grigorenko, K. S. Novoselov, T. J. Booth, T. Stauber, N. M. Peres, and A. K. Geim, "Fine structure constant defines visual transparency of graphene," *Science*, vol. 320, no. 5881, pp. 1308–1308, 2008.

## Bibliography

---

- [154] F. Xia, T. Mueller, R. Golizadeh-Mojarad, M. Freitag, Y.-m. Lin, J. Tsang, V. Perebeinos, and P. Avouris, "Photocurrent imaging and efficient photon detection in a graphene transistor," *Nano letters*, vol. 9, no. 3, pp. 1039–1044, 2009.
- [155] M. Spina, M. Lehmann, B. Náfrádi, L. Bernard, E. Bonvin, R. Gaál, A. Magrez, L. Forró, and E. Horváth, "Microengineered CH<sub>3</sub>NH<sub>3</sub>PbI<sub>3</sub> Nanowire/Graphene Phototransistor for Low-Intensity Light Detection at Room Temperature," *Small*, vol. 11, no. 37, pp. 4824–4828, 2015.
- [156] Y. Lee, J. Kwon, E. Hwang, C.-H. Ra, W. J. Yoo, J.-H. Ahn, J. H. Park, and J. H. Cho, "High-performance perovskite-graphene hybrid photodetector," *Advanced materials*, vol. 27, no. 1, pp. 41–46, 2015.
- [157] X. Hu, X. Zhang, L. Liang, J. Bao, S. Li, W. Yang, and Y. Xie, "High-performance flexible broadband photodetector based on organolead halide perovskite," *Advanced Functional Materials*, vol. 24, no. 46, pp. 7373–7380, 2014.
- [158] H. Wei, Y. Fang, P. Mulligan, W. Chuirazzi, H.-H. Fang, C. Wang, B. R. Ecker, Y. Gao, M. A. Loi, L. Cao, and others, "Sensitive X-ray detectors made of methylammonium lead tribromide perovskite single crystals," *Nature Photonics*, vol. 10, no. 5, p. 333, 2016.
- [159] X. Li, J. Carey, J. Sickler, M. Pralle, C. Palsule, and C. Vineis, "Silicon photodiodes with high photoconductive gain at room temperature," *Optics Express*, vol. 20, no. 5, pp. 5518–5523, 2012.
- [160] H. Wei and J. Huang, "Halide lead perovskites for ionizing radiation detection," *Nature communications*, vol. 10, no. 1, p. 1066, 2019.
- [161] C. Liu, H. Peng, K. Wang, C. Wei, Z. Wang, and X. Gong, "PbS quantum dots-induced trap-assisted charge injection in perovskite photodetectors," *Nano Energy*, vol. 30, pp. 27–35, 2016.
- [162] Y. Dan, X. Zhao, K. Chen, and A. Mesli, "A photoconductor intrinsically has no gain," *ACS Photonics*, vol. 5, no. 10, pp. 4111–4116, 2018.
- [163] J. Li, H.-L. Cao, W.-B. Jiao, Q. Wang, M. Wei, I. Cantone, J. Lü, and A. Abate, "Biological impact of lead from halide perovskites reveals the risk of introducing a safe threshold," *Nature Communications*, vol. 11, no. 1, pp. 1–5, 2020.
- [164] M. Acik, T. M. Alam, F. Guo, Y. Ren, B. Lee, R. A. Rosenberg, J. F. Mitchell, I. K. Park, G. Lee, and S. B. Darling, "Substitutional growth of methylammonium lead iodide perovskites in alcohols," *Advanced Energy Materials*, vol. 8, no. 5, p. 1701726, 2018.
- [165] H. Toraya, "Introduction to X-ray analysis using the diffraction method," *The Rigaku Journal*, vol. 32, no. 2, 2016.
- [166] T. Janssen, G. Chapuis, and M. De Boissieu, *Aperiodic Crystals: From Modulated Phases to Quasicrystals: Structure and Properties*. Oxford University Press, 2018.



- [167] K. Hasegawa, "Introduction to single crystal X-ray analysis," *The Rigaku Journal*, vol. 28, no. 1, pp. 14–18, 2012.
- [168] H. Rietveld, "Line profiles of neutron powder-diffraction peaks for structure refinement," *Acta Crystallographica*, vol. 22, no. 1, pp. 151–152, 1967.
- [169] A. Authier and G. Chapuis, *A Little Dictionary of Crystallography*. International Union of Crystallography, 2014.
- [170] W. David, "Powder diffraction: Least-squares and beyond," *Journal of research of the National Institute of Standards and Technology*, vol. 109, no. 1, p. 107, 2004.
- [171] T. Janssen and A. Janner, "Aperiodic crystals and superspace concepts," *Acta Crystallographica Section B: Structural Science, Crystal Engineering and Materials*, vol. 70, no. 4, pp. 617–651, 2014.
- [172] J. Sun, S. Lee, and J. Lin, "Four-Dimensional Space Groups for Pedestrians: Composite Structures," *Chemistry—An Asian Journal*, vol. 2, no. 10, pp. 1204–1229, 2007.
- [173] T. Janssen, G. Chapuis, and M. de Boissieu, *Aperiodic Crystals: From Modulated Phases to Quasicrystals*. Oxford University Press, 2007.
- [174] V. Petříček, M. Dušek, and L. Palatinus, "Crystallographic computing system JANA2006: general features," *Zeitschrift für Kristallographie-Crystalline Materials*, vol. 229, no. 5, pp. 345–352, 2014.
- [175] V. Dyadkin, P. Pattison, V. Dmitriev, and D. Chernyshov, "A new multipurpose diffractometer PILATUS@ SNBL," *Journal of synchrotron radiation*, vol. 23, no. 3, pp. 825–829, 2016.
- [176] L. Palatinus and G. Chapuis, "SUPERFLIP—a computer program for the solution of crystal structures by charge flipping in arbitrary dimensions," *Journal of Applied Crystallography*, vol. 40, no. 4, pp. 786–790, 2007.
- [177] A. Pisoni, J. Jacimovic, O. S. Barisic, M. Spina, R. Gaál, L. Forró, and E. Horváth, "Ultra-low thermal conductivity in organic–inorganic hybrid perovskite  $\text{CH}_3\text{NH}_3\text{PbI}_3$ ," *The journal of physical chemistry letters*, vol. 5, no. 14, pp. 2488–2492, 2014.
- [178] X. Mettan, R. Pisoni, P. Matus, A. Pisoni, J. Jaćimović, B. Náfrádi, M. Spina, D. Pavuna, L. Forró, and E. Horváth, "Tuning of the Thermoelectric Figure of Merit of  $\text{CH}_3\text{NH}_3\text{PbMI}_3$  (M Pb, Sn) Photovoltaic Perovskites," *The Journal of Physical Chemistry C*, vol. 119, no. 21, pp. 11506–11510, 2015.
- [179] A. Dualeh, P. Gao, S. I. Seok, M. K. Nazeeruddin, and M. Grätzel, "Thermal behavior of methylammonium lead-trihalide perovskite photovoltaic light harvesters," *Chemistry of Materials*, vol. 26, no. 21, pp. 6160–6164, 2014.

## Bibliography

---

- [180] I. R. Benmessaoud, A.-L. Mahul-Mellier, E. Horvath, B. Maco, M. Spina, H. A. Lashuel, and L. Forró, "Health hazards of methylammonium lead iodide based perovskites: cytotoxicity studies," *Toxicology research*, vol. 5, no. 2, pp. 407–419, 2016.
- [181] Z. Zhu, Q. Sun, Z. Zhang, J. Dai, G. Xing, S. Li, X. Huang, and W. Huang, "Metal halide perovskites: stability and sensing-ability," *Journal of Materials Chemistry C*, vol. 6, no. 38, pp. 10121–10137, 2018.
- [182] K. Ren, L. Huang, S. Yue, S. Lu, K. Liu, M. Azam, Z. Wang, Z. Wei, S. Qu, and Z. Wang, "Turning a disadvantage into an advantage: synthesizing high-quality organometallic halide perovskite nanosheet arrays for humidity sensors," *Journal of Materials Chemistry C*, vol. 5, no. 10, pp. 2504–2508, 2017.
- [183] Z. Weng, J. Qin, A. A. Umar, J. Wang, X. Zhang, H. Wang, X. Cui, X. Li, L. Zheng, and Y. Zhan, "Lead-Free  $\text{Cs}_2\text{BiAgBr}_6$  Double Perovskite-Based Humidity Sensor with Superfast Recovery Time," *Advanced Functional Materials*, p. 1902234, 2019.
- [184] F. Lazarini, "Caesium enneabromodibismuthate (III)," *Acta Crystallographica Section B: Structural Crystallography and Crystal Chemistry*, vol. 33, no. 9, pp. 2961–2964, 1977.
- [185] J. Zhao, N. Li, H. Yu, Z. Wei, M. Liao, P. Chen, S. Wang, D. Shi, Q. Sun, and G. Zhang, "Highly sensitive  $\text{MoS}_2$  humidity sensors array for noncontact sensation," *Advanced Materials*, vol. 29, no. 34, p. 1702076, 2017.
- [186] N. Agmon, "The grotthuss mechanism," *Chemical Physics Letters*, vol. 244, no. 5-6, pp. 456–462, 1995.

# Anastasiia Glushkova | CV

Lausanne – Switzerland

+41 78 674 47 11 • anastasiia.glushkova@epfl.ch

piuu@phystech.edu



## Education

### Ecole Polytechnique Fédérale de Lausanne (EPFL)

*PhD*

Doctoral Program in Physics (EDPY)

Lausanne, Switzerland

2017–2020

### Moscow Institute of Physics and Technology (MIPT)

*Masters, 4.8/5*

Physics and Technology of Nanostructures

Dolgoprudnii, Russia

2014–2016

### Moscow Institute of Physics and Technology (MIPT)

*Bachelors, 4.6/5*

Applied Physics and Mathematics

Dolgoprudnii, Russia

2010–2014

## Work and Research

### Laboratory of Physics of Complex Matter

*prof. László Forró*

Structure and structuring photovoltaic perovskite

EPFL

01.2017–05.2020

### Laboratory of Artificial Quantum Systems

*prof. Oleg Astafiev*

Fabrication of Superconducting circuits for quantum optics.

MIPT

08.2014–07.2016

### Internship at Laboratory of Photonics and Quantum Measurements

*prof. Tobias Kippenberg*

Microwave to optical conversion in electro-optical systems.

EPFL

07.2015–03.2016

### Laboratory of Satellite Monitoring Technology

*Evgenii Loupian*

Development of a method for creation and analysis of a time portraits of agricultural crops based on satellite data.

Space Research Institute (RAS)

07.2013–07.2014

## Research Topics

- Design & fabrication of nanostructures
- Quantum optics & Quantum Information
- Perovskite, Transition metal dichalcogenide (TMD)
- Superconducting circuits
- Satellite Data Processing
- Crystallography

## Skills & Experience

**Cleanroom fabrication:** 6 years experience: 2 years at MIPT and 4 at Center of MicroNanoTechnology (CMi), EPFL. Optolithography, electron-beam lithography, wet and dry etching, sputtering and evaporation, TMD transfer

**Measurements:** DC & Microwave & XRD measurements  
**Programming:** Python, C  
**Illustration:** Adobe Illustrator

## Languages

---

<b>Russian:</b> C2	<i>Mother tongue</i>
<b>English:</b> C1	<i>Fluent</i>
<b>French:</b> B1	<i>Intermediate</i>
<b>German:</b> A1	<i>Basic communication skills</i>

## Achievements

---

Owing to high scores at MIPT received a scholarship of the Foundation for the Development of Innovation Education.

During the Master studies, received Scholarship of the Moscow Government.

For the internship project at EPFL received a scholarship from Zeno-Karl-Schindler Foundation from July to December, 2015.

## Schools & Conferences

---

- 18th IEEE International Conference on Nanotechnology (IEEE NANO 2018), Cork, Ireland, 23-26 July, 2018
- 10th International Conference on Hybrid and Organic Photovoltaics (HOPV 18), Benidorm, Spain, 28-31 May, 2018
- 4th European Crystallography School (ECS4), Warsaw, Poland, 2-7 July, 2017
- International Conference on Hybrid and Organic Photovoltaics (HOPV 17), Lausanne, Switzerland, 21-24 May, 2017
- 18th CMi Annual Review Meeting, Lausanne, Switzerland, 2 May, 2017. Poster: On-chip microwave-to-optical quantum coherent converter
- Quantum Simulation and Computation Summer School, Gothenburg, Sweden, June 21-26, 2015
- Asia-Pacific Conference Workshop on Quantum Information Science 2014, Tainan, Taiwan (ROC), December 12-15, 2014
- XI Conference of Young Scientists - Fundamental and applied space research, Moscow, Space Research Institute of the Russian Academy of Sciences, 9-11 April, 2014
- The Eleventh Open National Conference - Modern problems of remote sensing of the Earth from Space 2013, Moscow, Space Research Institute of the Russian Academy of Sciences, 11-15 November, 2013

## Publications

---

- Rossi, L., Foschia, R., **Glushkova, A.**, Forró, L. and Horváth, E., Mechanical response of layered titanate nanowires. *Ceramics International* (2020)
- Mantulnikovs K., Szirmai P., Kollár M., Stevens J., Andričević P., **Glushkova A.**, Rossi L., Bugnon P., Horváth E., Sienkiewicz A. and Forró L., Light-induced charge transfer at the  $\text{CH}_3\text{NH}_3\text{PbI}_3$  and  $\text{CH}_3\text{NH}_3\text{PbBr}_3/\text{TiO}_2$  interface-a low-temperature Photo-EPR assay. *Journal of Physics: Photonics* (2019)

- Mantulnikovs K., **Glushkova A.**, Kollár M., Forró L., Horváth E. and Sienkiewicz A., Differential response of the photoluminescence and photocurrent of polycrystalline  $\text{CH}_3\text{NH}_3\text{PbI}_3$  and  $\text{CH}_3\text{NH}_3\text{PbBr}_3$  to the exposure to Oxygen and Nitrogen. *ACS Applied Electronic Materials*, 1(10), 2007-2017 (2019)
- **Glushkova A.**, Mantulnikovs K., Girit G., Semeniuk K., Forró L., Horváth E. and Arakcheeva A., Effect of Thermal Cycling on the Structural Evolution of Methylammonium Lead Iodide monitored around the Phase Transition Temperatures. *Solar RRL*, 3(7), 1900044 (2019)
- Arakcheeva A., Svitlyk V., Polini E., Henry L., Chernyshov D., Sienkiewicz A., Girit G., **Glushkova A.**, Kollar M., Náfrádi B. and Forro L., Pressure-induced transformation of  $\text{CH}_3\text{NH}_3\text{PbI}_3$ : the role of the noble-gas pressure transmitting media. *Acta Crystallographica Section B: Structural Science, Crystal Engineering and Materials*, 75(3) (2019)
- **Glushkova A.**, Arakcheeva A., Pattison P., Kollár M., Andričević P., Náfrádi B., Forro L. and Horvath E., Influence of the organic cation disorder on photoconductivity in ethylenediammonium lead iodide,  $\text{NH}_3\text{CH}_2\text{CH}_2\text{NH}_3\text{PbI}_4$ . *CrystEngComm*, 20(25), 3543-3549 (2018)
- Mantulnikovs K., **Glushkova A.**, Matus P., Ćirić L., Kollár M., Forró L., Horváth E. and Sienkiewicz A., Morphology and Photoluminescence of  $\text{CH}_3\text{NH}_3\text{PbI}_3$  Deposits on Nonplanar, Strongly Curved Substrates. *ACS Photonics*, 5(4), pp.1476-1485 (2018)
- Glushkov E., **Glushkova A.** and Man'ko V. (2015). Testing Entropic Inequalities for Superconducting Qudits. *Journal of Russian Laser Research*, 36(5), 448–457.
- Glushkov E., **Glushkova A.** and Man'ko V. (2015). Deriving Entropic Inequalities for Two Coupled Superconducting Circuits. ArXiv:1509.04341

## Teaching experience

---

- Correspondence physical and technical school, MIPT - math and physics teacher - 2013-2014
- Physics (for MAN), EPFL - Exercises -2016-2017
- General physics I, EPFL - Exercises -2017-2018
- General physics I, UNIL - Exercises -2018-2019
- General physics I, UNIL - Exercises -2019-2020